8-2016

Next Generation In-Vivo Forward Solution Physiological Model of the Human Lower Limb to Predict Implanted Knee Mechanics

Bradley Allen Meccia
University of Tennessee, Knoxville, bmeccia@vols.utk.edu

To the Graduate Council:

I am submitting herewith a dissertation written by Bradley Allen Meccia entitled "Next Generation In-Vivo Forward Solution Physiological Model of the Human Lower Limb to Predict Implanted Knee Mechanics." I have examined the final electronic copy of this dissertation for form and content and recommend that it be accepted in partial fulfillment of the requirements for the degree of Doctor of Philosophy, with a major in Engineering Science.

Richard D. Komistek, Major Professor

We have read this dissertation and recommend its acceptance:

Mohamed R. Mahfouz, Aly Fathy, Adrija Sharma

Accepted for the Council:
Dixie L. Thompson

Vice Provost and Dean of the Graduate School

(Original signatures are on file with official student records.)

Next Generation In-Vivo Forward Solution Physiological Model of the Human Lower Limb to Predict Implanted Knee Mechanics

A Dissertation Presented for the

Doctor of Philosophy

Degree

The University of Tennessee, Knoxville

Bradley Allen Meccia

August 2016

Dedication

This dissertation is dedicated to my father, Robert Meccia, who possessed ac MS in environmental engineering in addition to being a two sport varsity athlete at West Point a member of the U.S. Army Rangers. It is from him that I learned to love academics which has drove me to gain the knowledge necessary to complete this dissertation. His coaching in athletics also taught me the determination necessary to complete this PhD. In both his life, sickness, and death, he always placed his family first and for that I am forever grateful. Thank you, Dad.

Acknowledgements

First, I would like to thank Dr. John Mueller for developing this model which I have had the privilege of refining for the last several years. I would also like to thank Dr. Sharma for countless hours of help in the lab over the years. Most importantly, I would like to thank Dr. Komistek for his guidance in this project. His education on the theory and practice of modeling has been invaluable.

Abstract

Current total knee arthroplasty (TKA) evaluation methods are both time consuming and expensive. They require fabrication of the TKA and then utilize a wear or cadaveric simulator which does not necessarily replicate in-vivo conditions. Other analysis methods involve following the long-term success of TKA in subjects for five or more years. Mathematical modeling of TKA provide an efficient method at a greatly reduced cost for evaluating TKA. Obviously, the accuracy of a mathematical model is extremely important to the validity of the results.

Mathematical modeling of the knee faces many difficulties. The number of muscles actuating the knee is much larger than the number of equations of motion, producing an indeterminate system. Furthermore, the complex shapes of both the tibial plateaus and femoral condyles result in interactions which must be modeled using non-holonomic constrains. A forward solution mathematical model has been developed which overcomes these difficulties to serve as a theoretical simulator.

In this model, the articulating geometry of the TKA is defined mathematically. The trochlear groove, medial and lateral polyethylene plateaus, and post (in posterior stabilized designs) are defined using mathematical surfaces. Then, the femoral condyles, the patella surface, and the cam (in posterior stabilized designs) are defined using point clouds. Contact forces are computed by searching for contact between the defined surfaces and point clouds. The muscle forces are computed using control systems to generate the desired motion of the knee.

In addition the model, a graphical user interface (GUI) was developed which allows users to efficiently set up simulations for the model. This program guides the users step-by-step through mathematically defining the surfaces, selecting the orientation of the implants on the bones, and setting up initial

conditions. It also gives users the option to adjust patient specific parameters such as ligament origins, insertions, and stiffness.

Using this model, many simulations have been performed to explore the effect of varying implant designs. With the knowledge gained from these designs, a new TKA was developed. A desired kinematic profile was selected, and the TKA was modified based on the results of successive simulations until the desired results were obtained.

Table of Contents

List of Figures

Chapter 1: Background

The human knee joint is extremely complex, made of three articulating surfaces. The tibia and the femur articulate, with respect to each other, on both the medial and lateral surfaces, comprising the tibiofemoral joint, while the femur and patella articulate to form the patellofemoral joint. The tibiofemoral joint is responsible for carrying the weight of the upper body and thigh throughout daily living and during athletic activities. These joints, therefore, frequently experience loads much larger than the body weight of the subject during dynamic activities.

The patella functions to redirect the line of action of the quadriceps muscle and transmit force to the patellar tendon. Since this change in the line of action is minimal at full extension, patellofemoral forces are also minimal. As flexion increases, so does the change in the line of action and the amount of patellofemoral force. The quadriceps muscles comprise a large muscle group capable of generating force well in excess of the body weight of a subject. Correspondingly, patellofemoral forces frequently exceed body weight during activities involving flexion. Since there are large forces at both the tibiofemoral and patellofemoral joints, pain and loss of function can easily occur when the articulating surfaces are not healthy.

Osteoarthritis of the knee is the most common cause of this pain and reduced mobility. As a last stage in treatment options, total knee arthroplasty removes the affected structures and replaces them with metal, polyethylene, and/or ceramic surfaces. In most implants, the articulating surface of the femur and tibia are replaced with a cobalt chrome or titanium component. Between the femoral and tibial components is an ultra-high molecular weight polyethylene insert, replacing the function of the cartilage. Many implants also include a polyethylene insert that resurfaces the articulating portion of the patella.

Modern TKAs have several different categories. One division rests on whether the polyethylene bearing is rigidly fixed to the tibial tray or is free to axially rotate. The rigidly mounted designs are known as fixed bearing (FB) TKA. The designs with the freedom to axially rotation are known as mobile bearing (MB) TKA.

Furthermore, most implants sacrifice the anterior cruciate ligament (ACL). Some also sacrifice the posterior cruciate ligament (PCL) which functions to hold the femur posteriorly on the femur in flexion. These TKA, commonly referred to as a posterior stabilized (PS) TKA, replace the functionality of the PCL with a cam/post mechanism between the femur (cam) and polyethylene (post) which contact in deep flexion, allowing the femur to roll in the posterior direction with increasing knee flexion. Implants which sacrifice the ACL, but do not sacrifice the PCL are called posterior cruciate retaining (PCR) TKA. Some implants retain both the ACL and PCL and are commonly known as bi-cruciate retaining (BCR) TKA.

In a healthy, normal knee experiencing flexion, the lateral condyle of the femur rolls posteriorly a considerable amount while the medial condyle displays much less motion. This results in external rotation of the femur relative to the tibia in excess of 15° (Dennis 2004). Furthermore, many subjects with healthy knees have weight bearing flexion in excess of 120° while this range of motion is rarely achieved by subjects with a TKA. Even the most modern implants still fail to accurately reproduce the kinematics of the native knee. Posterior stabilized knees produce rollback, but fail to generate as much axial rotation as a healthy knee. Posterior cruciate retaining knees frequently exhibit paradoxical anterior sliding throughout flexion and less axial rotation. All TKA types also exhibit a reverse axial rotation pattern during flexion, which is evident in as high as 50% of the TKA subjects (Dennis 2004).

In addition to altered kinematics, implanted knees also feature altered kinetics. During a deep knee bend, telemetric implants have revealed that TKA will frequently have forces higher than 3.5 times body weight (x BW) at the articulating tibiofemoral joint. Based on mathematical modeling, healthy knees are

believed to have forces in the 2.5 x BW range, though this number cannot be directly verified using telemetry (Komistek 1998).

To reduce the forces, provide a better range of motion, and improve patient satisfaction, a TKA should replicate native knee kinematics. However, there is currently no method to accurately predict the kinematics of a new TKA. Three common methods of analyzing new TKA include wear simulators, cadaveric simulators, and mathematical modeling.

Wear simulators place the TKA in a mechanical device which attempts to replicate the in-vivo loading conditions over millions of cycles. While valuable, these simulations are costly both financially and in the amount of time necessary to perform the simulation, since they require the implants to be manufactured and considerable testing time. Therefore, wear simulators are useful in refining a nearly-final design, but are limited in the number of implants they can analyze.

Cadaveric simulators do allow an opportunity to implant the TKA into a cadaver leg which is then manipulated by applying forces along the extensor mechanism. These simulators provide conditions closer to those under in-vivo conditions because they analyze the kinematics of the knee utilizing the soft tissue constraints of the ligaments around the knee joint. There is a debate, however, as to whether a cadaver truly represents in-vivo conditions since the soft-tissue conditions are altered. Furthermore, cadaveric simulators have the same drawback as wear simulators in that they require physical manufacturing of the implants. Therefore, they are appropriate for analyzing a final design but are not as helpful with analyzing numerous designs during an iterative design process.

The final tool for analyzing a new TKA is mathematical modeling. Mathematical modeling simulates a TKA subject using a series of dynamic equations which are solved using a computer. Mathematical models which input the forces and solve for the motions are known as forward solution models. Such a

model can input implant geometry and muscle forces into the equations and then solve for the resulting joint forces and kinematics.

Mathematical modeling is a useful tool during the entire design process because it does not require the physical manufacturing of the implants and provides quick feedback of the design. Using the feedback from a simulation, a new implant can be designed and then immediately analyzed. This saves both the time and money of fabricating the TKA. However, the human body is a very complex physical system with multiple degrees of freedom, and even a simple model could have at least 30 unknowns for which to solve. For this reason, choosing a computationally efficient software is important.

Previously, a forward solution model of the knee (FSM) was developed using Autolev®, which is a symbolic dynamics program in which a user can define a physical system (Mueller 2011). The program then solves for the equations of motion using Kane's dynamics, which is a computationally efficient method of solving multi-body systems. This model is very powerful and has been validated, but nonetheless suffers from some important limitations. Most notably, the model focused primarily on FB PCR TKA. The research presented here will further develop this model in order to analyze PS implants, MB implants, and other less common designs such as bi-cruciate substituting designs and even tri-condylar designs.

Chapter 2: Literature Review

The kinematics of the native knee are well understood from fluoroscopic analysis. During a deep knee bend activity, the lateral condyle of a healthy knee rolls back an average of -14.1 mm from full extension to 90 degrees of knee flexion (Komistek 2003). The medial condyles move much less with an average of -1.5 mm of motion. This results in the knee externally rotating an average of 16.8°. Other studies have documented even larger translations with the lateral condyle rolling -19.2 mm posteriorly and the medial condyle moving -3.4 mm posteriorly on average.

However, many studies documented that the knee performs much differently after TKA surgery. TKA fails to replicate the posterior motion of the lateral condyle resulting in decreased external rotation (Dennis 2003). The degree to which the posterior condyle rolls back is heavily dependent on the type of TKA used. One study revealed that PS TKA subjects averaged 6.4 mm of lateral condyle roll back with only 2.9° of axial rotation (Cates 2008). The PCR TKA subjects had less rollback with -4.9 mm but more axial rotation at 4.8°. The PCR subjects had more axial rotation with less rollback because the medial condyle rolled back only -1.0 mm versus -4.2 mm for the PS subjects. Essentially, the post in the PS design forced both condyles back evenly.

In addition to kinematics, a significant amount of research has focused on computing the kinetics at the knee. The two methods of computing the forces in these joints are mathematical modeling and telemetry. Telemetry has provided data on several subjects which are often used to validate mathematical models or may even function as an input for a mathematical model (D'Lima 2005, D'Lima 2008). A mathematical model can be categorized into two main types. The first represents a larger number of muscles forces in the system than can be directly solved for and uses optimization to obtain a solution (Anderson 2001). The second method models only the major muscles driving the activity and is known as the reduction technique (Komistek 1998). Another distinction in mathematical modeling

comes from which variables are input and which are predicted. Those which input kinematics and predict kinetics are known as inverse models, while those that predict kinematics based on kinetics are known as forward models (Komistek 2005).

There are currently many software programs available for developing simulations of the human body. OpenSim is open source software that includes built-in models of various joints. LifeMod and AnyBody Modeling System are commercial software programs developed specifically for this purpose. Autolev® is a program designed for the simulation of any physical system. This provides the freedom to develop a model of the human body with any desired characteristics.

Methods of Rigid Body Knee Modeling

OpenSim

OpenSim is open source software that allows for increased collaboration between biomechanics researchers. Most previous mathematical modeling software was custom built by the specific researcher, making it very challenging for other researchers to reproduce the results. OpenSim uses a set of muscle excitation profiles to compute muscle forces which then drive the forward model (Delp 2007). Often, the excitation profiles are determined through optimization to match a desired kinematic profile. Once the excitation profiles are known, it is possible to evaluate how each muscle affects motion by altering that muscle's excitation profile.

OpenSim allows users to generate a model in a four step process starting with motion capture and force plate data. The steps, which have been greatly simplified for brevity, are as follows. In the first step, a given model, which includes all of the given body segments, muscles, and ligaments, is scaled to match a subject's patient-specific anthropometry. For example, limb lengths are scaled and limb masses are adjusted to match that specific patient. In the second step, the translations and rotations at all joints are computed to reproduce the patient-specific motion as closely as possible. In the third step, the

patient's mass parameters are adjusted to match the force plate data predicted by the model to the force plate data measured (e.g. the mass center of the trunk may be moved). The fourth and final step uses computed muscle control to generate the muscle excitations that produce the motions determined in step 1.

One frequently used OpenSim model is based on a 21 degree-of-freedom model with 92 muscles simulating gait (Thelen 2006). In an early implementation, this model was used in a case study to model a 12-year-old male with stiff-knee gait resulting from cerebral palsy (Delp 2007). The model determined that the reduced swing-phase flexion was a result of excessive activity of the vasti and rectus femoris during the preswing phase. Two treatment options for this condition are botulin injection into the rectus femoris and rectus femoris transfer. By simulating these treatments, increases in knee flexion of roughly 10° and 30° were predicted. The subject was eventually treated by rectus femoris transfer with results similar to those predicted. More recently, the detailed anatomy of 21 cadavers was measured to produce a detailed model of the lower limb (Arnold 2010). They compared moment arms and passive joint moments predicted by the model to the literature. They found the moment arms to be accurate for all knee flexion angles while the passive moments were less accurate at full extension and maximum flexion. The model has been made available to the public for modification and application.

LifeMod

LifeMod is commercial modeling software that allows the simulation of biomechanical systems with muscles, ligaments, and specific contact geometries. The software includes building wrapping algorithms for the soft tissues. Contact forces are computed using a damping and penetration algorithm. One application of this software involves performing a sensitivity analysis of different factors affecting post-TKA forces in four different types of implants (Innocenti 2011). The study considered Fixed Bearing and Mobile Bearing PS, a High Flex fixed bearing design, and a Hinge design. A

mathematical model was then built based on a previously tested cadaveric rig where the pelvis can translate vertically enabling hip flexion and the ankle can tibia can translate medially and laterally. The tibia is allowed to rotate in all three directions while the pelvis can only flex and extend. A mathematical model was preferable to the use of a cadaveric rig because the model allows the systematic evaluation of parameters in a single subject. E.G. it would be difficult to examine both patellar baja and patella alta in the same subject.

Using this model, peak patellofemoral forces were computed to be between 2.1 and 6.5 times body weight (BW) which is consistent with the literature. Furthermore, they show that increasing patellar height and anteriorization of the tibial component result in increased peak patellofemoral forces, as has been shown in previous studies. Tibiofemoral forces were demonstrated to peak between 1.6 and 5.4 times BW, which mostly falls in the ranges found in previous literature. The range is so wide as many parameters were varied. Sensitivity analyses like these provide valuable feedback to both surgeons and design engineers by demonstrating which factors heavily influence resulting peak forces.

AnyBody Modeling System

AnyBody Modeling System (AMS) was originally an optimization-based, inverse dynamic analysis modeling tool developed with four goals in mind as stated by the author (Daamsgaard 2006):

1) It should be a modeling system, i.e., a tool that allows users to construct models from scratch or use or modify the existing models to suit different purposes.
2) The system should facilitate model exchange and cooperation on model development, and it should allow models to be scrutinized.
3) If possible, it should have sufficient numerical efficiency to allow ergonomic design optimization on inexpensive computers.
4) The system should be capable of handling body models with a realistic level of complexity such as that shown in Fig. 2.

Recently, this software was used to build a subject-specific model which was validated against available telemetric and motion capture data (Marra 2015). The AMS was initially used to construct an inverse model where the tibiofemoral and patellofemoral joints were assumed to be a hinge joints. Joint angles

and ground reaction forces data were used as the inputs allowing the computation of muscle forces and joint forces using an optimization technique. Next, a second model was created with 11 degrees of freedom at the knee (3 translations and rotations at the tibiofemoral joint; 2 translations and 3 rotations at the patellofemoral joint; patellar tendon length assumed constant). The new model was a force-dependent kinematics (FDK) approach. In this approach, knee flexion is still determined from motion capture data, but the other 10 degrees of freedom are chosen based on a quasi-static equilibrium. In simplified terms, quasi-static equilibrium is where the model searches for an orientation of the knee that balances all of the ligament and muscle forces to hold the knee in a stable positon. Both models predicted tibiofemoral forces during gait with a root mean square error of less than 0.3 BW. Secondary knee kinematics (rotations and translations of the tibia and femur other than tibiofemoral flexion) were in general better predicted by the FDK model.

Autolev®

Autolev® is a programming language designed to simulate rigid body systems. Autolev® is frequently used to model systems in aerospace engineering due to their complexity. The same traits that make Autolev® useful in that field also make it useful in biomechanical engineering; the human body is also a very complex multi-body system with many degrees of freedom. Autolev® is useful in these multi-body systems because it is based on Kane's dynamics, a very computationally efficient method of solving both forward and inverse modeling problems.

In the biomechanics field, two notable models have been developed using Autolev. First, an inverse kinematic model was developed which calculates contact forces based on rigid body kinematics (Sharma 2008). The known kinematics are then used as input to drive a model which uses a discrete element analysis. In discrete element analyses, a network of springs is used to simulate the deformational properties of the polyethylene. This process provides the benefits of FEA while still maintaining the

speed of a rigid body model. This model was demonstrated to produce an accurate prediction of peak knee forces (3.81 x BW in model vs 3.84 x BW measured using telemetry). Furthermore, the differences were less than 15% for contact pressure and kinematics when compared to finite element analysis. However, the discrete element analysis took less than 4 minutes to solve while finite element analysis took over 3 hours.

More recently, a forward solution model was developed to predict knee mechanics based on the geometry of a native knee or TKA. This is the model previously developed by Dr. Mueller. The model is detailed thoroughly in the Description of Original Model and General Updates section. Telemetry was used to validate the model. The model found peak knee forces during a deep knee bend of 3.96 x BW while telemetry found a peak force of 3.84 x BW (Mueller 2011).

Chapter 3: Methods

Overview

The FSM was initially developed in Autolev® to simulate a post-TKA subject performing a deep knee bend. Autolev® is an extremely powerful tool for simulating multi-body systems. However, it has some limitations when used for simulating the human body. First, the human body has many muscles serving similar roles making it an indeterminate system. Secondly, it does not have built-in contact detection algorithms. The indeterminacy is overcome by using a reduction technique where only the major muscles are assumed to play a contributing role to the activity. In the case of a deep knee bend, the quadriceps are the only major active muscles. The hamstring is also included as a constant force. The second limitation was overcome by Dr. Mueller by specifying all contact points. The contact points were specified on both the femoral and patellar components as a function of flexion. This allows the Autolev® code to apply non-holonomic constraints at the known contact points. However, assuming these contact points is ultimately inaccurate as the true contact location should be calculated.

The greatest changes from Dr. Mueller's original model and the final model focus on a more accurate geometrical representation of the articulating surfaces and the inclusion of contact detection. These inclusions allow for real time calculation of contact points instead of assuming them. Furthermore, the graphical user interface (GUI) used to create the model has been improved. Finally, the model has been modified to include both flexion and extension activities such as a deep knee bend and rise. The methods section will open by detailing the overall design of the model which includes the bodies and function of muscles and ligaments, as these remain essentially unchanged from the original model. The progression from a fixed bearing (FB) to mobile bearing (MB) simulation will be documented. Then, the changes of the articulating geometries will be defined for the tibiofemoral joint, patellofemoral joint, the cam and post, and for the incorporation of new contacting surfaces. Finally, modification to the

muscle force controller which allows both flexion and extension activities will be detailed along with the contact force algorithm. The outline of this section will be as follows:

1. Description of Original Model and General Updates
2. Inclusion of Mobile Bearing Polyethylene
3. Improvements at Tibiofemoral Joint
4. Improvements at Patellofemoral Joint
5. Improvements at Cam/Post
6. Ability to Model New Contact Surfaces
7. Modifications to Muscle Controller
8. Contact Force Algorithm

Description of Original Model and General Updates

Overview and General Updates

The original model features four bodies: the tibia, patella, femur, and pelvis (Figure 1). The rotations of the tibia are specified around the ankle center. The femur is then constrained to translate such that the femur remains in contact with the tibia. Also, the medial/lateral translation of the femoral head is specified. The femur is free to rotate, with respect to the tibia, in all three degrees of freedom. Next, the patella is constrained by a medial and lateral contact point to stay in contact with the femur. The patella is free to tilt and axially rotates, but flexion is specified. All translations and rotations of the pelvis are specified.

In this model, known ground reaction forces are applied at the ankle center which is fixed to the ground. The quadriceps force is computed by a PID controller to make knee flexion match a desired profile. Ligaments are modeled as springs with a linear and non-linear region. The assumptions and an overview of the model are detailed in Table 1. For complete details as well as results, see Dr. Mueller's dissertation (Mueller 2011).

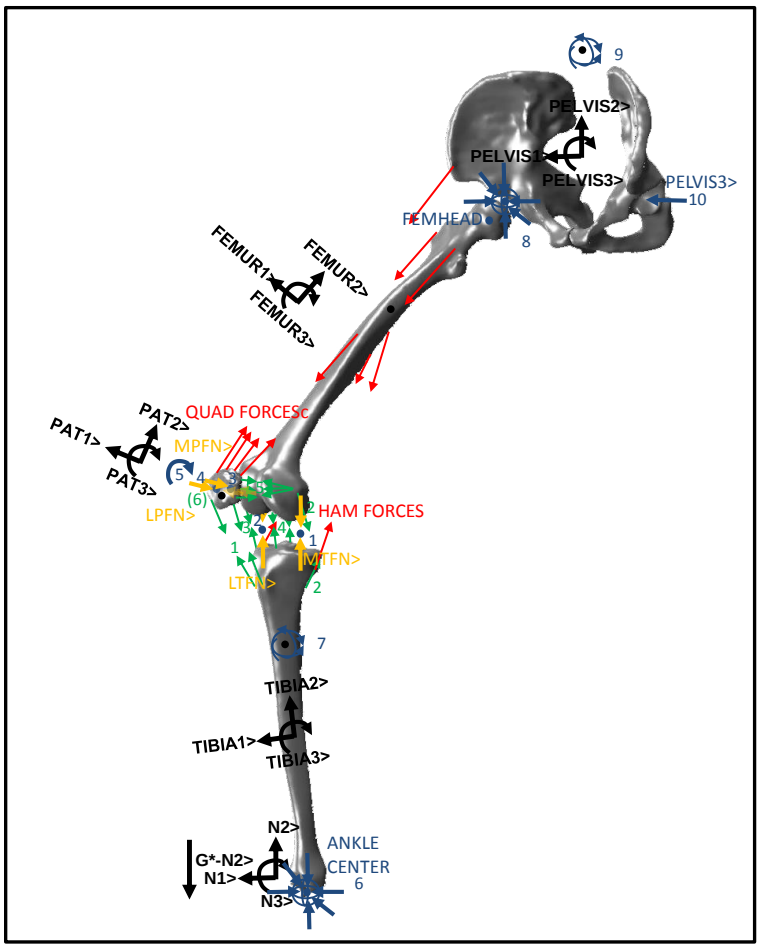

Figure 1: The Free Body Diagram of the Deep Knee bend simulation is shown. It includes the tibia, patella, femur, and pelvis as well as all active and passive forces. Image borrowed from Dr. Mueller's dissertation with permission.

Table 1: Description of Weight Bearing Deep Knee Bend model. Table borrowed from Dr. Mueller's dissertation with permission.

SUMMARY OF WEIGHT BEARING DEEP KNEE BEND MODEL OF A RIGHT LEG	
GRAVITY	Gravity acts in the –1*N2> direction
BODIES	-PELVIS (3 rotations specified, fixed to femoral head), FEMUR (3 DOF), PATELLA (3 DOF), TIBIA (3 rotations specified, fixed to N (ground) at the ANKLE CENTER) -Mass and inertial properties calculated from literature -Orthogonal system of unit vectors established for each body 1> points anterior 2> points superior 3> points lateral
CONSTRAINT FORCES (BLUE NUMBERS AND BLUE AND YELLOW ARROWS ON Figure 1)	1. Medial TF Geometric Constraint force acting between FEMUR and TIBIA in the MTFN> direction 2. Lateral TF Geometric Constraint force acting between FEMUR and TIBIA in the LTFN> direction 3. Medial PF Geometric Constraint force acting between FEMUR and TIBIA in the MPFN> direction 4. Lateral PF Geometric Constraint force acting between FEMUR and TIBIA in the LPFN> direction 5. Constrain Rotation of PAT in PAT3> with Knee Flexion 6.TIBIA translation constrained to N (ground) at ANLE CENTER 7. 3 TIBIA rotations specified as function of knee flexion 8. PELVIS translation is constrained to the femoral head on FEMUR (FEMHEAD) 9. 3 PELVIS rotations in N are specified as a function of knee flexion 10. Mediolateral translation of the point on FEMUR, FEMHEAD, in the PELVIS3> direction is specified as a function of flexion
LIGAMENT FORCES (GREEN NUMBERS AND ARROWS ON Error! Reference source not found.)	1. Patella Ligament Medial and lateral, Two Bundles Each 2. Medial Collateral Ligament Three Bundles includes wrapping 3. Lateral Collateral Ligament One Bundle 4. Posterior Cruciate Ligament and Anterior Cruciate Ligament Two Bundles Each 5-6. Lateral and Medial Patellofemoral Ligaments Three Bundles for Each
ACTIVE MUSCLE FORCES (IN RED ON Error! Reference source not found.**)**	-QUAD FORCES are applied to PAT at the insertion points and FEMUR at the muscle origin points. Controlled using a PID controller with an additional flexion acceleration feedback element and a PD controller which stabilizes PAT tilt -HAM FORCES may be applied to the insertion point on the tibia and origin point on the femur and are a function of knee flexion
IMPORTANT ASSUMPTIONS	-Rigid body model does not allow for condylar lift-off. As long as the TF constraint forces (1,2 above) are in compression this is a reasonable assumption -PAT flexion is prescribed as a function of knee flexion -The mediolateral constraint at FEMHEAD acts as the stabilization provided by the contralateral leg -Contact point on FEMUR and on PAT are prescribed as a function of flexion -Geometry represented by constraining the velocity of contact points in the direction of the tibial or trochlear groove surface normals (LTFN>, MTFN>, LPFN>, MPFN>) to 0. -Ligaments are modeled as non-linear springs with damping

General Changes to the Original Model

The most notable general change to the model is the addition of the torso, which includes all portions of the body above the pelvis. By including a whole body in the model, ground reaction forces can be computed instead of input. This allows the model to function more adequately as theoretical simulator as ground reaction forces do not need to be measured.

Secondly, the tibial rotations were originally specified around an orthogonal coordinate system. The rotations are now defined to occur about the ankle axis and subtalar axis as well as axial rotation about the long axis of the tibia. This change was incorporated so that kinematic data from other programs using these reference frames could be input into the FSM.

Furthermore, by modifying the PID controller, the FSM has been modified to be able to both flex into a deep knee bend and extend out of one. Therefore, the FSM is actually a continuous flexion and extension simulator. This means it is capable of simulation activities such as a deep knee bend or a partial knee bend followed by extension.

Finally, the medial/lateral motion of the pelvis is no longer specified. The motion of the hip is stabilized by a spring and damper system in the medial and lateral direction to represent the force of the other leg. Specifying this motion resulted in a simulator which was less sensitive to geometrical changes at the tibiofemoral joint.

Original Tibiofemoral and Patellofemoral Joint Definition

The original tibiofemoral joint was defined using normal vectors on the polyethylene and contact points on the femoral component. The normal vectors on the polyethylene component were computed for the articulating surface (Figure 2). They were then mapped to the transverse plane (Figure 3). Next, a

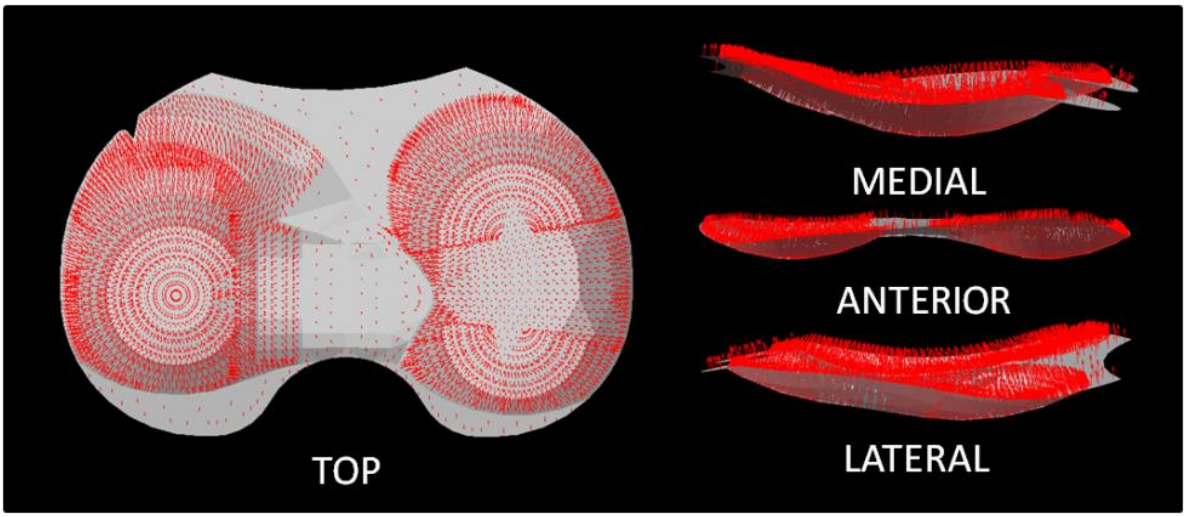

Figure 2: The articulating surface of a PCR polyethylene insert can be defined using the normal vectors. Image borrowed from Dr. Mueller's dissertation with permission.

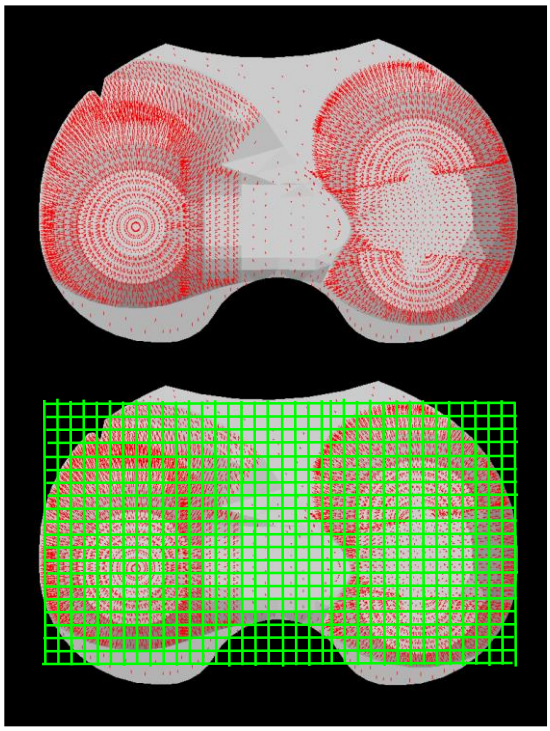

Figure 3: The normal vectors of a PCR polyethylene insert are mapped to a transverse plane. Then, a polynomial is fit to define the vectors based on the location in the transverse plane. Image borrowed from Dr. Mueller's dissertation with permission.

polynomial was fit which used the ML and AP position as an input and the direction of the normal vector as the output. The normal vector was defined by two sequential rotations.

Next, contact points were defined on the femoral component as the lowest point on the femur in the polyethylene reference frame. Then, the motion of the contact point was defined by fitting a polynomial to its path in the AP, ML, and SI directions (Figure 4). The current method for defining these points is the same, except two polynomials are utilized, one before 90° and one after. This change was necessary as some of the newer designs that were analyzed could not be accurately defined by a single polynomial due to extreme changes in radius of curvature.

Since the normal vectors of the polyethylene and the contact points of the femur were defined, the femoral contact points were constrained to only move perpendicular to the normal vectors (Figure 5). The same method was used at the patellofemoral joint (Figure 6). The normal vectors were defined on the trochlear groove, and the contact points were defined on the patella or patella component. There is no corresponding lowest point assumption for patella contact points as there is for the femoral contact points. Therefore, the points were defined to move superiorly and away from the centerline with flexion as has been seen in-vivo.

Inclusion of Mobile Bearing Polyethylene

The model was further modified to incorporate a mobile bearing polyethylene insert. This required the inclusion of the polyethylene as a separate body, defining the vector from the tibia component's center of mass to the point connecting the tibia component and center of axial rotation for the polyethylene component. A second vector was then defined from this intersection point to the center of the polyethylene bounding box. It was assumed that the polyethylene bounding box corresponds to the center of mass for the polyethylene. The polyethylene was then constrained to have no translation,

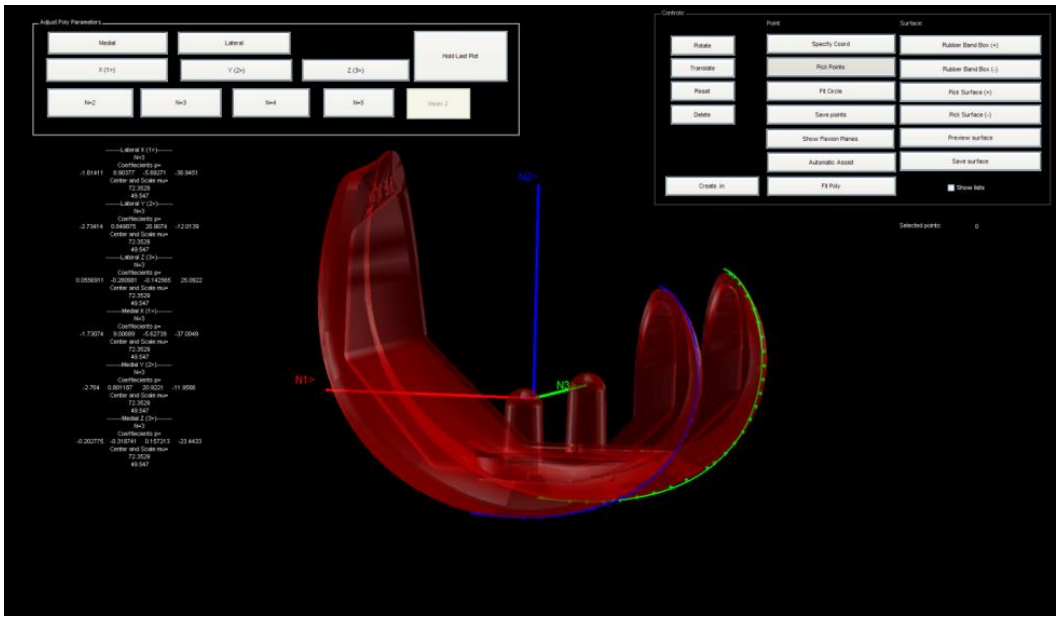

Figure 4: The graphical user interface selects the lowest point on the femoral component at each flexion angle and fits a polynomial to the points. Image borrowed from Dr. Mueller's dissertation with permission.

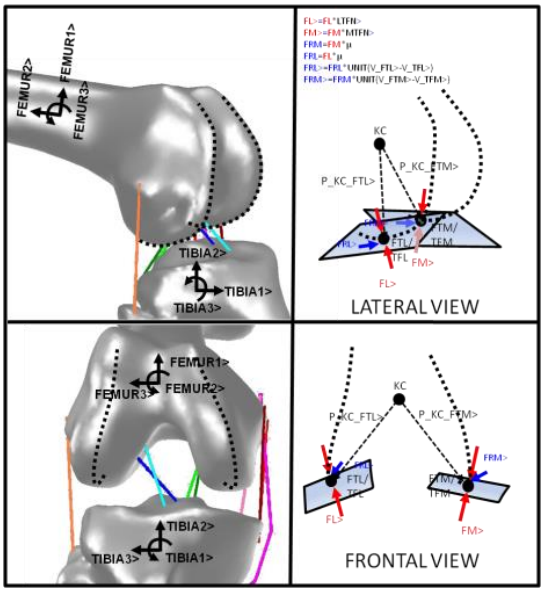

Figure 5: The TFL (lateral) and TFM (medial) are the tibial contact points and are constrained so as not to move along the normal vectors to the tibial surface. These constraints are used to calculate the normal joint interaction forces FL (lateral) and FM (medial) which are applied along the surface normal vectors. FRL and FRM are the frictional forces. Image borrowed from Dr. Mueller's dissertation with permission.

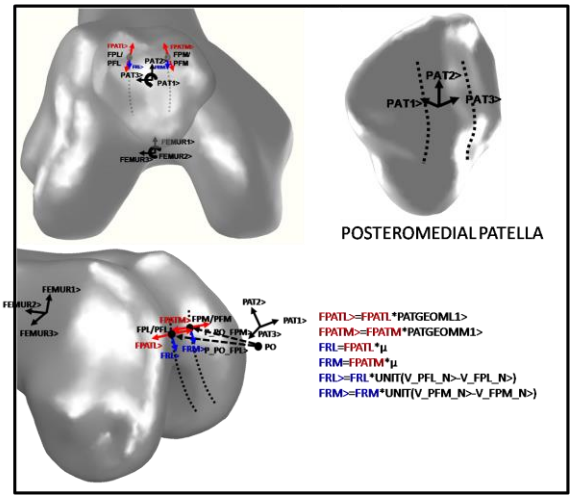

Figure 6: The patella contact points (PFM and PFL) are constrained not to move in the normal direction of the trochlear groove. The normal contact forces FPATM (medial) and FPATL (lateral) are applied along the trochlear grove normal vectors and calculated based on the constraints. FRL and FRM are the frictional forces Image borrowed from Dr. Mueller's dissertation with permission.

flexion, or abduction/adduction relative to the tibia component. This left a 1 DOF union to occur, allowing for axial rotation of the polyethylene insert with respect to tibial baseplate.

Since the intersection of the polyethylene and the tibial component is a flat surface on which the polyethylene rotates rather than translates, a traditional friction model is not appropriate. Instead of frictional forces applied at discrete points in the opposite of the direction of motion, a rotational friction model was used. This model applies an interactive torque between the poly and the tibial component. The torque is proportional to the angular velocity of the polyethylene in the tibial component reference frame, but opposite in direction as shown in equations (1) and (2).

$$\overrightarrow{Torque_{Poly}} = -\mu_{Rotational} * \overrightarrow{\omega_{TibiaComp}^{Poly}} \quad (1)$$

$$\overrightarrow{Torque_{TibiaComp}} = -\overrightarrow{Torque_{Poly}} \quad (2)$$

Improvements at Tibiofemoral Joint

The tibiofemoral joint, as described in the original model by Dr. Mueller, incorporates several simplifying assumptions. The first assumption is the elimination of coronal curvature so that only sagittal curvature of the polyethylene surfaces is represented. The second is that the lowest point of the femur in the tibial reference frame is where contact occurs while the contact point actually shifts away from the lowest point when the femur leaves the dwell point of the polyethylene (Figure 7). While both of these assumptions provide a good starting point, it is ideal to eliminate them in favor of a contact detection model that more accurately represents the geometries involved.

In order to properly model this interaction, an iterative process was used. Originally, the coronal curvature was not modeled because doing so caused the code to "crash," nearly immediately. This occurred because the original constraints were slightly inaccurate. The original method calculated the dot product of a position vector from the tibia component's mass center to the tibiofemoral contact

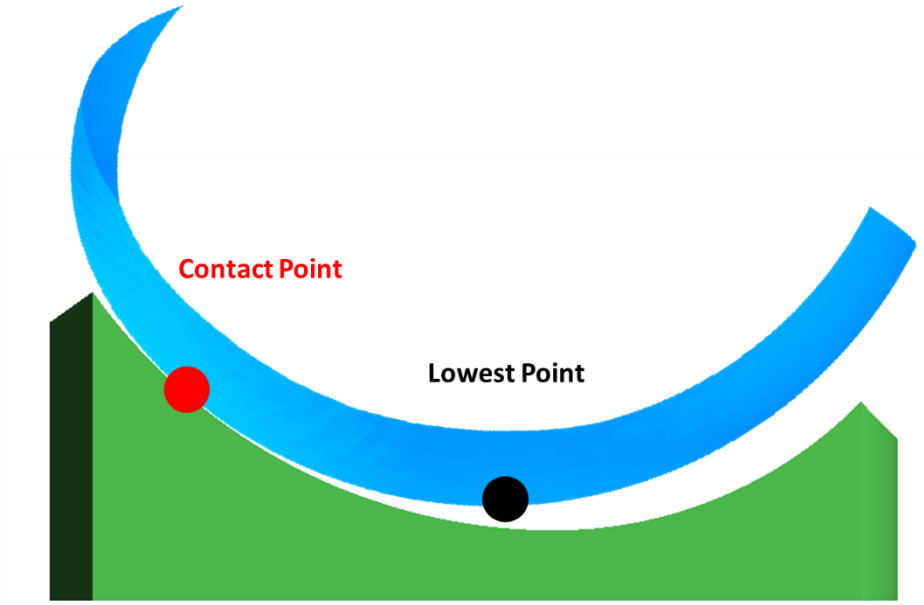

Figure 7: A model which works using contact detection allows for the inaccurate assumption that the lowest point is in contact to be discarded.

point with the normal vector of polyethylene at the contact point (on both the medial and lateral condyles). Then, the derivative of this value was constrained to be 0. While this method is approximate, the constraint should be applied to velocity, not position.

To correct the constraints, the derivative of the vector between the reference point on the tibia component and the contact point on the femur is taken in the polyethylene reference frame. This allows for the velocity of the femoral contact point to be in the polyethylene reference frame. Then, the dot product of this velocity and the normal vector of the polyethylene, at the contact point, is constrained to be 0.

With the new constraints, the full curvature of the polyethylene can be represented accurately. However, contact was still assumed to occur at only the low point of the femur. The next iteration still assumed that contact always occurred at the lowest point, but also searched for penetration of the femur into the polyethylene. The first step in finding penetration is knowing the height of the polyethylene in the polyethylene's reference frame. This was done by modifying the GUI, which produced polynomials to describe the sequential rotation as described in Dr. Mueller's model. Instead of fitting polynomials to the rotations, a surface polynomial was generated which accurately describes the polyethylene's articulating surface (Figure 8). Then, the gradient of this surface was computed to generate the normal vector for the constraints.

After defining a surface polynomial, a 7 x 7 grid of 49 points was placed on both the medial and lateral condyle of the femoral component with the lowest point at the center (Figure 9). The center point always remained in contact with the surface, while the other points may or may not penetrate the surface. Penetration was detected by comparing the height of each point on the grid in the polyethylene reference frame to the height of polyethylene surface polynomial at the corresponding

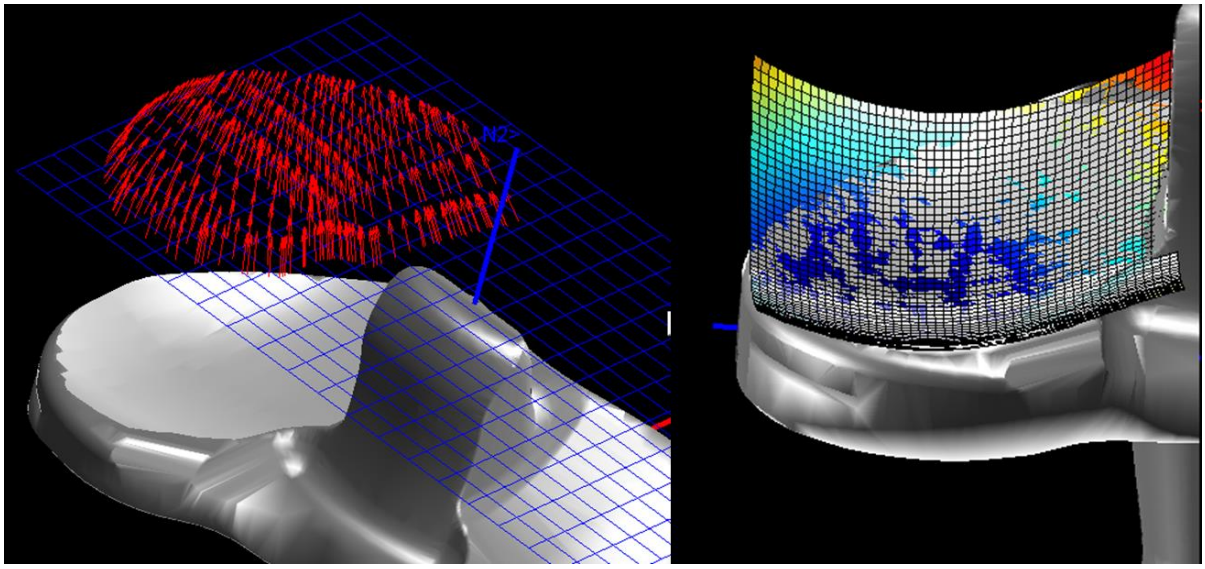

Figure 8: The old method fits a polynomial to the normal vectors (left) while the new method fits a surface polynomial to the geometry (right).

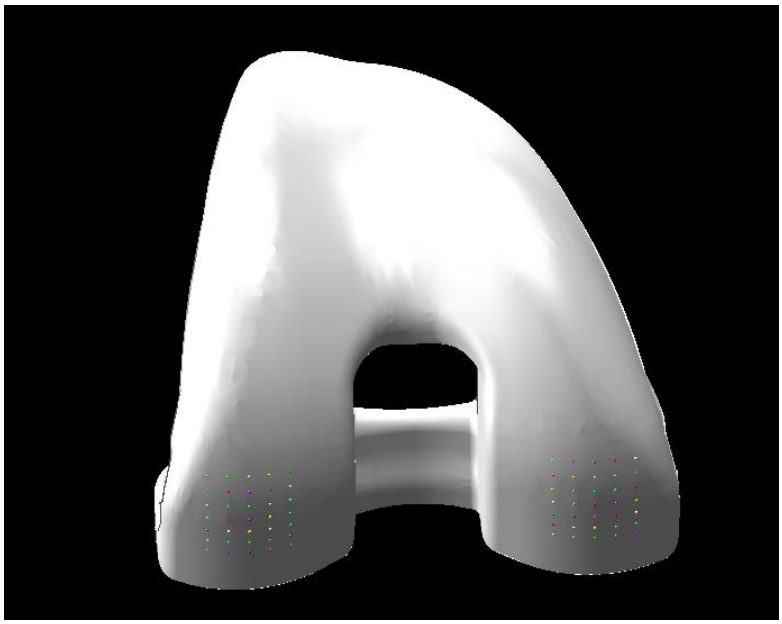

Figure 9: The potential contact points are shown on the femoral surface. Thirty-five of the 49 are visible on each condyle in this simulation.

location. If contact was detected, the contact force was distributed among all penetrating points on that femoral condyle with the amount of force at any point proportional to the total penetration (Figure 10).

This method allowed for contact to occur at points of interaction, not the lowest point. Therefore, the femur stayed more stable on the polyethylene because contact on the anterior and posterior lips of the polyethylene could be detected. However, the contact areas were distorted by the fact that the lowest point on the femur was always assumed to be in contact. To solve this issue, all constraints were removed and the contact force was based purely on contact detection. Points were defined on the femoral component, and if these points were below the height of the surface polynomial, a force was applied proportional to the penetration. A damping force was also applied to make the model more stable.

Initially, only ten points were included on each condyle. As the model functioned as predicted, several weeks were spent expanding the Autolev® code so that over 1000 points per condyle could be modeled. Further time was spent compiling the Autolev® code and the C code. Finally, with over one million lines in C code compiled, the executable was run and immediately crashed as this method required more memory than available. A new approach was adopted. No points or surface polynomials were defined in Autolev. Instead, three forces and three torques are applied at the tibial component's and femoral component's centers of mass for both the medial and lateral condyle. Then, the locations of the femoral points are placed in an input file along with the coefficients of the surface polynomials (Figure 11). The C code uses this data to detect penetration between the femoral condyle and surface polynomial and computes the resulting force. This force is then used to compute an equivalent force and torque at the femoral center of mass. The resulting forces and torques are summed for all contact points and applied at the femoral mass center. The force calculation algorithm is detailed in a separate section. The

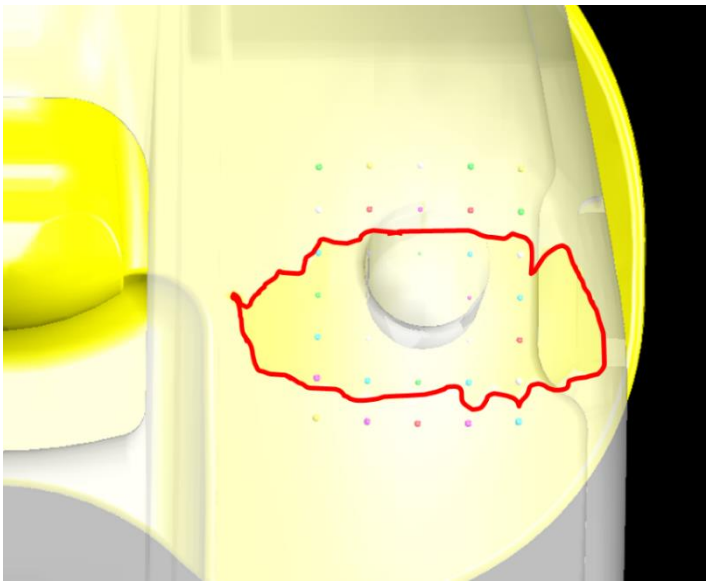

Figure 10: The red outline shows the area which is in contact (represented by the darker yellow). All points inside this outline are contact points, and the contact force is distributed among them proportional to penetration squared.

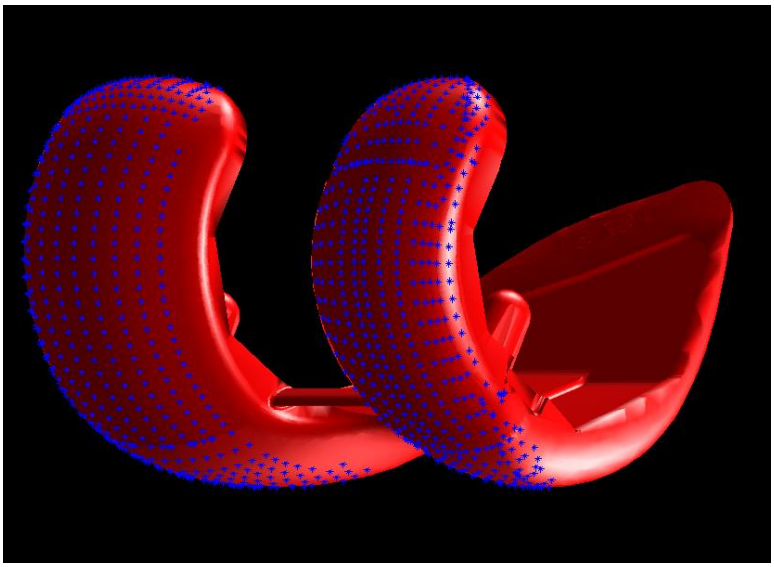

Figure 11: The femoral component is represented as a point cloud in the FSM. The blue points show the locations where the model searches for contact.

resulting force and torque are then applied at the polyethylene center of mass. N.B.: The forces applied to the femoral component and polyethylene are identical due to Newton's second law while the torques are different because they have different moment arms. The selection of the femoral points is now performed in the GUI. An algorithm selects a grid of points along the articulating surfaces of the femoral condyle based on user input parameters. Three dimensional coordinates of that point in the femoral component reference frame are then exported to a text file for the model to read at run time. The polynomial defining the low point of the femoral component is still generated, and the low point is used for computing lateral AP contact position, medial AP contact position, and axial rotation. This method is used because it is the same method used in fluoroscopic studies; the forward model results can therefore be directly compared to fluoroscopic results.

Improvements at Patellofemoral Joint

The patellofemoral joint in the Mueller model was very similar to the tibiofemoral joint in terms of the assumptions made. The medial and lateral portions of the trochlear groove were defined separately with each having only sagittal curvature. Furthermore, the actual surface definitions were only applied for the first 90 degrees of flexion. After this, an idealized sagittal curvature was assumed. Secondly, the medial and lateral contact points on the patella were specified. Finally, the flexion of the patella was specified.

The coronal curvature was neglected as before because of the incorrect constraints. The dot product of the vector from the femoral component reference point to the contact point with the normal vector of the contact surface was taken. Then, the derivative of this dot product was constrained not to change. The assumption was fixed by first taking the derivative of the vector from the reference point to the contact point both medially and laterally. This generates the velocity of the contact point in the femoral reference frame. Then, the dot product of the velocity was taken with the normal vector of the surface.

This yields the velocity of the contact point away from the surface which was constrained to be 0. The idealized trochlear groove was still used past 90 degrees.

The next step in the process modified the polynomial representation of the trochlear groove. Originally, the polynomial defined the normal vectors of the trochlear groove. The GUI was modified to instead generate a surface polynomial. Because the surface of the trochlear groove is mapped to the coronal plane, it is unable to recreate the most inferior portion of the trochlear groove (Figure 12). This is because the bottom portions of the trochlear groove are initially perpendicular to the coronal plane, which would result in a function that is not injective. To account for this, the femur component was rotated 45 degrees before generating the surface polynomial (Figure 13). This allows the entire articulating surface to be mapped. However, the surface is now mapped to a body which does not exist in the FSM, a problem which is addressed in the FSM code.

The first step in addressing this problem involves rotating the vector from the femoral component center to patellofemoral contact points by 45 degrees to produce a pseudo contact point on the 45 degree rotated femoral component (Figure 14). Then, the gradient on the rotated component is calculated to generate a pseudo normal vector (Figure 15). Finally, this normal vector is rotated back -45 degrees to generate the actual normal vector for the non-holonomic constraint (Figure 16).

With the trochlear groove accurately represented, the focus turned to refining the contact points on the patella. Initially, two contact points were prescribed on the patella. Accurately prescribing the contact points is difficult. While it is known generally that the contact moves superiorly and away from the center line with increasing flexion, there is no definitive way to know where contact will occur. Due to this concern, the Mueller model could not accurately predict patellar flexion. Changing the contact points would greatly change the moment arm of the quadriceps tendon and patellar ligament.

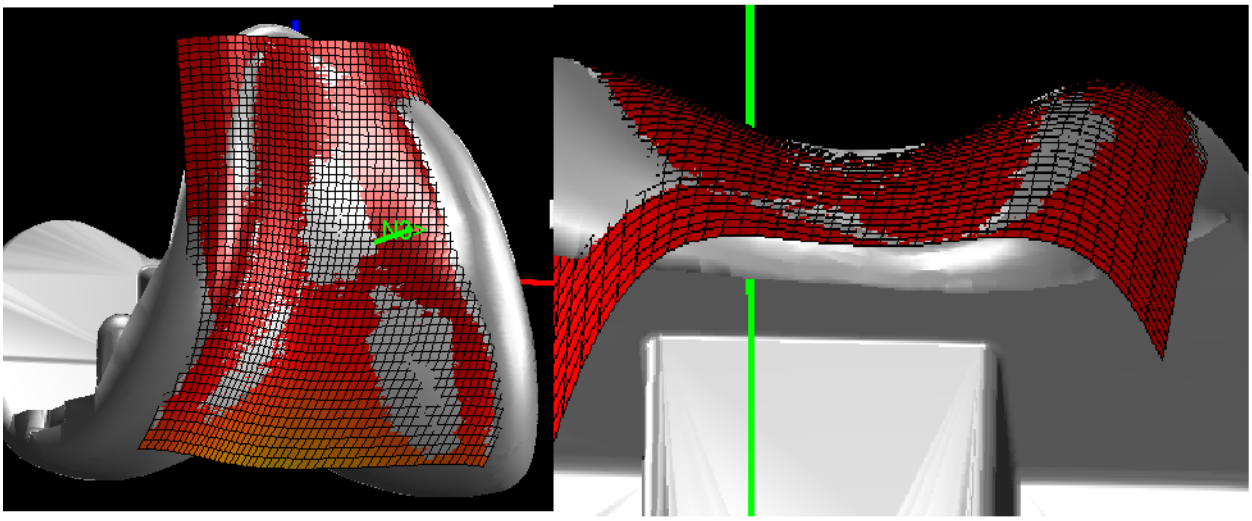

Figure 12: The trochlear groove is defined using a surface polynomial. However, it did not initially describe the most inferior portion of the trochlear groove.

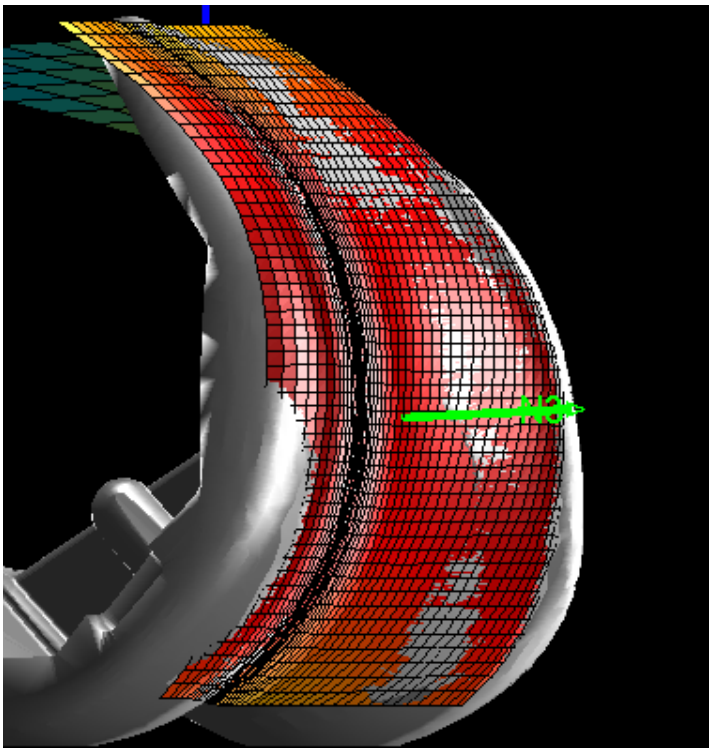

Figure 13: The femoral component is rotated 45 degrees before the surface polynomial is fit. This allows the entire trochlear groove to be represented.

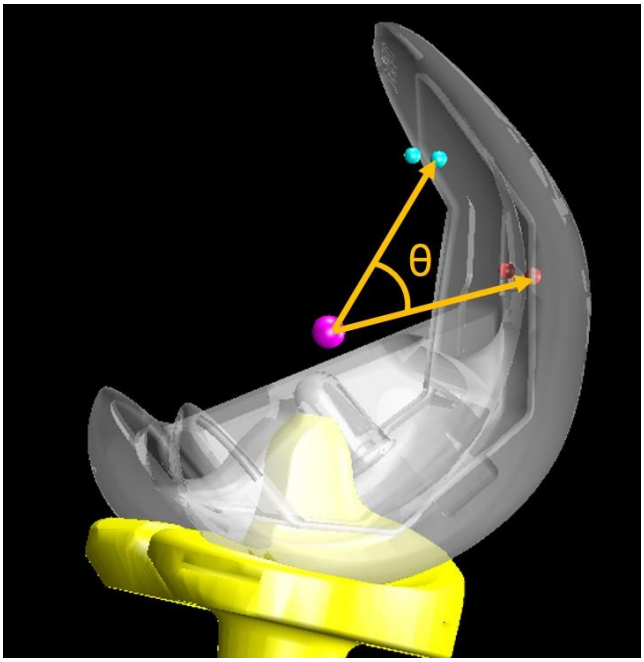

Figure 14: The actual patellofemoral contact points are shown in red. The rotated pseudo contact points are shown in blue (θ=45°).

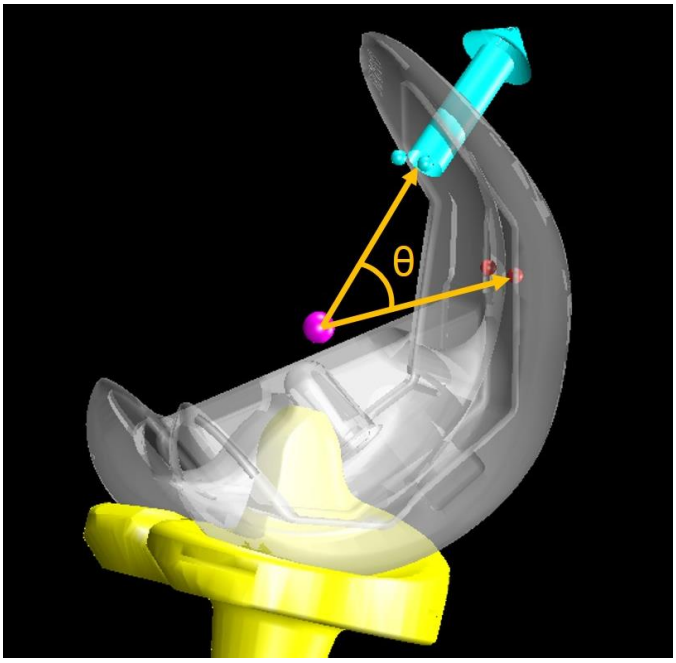

Figure 15: The pseudo normal vector is calculated at the pseudo lateral patellofemoral contact point.

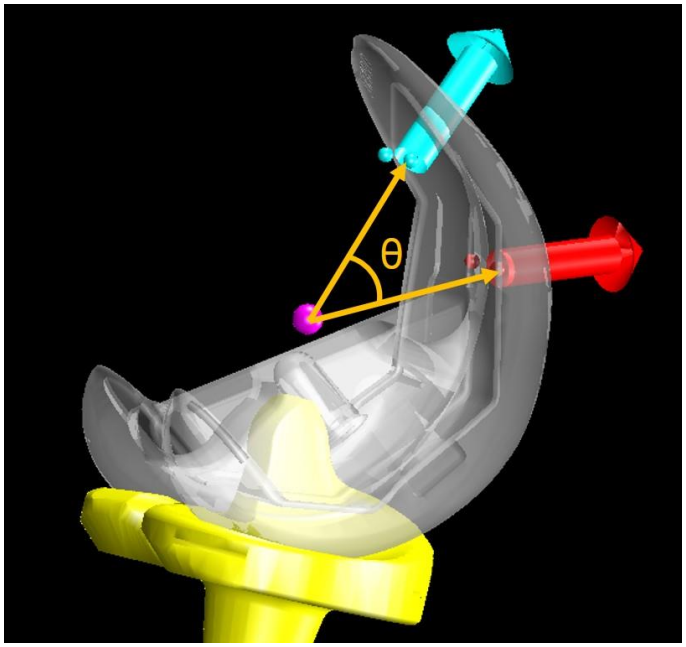

Figure 16: The pseudo normal vector is rotated 45° back to produce the actual normal vector.

Therefore, the contact points affect patellar flexion, and since the contact points were not accurately known, any resulting patellar flexion calculations would be inaccurate. For this reason, patellar flexion was specified.

To solve these problems, two changes were simultaneously implemented. First, the constraint on patellar flexion was removed, adding an additional degree of freedom. Simultaneously, fixed potential contact points were selected across the surface of the entire patellar component (Figure 17). Since over 100 contact points are frequently placed on the patella, these points are placed in a separate file which the C code reads. The C code then checked for penetration of each point into the trochlear groove surface polynomial. If penetration is detected, a force proportional to the penetration was applied. More on the force calculation algorithm can be found in that section. In the final version of the code, the method of rotating the contact points 45° was replaced. Instead, a trochlear groove reference frame was defined as being rotated -45° around the femoral component ML axis (Figure 18). The trochlear groove reference frame is used for all contact calculations.

Improvements at Cam/Post

While not included in his dissertation, a rudimentary cam/post mechanism was developed in the original model by Dr. Mueller. This version modeled the post as a vertical plane. The motion of a medial and lateral cam contact point was prescribed on the femur. If the contact points crossed the plane, a force was applied equal to the penetration squared. This method provided a good starting point but was problematic in that it required the user to predict where contact was likely to occur when specifying the motion of the contact points.

In order to make further improvements, the post is represented with a surface polynomial as described previously for the tibiofemoral and patellofemoral joints (Figure 19). Twelve points are placed on the cam with 4 points in a medial row, 4 in a lateral row, and 4 in a central row (Figure 20). The code then

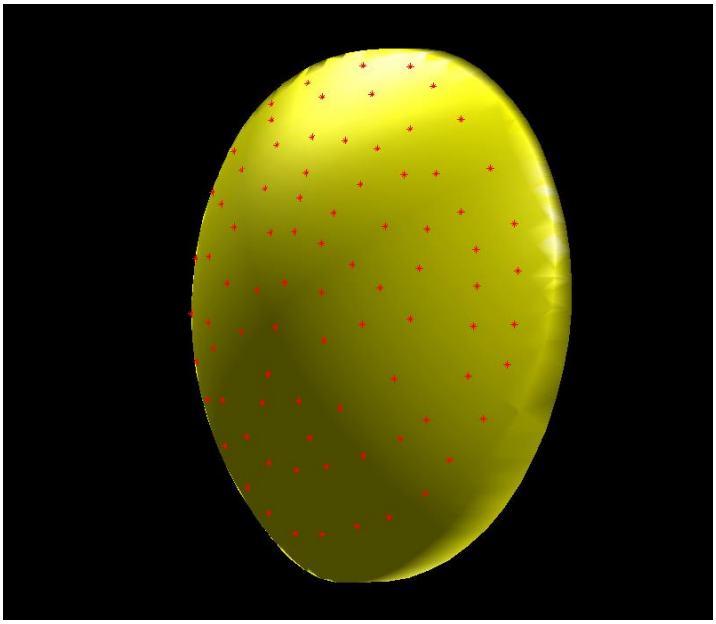

Figure 17: The patella component is represented as a point cloud in the FSM. These are the locations where the model searches for contact.

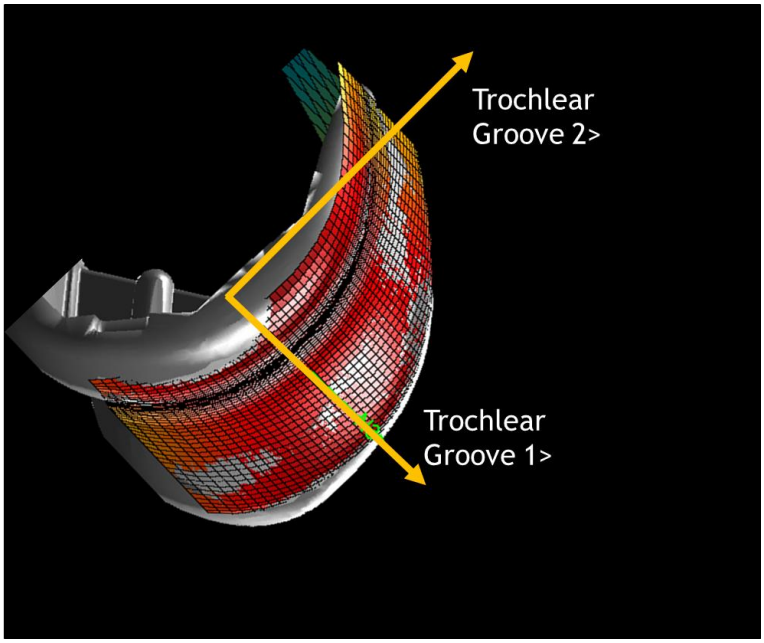

Figure 18: A trochlear groove reference frame is defined which is rotated -45° around the femoral component ML axis. This reference frame is used for all contact algorithm calculations.

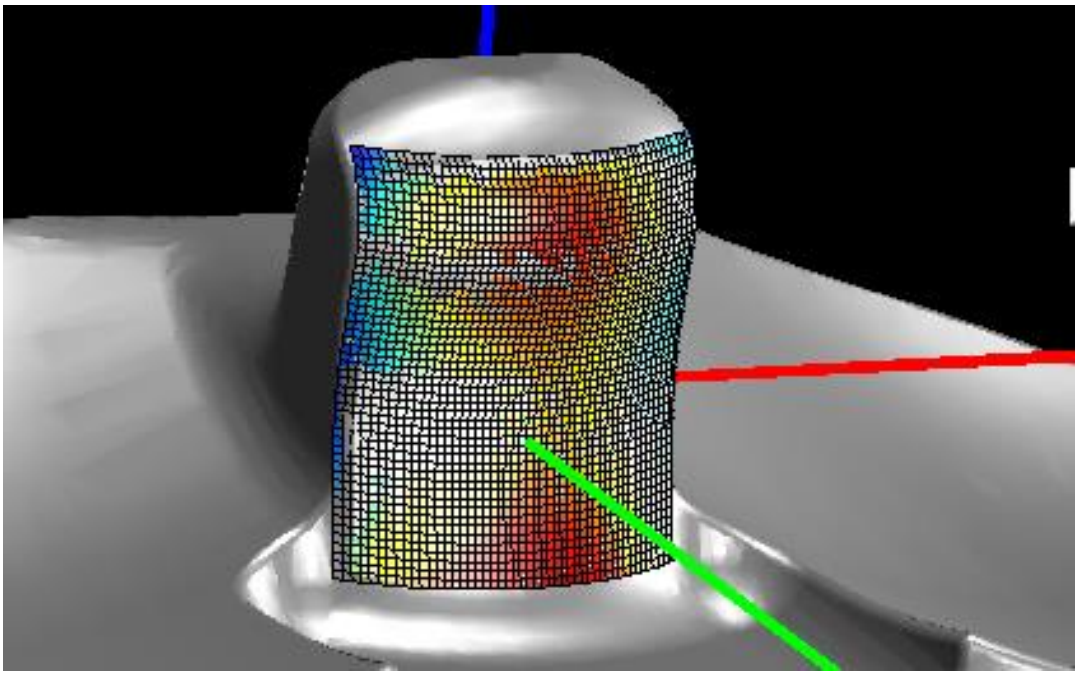

Figure 19: The post is defined by a surface polynomial.

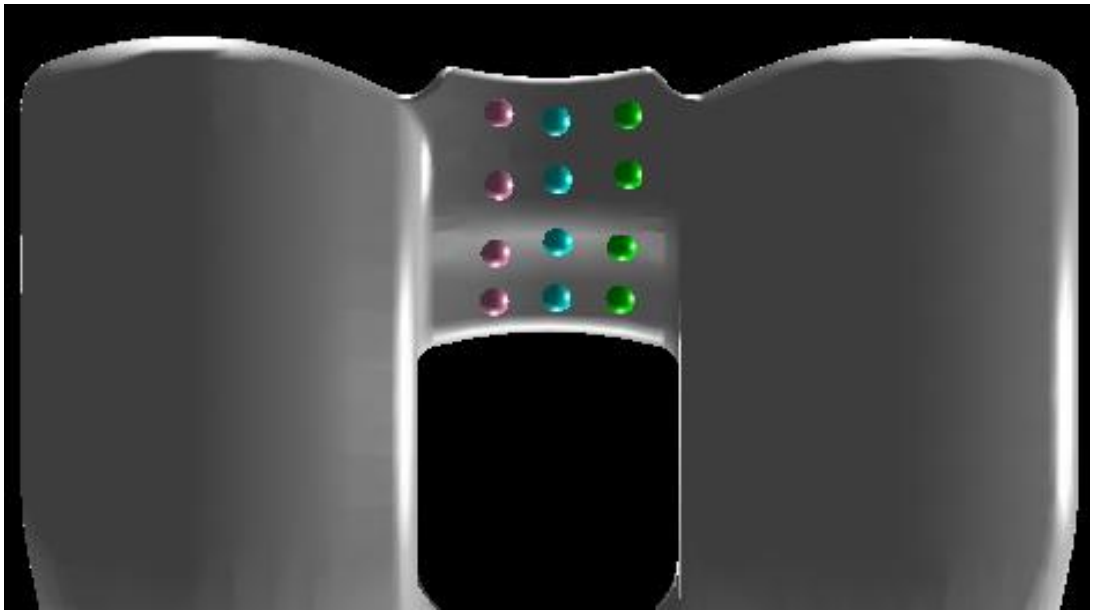

Figure 20: Twelve contact points are defined on the cam.

searches for penetration and applies a force equal to the penetration squared on the cam and post. The force is applied in the direction of the normal vector of the surface polynomial on the post. The algorithm used to compute the points is much simpler at the cam post as it neglects friction (Equation & 4).

$$\overrightarrow{Force_{Cam}} = K_{Post} * Penetration^2 * \overrightarrow{Post_{normal}} \quad (3)$$

$$\overrightarrow{Force_{Post}} = -\overrightarrow{Force_{Cam}} \quad (4)$$

Finally, the cam and post contact detection method was modified to work the same as the tibiofemoral and patellofemoral contact detection methods. This was done by defining a point cloud for the cam (Figure 21). The code now contacts all of these surfaces and computes the contact force as described in the Contact Force Algorithm section. An identical method is employed for the inclusion of a second cam/post in bi-stabilized designs (Figure 22).

Ability to Model New Contact Surfaces

So far, four contact surfaces have been modelled using very similar methods. The first was the tibiofemoral joint. The patellofemoral joint uses the same process, with only the additional step of remapping to a rotated pseudo femoral component to represent the entire surface. The cam and post interaction uses the same method as well for PS and bi-stabilized designs. Using these same concepts, additional contact surfaces could easily be represented.

A more novel design, which could be analyzed, includes the tri-condylar design featured (Figure 23). Using a traditional non-holonomic constraint, this would be impossible for many reasons. First, the number of constraints is limited, and this would remove a degree of freedom. Secondly, non-holonomic constraints require contact to occur at all times. The center condyle of the tri condylar design only engages in deep flexion. It also has the potential to cause one of the other condyles to lift-off, which could not happen in a non-holonomic constraint.

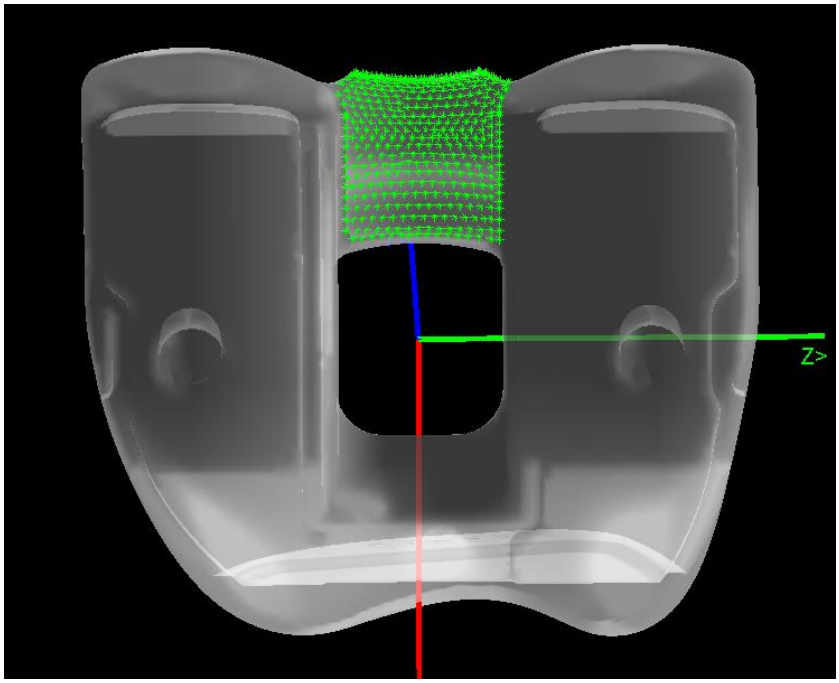

Figure 21: A point cloud is shown on the cam for detecting cam/post contact.

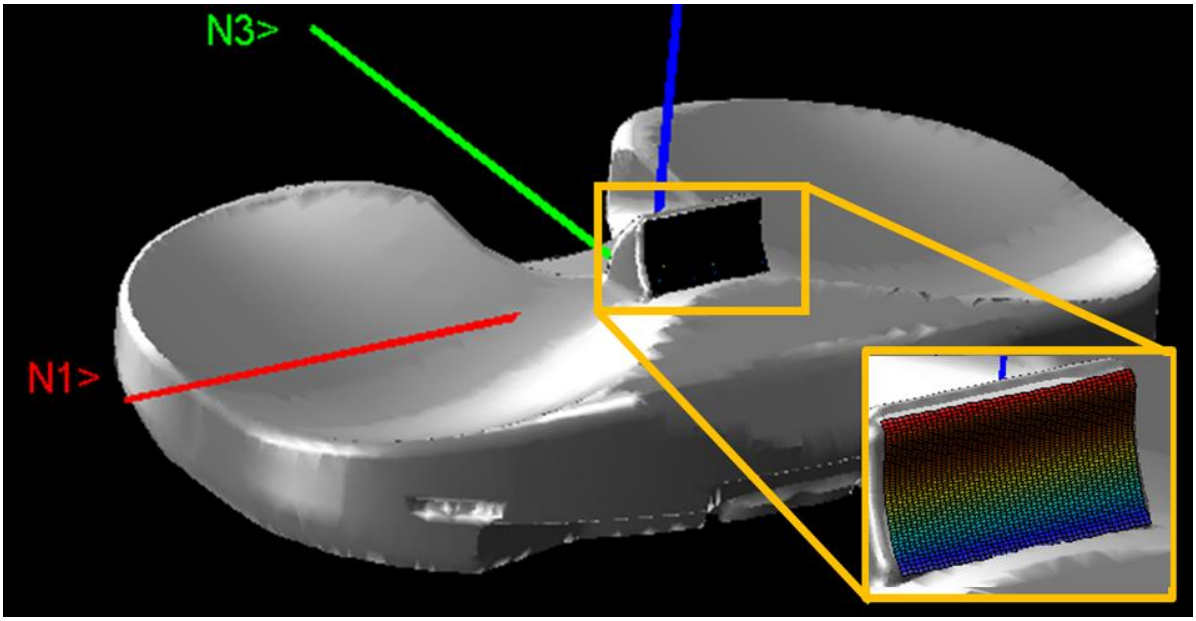

Figure 22: The anterior post is input to the simulation using a surface polynomial.

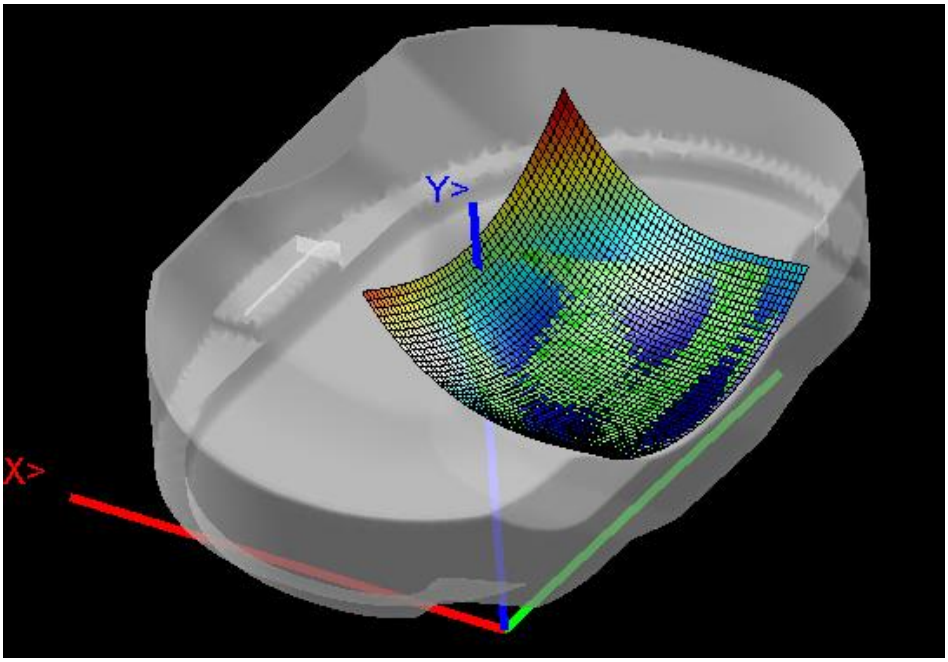

Figure 23: A contact surface could be fit to the third condyle of a tri-condylar design.

Other potential contact surfaces could be placed on the side of the post and on the inside of the intercondylar box to simulate a constraining design such as many revision TKAs. There has been debate as to whether revision TKA should be fixed or mobile bearing based on kinematics. This research could provide data about the cam and post torque in the fixed bearing designs. This torque is transmitted from the polyethylene to the tibial tray and to the component bone interface. It is hypothesized this may cause implant loosening. By incorporating such a contact surface, the magnitude of this torque could be predicted.

Modifications to Muscle Controller

The muscle controller was originally defined as a PID controller on the femur's position with an additional acceleration term making a PIDA controller. While typically a PID controller generates most of its output from the proportional term, the controller in the knee was found to produce smoother and more desirable results when the derivate gain was much larger than the proportional gain.

Furthermore, steady state errors were unimportant, as the knee is still following the desired flexion path even with a steady state error (Figure 24). This meant the integral term of the PIDA controller was unnecessary and therefore removed. This results in a PDA controller on flexion angle. However, this is equivalent to a PID controller on the flexion speed. While this change is ultimately one of nomenclature and not substantial, it has achieved two major benefits. First, there are now only three gains to tune instead of four. Second, it allows for previously established methods of PID tuning to be utilized. With the new PID controller, more complex activities have been simulated such as a partial knee bend and extension before a deep knee bend (Figure 25). The partial deep knee bend serves as a settling algorithm to detect the correct initial conditions for the deep knee bend.

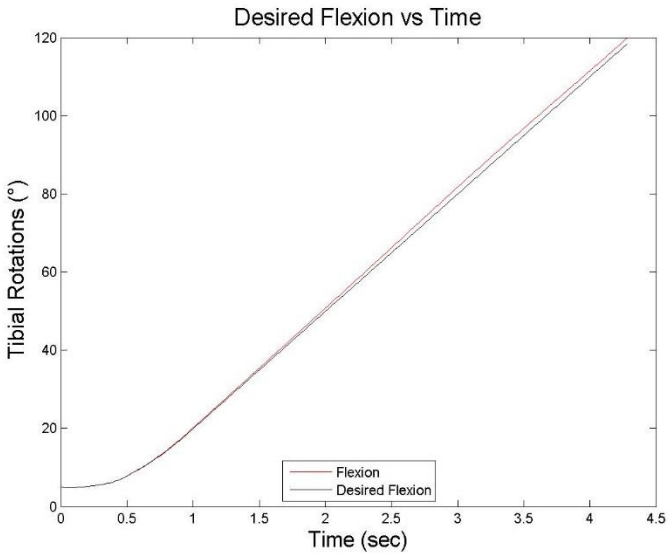

Figure 24: With the PID controller placed on angular speed, the knee has a very smooth velocity, but the potential for steady state error.

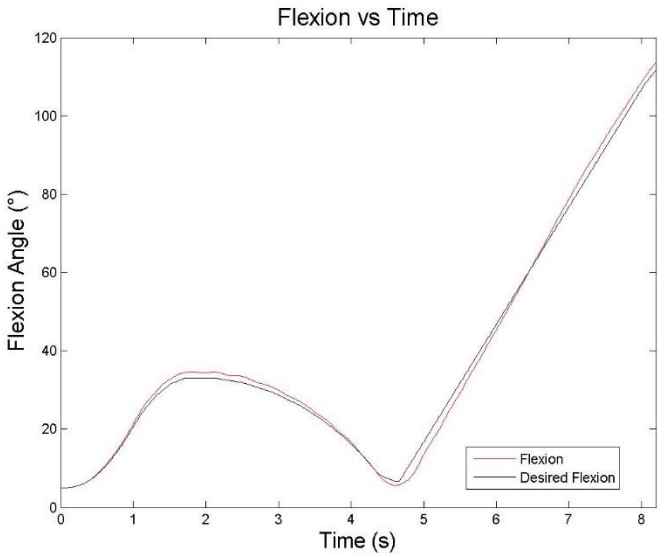

Figure 25: The PID controller can be used to represent more complex activities. A bend to 30° and then extension followed by full flexion functions as a built in settling algorithm for detecting initial conditions is shown.

Contact Force Algorithm

The first step in detecting contact requires the contact point positions to be transformed to the correct reference frame. In the case of the tibiofemoral joint and cam/post interaction forces, contact points are known in the femoral component reference frame and must be transformed to the polyethylene reference frame. First, the location is found for the contact points relative to the femoral component origin using the polyethylene reference frame is found. This is done using the transformation matrix of the femur relative to the polyethylene. Then, the distance from the polyethylene origin to the femoral component origin is added to the resulting location, yielding the contact point position in the polyethylene reference frame. The contact force algorithm checks each potential contact point for penetration with the contact surface. The first step is to ensure that the contact point is within the range of the contact surface. This is done using a convex hull of points around the edge of the contact surface (Figure 26). First, the position vector from the contact point to a point on the convex hull is projected into in the transverse plane. Then, the same projection is found for the next point counterclockwise around the hull. The cross product of these vectors produces a value in the SI direction. If the cross product is negative, it is known that the point is outside of the range and can be ignored (Figure 27). If the cross product is positive, the procedure is repeated shifting over one point counterclockwise around the convex hull. This process is repeated until all points on the convex hull have been used or until a negative cross product is found. If the algorithm finds only positive cross products, the point is determined to be inside the convex hull (Figure 28).

Once it is established that the point exists inside of the convex hull, that point is checked for penetration. The vertical distance from the polyethylene origin to the contact point is compared to the height of the surface polynomial at the corresponding location. If the contact point is lower than surface polynomial, a contact force is applied. First, the normal force is calculated based on the amount

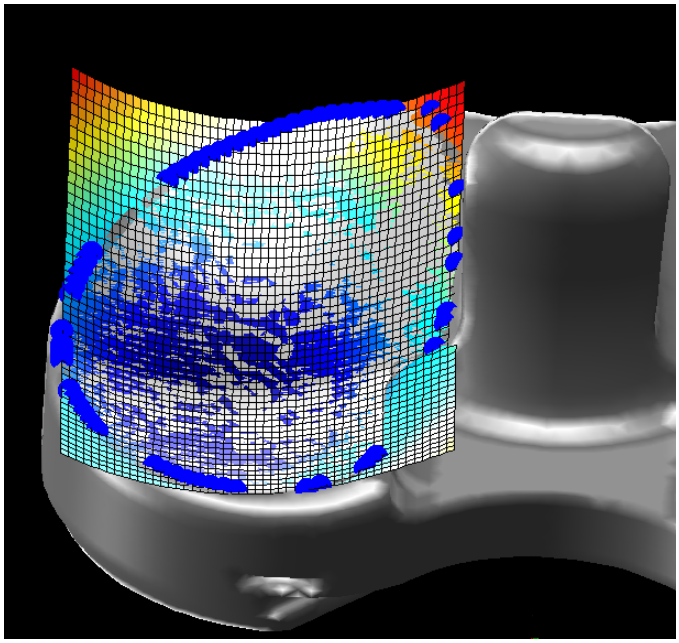

Figure 26: The blue points show the convex hull of the articulating surface.

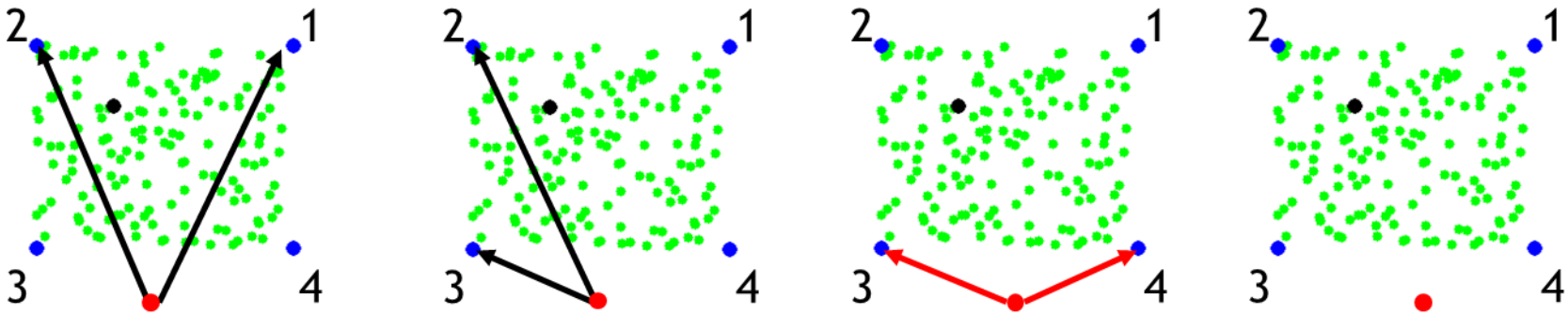

Figure 27: The red point is not inside of the convex hull. The four blue points define the convex hull and are numbered in a counter-clockwise manner. Each cross product is computed from one point to the next sequentially numbered point. The cross product in the third image points into the page (is negative) so the algorithm would exit. The black point is inside of the convex hull because all cross products point out of the page (are positive) as shown in Figure 28.

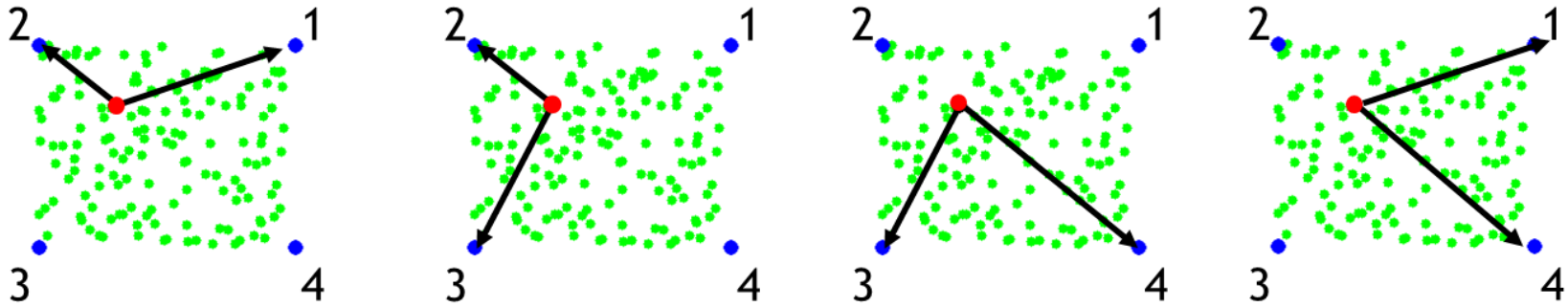

Figure 28: The red point is checked to see if it is inside of the points. The four blue points define the convex hull and are numbered in a counter-clockwise manner. Each cross product going from one point to the next sequentially numbered point is out of the page (is positive). Therefore, the red point is inside of the convex hull.

of penetration and applied along the normal vector, which is calculated by taking the gradient of the surface polynomial and normalizing it. Additionally, a vertical damper force is applied based on the rate of change of penetration (Eq 5, 6, & 7). A frictional force is also applied based on the velocity of the contact point in the X and Z direction (Eq (8, 9, &10).

$$\overline{Normal\ Force_{x}} = \frac{-\frac{\partial y}{\partial x} * K * Pen}{\sqrt{\left(\frac{\partial y}{\partial x}\right)^2 + \left(\frac{\partial y}{\partial z}\right)^2 + 1}} \quad (5)$$

$$\overline{Normal\ Force_{y}} = \frac{K * Pen + B * \frac{dPen}{dt}}{\sqrt{\left(\frac{\partial y}{\partial x}\right)^2 + \left(\frac{\partial y}{\partial z}\right)^2 + 1}} \quad (6)$$

$$\overline{Normal\ Force_{z}} = \frac{-\frac{\partial y}{\partial z} * K * Pen}{\sqrt{\left(\frac{\partial y}{\partial x}\right)^2 + \left(\frac{\partial y}{\partial z}\right)^2 + 1}} \quad (7)$$

$$\overline{Friction\ Force_{x}} = -\mu * \frac{V_x}{V_{Tot}} * \left|\overline{Normal\ Force}\right| \quad (8)$$

$$\overline{Friction\ Force_{y}} = -\mu * \frac{V_y}{V_{Tot}} * \left|\overline{Normal\ Force}\right| \quad (9)$$

$$\overline{Friction\ Force_{z}} = -\mu * \frac{V_z}{V_{Tot}} * \left|\overline{Normal\ Force}\right| \quad (10)$$

Once the contact force is calculated, the resulting moment it generates on the femoral component is calculated by taking the cross product of the position of the contact point relative to the femoral component center of mass and the force at that contact point (Equation 11). Then, all contact forces and all contact torques are summated, and the resultant is applied at the center of the femoral component reference frame. The equal and opposite force is applied at the center of the polyethylene reference frame. The resultant torque on the polyethylene is computed by taking the cross product of the position of the contact point relative to the polyethylene center of mass and the resulting force on the polyethylene.

$$\overline{Torque} = \overline{Position}\ X\ \overline{Force} \quad (11)$$

The method for computing the force at the patellofemoral joint is essentially identical to the method of computing the force at the tibiofemoral joint. There are two notable exceptions. First, the trochlear groove is given its own coordinate system which is rotated -45° about the ML femoral component axis. This is done because the femoral component was rotated 45° before the surface polynomial was fit as described in the Improvements at Patellofemoral Joint section. Secondly, the contact occurs in the AP direction and not the SI direction, resulting in a slight change to Equations 5 - 7 producing Equations 12 - 14. Friction was still computed as before.

$$\overline{Normal\ Force}_x = \frac{K * Pen + B * \frac{dPen}{dt}}{\sqrt{\left(\frac{\partial x}{\partial y}\right)^2 + \left(\frac{\partial x}{\partial z}\right)^2 + 1}} \quad (12)$$

$$\overline{Normal\ Force}_y = \frac{-\frac{\partial y}{\partial z} * K * Pen}{\sqrt{\left(\frac{\partial x}{\partial y}\right)^2 + \left(\frac{\partial x}{\partial z}\right)^2 + 1}} \quad (13)$$

$$\overline{Normal\ Force}_z = \frac{\frac{-\partial x}{\partial z} * K * Pen}{\sqrt{\left(\frac{\partial x}{\partial y}\right)^2 + \left(\frac{\partial x}{\partial z}\right)^2 + 1}} \quad (14)$$

Chapter 4: Development of Graphical User Interface

Objectives

The initial Graphical User Interface (GUI) was a very powerful tool and provided a way to process 3D models into a readable format for the text-based Autolev Code and C++ derived executable. However, interfacing the three different programs required extensive knowledge of how all three programs worked. Continued research would have been greatly slowed by the learning curve of any user other than the software's initial developer. It is the objective of a new user friendly GUI to enable continued research with only days of training as opposed to months.

The general relationship interaction of the programs must be understood before the GUI can be described. First, a physical system is set up in Autolev. This includes definitions of all the bodies (bones and components) and the forces and torques which act on them. When the Autolev code is executed, it produces the equations of motion for the system and saves these to a C++ file. It also generates an input file with values (e.g. the mass of objects) needed to run the simulation.

The C++ file is then heavily modified to fit the desired simulations. This is where the PID controller, the nonlinear function for ligament forces, and the contact force algorithms are defined. It is also modified to read additional input files such as point clouds for contact detection and the convex hull files. Executing the C++ file produces numbered output files containing the results of the simulation. Finally, the GUI (written in MATLAB) serves to produce the input files and plot the output files. In summary, AutoLev® defines the physical system, the MATLAB GUI assigns numerical values to the physical system, and the C++ executable performs the simulation. For the GUI to be considered user friendly, the following conditions must be met.

1. Guide users step by step through creating a new simulation
2. Allow for modification once simulation is set up

3. Save and load simulations for later modification
4. Select simulation conditions (FB vs RP, PCR vs PS)
5. Contain modifiable default values for patient specific properties (ligament insertions, stiffnesses, reference strains, etc.)
6. Scale bones to fit different implant sizes
7. Automatically run the simulation from the GUI window
8. Display results

The code fulfills this requirement by saving all simulation parameters internally until the simulation is executed and generating input files at runtime. To develop a new simulation, the USER loads all bones, implant components, medial and lateral polyethylene plateau surfaces, cam/post contact surfaces, and trochlear groove/patella surfaces. The tibiofemoral contact surface on the femur is determined automatically and does not need to be loaded. With the surfaces, bones, and implant components loaded, the GUI will walk the USER through the simulation setup.

Initial Simulation Set Up

Once the GUI is opened and the necessary objects are loaded, the USER can select to create a new simulation. At this point, the code will walk the USER step by step through creating the simulation. Throughout this process, the USER will be asked to select both surfaces and bodies. Bodies are 3D geometries represented by STL files. The surfaces are two-dimensional and are on one of the 3D bodies. When a surface (or body) needs to be selected, the GUI will only display the surfaces (or bodies). This avoids the possibility of mistakenly the patella component body when the GUI is expecting the patella component surface.

First, the USER is asked to select the medial polyethylene plateau from the list of defined surfaces (Figure 29). Once the USER selects the surface from the list, a new window appears with a mathematically defined surface (blue, yellow, and red) fit to the USER defined surface (green). There are a variety of options for changing the height, conformity, and rotation of this surface as well as for

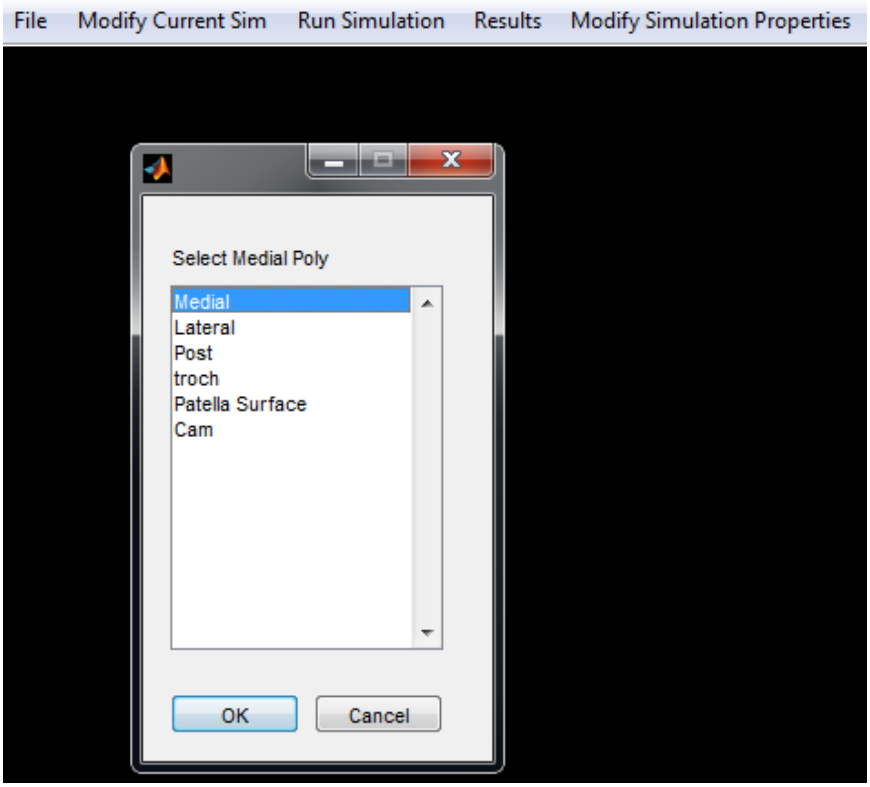

Figure 29: The user is asked to select the medial polyethylene plateau surface.

outputting the surface definition to a text file (Figure 30). Once the USER is happy with the selection, they choose to accept the surface and proceed. The convex hull is also saved (shown in blue spheres).

Next, the process is automatically repeated for the lateral polyethylene and the trochlear groove (Figure 31). Manually modifying the trochlear groove is possible but not recommended, as it may produce unexpected results. Next, the USER is prompted to select the femoral component from a list of bodies (Figure 32). The USER is then asked what flexion angles the code should search for contact points (Figure 33). Next, the code automatically searches for the contact points on the femur by selecting the lowest points on both the medial and lateral condyle and specified flexion angles. The selected points are displayed for the USER (Figure 34).

The code then prompts the USER to select at what increment of flexion angles the lowest point should be computed (Figure 35). The lowest point on the femur is computed at these flexion angles, and the femur low point polynomial is fit to the computed points. The resulting medial and lateral polynomials are displayed and can be edited to change the degree of the polynomial (Figure 36). This process is done twice, first for the polynomial that describes the low point for the first 90° of flexion, and again for flexion deeper than 90° (Figure 37).

Next, the GUI displays a question to the USER with respect to if there is a PS cam/post mechanism to model (Figure 38). If so, the user is asked to select the surface of the cam (Figure 39). All points on the cam are then displayed for the user (Figure 40). Next, the user is prompted to select the post (Figure 41). A surface polynomial is then fit to the post, which can be modified as with the polyethylene plateaus (Figure 42). The convex hull is also saved. Once the user accepts the surface, the GUI proceeds to ask if an AS cam/post mechanism is present (Figure 43). If so, the process is repeated (not pictured).

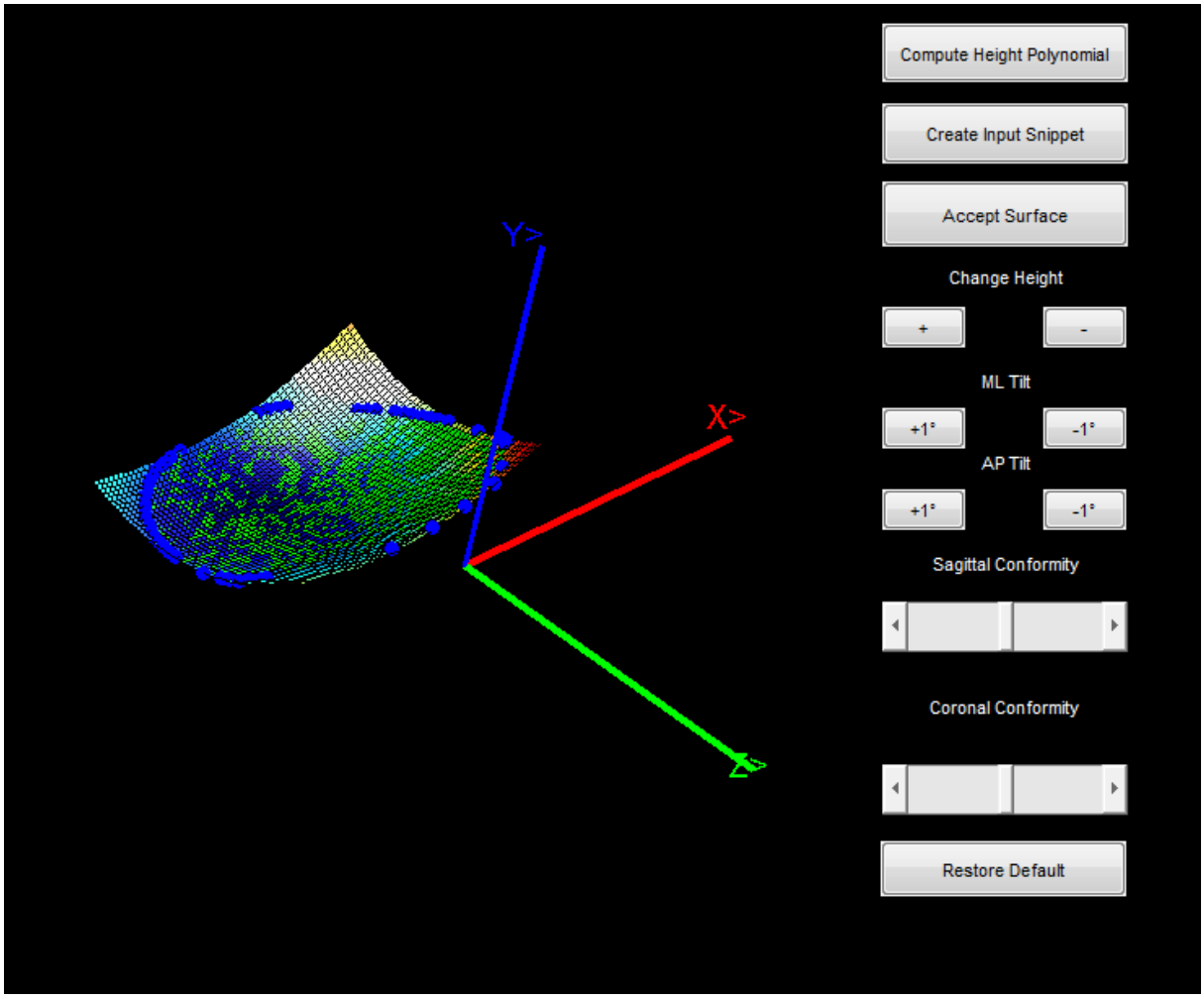

Figure 30: A surface polynomial is fitted to the surface and displayed. Options for shifting the surface vertically or rotating it are displayed to the right. The convex hull points are displayed in blue.

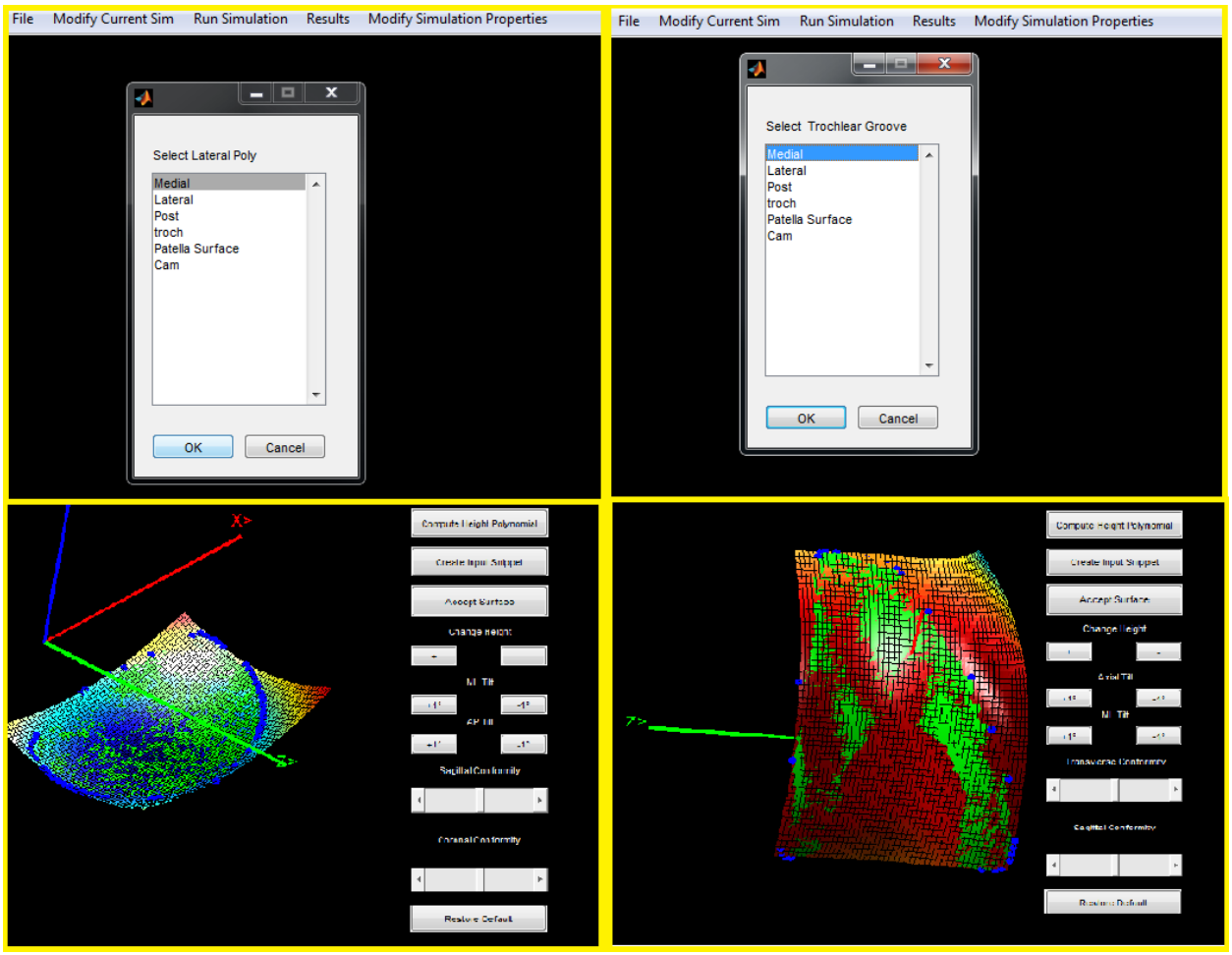

Figure 31: The surface fitting process is repeated for the lateral polyethylene plateau and the trochlear groove. It is not recommended to modify the trochlear groove surface although it is theoretically possible.

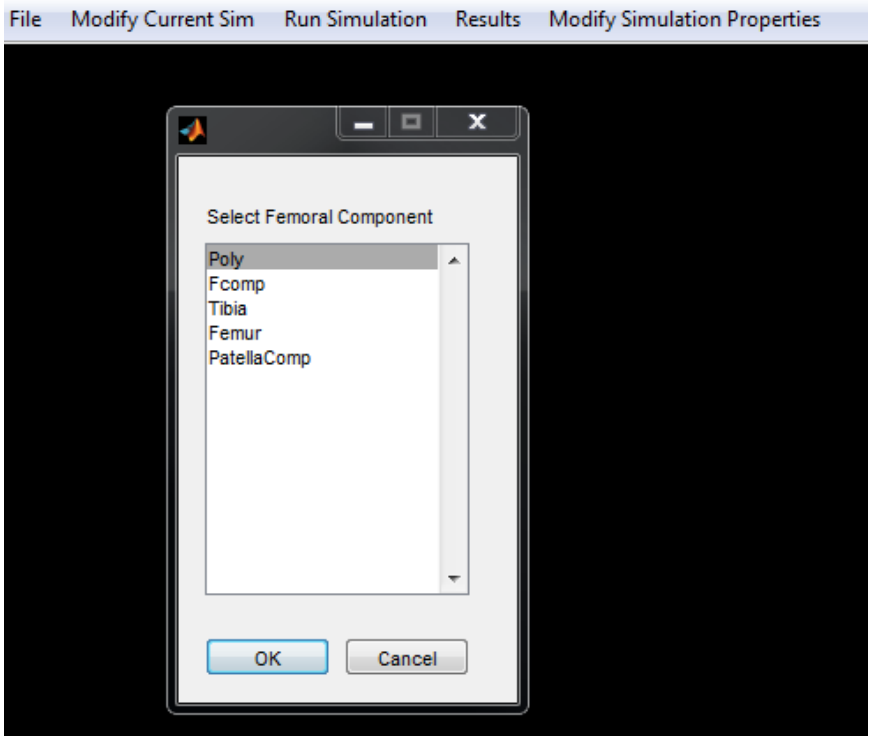

Figure 32: The user is prompted to select the femoral component.

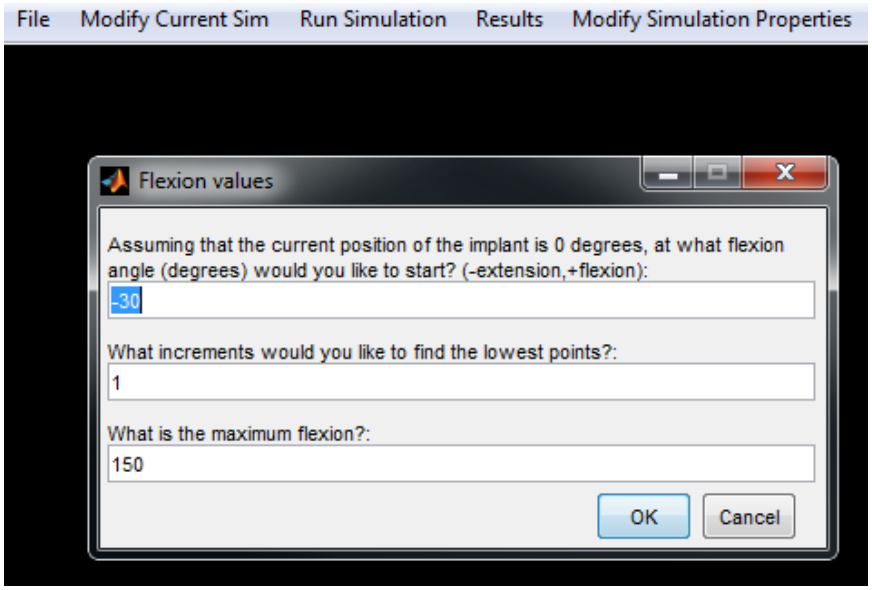

Figure 33: The user picks the start angle, angle increment, and end angle for where the femoral contact points are automatically generated.

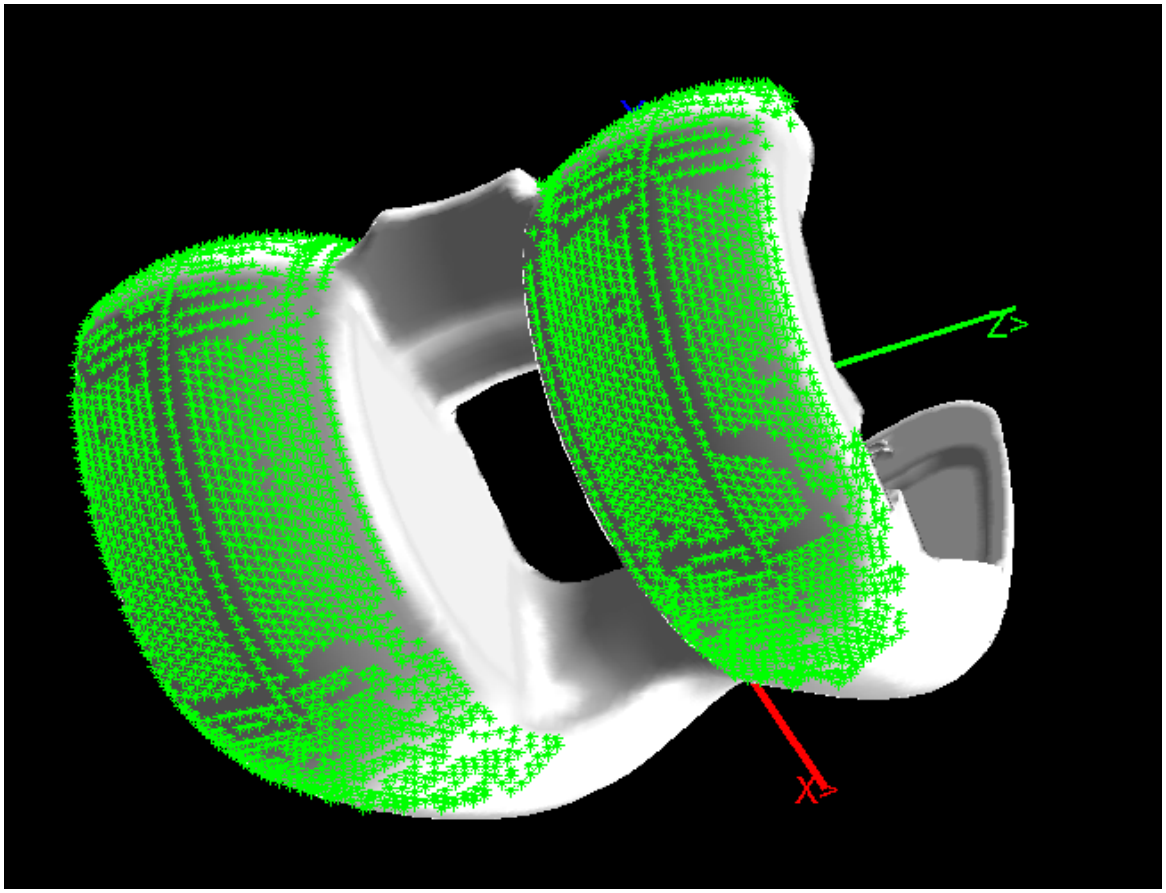

Figure 34: The contact points on the femoral condyles are shown.

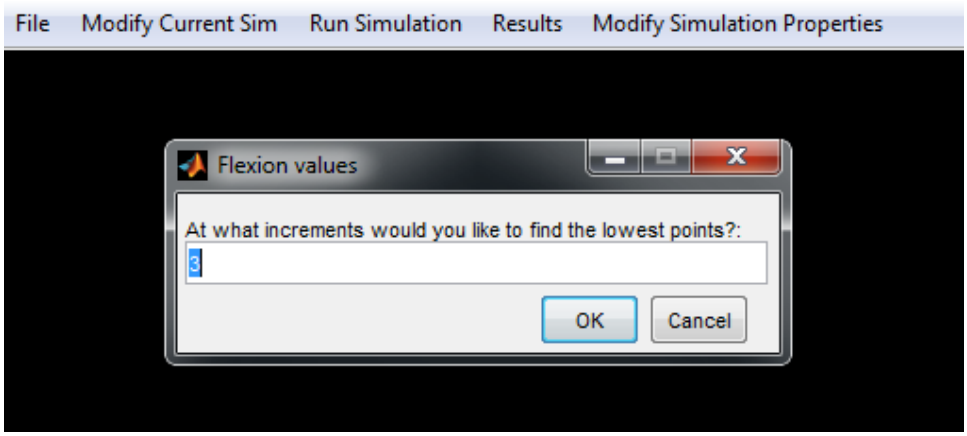

Figure 35: The user selects the flexion angle for picking points for fitting the femoral low point polynomial in early flexion.

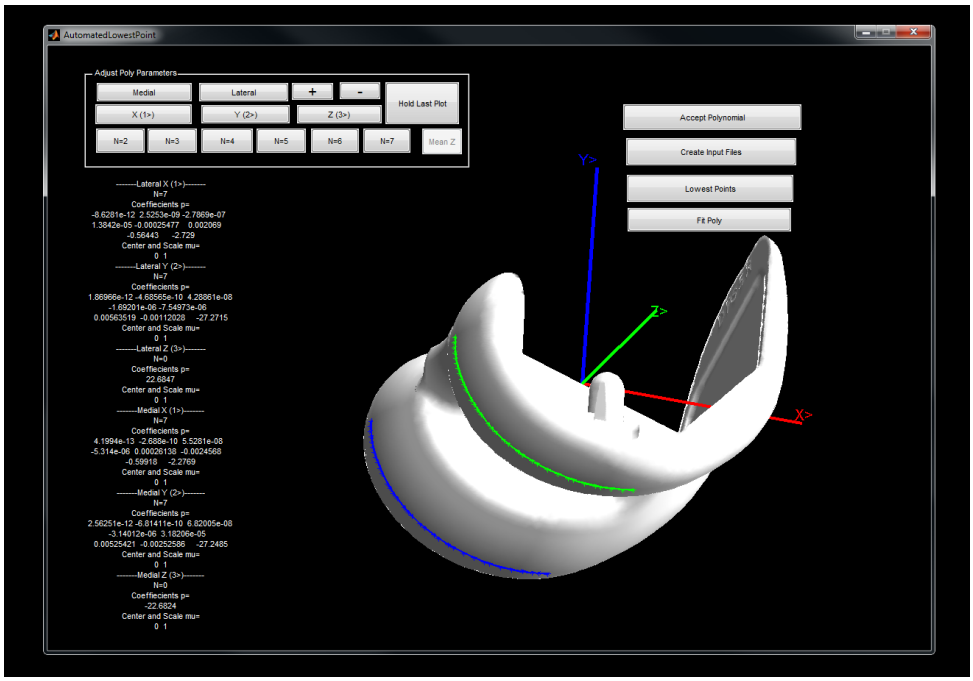

Figure 36: The path of the low point on the femoral condyles in the first 90 degrees of flexion is shown.

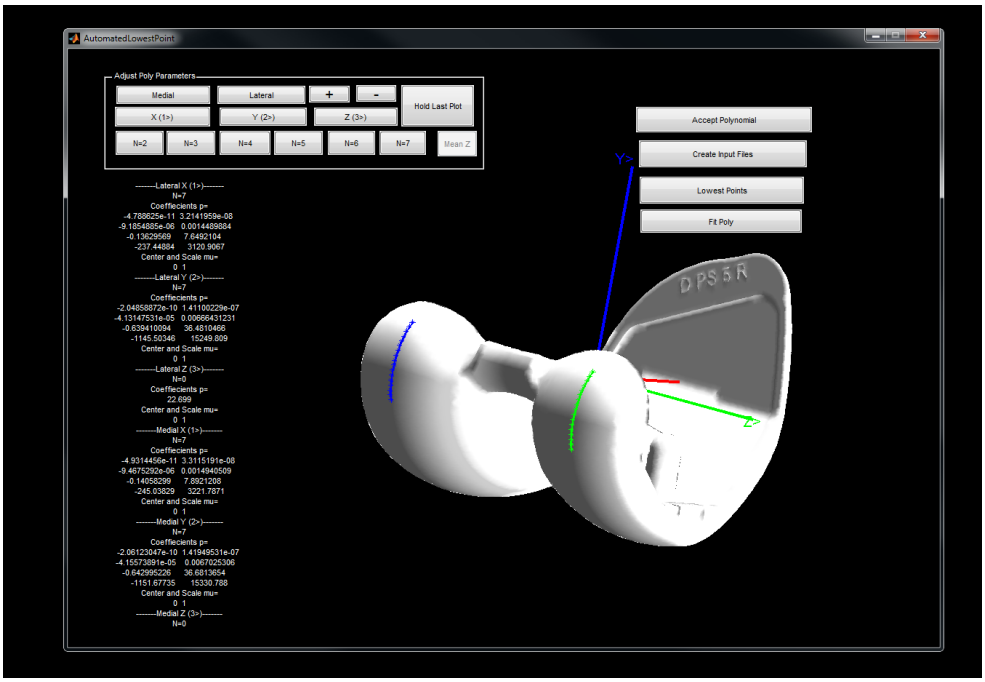

Figure 37: The low point path is shown for 90 degrees of flexion to full flexion.

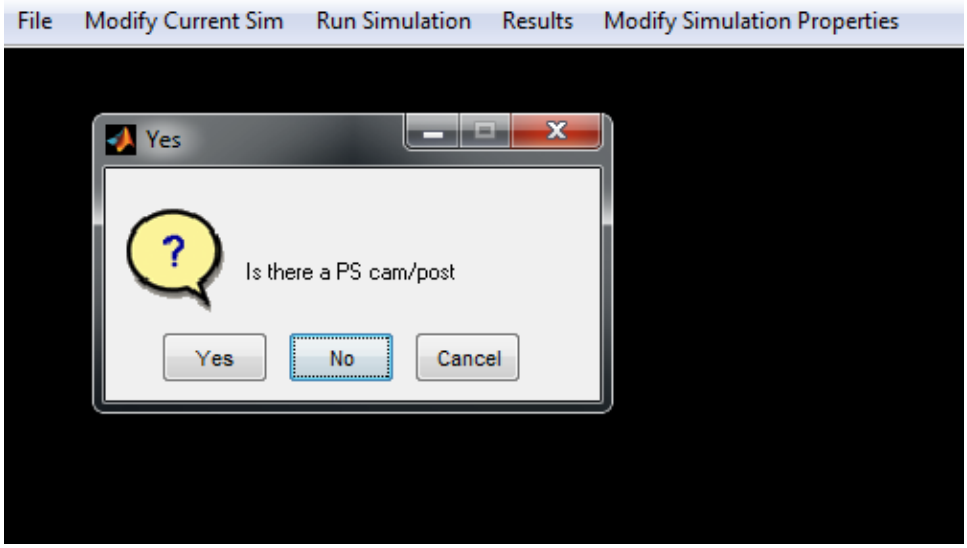

Figure 38: The user is asked to select if the model contains a PS cam/post.

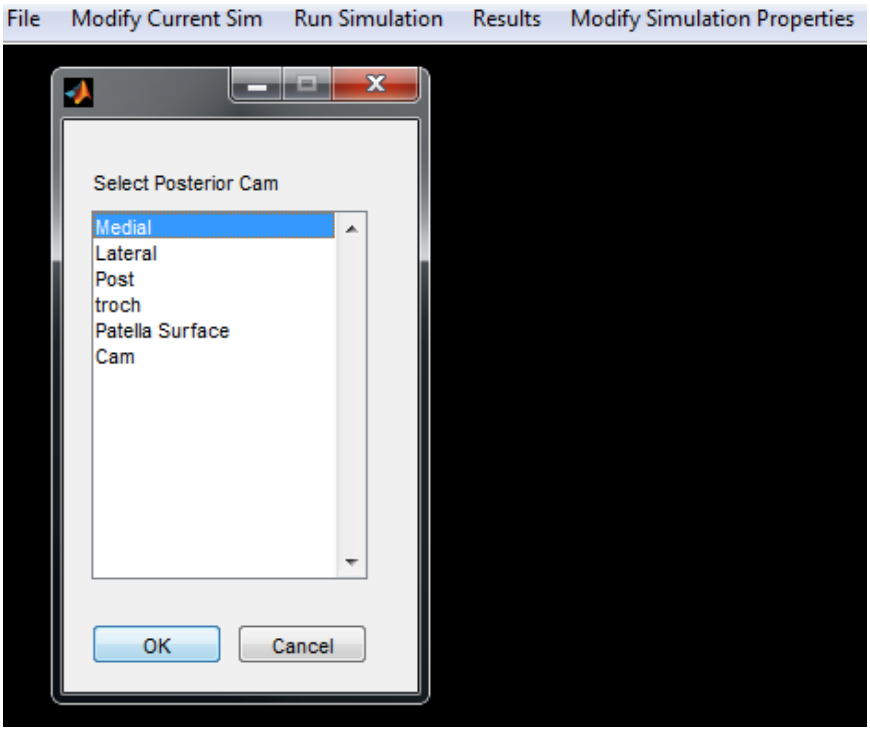

Figure 39: The user is prompted to select the posterior cam surface.

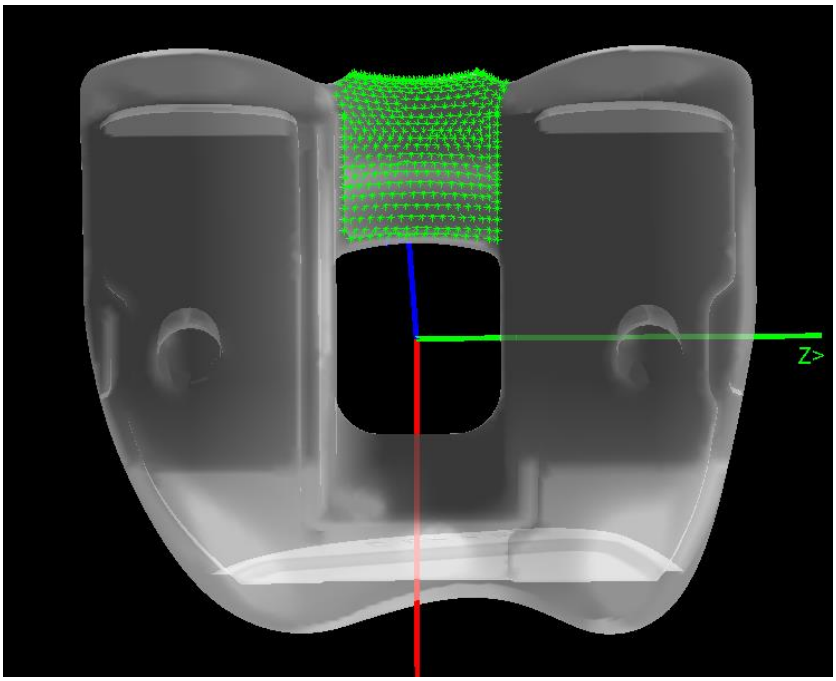

Figure 40: The code selects all vertices in the posterior cam surface as contact points and displays them.

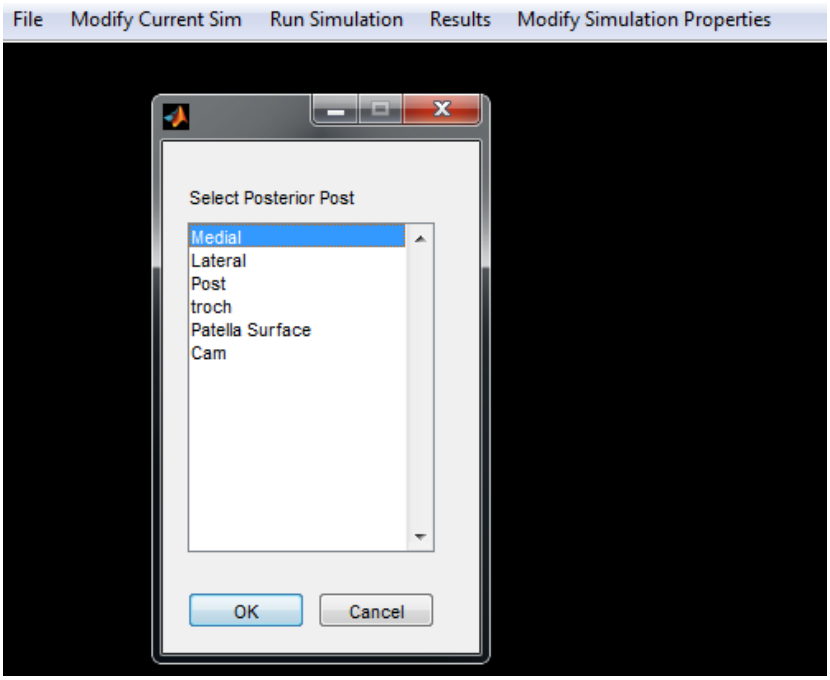

Figure 41: The user is prompted to select the posterior post surface.

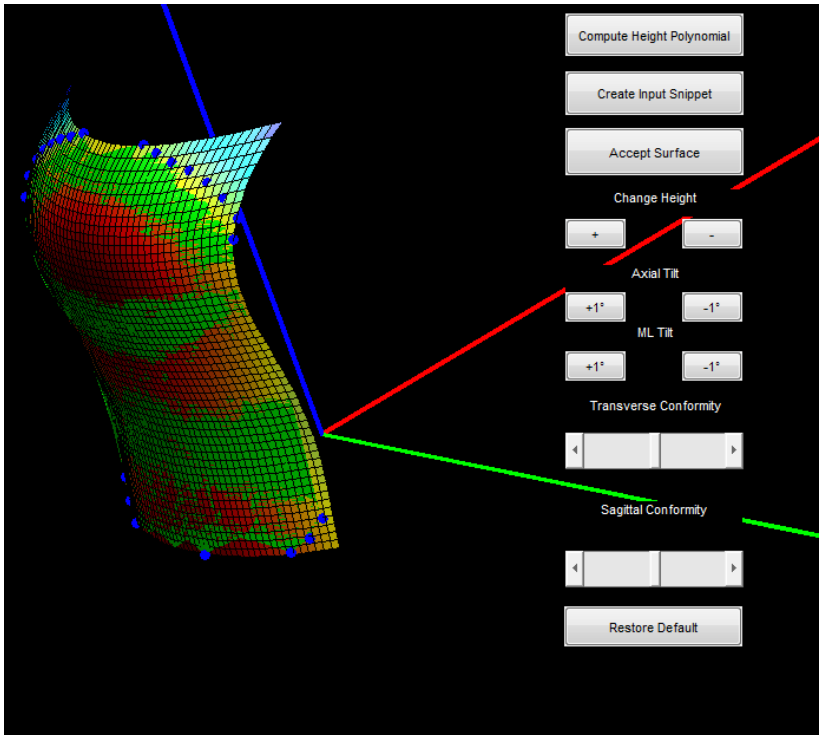

Figure 42: The posterior cam surface polynomial is displayed. This surface can be shifted in the AP direction or rotated. The conformity can also be edited. Convex hull points are shown in blue.

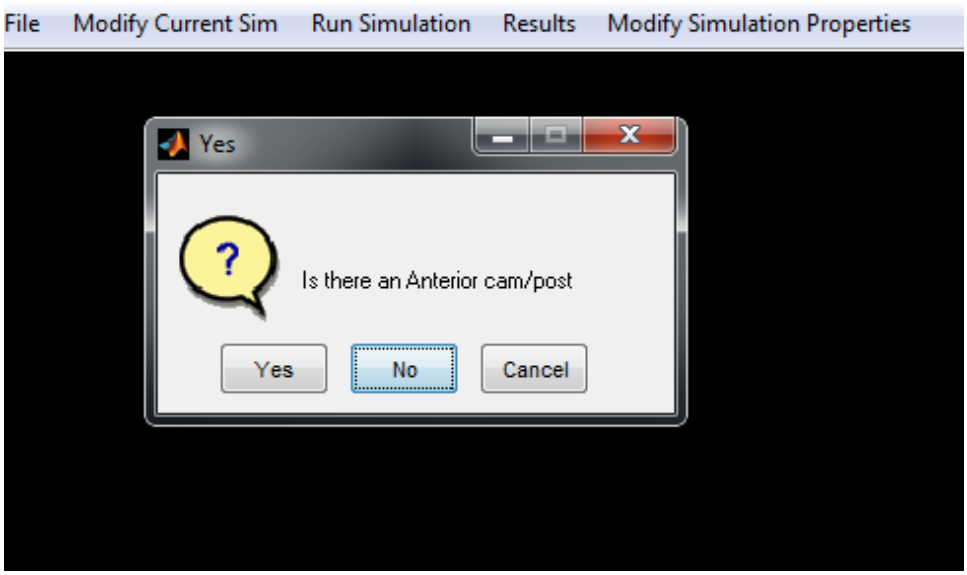

Figure 43: The user selects if an anterior cam/post mechanism is present such as in a bi-stabilizing design. If the user selects yes, the same process will be repeated as with the posterior cam/post.

Next, the USER is prompted to select the patella component as well as the articulating surface of the patella (Figure 44 & Figure 45). The points comprising the surface are then displayed on the patella component (Figure 46). These are the points where the model will search for patellofemoral contact.

Then, the USER selects the femoral bone, and the bone and component are both displayed at the origin (Figure 47). The USER can adjust the position and rotation of the femoral component until the desired surgical placement is achieved (Figure 48 & Figure 49). It is during this process that the femoral bone can be scaled to fit the implant.

Next, the process is repeated for the tibia component on the tibia (Figure 50 - Figure 53). If the USER wishes, she or he may instead select the polyethylene instead of the tibia component. This would allow the USER to place the polyethylene directly on the bone. As before, the USER may scale the tibia bone.

After the tibia component has been placed, the USER is prompted to select the polyethylene (Figure 54). The polyethylene is then placed on the tibia component (Figure 55). There is also an option to move the rotation center of the polyethylene. The red sphere represents the polyethylene rotation center and should be placed on the axis of polyethylene rotation. The SI position of the sphere on that axis is irrelevant.

With all surfaces defined and all components placed, the only remaining task is to set up the simulation's initial position. This includes translation and rotation of the femur and patella relative to the tibia. The model automatically loads the patella, tibia, tibial component, femur, femoral component, and patellar component in a new window. The femur and patella are then manually moved until the model is in the desired initial position (Figure 56). A particularly useful feature in this process is the display of the contact surfaces for the medial and lateral polyethylene plateaus. These are the same polynomial surfaces the USER defined previously. By checking the box to make the surface visible and

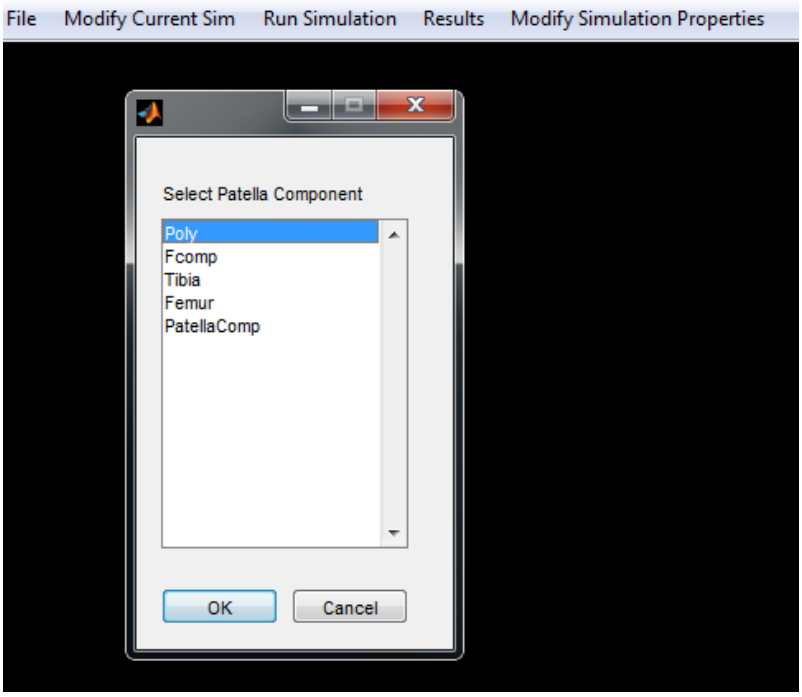

Figure 44: The USER is prompted to select the patella component.

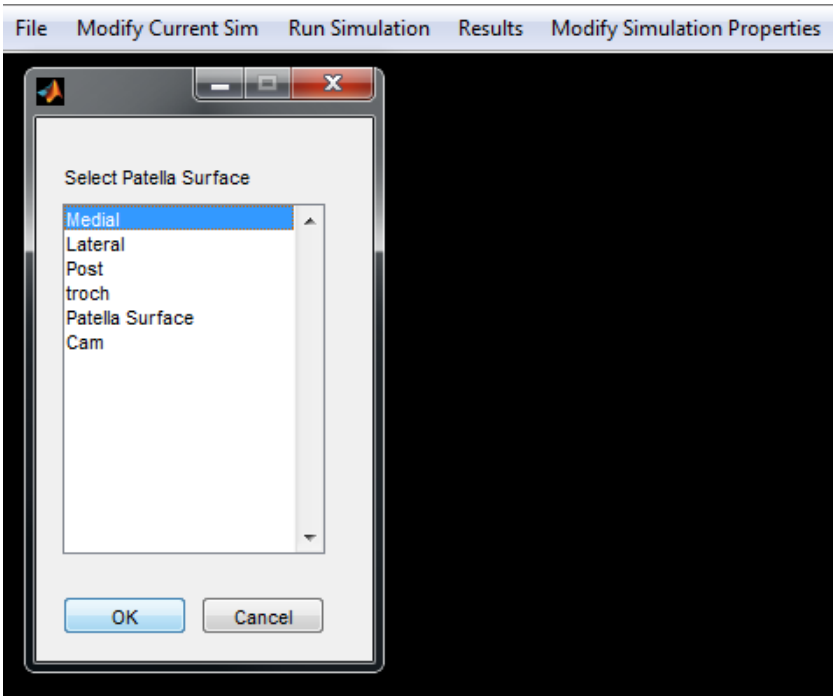

Figure 45: The USER is prompted to select the patella component surface.

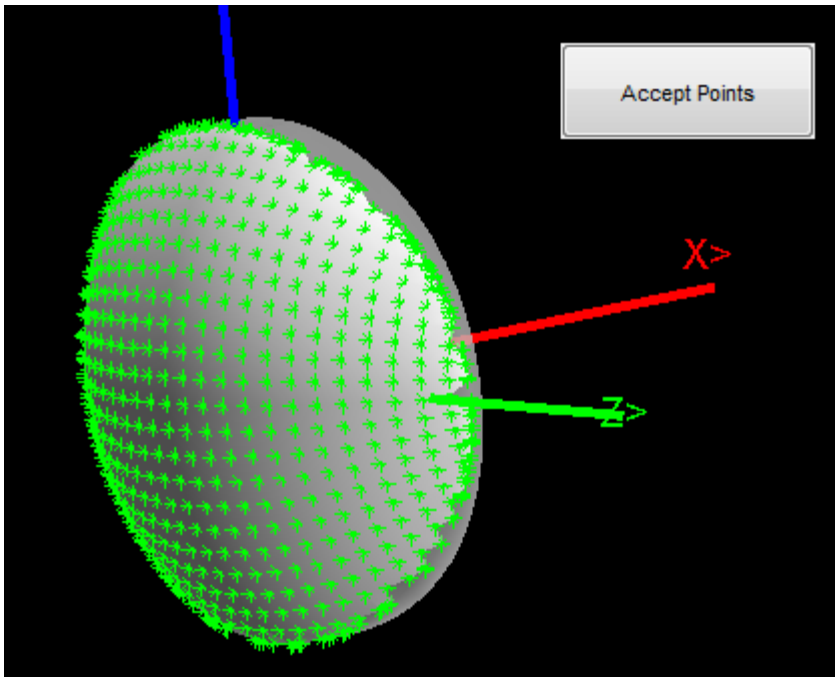

Figure 46: The contact points are determined from the vertices of the contact surface and displayed.

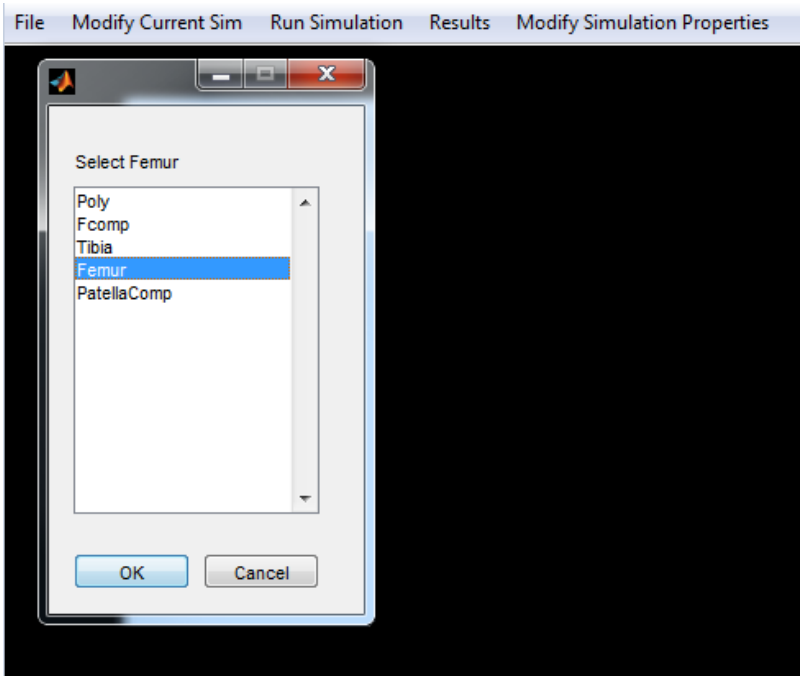

Figure 47: The USER is prompted to select the femur bone.

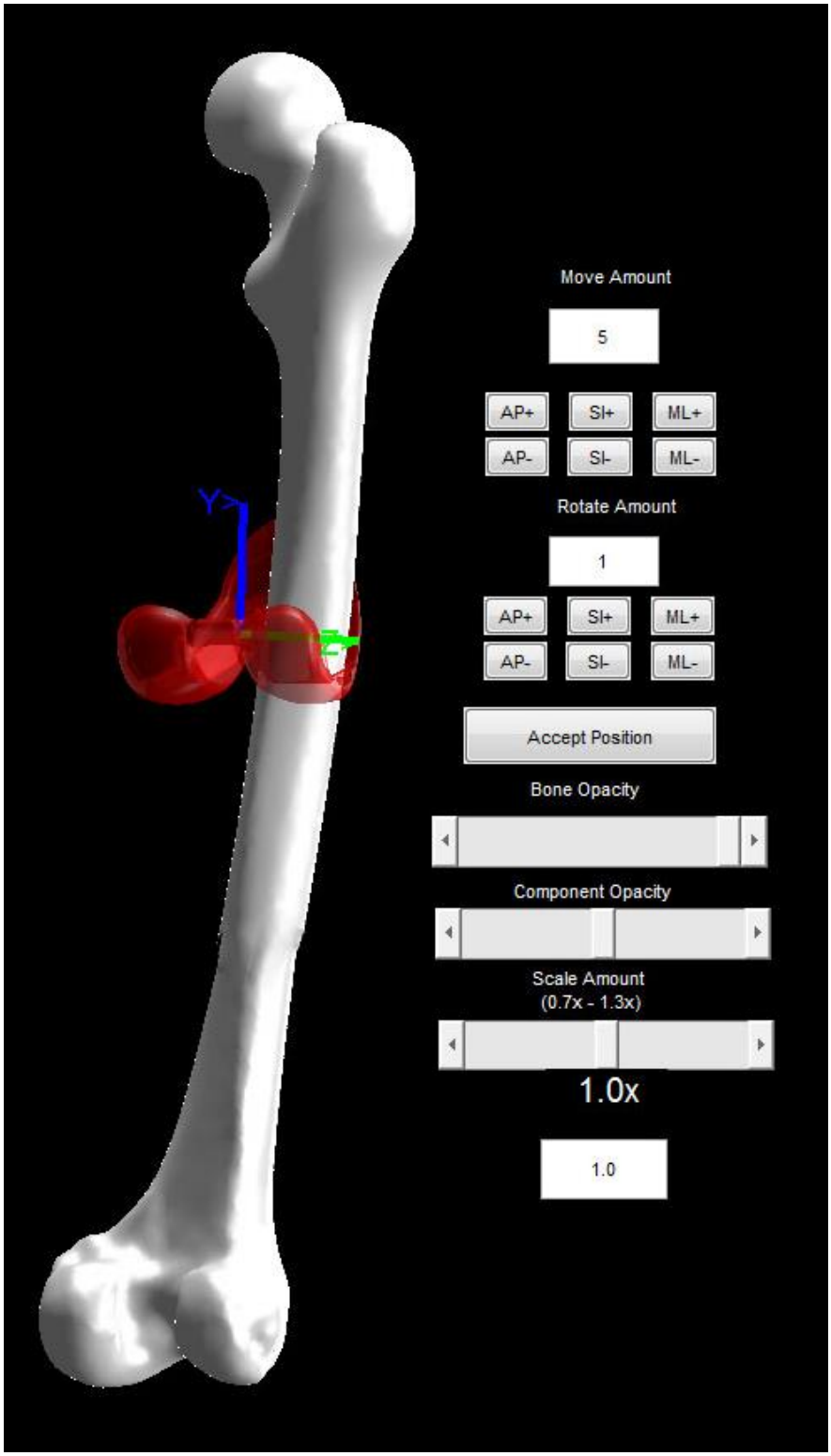

Figure 48: The USER must manually fit the femoral component to the femur in the desired position.

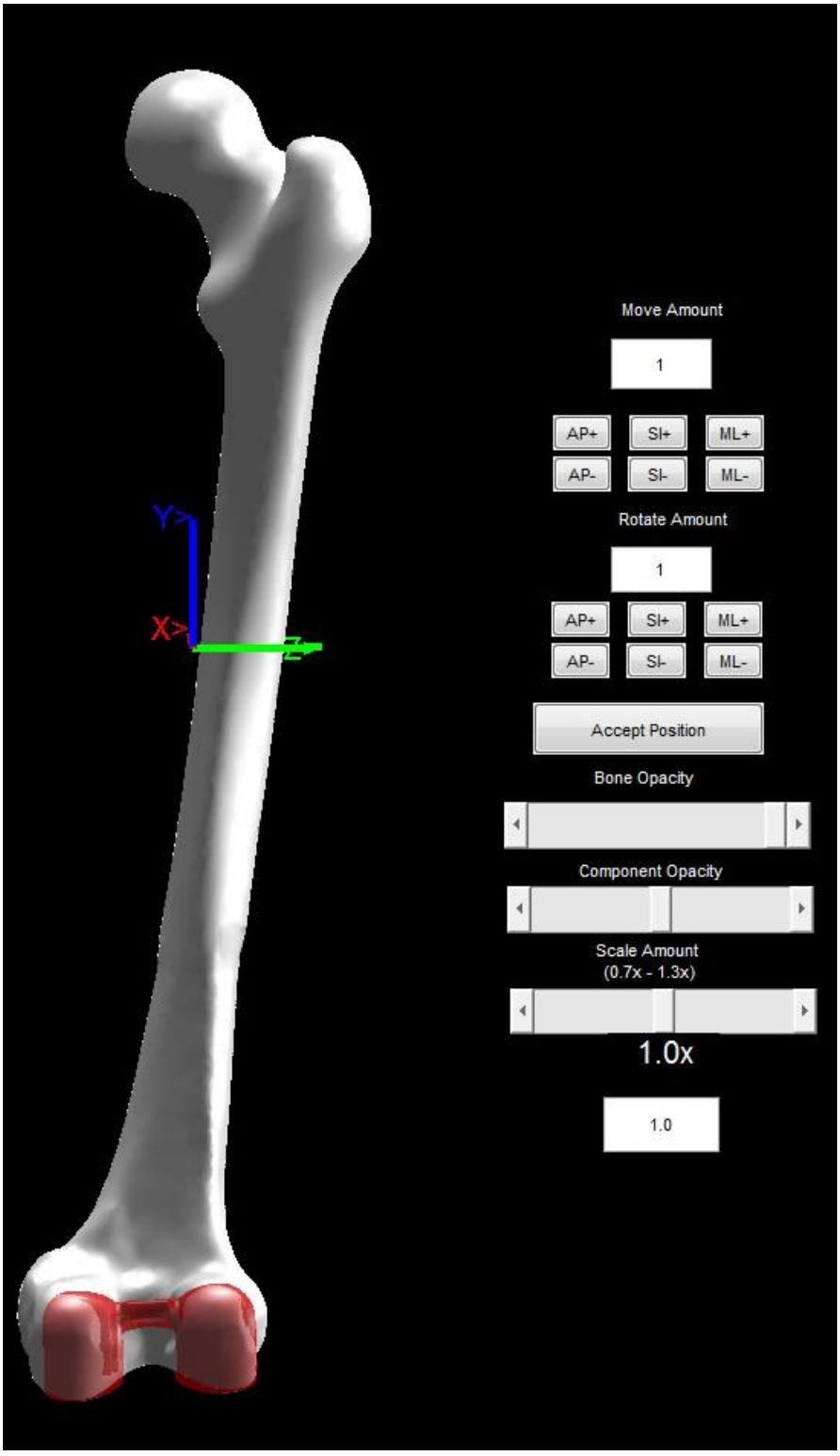

Figure 49: The desired placement of the femoral component on the femur is achieved.

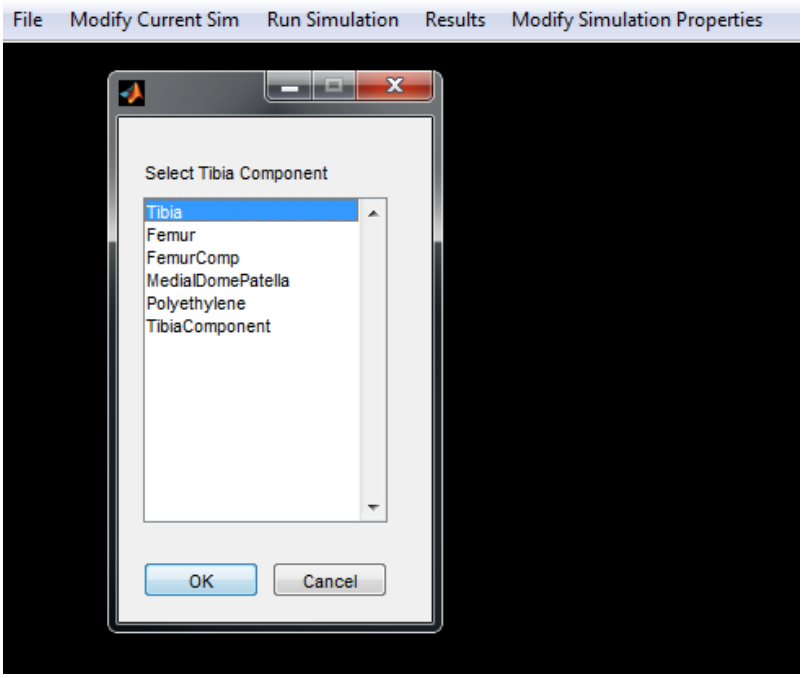

Figure 50: The USER is asked to select the tibial component. The polyethylene component may be selected instead.

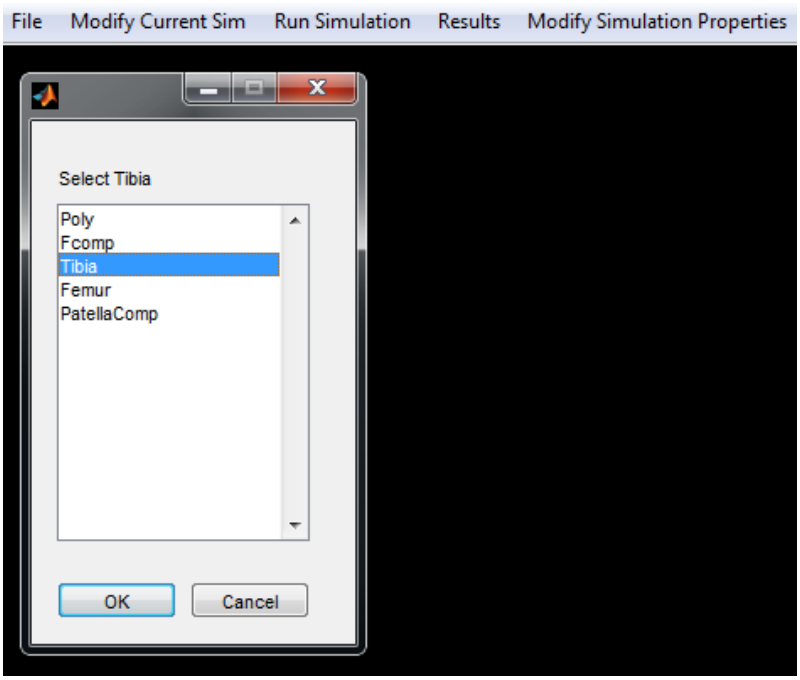

Figure 51: The USER is prompted to select the tibia bone.

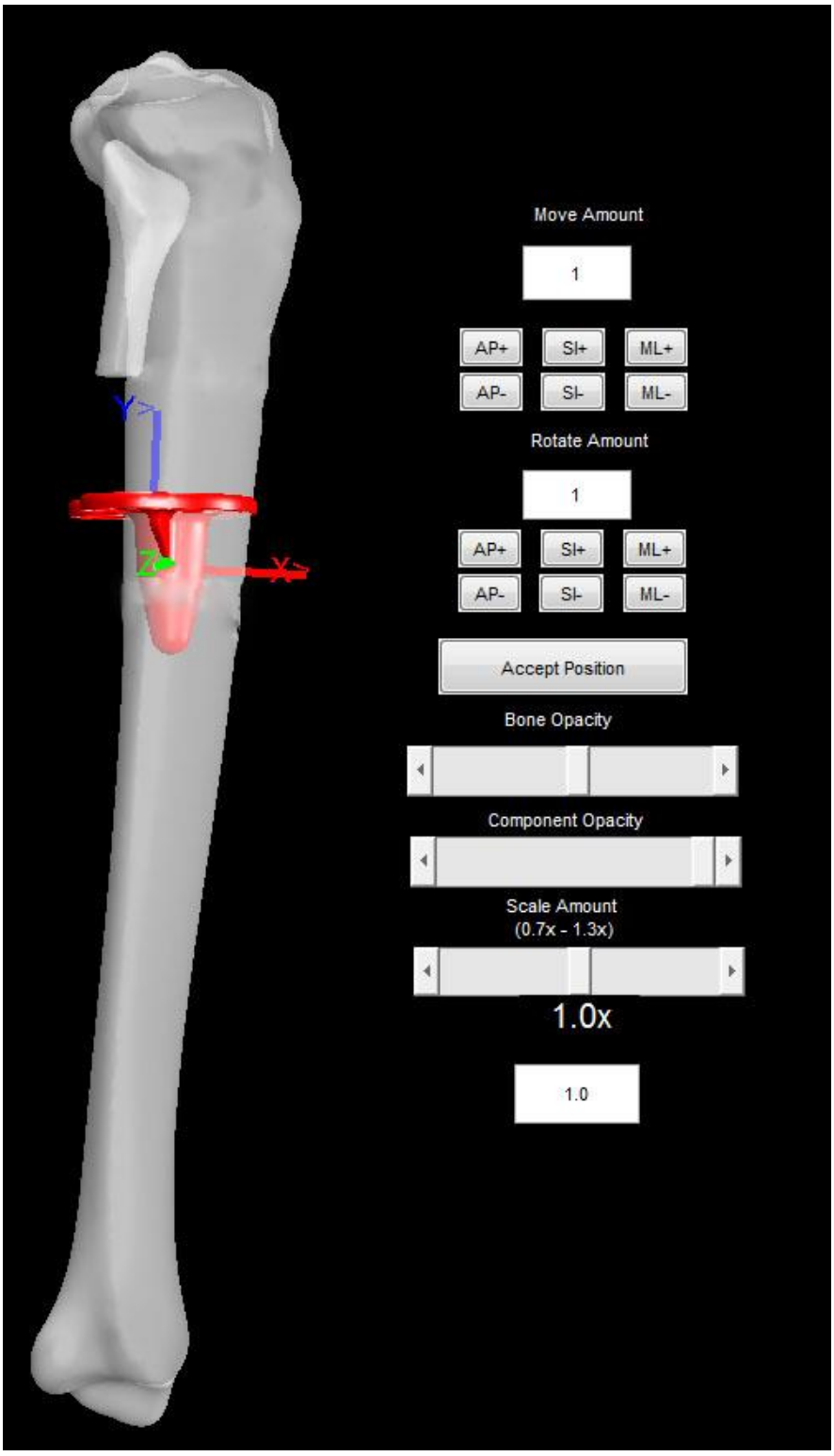

Figure 52: Both the tibial component and the tibia load at the origin and the desired fit must be manually selected.

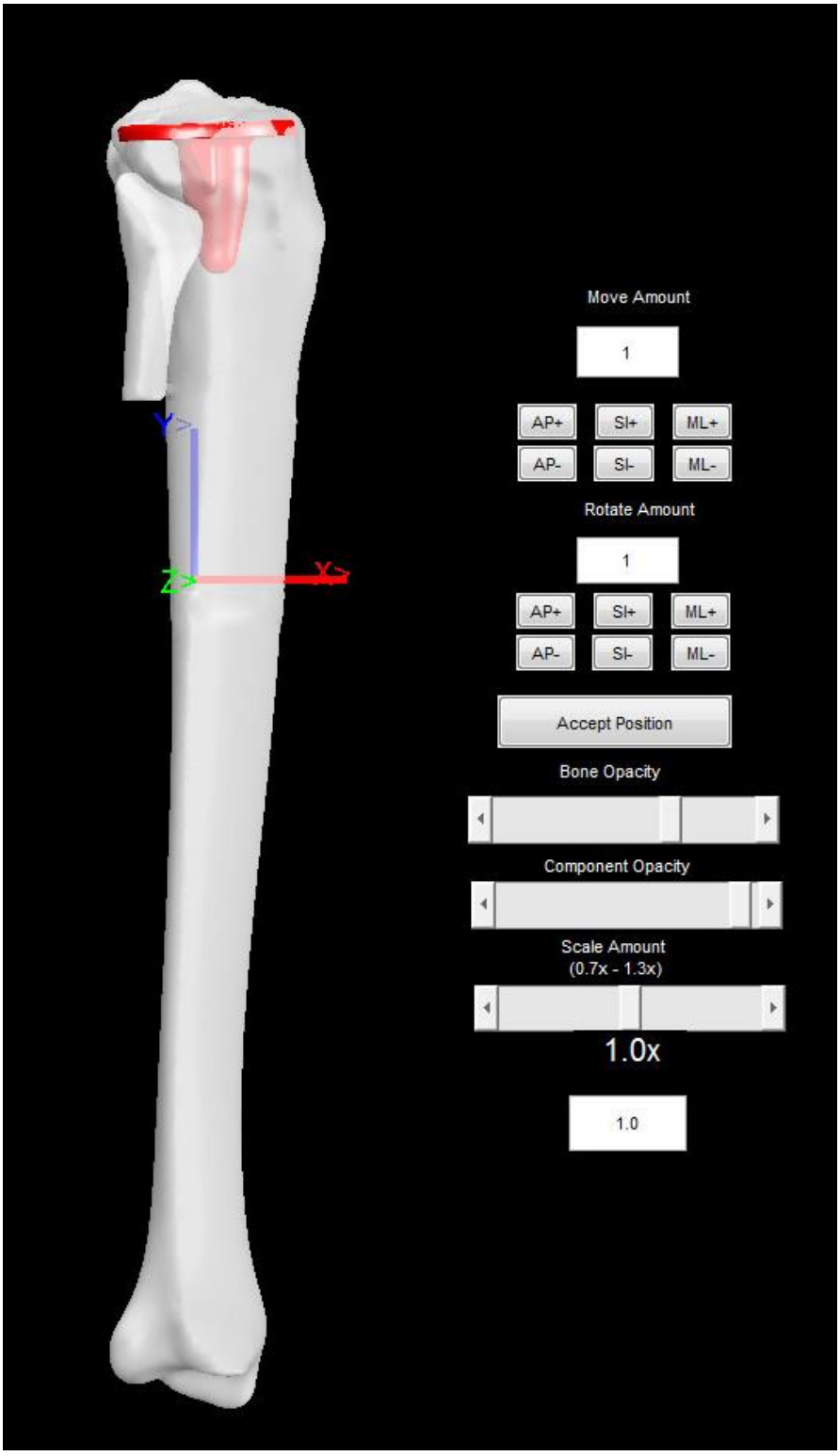

Figure 53: The desired placement of the tibial tray on the tibia is achieved.

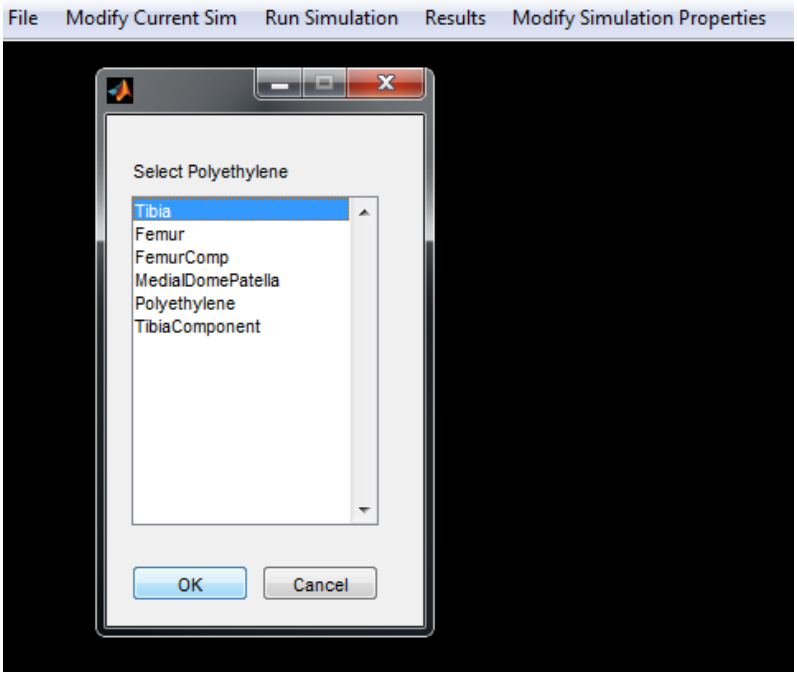

Figure 54: The USER selects the polyethylene component. If the polyethylene component was selected instead of the tibial component, it should still be selected again.

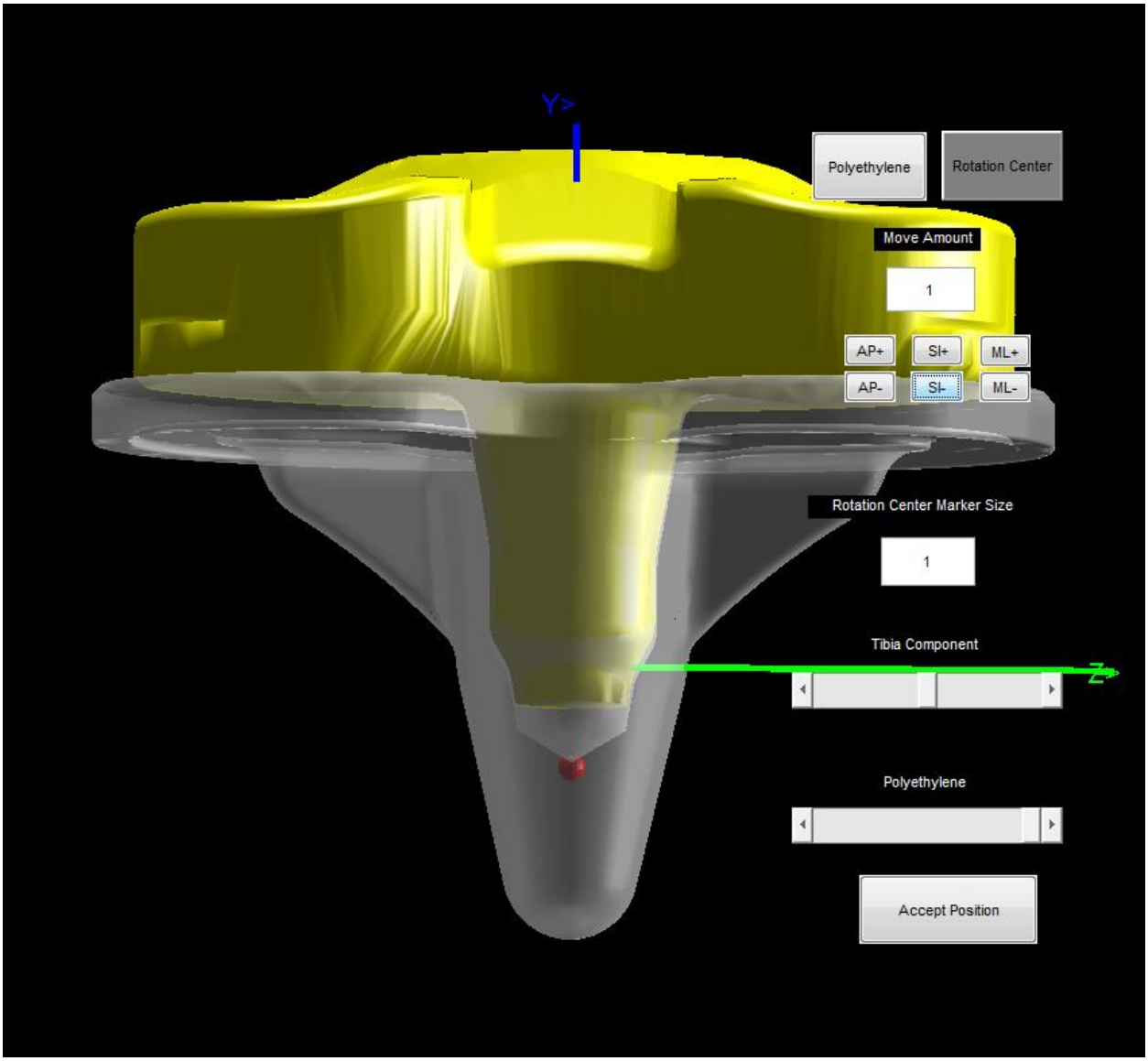

Figure 55: The USER places the polyethylene on the tibial component. If the polyethylene was selected instead of the tibial component, both bodies should be left at the origin. The red dot is the center of rotation for the polyethylene. It has no effect if the simulation is FB.

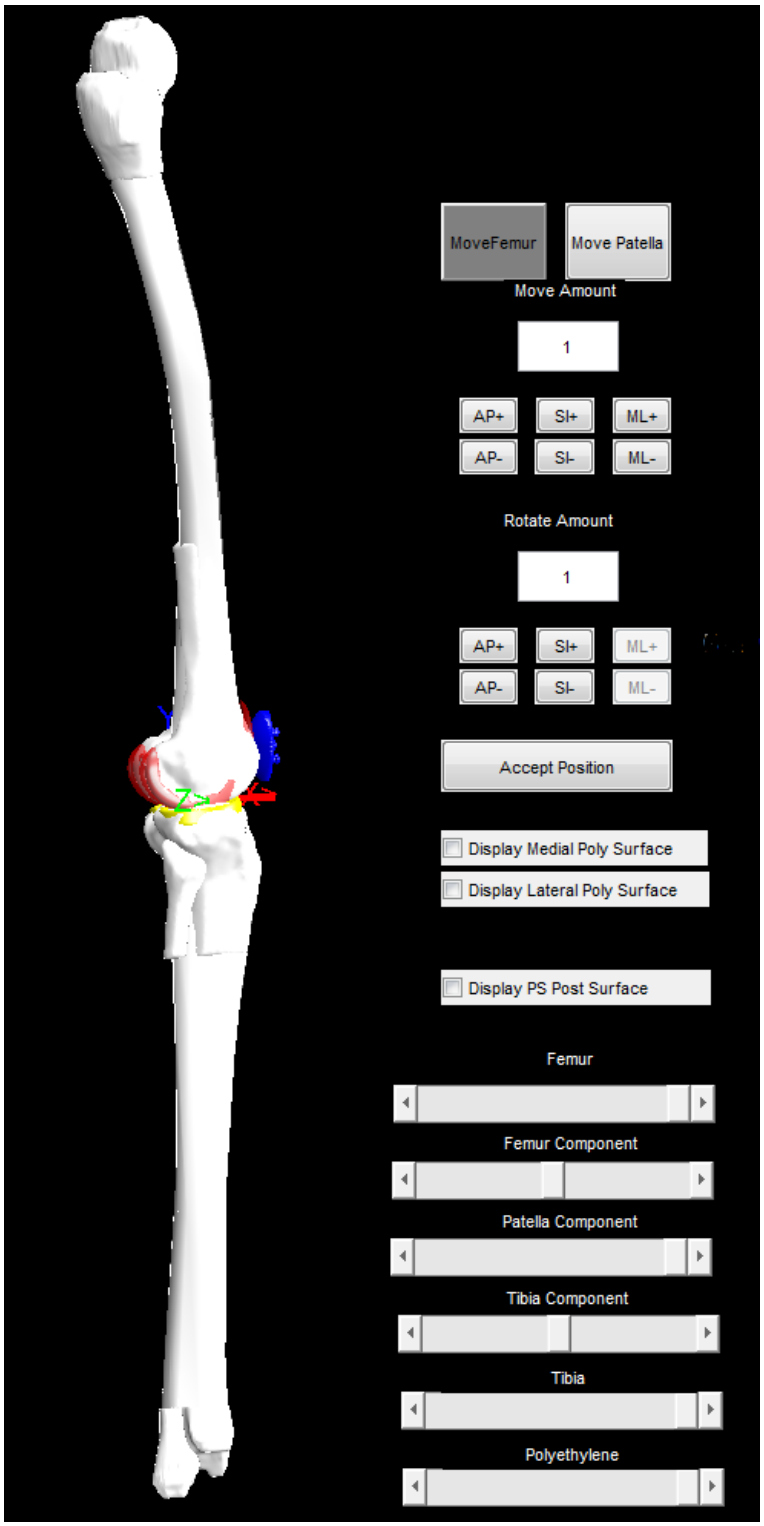

Figure 56: The femoral, tibial, and patellar components are all loaded at the origin. The patella and femur are shifted and rotated until the desired initial positions are achieved.

viewing the femoral component from below, it is possible to see if the model's initial position has contact between the polyethylene and femoral component (Figure 57). Contact is undesirable, as penetration will cause an initial impulse of force from the contact detection algorithm that may lead to the simulation crashing. The USER can manually move the femur vertically to eliminate contact (Figure 58). Ideally, the femoral component should start within 0.01 mm of the polyethylene surface. This process is then repeated to place the patella near the femoral component.

Save and Load Simulations

With the simulation defined, the USER may save it for easy editing to be conducted at a later time (or rerunning the simulation). The USER may also load existing simulations or export the simulation to the workspace in MATLAB (Figure 59). This allows the USER to easily view the variables involved with the simulation. The variables can be edited in the workspace and imported back to the model if desired. In addition to loading an entire simulation, the USER may also load bodies or surfaces from the MATLAB workspace. This tool is useful if a USER wishes to, for example, load a new polyethylene with a new surface without starting a simulation from scratch.

Modify Simulation

The model also offers options to modify an existing simulation. The USER has the ability to change the 3D models for the femur, femoral component, tibia, tibial component, polyethylene, and patella (Figure 60). The USER can also change the surface polynomials for the polyethylene plateaus, trochlear groove, and anterior or posterior posts. The point clouds of the femoral condyles, anterior and posterior cams, and patella can be changed. Furthermore, the low point definition of the femoral condyles can be modified. Finally, the alignment of the femoral component on the femur, tibial component on the tibia, or polyethylene on the tibial component can be edited along with the starting position of the simulation.

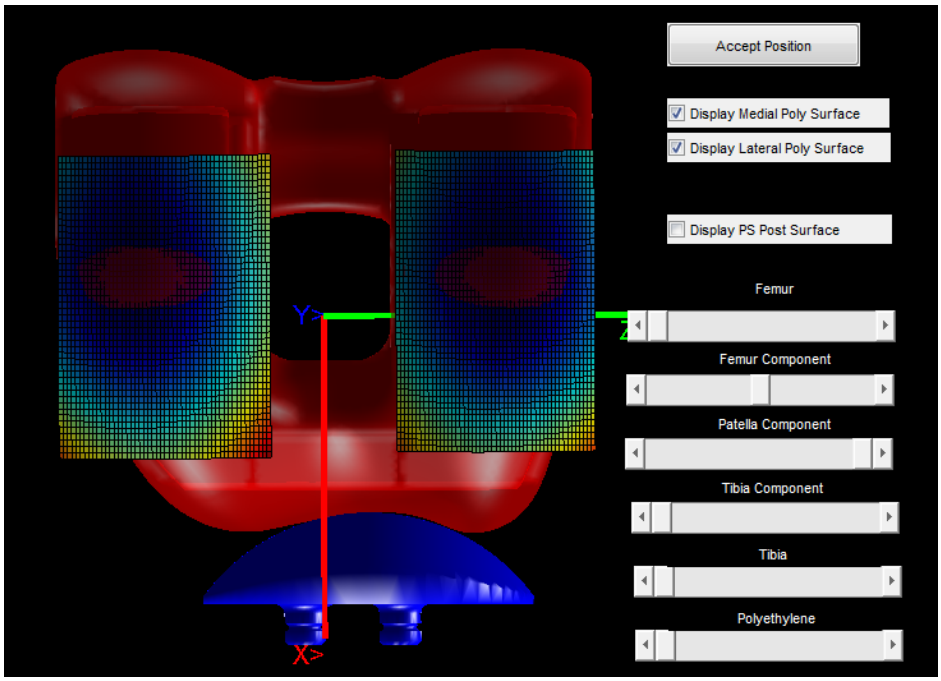

Figure 57: There is slight contact between the polyethylene contact surfaces and the femoral component.

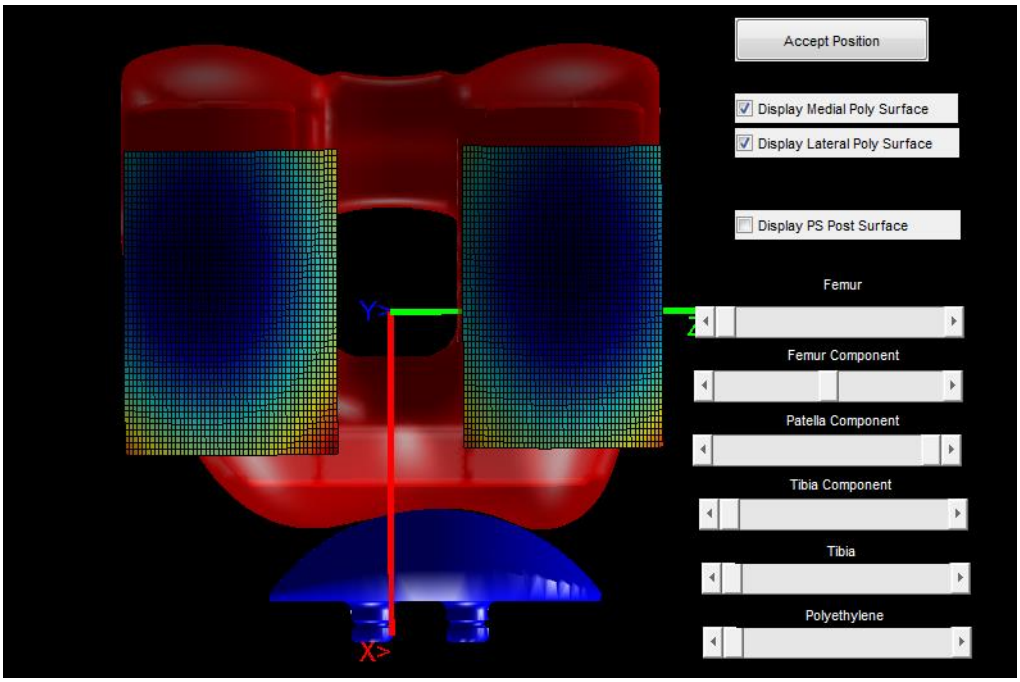

Figure 58: Shifting the femur vertically removes the contact between the femoral component and the polyethylene surfaces.

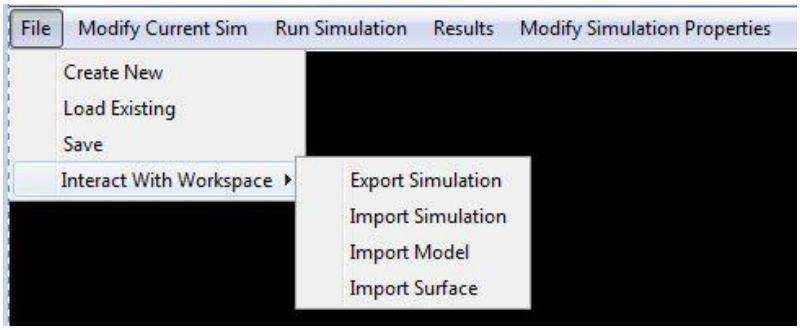

Figure 59: The user may save and load simulations or import/export a simulation to the MATLAB workspace.

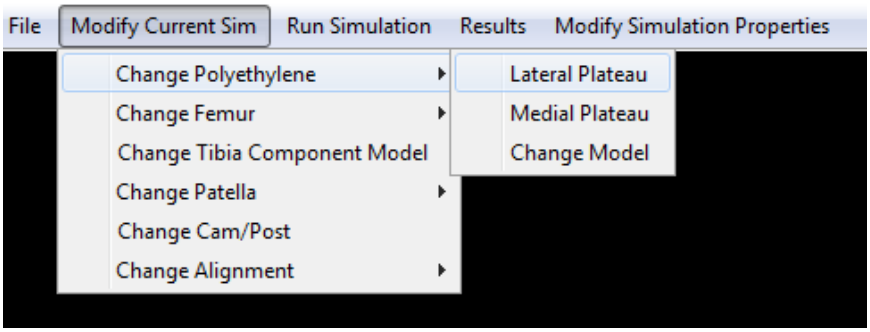

Figure 60: All values which are defined in the initial set up can also be modified later to correct errors or run subsequent simulations.

These changes are made on the same interface as was used initially defining the surface. I.E. if changing the lateral plateau was selected, the USER would be prompted to select the lateral plateau surface and modify it as before.

Change Default Simulation Parameters

Within the GUI, there are four different parameters, with default values. The first type of parameter is referred to as "ZEXTRA", which are variables that are used in the C++ code but not used in the AUTOLEV code. They include features such as PID gains, the flexion angle where wrapping starts, the maximum quadriceps force, and the desired velocity for flexion/extension. The second set pertains to the ligament stiffness. These are essentially the spring constants of the ligaments. The third set is the ligament strain, which is the strain of the ligament in the model starting position. While these parameters have default values, they can all be edited in the "Modify Simulation Properties" tab of the GUI (Figure 61). Once the desired Parameter (either ZEXTRA, Ligament Stiffness, or Ligament Strain) is selected, a table opens displaying the values of the parameters and their names. The USER can then edit the value directly in the table (Figure 62 - Figure 64). The GUI also features a "restore default" option for each parameter.

The fourth parameter, within the GUI, contains default information for the origin and insertion of the MCL, LCL, and PCL bundles. If the USER chooses to edit these parameters, a new window will open, displaying the ligament origins and insertions in their default positions (Figure 65). Each origin/insertion pair features the same color for ease of viewing. The color can be changed for the pair by clicking on the associated box and selecting a new color, but the origin and insertion are changed together (Figure 66). The USER can then also define a new origin or insertion by selecting the appropriate checkbox. With the checkbox selected, the USER simply clicks on the desired location for the new origin or insertion on the

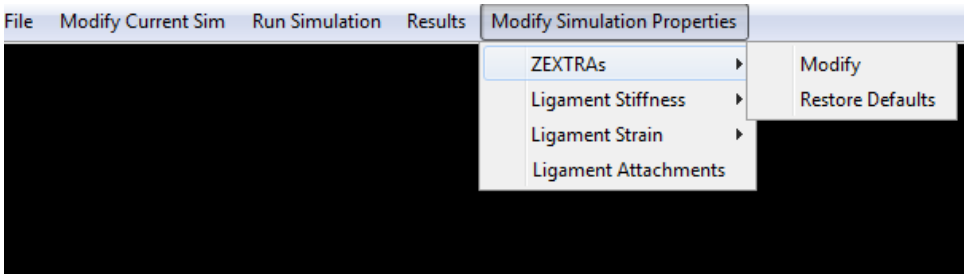

Figure 61: The ZEXTRAs, ligament stiffness, ligament strains, and ligament attachments have modifiable default values.

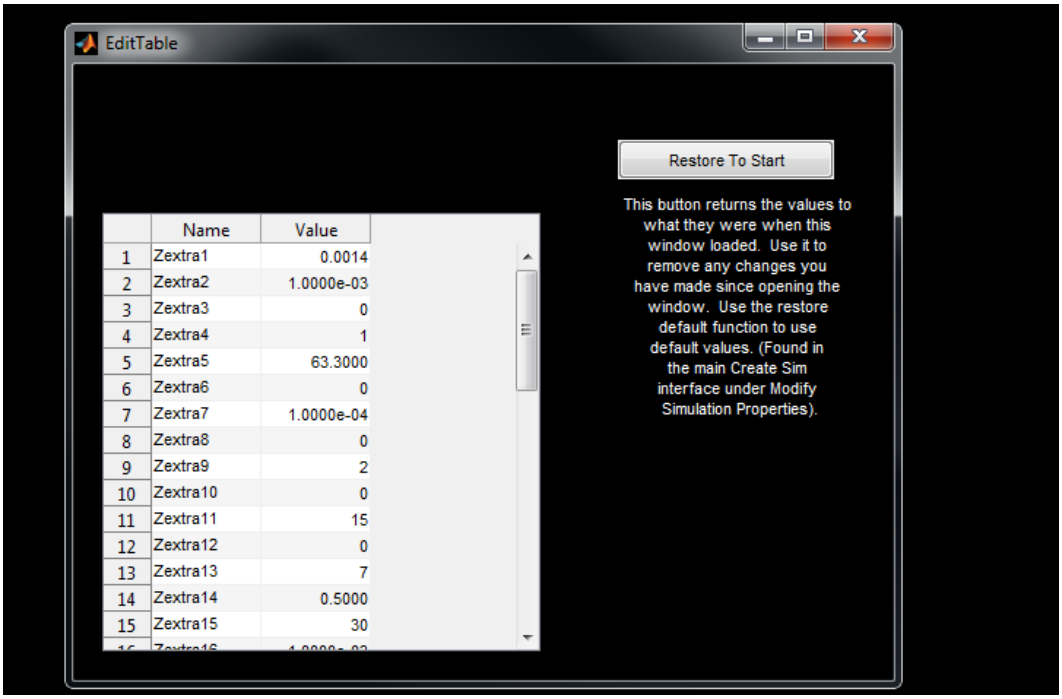

Figure 62: The default ZEXTRA values are shown which can be edited in this table.

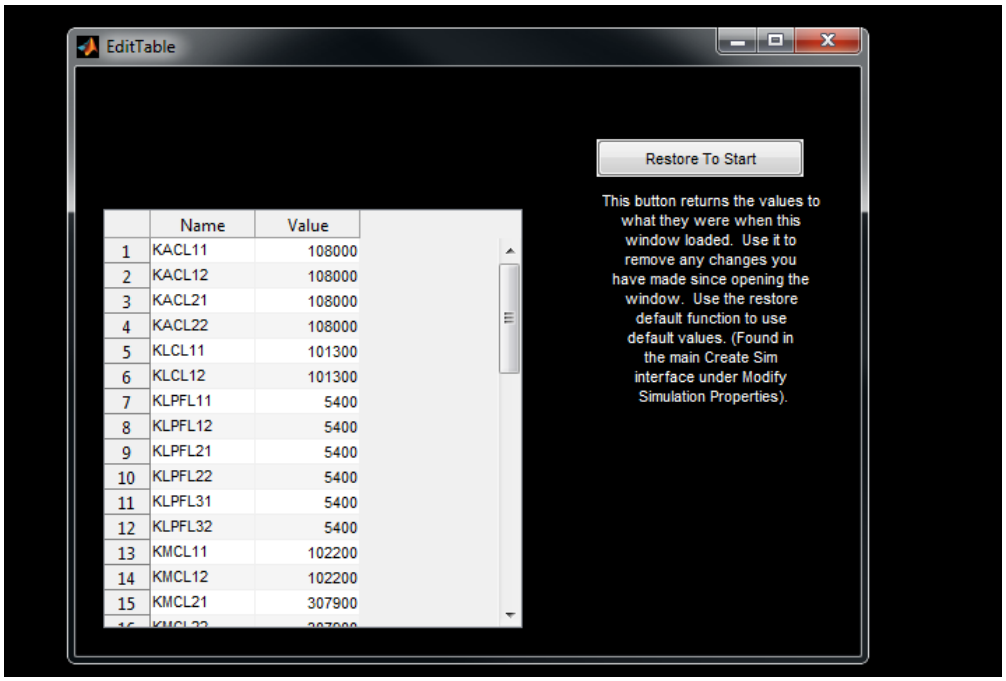

Figure 63: The default ligament spring stiffnesses are shown which can be edited in this table.

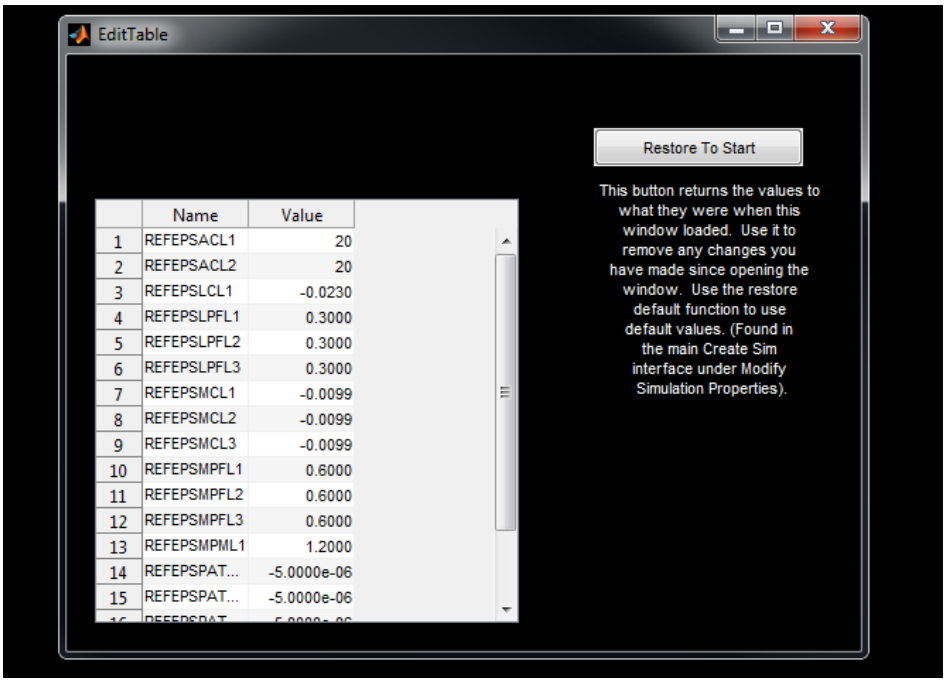

Figure 64: The default references strains are shown which can be edited in this table.

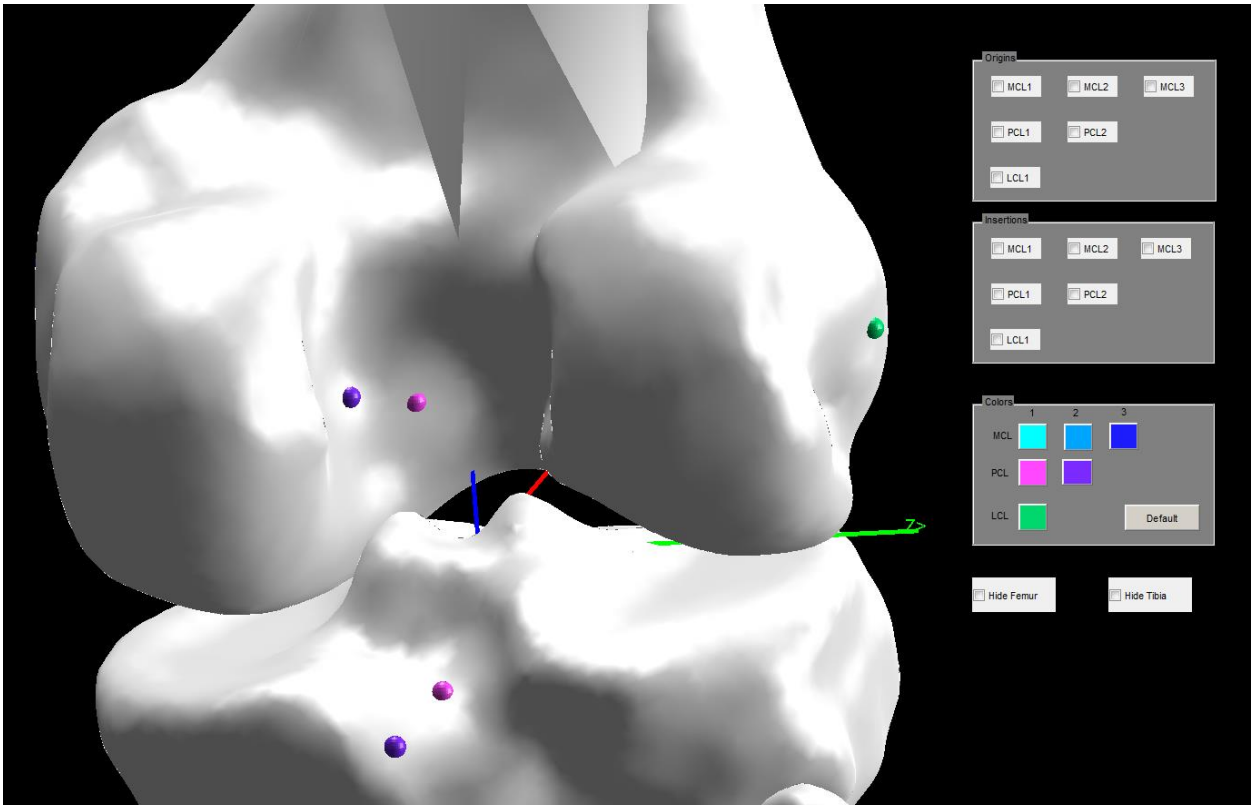

Figure 65: The default PCL origin and insertion (purple, two bundles) and LCL (green, one bundle) origin are shown.

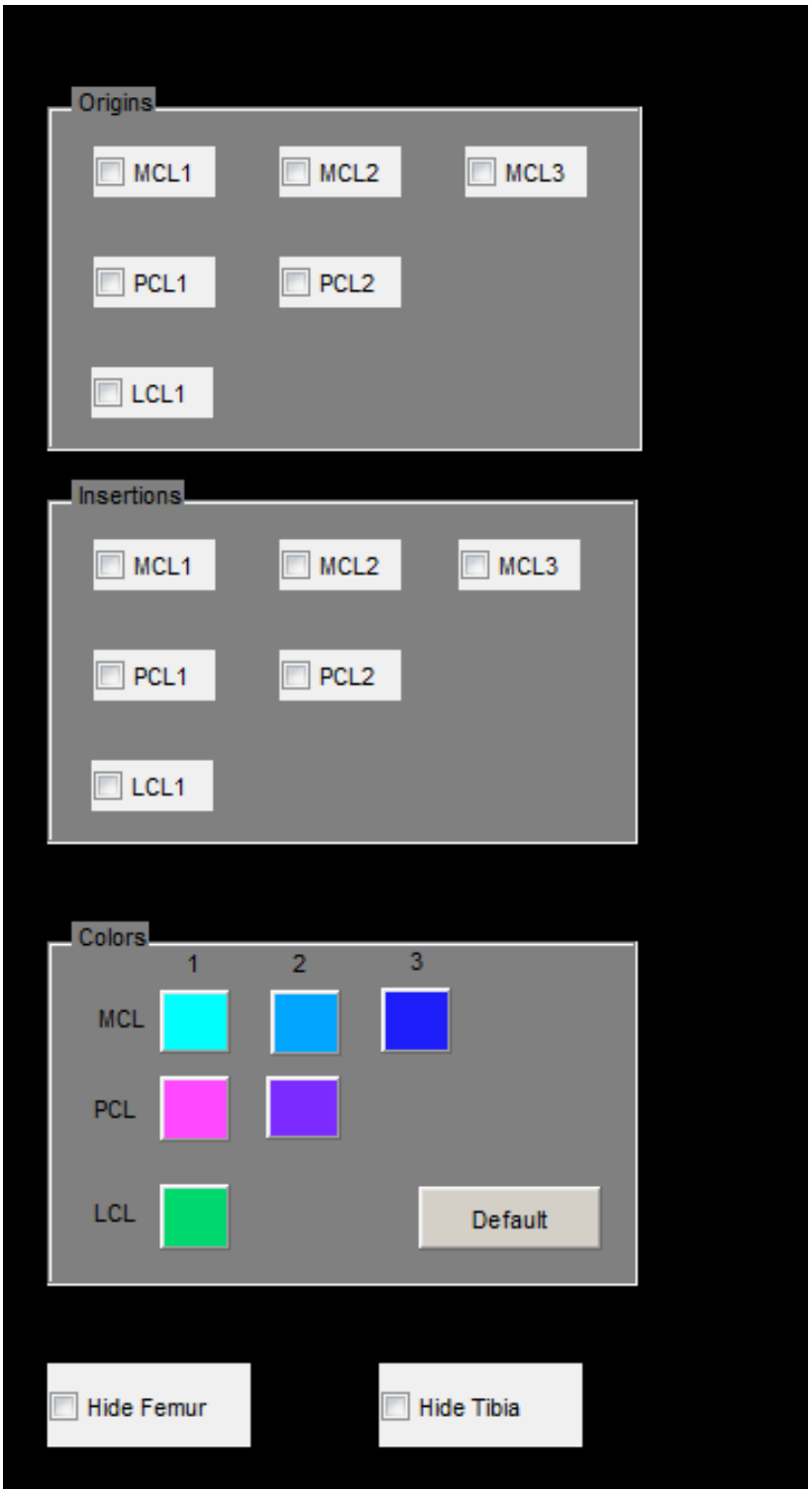

Figure 66: By selecting a checkbox and clicking the appropriate bone, the origin or insertion will be moved to the clicked location. Origin/Insertion pairs may have their color changed by clicking on one of the colored squares which will open a color selection window.

bone. The sphere displaying the origin or insertion will move to the clicked location, and the simulation will be automatically updated.

Run a Simulation from the GUI

To run a simulation utilizing the GUI, a USER only has to select "Run Simulation" from the start menu. The USER is then prompted to select a folder for the simulation (Figure 67). Next, the USER is asked two questions. First, the USER must select the type of simulation, whether it is fixed or mobile bearing and if it is only flexion or flexion and extension (Figure 68). This allows the GUI to know which version of the C++ code should be executed. Next, the USER may select to update the initial ligament length (Figure 69). If the USER selects "yes," the length of the ligament will be set such that the reference strain is the actual strain. It is recommended that the USER always selects "Yes."

With these selections made, the GUI copies all files necessary to the selected folder. This includes the C++ executable and all of the *.in files (simulation parameters, point clouds, convex hulls, and others). Finally, the GUI executes the C++ file to begin the simulation. If the USER has selected to update initial ligament lengths, the code will run for one time step to determine the initial ligament lengths. Then, the appropriate *.in file is overwritten with the new ligament lengths and the code is executed again for a full simulation.

Automatically Plot Results

Once the simulation is completed, the USER can use the Results tab to visualize the results. If "Plot Results" is selected, the USER receives standard plots for rotations, translations, forces, and other data for the selected simulations (Figure 70). The first time a USER plots a given simulation, they must select the *.1 file. Once the plotting is complete, the Output.ALO file is generated (Figure 71). This contains the data of all the output files, condensed into a single file. If the USER wishes to plot the data again, he

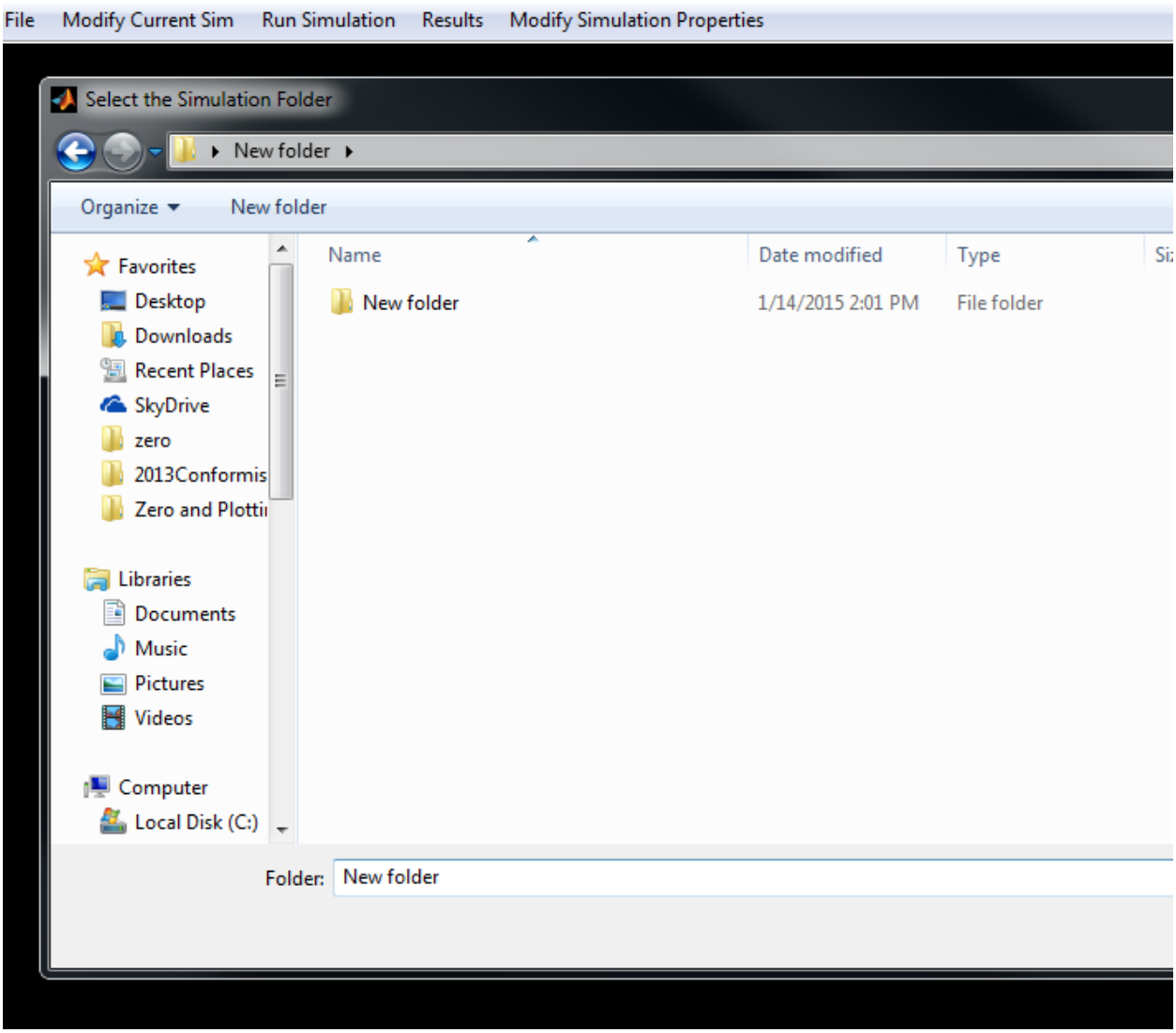

Figure 67: To run a new simulation, the user is asked to select a folder which will contain the input files, executable, and results.

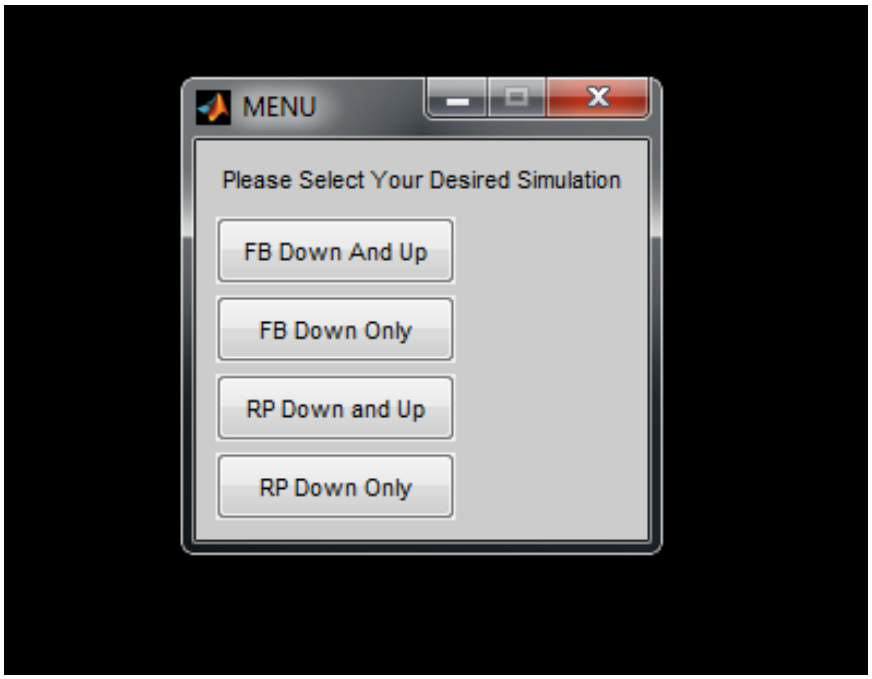

Figure 68: Next, the user must specify if the implant is FB or RP and if the activity is only flexion or flexion/extension.

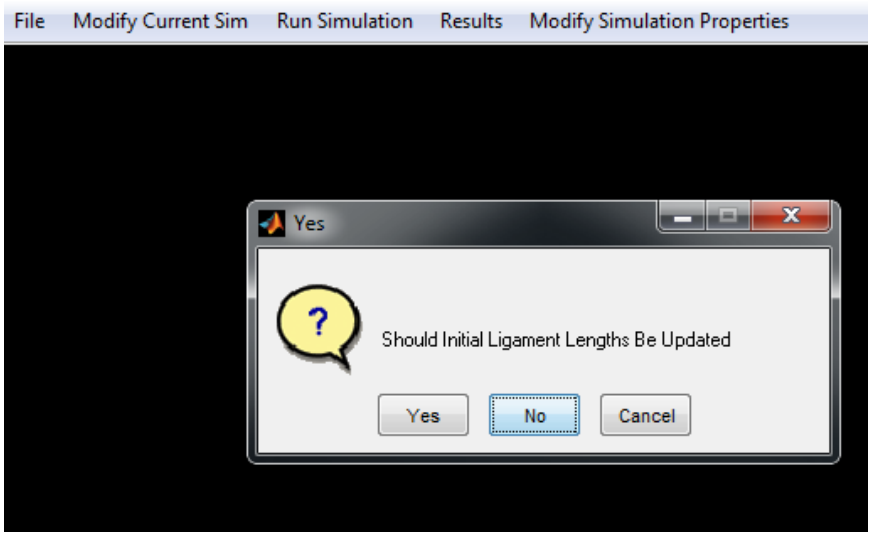

Figure 69: Finally, the user is given the option to update initial ligament lengths. This is highly recommended as otherwise the initial ligament strain will not match the specified reference strain.

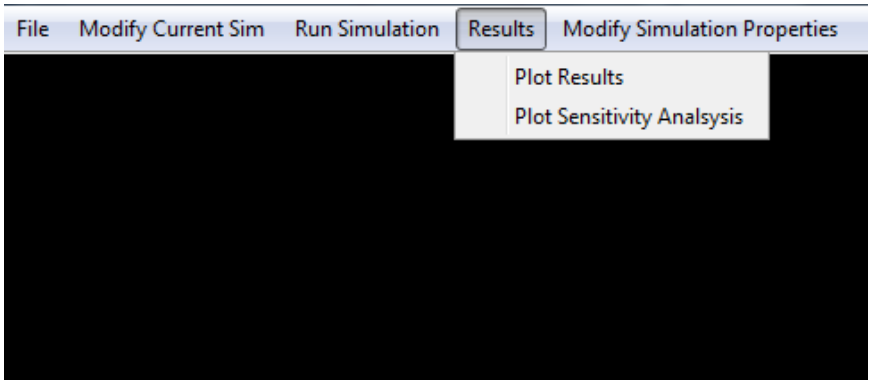

Figure 70: The user can plot a results of an individual simulation or a sensitivity analysis of multiple simulations

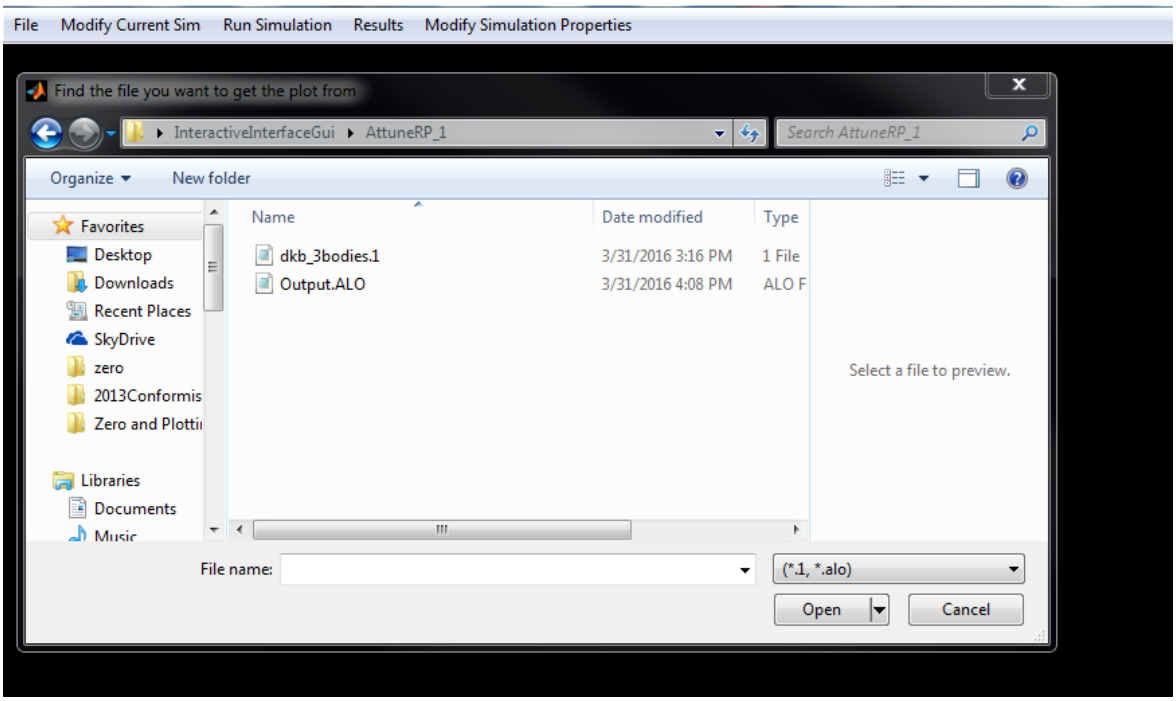

*Figure 71: Results must be plotted from the *.1 file the first time the results are analyzed. Subsequent plottings can be done using the *.alo file which will perform faster.*

or she may select the Output.ALO file. Since the data is condensed in this file, it will execute much faster than selecting the *.1 file.

If a USER wishes to compare the results of multiple sensitivity analyses, they may select the “Plot Sensitivity Analysis” option. This feature requires each simulation to be stored in a separate folder within the same directory (Figure 72). Furthermore, they must have identical filenames ending with an underscore followed by sequential numerals. The USER may then select which of the files to include in the plots (Figure 73). The simulations are then named for the legend (Figure 74). Each plot will contain a single variable plotted for each simulation (Figure 75). The plots will be placed in the folder with the “_1” ending. It is recommended that each simulation is plotted with the “Plot Results” function first to generate an Output.ALO file. This will allow the sensitivity plot to be performed faster.

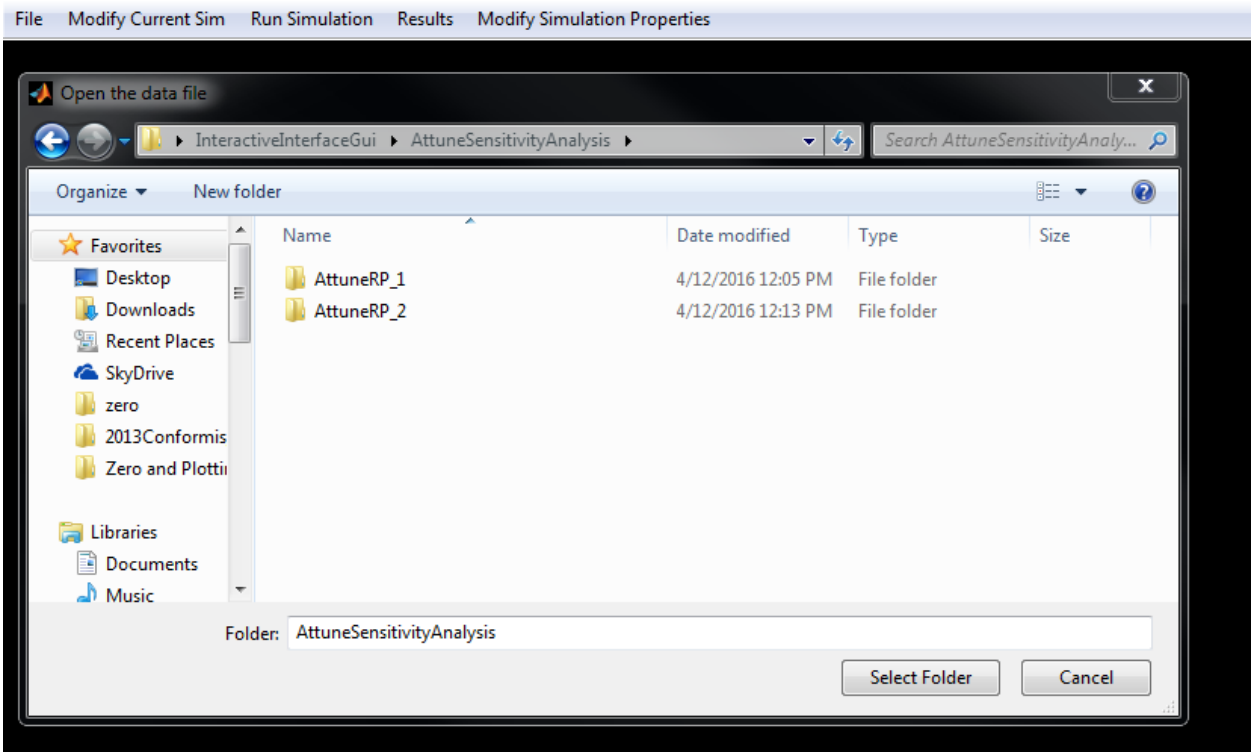

Figure 72: The folder ending with _1 is selected to run a sensitivity analyses.

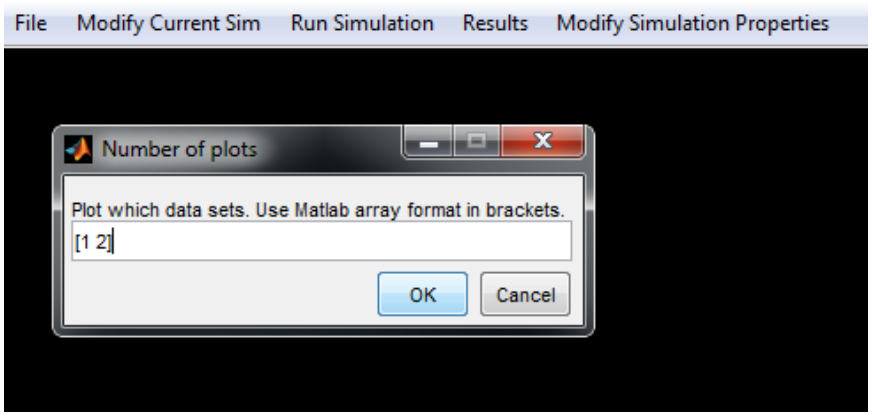

Figure 73: The folders which will be included in the plot are placed in MATLAB array format.

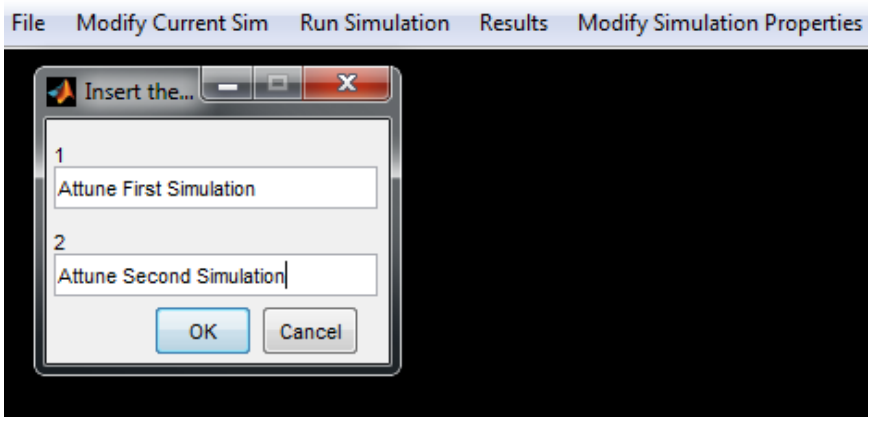

Figure 74: The different simulations are given names for the plot legends.

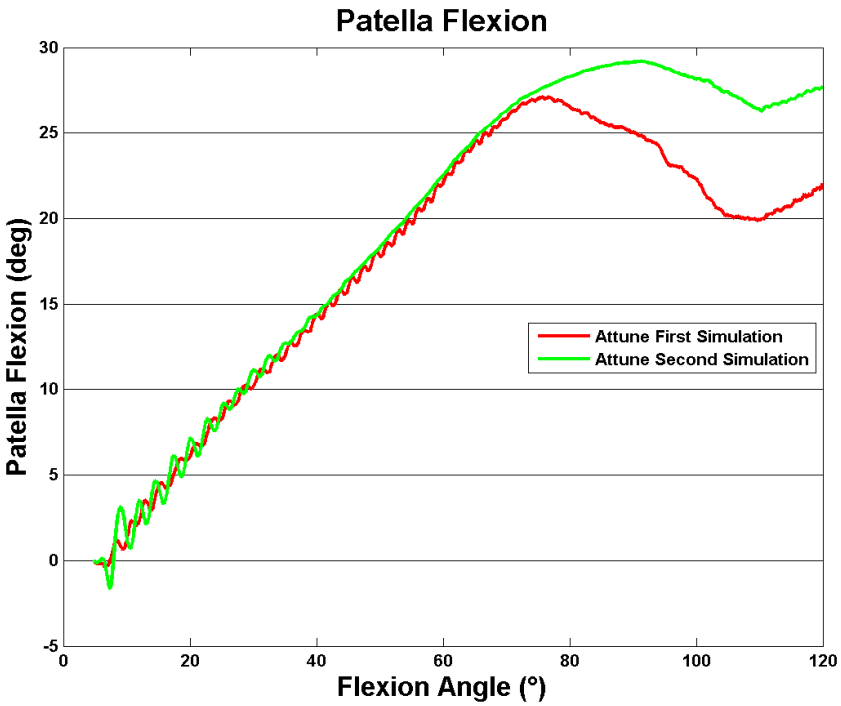

Figure 75: An example sensitivity plot analysis is shown. The difference between these simulations was a slight change to the patella stabilization controller resulting in different patella flexion.

Chapter 5: Results

Changing Polyethylene Rotation Center

One of the initial studies focused on varying the polyethylene rotation center (PRC) in different mobile bearing implants. Typically, the PRC is in the midline of the tibial component so that the polyethylene rotates about its center. However, with this model it is possible to theoretically shift the PRC, allowing the polyethylene to rotate around a medially or laterally shifted PRC. In this early study, two PCR implants (TKA-I; TKA-II) were analyzed with a 10 mm medial, 5 mm medial, center, 5 mm lateral, and 10 mm lateral PRC. Ideally, the model should be robust enough to detect general trends resulting from changing the PRC but sensitive enough to detect differences between the implants.

Overall, moving the PRC laterally increases external rotation of the polyethylene. As it moves medially, external rotation decreases and internal rotation of the polyethylene became evident. While both implants displayed similar polyethylene rotations for a given PRC, the trends were significantly different (Figure 76 & Figure 77). The TKA-I has relatively little rotation of the polyethylene in early flexion. At approximately 50° of flexion, the PRCs of TKA-I began to display different characteristics. The two medial pivot points displayed internal polyethylene rotation. The centered and two lateral pivot points displayed external rotation.

For TKA-II, the rotations displayed a less stable pattern. In early flexion, the polyethylene rotated the opposite direction, as it did in later flexion. The two medial and centered PRCs showed initial external rotation, followed by internal rotation, with a brief period of external rotation at the end of the activity. The lateral PRCs showed early internal rotation followed by external rotation in deeper flexion. Overall, the rotation patterns of the TKA-I seem to behave more predictably than the TKA-II. In these graphs,

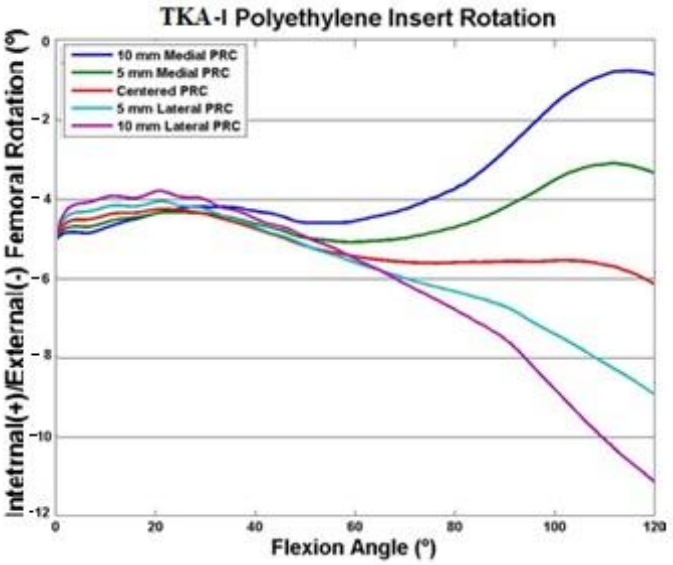

Figure 76: The TKA-1 polyethylene insert rotation is compared for the various PRCs.

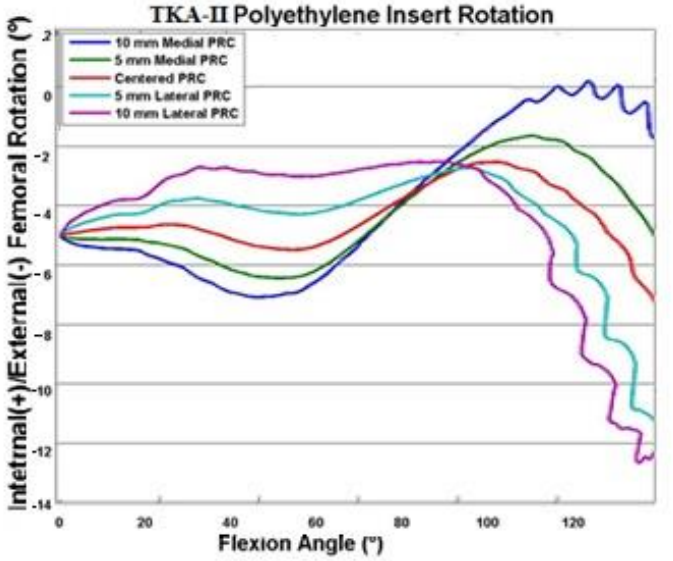

Figure 77: The TKA-II polyethylene insert rotation is compared for the various PRCs.

rotation starts at 5° of external rotation because the tibia has been rotated internally with respect to the polyethylene and femur.

When comparing the relative rotation of the femoral component and the polyethylene insert, the effect of the PRC is obvious (Figure 78 & Figure 79). Moving the PRC laterally caused the femoral component to rotate more internally compared to the polyethylene insert. The TKA-II implant had the least relative rotation with the centered PRC. This simulation experienced approximately 1° of relative rotation. The medial PRCs showed considerable external rotation relative to the polyethylene insert while the lateral PRCs showed considerable internal rotation relative to the polyethylene insert. For the TKA-I, the 5 mm lateral PRC performed the best with some initial external rotation of the femoral component relative to the polyethylene insert (which was present for all PRCs) followed by slightly over 1° of relative internal rotation of femoral component.

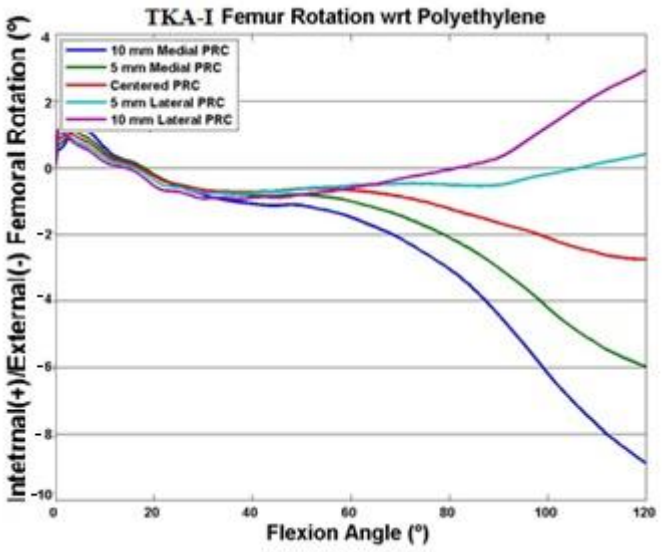

Figure 78: THE TKA-I relative rotation of the femoral component with respect to the polyethylene insert is compared for the various PRCs.

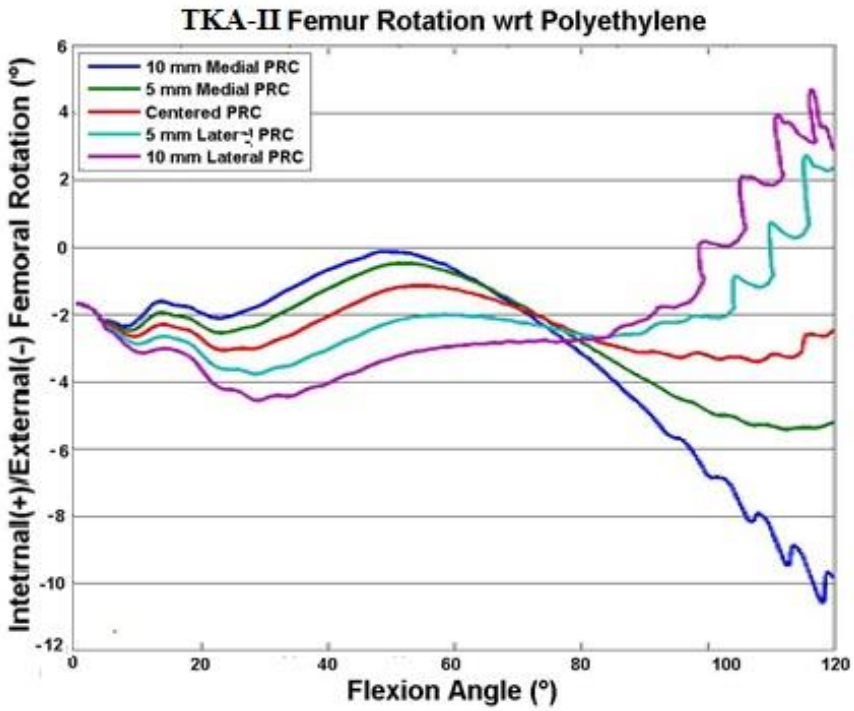

Figure 79: The TKA-II relative rotation of the femoral component with respect to the polyethylene insert is compared for the various PRCs.

Sensitivity Analysis

To improve the understanding of the geometrical design of the knee implant components influences kinematic performance, multiple simulations were performed with numerous component designs. These what-if scenario design geometries included both fixed and mobile bearing designs. The focus of the analyses was to explore how axial rotation of the femoral and polyethylene components change during a deep knee bend activity. Both symmetric and asymmetric femoral and polyethylene components were analyzed. The effect of shifting the cam and post mechanism, as well as the pivot point for the rotating platform designs was studied. The following eight simulations were performed for fixed bearing, rotating platform with a central pivot, and rotating platform with a lateral pivot, for a total of 24 simulations:

1) Femur Symmetric; Center Cam and Post; Polyethylene Insert Symmetric
2) Femur Symmetric; Center Cam and Post; Polyethylene Insert Asymmetric
3) Femur Symmetric; Lateral Cam and Post; Polyethylene Insert Symmetric
4) Femur Symmetric; Lateral Cam and Post; Polyethylene Insert Asymmetric
5) Femur Asymmetric; Center Cam and Post; Polyethylene Insert Symmetric
6) Femur Asymmetric; Center Cam and Post; Polyethylene Insert Asymmetric
7) Femur Asymmetric; Lateral Cam and Post; Polyethylene Insert Symmetric
8) Femur Asymmetric; Lateral Cam and Post; Polyethylene Insert Asymmetric

The same femurs were used for both the mobile and fixed bearing simulations with the asymmetric femur having a smaller radius of curvature on the lateral side. The symmetric rotating platform polyethylene inserts were symmetric about a sagittal plane. The asymmetric rotating platform polyethylene inserts had the same medial plateau as the symmetric inserts, but they had a smaller posterior lip on the lateral side. The symmetric fixed bearing had less of a posterior lip than the symmetric rotating platform design on both sides. The asymmetric fixed bearing had more of a posterior lip on the medial plateau and less of one on the lateral plateau. The lateral post designs shifted the cam and post 5 mm laterally. To compensate for this, the medial plateau and condyle were

made wider while the lateral plateau and condyle were made narrower. Additionally, the inferior portion of the trochlear groove was shifted laterally to remain between the femoral condyles. Moving from a center pivot point to an 8 mm lateral pivot point did not affect the articulating geometry.

Fixed Bearing

Since the polyethylene component is rigidly fixed with the tibial component in fixed bearing designs, the analysis focused on the axial rotation of the femur with respect to the tibia/polyethylene. These simulations revealed that the symmetric femur rotates more externally than the asymmetric femur (*Figure 80*). Both designs begin with external rotation, but the asymmetric femurs rotate internally in mid flexion and then externally again in late flexion. The symmetrical femoral components rotated externally throughout flexion. The symmetrical femoral components ended with between 4.5° and 5.5° of external rotation relative to the tibia. The asymmetric femurs ranged from 3° to 3.5° of external rotation. For both the asymmetric and symmetric femurs, the simulation with the centered post and symmetric polyethylene insert had the most rotation. The centered post with the asymmetric polyethylene insert had the next most rotation, followed by the lateral post with the symmetric polyethylene insert. The lateral post with the asymmetric polyethylene insert showed the least rotation. The asymmetric polyethylene inserts caused a rapid external rotation in early flexion compared to the symmetric polyethylene inserts. This finding is most likely caused by the large posterior shift of the femur in early flexion (*Figure 81* & *Figure 82*). When it moves posteriorly, the lip on the medial side of the polyethylene interacts with the femur while the flatter lateral side allows the polyethylene to slide over it resulting in external rotation. The eventual implementation of contact detection minimizes this slip effect. Overall, the most important driver was the femur shape.

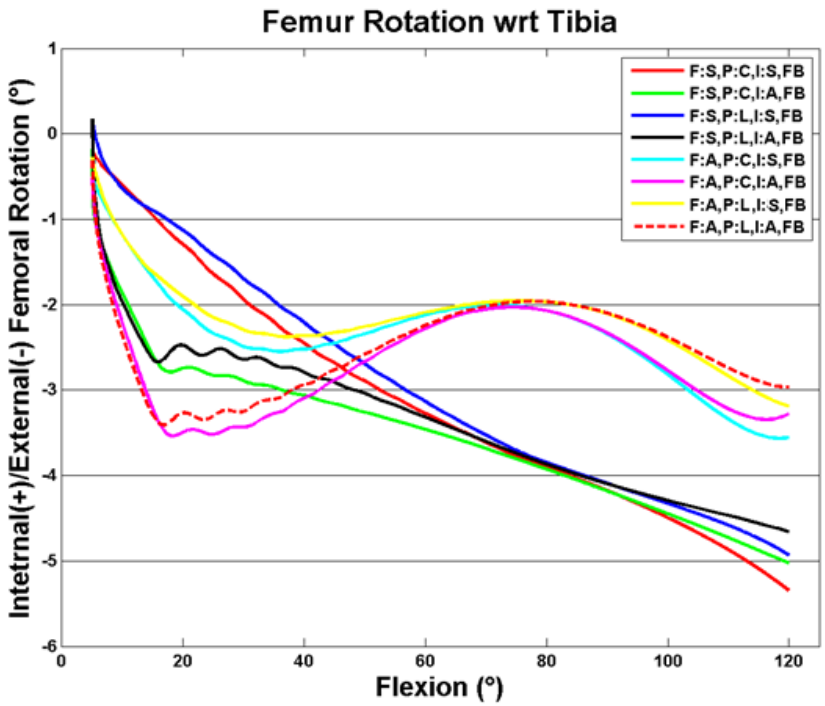

Figure 80: Symmetric femoral components showed considerably more external rotation of the femur relative to the tibia than the asymmetric femoral components in a fixed bearing simulation. The legend describes the simulation. F:S/A describes whether the femur is symmetric or asymmetric. P:C/L describes whether the post is centered or lateral. I:S/A describes whether the polyethylene insert is symmetric or asymmetric. FB,RP:C, and RP:L describe whether the simulation is fixed bearing, rotating platform with a center pivot, or rotating platform with a lateral pivot, respectively.

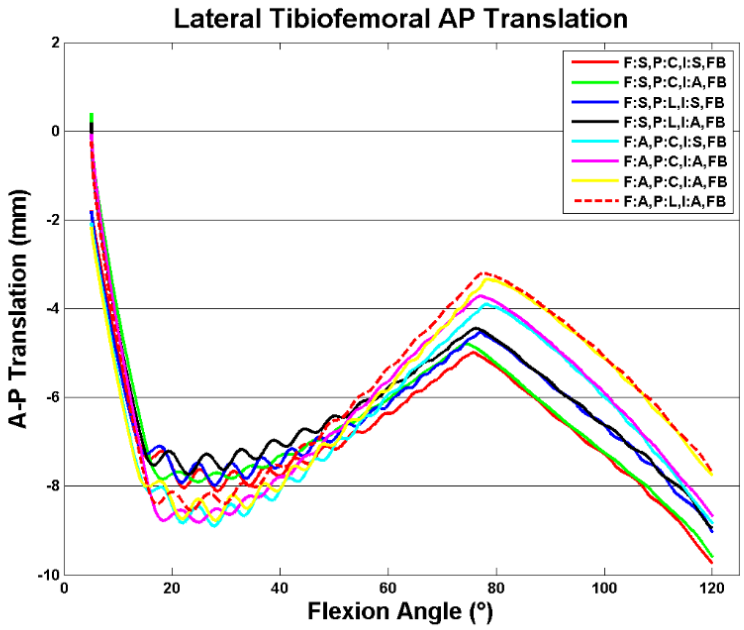

Figure 81: The lateral tibiofemoral contact point shows considerable posterior slide in early flexion during a fixed bearing simulation.

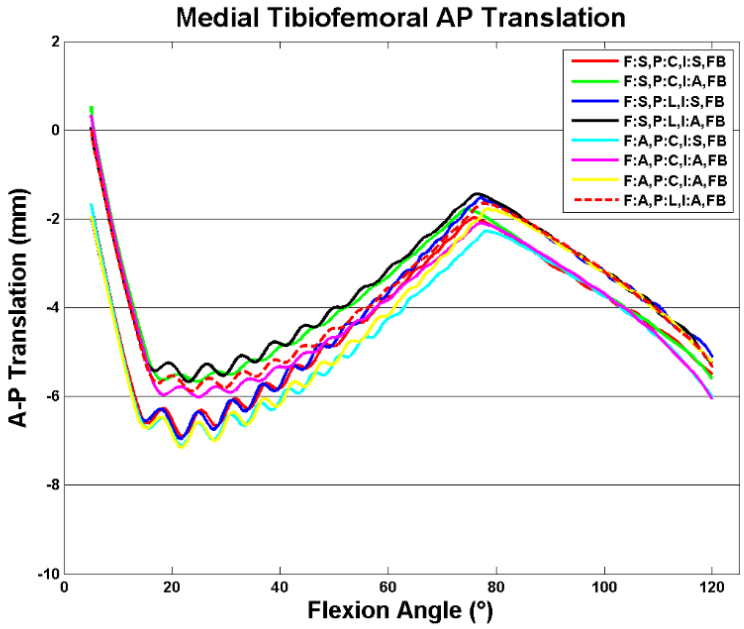

Figure 82: The medial tibiofemoral contact point shows considerable posterior slide in early flexion during a fixed bearing simulation.

Rotating Platform – Center Pivot Point

When analyzing the rotating platform designs, three rotations must be considered: 1) femur with respect to tibia, 2) polyethylene insert with respect to tibia, and 3) femur with respect to polyethylene insert. Once again, the asymmetric femoral design revealed less rotation with respect to the tibia than the symmetric design (*Figure 83*). The asymmetric femoral design had between 3° and 4° of external rotation while the symmetric femoral design had between 4.5° and 5.5° of external rotation. Like the fixed bearing simulation, the asymmetric designs rotated internally in mid flexion and externally in late flexion. The symmetric femoral design rotated externally throughout flexion. The remaining design considerations had less effect. The simulations with an asymmetric polyethylene insert showed a large internal rotation in early flexion. This is likely a result of the large posterior movement of the femur in early flexion which could be attributed to the FSM version used (*Figure 84* & *Figure 85*). These simulations were run while a single low-point contact point was used. It is likely the results would differ if rerun with the most recent version of the code using contact detection.

The polyethylene rotations had much more variability than the femur rotations. The asymmetric polyethylene inserts all experienced a large internal rotation in early flexion which is likely for the same reason as the femur external rotation in early flexion (*Figure 86*). The femur shifts posteriorly in early flexion and catches the posterior lip on the medial side of the polyethylene, causing it to rotate internally while the flat lateral side provides little resistance. The asymmetric polyethylene inserts then rotate externally in mid flexion and internally again in late flexion. Overall, the largest driver of total polyethylene rotation appears to be the polyethylene insert symmetry. Symmetric polyethylene insert simulations had between 1° of internal rotation and 4° of external rotation. Asymmetric polyethylene designs displayed between 2° and 7° of internal rotation. The post location also seemed to be an impacting factor, with center post simulations having about 2° more external rotation (or less internal rotation).

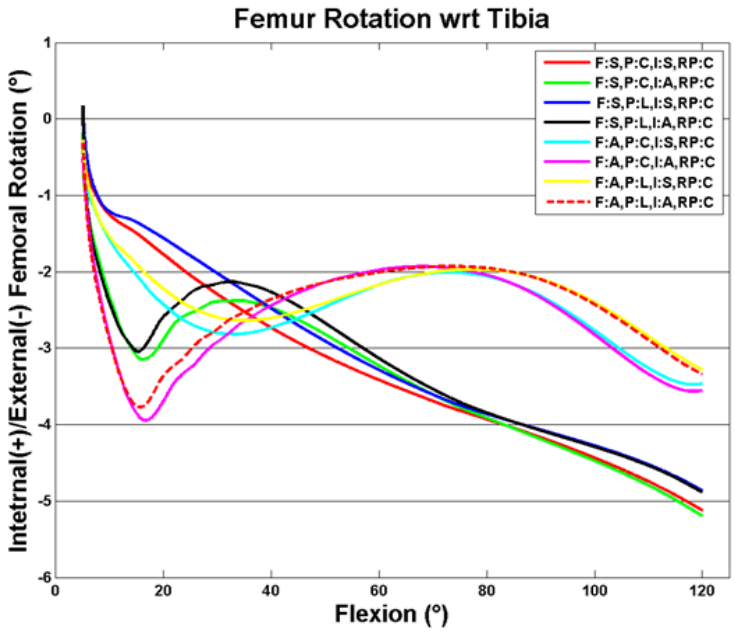

Figure 83: Symmetric femoral components showed considerably more external rotation of the femur relative to the tibia than asymmetric femoral components in a center pivot rotating platform simulation.

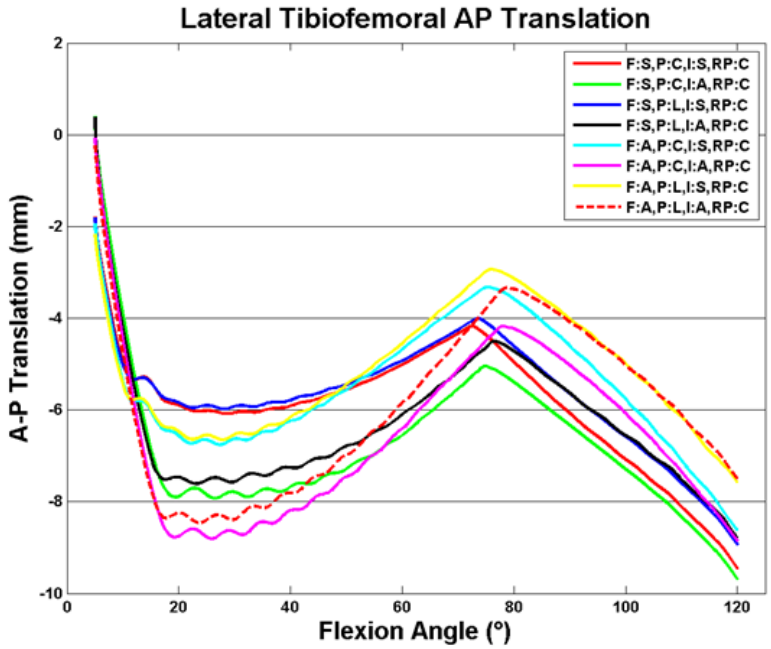

Figure 84: The lateral tibiofemoral contact point translates posteriorly a considerable amount in early flexion in a center pivot rotating platform simulation.

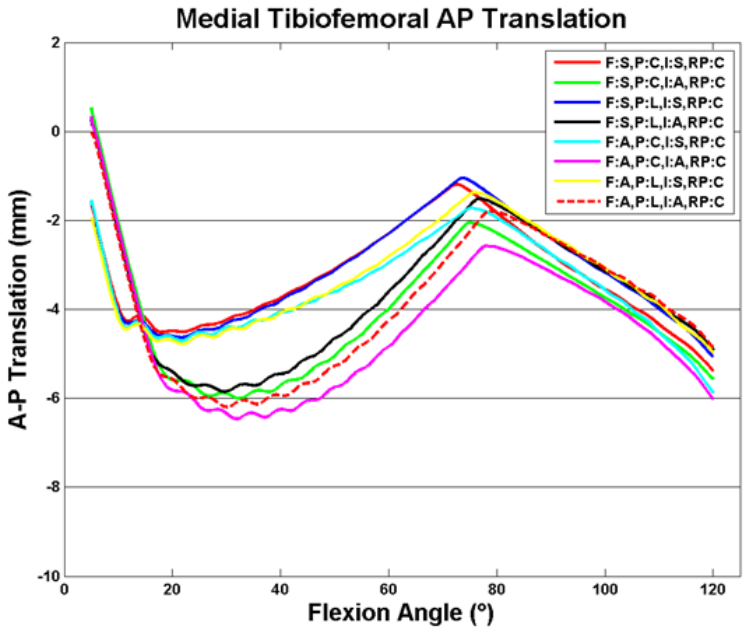

Figure 85: The medial tibiofemoral contact point also translates posteriorly a considerable amount in early flexion in a center pivot rotating platform simulation.

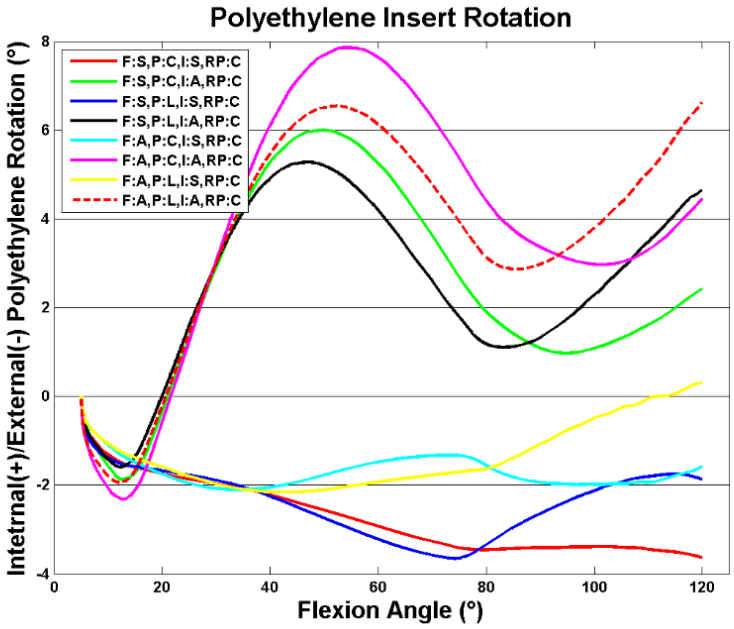

Figure 86: The symmetric polyethylene insert simulations showed a slightly externally or neutrally rotating polyethylene as expected. The asymmetric insert simulations had large internal polyethylene rotations.

This difference occurred in late flexion after the post had engaged, indicating that the lateral post contact drove the polyethylene into internal rotation. Symmetric femoral component design simulations also experienced approximately 2° more polyethylene external rotation than their asymmetric counterparts.

When comparing the femur rotation to polyethylene rotation, the asymmetric polyethylene components performed poorly with between 7° and 10° of external rotation. This finding may be due to the large internal rotation of the polyethylene components resulting in a large external rotation of the femur relative to the polyethylene. The symmetric polyethylene insert simulations performed well with between 1° and 4° of external rotation of the femur relative to the polyethylene (*Figure 87*). The lateral post simulations rotated almost 2° more externally than the corresponding center post designs after the cam and post contact occurred. This revealed that the rotation of the femur, relative to the polyethylene insert, is affected considerably by post location. The underlying mechanism appears to be the lateral post contact driving the polyethylene internally. Furthermore, the difference between symmetric and asymmetric femoral components was negligible. The symmetric femoral component simulations had both more femur and more polyethylene external rotation than the asymmetric femoral component simulations. This indicates femur symmetry may not play a large role in the rotation between the femur and polyethylene.

Rotating Platform – Lateral Pivot Point

The external rotation of the femoral component with respect to the tibia behaved very similarly with a lateral pivot point as it did with a center point. The symmetric femoral designs rotated externally through all of flexion, and the asymmetric femoral designs rotated internally during mid flexion only. There was slightly less external rotation in the lateral pivot point simulations with the femur rotating between 2.5° and 3.5° for the asymmetric femurs and 4° and 5° for the symmetric femurs (*Figure 88*).

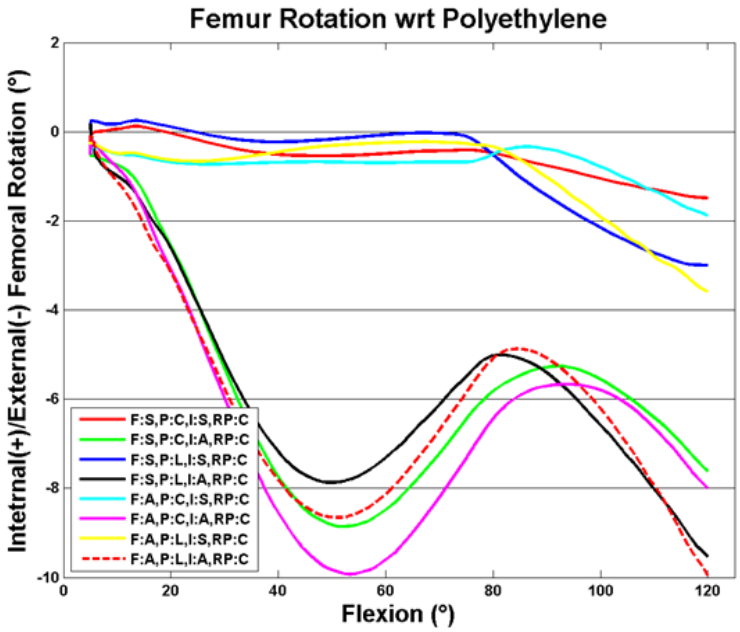

Figure 87: The femur rotated slightly more externally than the polyethylene for the symmetric polyethylene insert simulations. The femur rotated considerably more externally than the asymmetric polyethylene inserts.

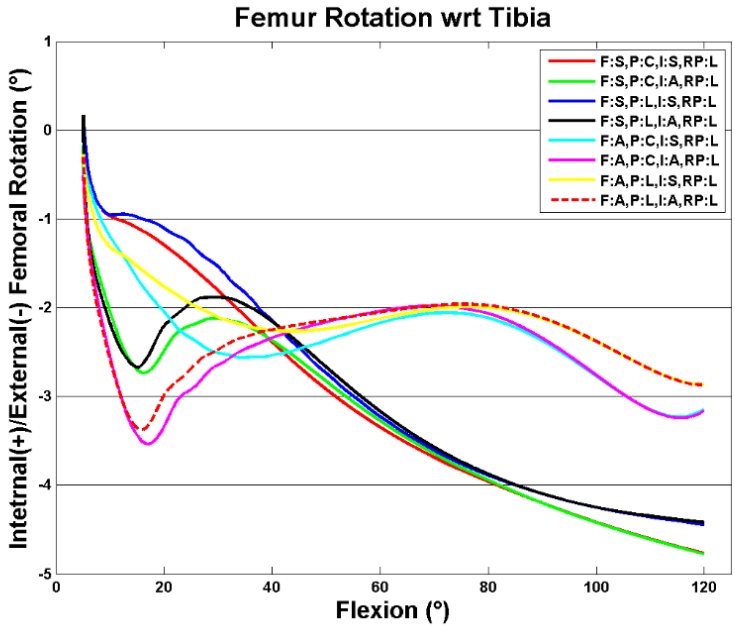

Figure 88: The symmetric femurs rotated more than asymmetric femurs during the lateral pivot rotating platform simulations. The other design considerations had minimal effects.

The asymmetric polyethylene insert designs once again resulted in a large external rotation of the femur in early flexion. Again, this is attributable to the large posterior shift which will be addressed in future versions of the model (*Figure 89* & *Figure 90*).

The lateral pivot point simulations had considerably more polyethylene external rotation with respect to the tibia. There was between 2° and 4° of external rotation for the asymmetric polyethylene insert simulations (*Figure 91*). The asymmetric polyethylene inserts rotated internally in early flexion due to the posterior slide of the femur and then externally in later flexion. The symmetric polyethylene insert simulations rotated externally for all of flexion and ended with between 4.5° and 7° of external rotation. Within each of those categories, the center post symmetric femoral component simulations had the most polyethylene insert rotation. The lateral post, symmetric femoral component simulations came in second with 1° less external rotation than the center post symmetric femoral component simulations. The center post asymmetric femoral design had the third most external rotation, and the lateral post asymmetric femoral design simulation had the least external rotation of the polyethylene relative to the tibia. The difference between the lateral post and center post simulations occurred in deep flexion after cam and post contact had occurred.

In the simulations with a symmetric polyethylene insert, the femur rotated between 1° and 3° internally relatively to the polyethylene (*Figure 92*). It rotated slightly externally relative to the polyethylene in early flexion, and then internally relative to the polyethylene for the remainder of flexion. It rotated between 1° and 2° externally relative to the polyethylene in the asymmetric simulations, but displayed temporary external rotations of greater than 8° in mid flexion. This is due to the early internal rotation of the polyethylene. The other design considerations had relatively little impact. This confirms that femur design symmetry seems to have little effect on rotation of the femur with respect to the polyethylene.

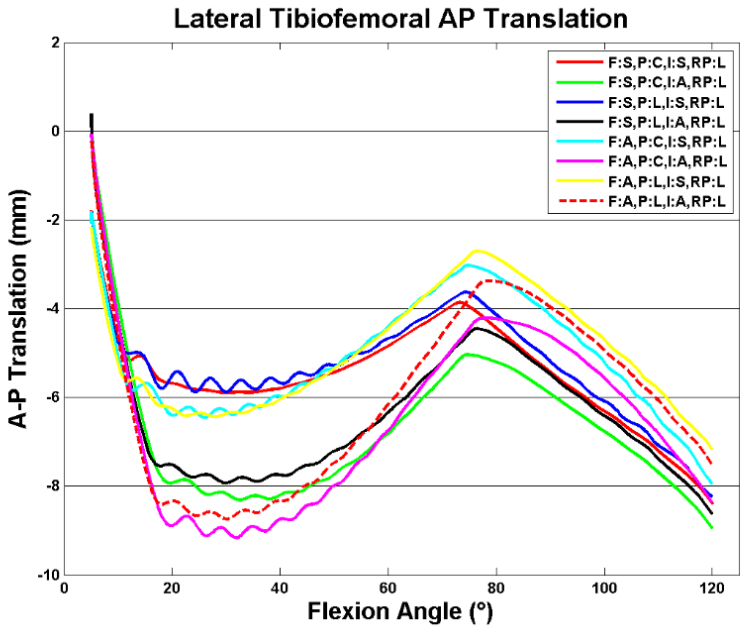

Figure 89: The lateral tibiofemoral contact point translates posteriorly a considerable amount in early flexion in a lateral pivot rotating platform simulation.

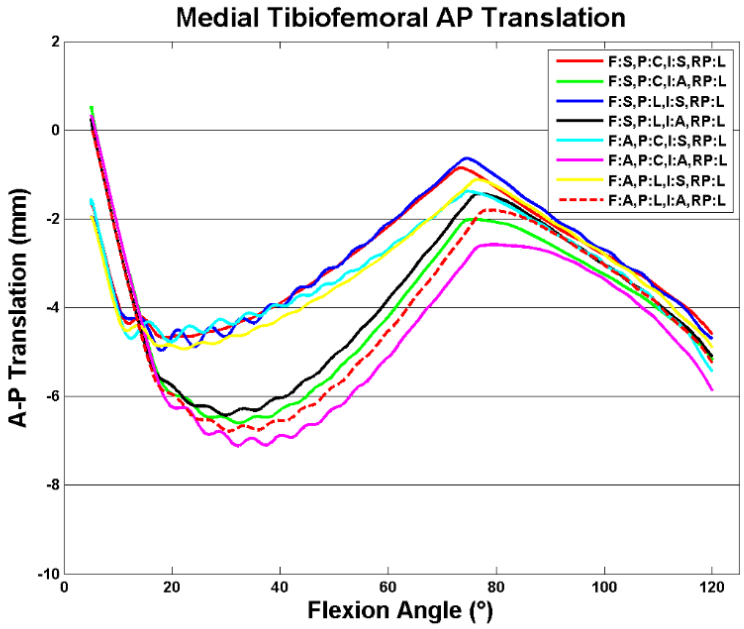

Figure 90: The medial tibiofemoral contact point also translates posteriorly a considerable amount in early flexion in a lateral pivot rotating platform simulation.

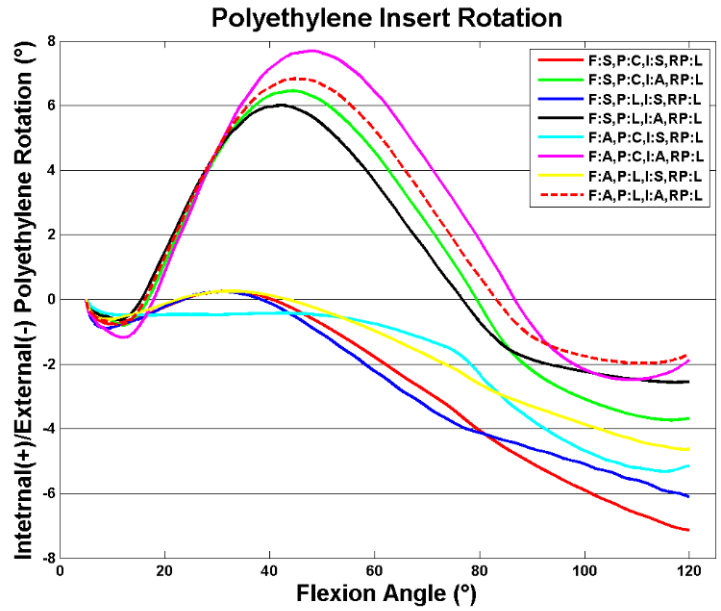

Figure 91: The asymmetric polyethylene inserts had less total external rotation than the symmetric inserts. They also showed internal rotation in early flexion.

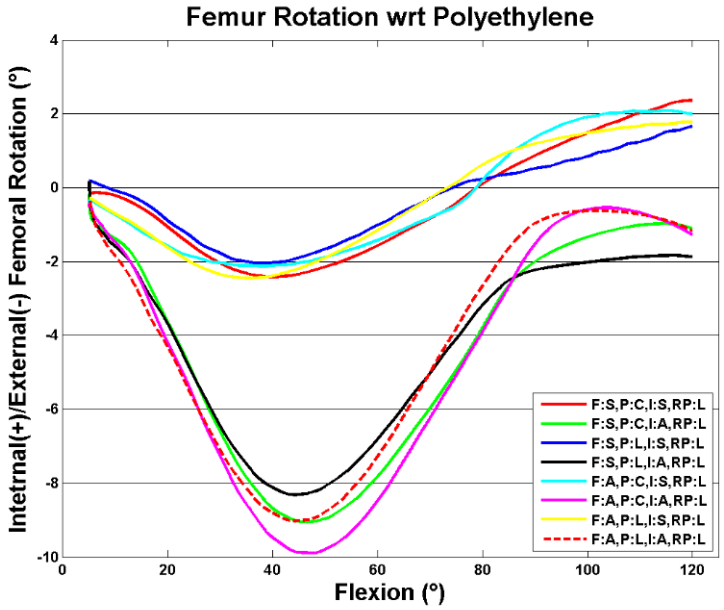

Figure 92: The symmetric polyethylene inserts rotated slightly more externally then the femurs during the lateral pivot rotating platform simulations. The femur rotated considerably external relative to the asymmetric polyethylene designs in early flexion and ended slightly more external.

Sensitivity Analysis Summary

The asymmetric polyethylene insert did not perform well. It resulted in very rapid external rotation of the femur in early rotation for all fixed bearing and rotating platform simulations. It also resulted in large internal rotations of the polyethylene in mid flexion during the rotation platform simulations. This was caused by the posterior surface of the medial polyethylene plateau interacting with the femur during the initial posterior shift of the femur. In the symmetric designs, the interaction on the lateral polyethylene plateau would stabilize the rotation. However, the asymmetric design did not have enough lip on the lateral plateau to create this stabilizing force.

The symmetric and asymmetric femoral designs performed fairly similarly. The asymmetric designs displayed internal rotation during mid flexion for all simulations. The asymmetric designs also had slightly less total external rotation with respect to the tibia. However, the two femur designs had very similar rotation with respect to the polyethylene in the rotating platform simulations, indicating femoral design may not be a large factor in femur to polyethylene rotation.

The center and lateral post simulations performed very similarly in early flexion. After the cam and post engaged, the lateral post tended to cause the polyethylene to rotate slightly internally (or less externally) when compared to the center post design. This also resulted in more external rotation of the femur relative to the polyethylene in late flexion. The effect of post location was lessened by the lateral pivot point, indicating that a lateral pivot point may be useful if a lateral cam will be included.

The lateral pivot point resulted in considerably more external polyethylene rotations. Conversely, it resulted in significantly more internal femur-to-polyethylene rotations. All of the symmetric polyethylene insert simulations with a center pivot point showed the femur rotating more externally than the polyethylene. In the lateral pivot point simulations, the femur rotated less externally than the polyethylene. This indicates that the 8 mm shift of the pivot point may be too large if the objective is to

match femur and polyethylene rotation. Some value between a center pivot point and an 8 mm lateral pivot point may result in 0° of femur-to-polyethylene rotation.

Transitioning to Multiple Contact Points – Proof of Concept

Before designing the contact detection algorithm, a proof of concept model was designed to analyze the effect of having a contact area versus a single contact point. Instead of an extensive contact search, the refined model assumes contact occurs at four points instead of one point on both condyles (*Figure 93*). These points are arranged in a rectangular pattern on the femur and are analogous to the corners of the bounding box created by the contact patch. The force at each point is applied at the normal direction of the polyethylene at that location.

To determine the effect of multiple contact points, two sensitivity analyses were run. These included changing the width of the box as well as the length of the box. Additionally, the force was varied between the points. Because the femur, in general, rotates externally and drives the polyethylene externally during a deep knee bend, it was assumed that the front right and back left contact points would have more force as they drove external rotation (*Figure 93*). For the same reason, the front left and back right contact points would experience less force.

The results revealed that changing the width of the contact box has a considerable effect in early rotation (*Figure 94*). However, once the post engages at approximately 80° of flexion, the polyethylene rotation is less affected by the width of the contact box. The length of the box also plays a considerable role in early flexion, but continues to play a role even in later flexion (Figure 95). The length of the box is measured in degrees instead of length. This is because the contact box length varies so it will be larger in early flexion when the femur is flat and smaller in later flexion when the femur is more rounded. The degree measurements refer to the number of degrees the femur would have to rotate before posterior corners of the rectangle would be the most inferior point. For example, if the 8° length contact box

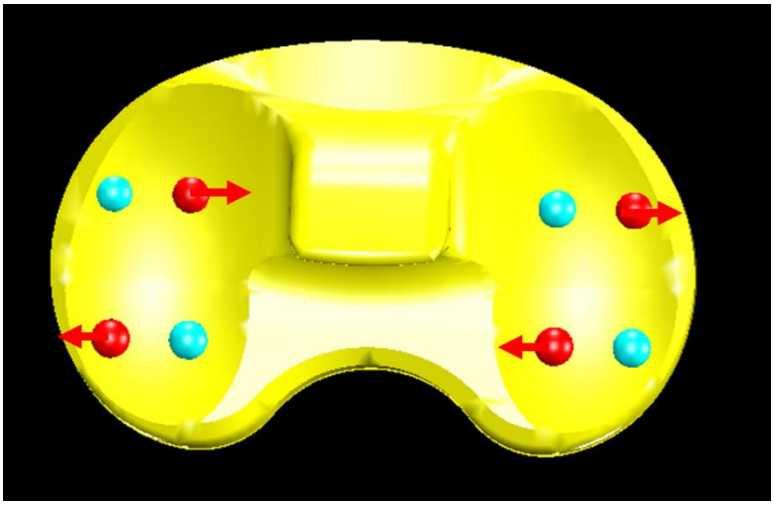

Figure 93: An example contact distribution is shown for a PS insert. The red spheres show the high force contact points for a right knee while the blue spheres show the low force contact points. The vectors show the direction the femur is turning the polyethylene during external rotation resulting in higher force.

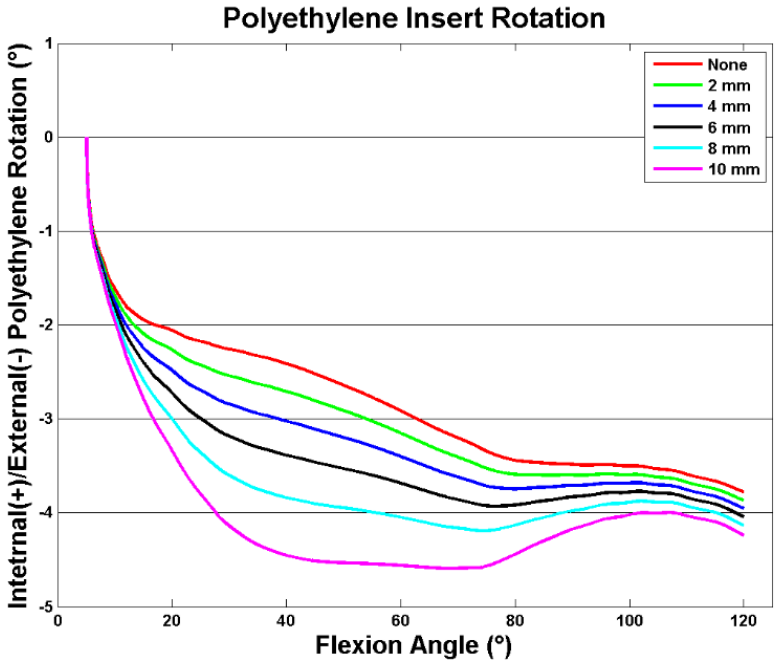

Figure 94: A wider contact box results in more polyethylene rotation. The width shown is the distance from the center of the box to the edge (half the total width).

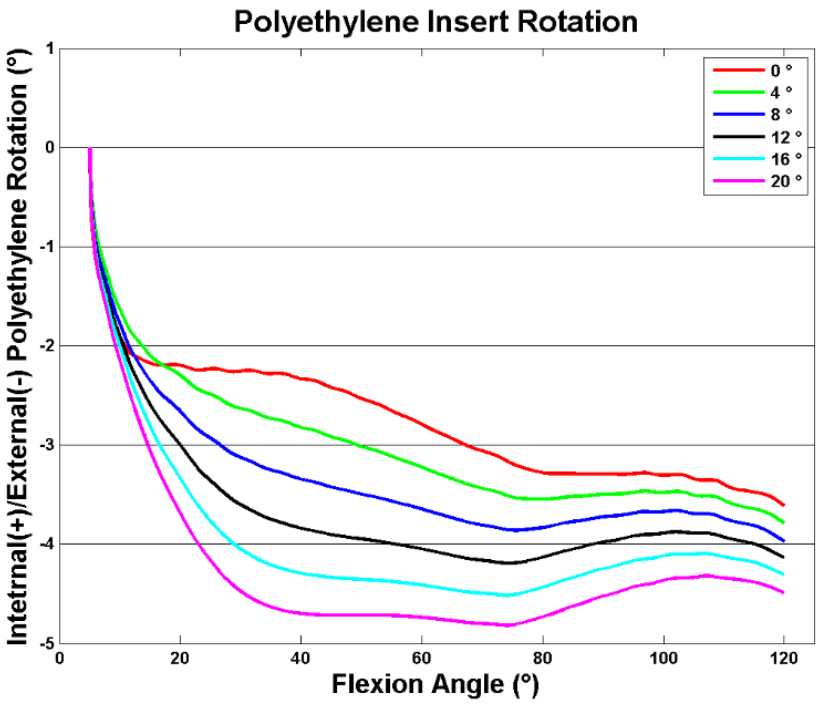

Figure 95: Expanding the box in the anterior-posterior direction results in more polyethylene rotation.

simulation was at 100°, it would assume the contact box spread from what was the most inferior point at 92° to what will be the most inferior point at 108°. Both simulations revealed that a larger box results in more polyethylene insert rotation. This finding demonstrated the importance of expanding to a contact area from a contact point if kinematics are to be accurately determined.

When the amount of force applied between the high force points on the anterolateral and posteromedial of the polyethylene and the low force points on the anteromedial and posterolateral of the polyethylene was varied, the polyethylene rotation was greatly affected (*Figure 96*). Most of this affect occurred in early flexion and was reduced when the cam and post engaged. However, the difference between the simulations was still approximately 2° in late flexion. This shows future model developments need a way to accurately predict not only the contact area but the distribution of force within that area.

Contact Detection 49 Points

Next, one of the previous simulations from the sensitivity analysis was repeated in two ways (Femur: Symmetric;Post: Center;Polyethylene: RP Asymmetric;Pivot Point: Center). First, height polynomials were used with only a single point instead of the normal vectors used with the previous simulation (Figure 8). Next, the simulation was run using 49 contact detection points on each condyle (Figure 9). Since turning on the contact detection at the initial 5° of flexion resulted in instability, the contact points were enabled at 6° of flexion. The simulation with contact detection posteriorly slid to slightly over 4 mm posterior while the single point contact simulation slid to nearly 6 mm posterior (Figure 97). For reference, the previous simulation computed using normal vectors behaved like the single point contact detection simulation and also slid to 6 mm posterior.

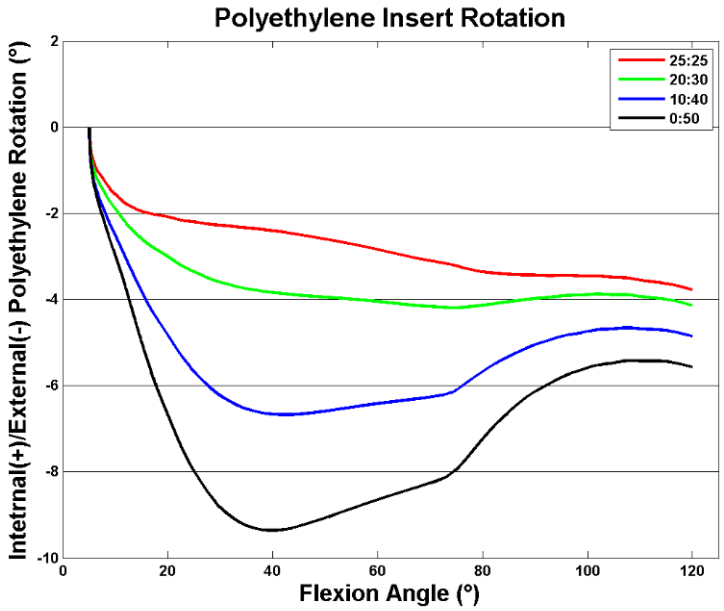

Figure 96: Applying more force at the high force contact points results in greater polyethylene rotation. The results are presented as a ratio of percentage of condyle force at low force point to percentage of condyle force at high force points.

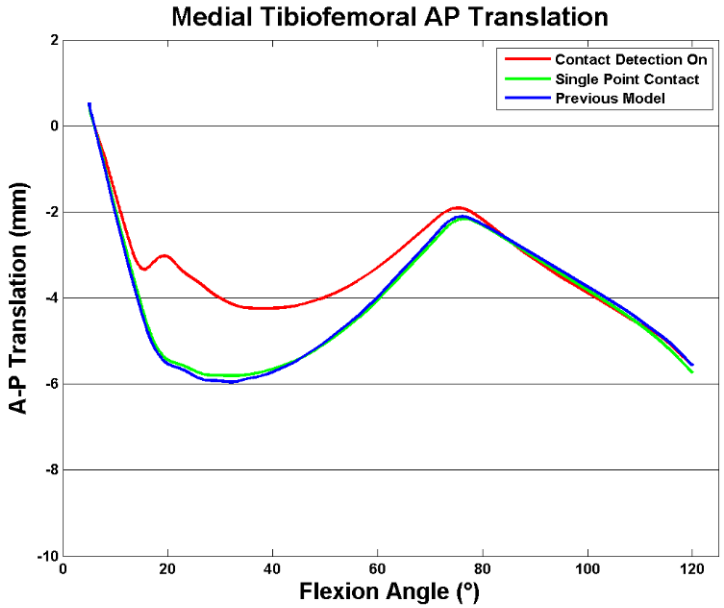

Figure 97: By enabling contact detection, the slip at the medial condyle was reduced by nearly 2 mm.

Laterally, contact detection resulted in roughly 6 mm of slip. The previous simulation and single point contact detection resulted in approximately 8 mm of slip (Figure 98). In deep flexion with the post engaged, all three models had very similar AP translations.

By reducing the amount of initial slip, the atypical dip of femur rotation during early flexion was minimized. Between 15° and 20° of flexion, the previous model and single point contact model showed a dip to 3° of external rotation (Figure 99). Enabling contact detection lessened this dip to only 1.75° of external rotation. After 45° of flexion, there are no notable differences in the external rotation of the femur among the three models.

While the hypothesis that contact detection would minimize the initial slip and femoral rotation held true, the polyethylene rotation did not respond as expected. Instead, the initial internal rotation of the polyethylene increased from 5.5° with the single point contact and 6° with the previous model to 7.5° (Figure 100). This is most likely caused by penetration of the femur into the medial side of the polyethylene being minimized. As the femur tried to slip back, the contact detected on the medial side of the knee caused the medial plateau of the polyethylene to be driven back more. Therefore, the polyethylene rotated more internally.

The rotation of the femoral component with respect to the polyethylene was even worse with contact detection enabled. All three models experienced a large relative external rotation occurred between 40° and 55°. However, the previous model and single point contact model had between 8° and 9° of relative external rotation while the model with contact detection had a full 10° of external rotation (Figure 101). All three models then had internal rotation of the femur relative to the polyethylene followed by external rotation. The ending relative rotations were 6.5°, 7.5°, and 10° for the single point contact model, previous model, and contact detection model, respectively. While the previous model was useful, it made the incorrect assumption of a single contact point. This assumption

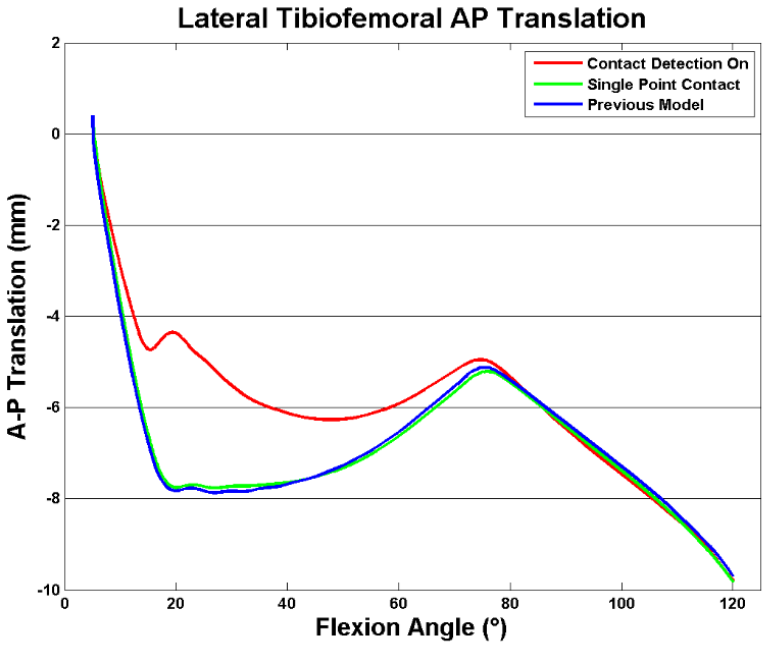

Figure 98: By enabling contact, the slip of the lateral condyle was reduced by nearly 2 mm.

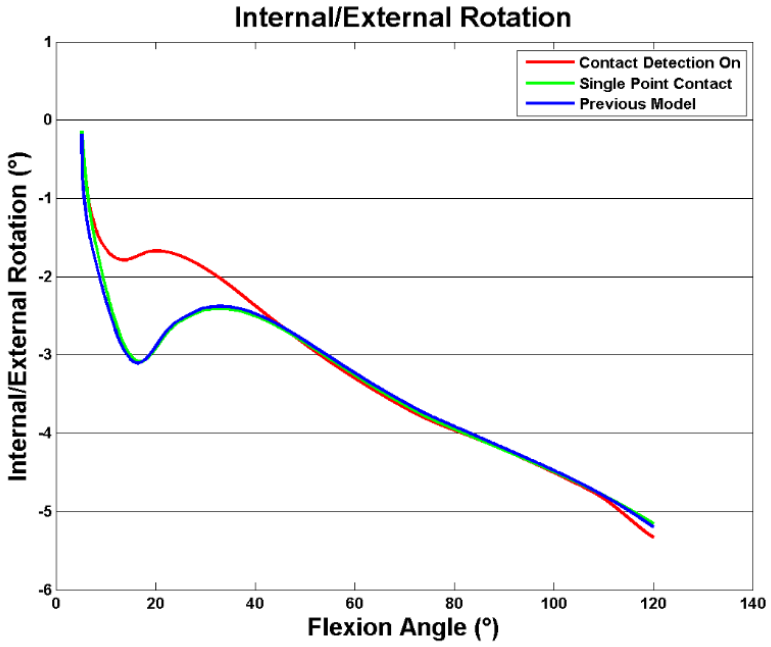

Figure 99: Contact detection resulted in a less pronounced reversal of rotation in early flexion.

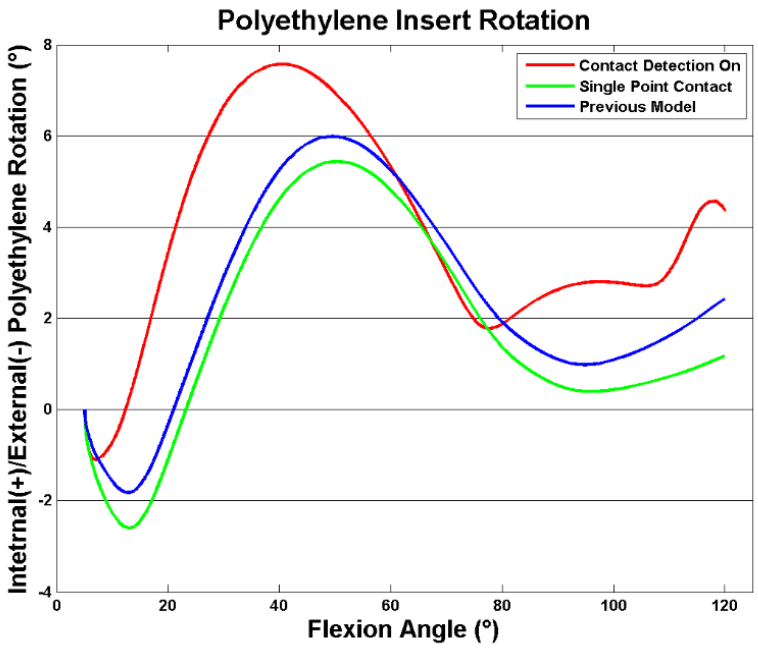

Figure 100: The internal rotation of the polyethylene in early flexion was exacerbated by contact detection.

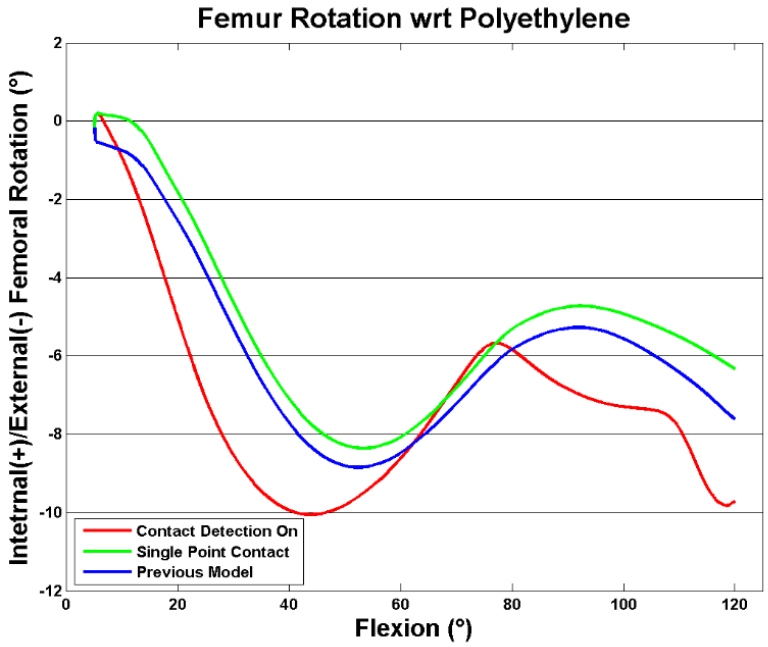

Figure 101: Contact detection resulted in even more external rotation of the femur with respect to the polyethylene.

was partially responsible for a large posterior slip of the tibiofemoral contact points in early contact. By comparing the results for the previous model using normal vectors and the model using height with a single contact point, it was established that transitioning from normal vectors to surface polynomials does not have a significant effect. However, the results contain considerable variation when contact detection was enabled. First, the posterior slip was reduced by approximately 2 mm. Second, the model with contact detection had less of a dip in femoral rotation during early flexion. The resulted depicted a dip in external rotation to 1.75° while the models without contact detection had a temporary external rotation of over 3° in early flexion. Therefore, contact detection is important because it provides a better approximation of actual contact and has a non-negligible effect on results.

Femur 123 - 127

In order to understand the effect of trochlear groove design on the performance of the knee after TKA, several theoretical femoral and polyethylene component designs were analyzed. These designs included both fixed bearing (FB) and rotating platform (RP) designs. The designs focused on the effect of rotating and shifting the trochlear groove.

The first design, Femur 123, was utilized as a baseline reference (Figure 102). It featured a wider medial condyle than lateral condyle resulting in a cam which was offset 3 mm laterally. Femur 124 was very similar but designed to work with an anatomic patella (not pictured). Femur 125 has a trochlear groove which has the same superior portion as Femur 123 but has rotated 5° internally at 90° of flexion (Figure 103). Femur 126 is similar to Femur 125 but has a more pronounced rotation (Figure 104). It is rotated 10° at 90° of flexion. Femur 127 has the same rotation as Femur 125, but the superior aspect of the trochlear groove is shifted medially (not pictured).

Femurs 123, 124, 125, and 126 each have a unique fixed bearing and mobile bearing insert. Femur 127 uses the same polyethylene as Femur 125 due to the similarities between these designs. All FB

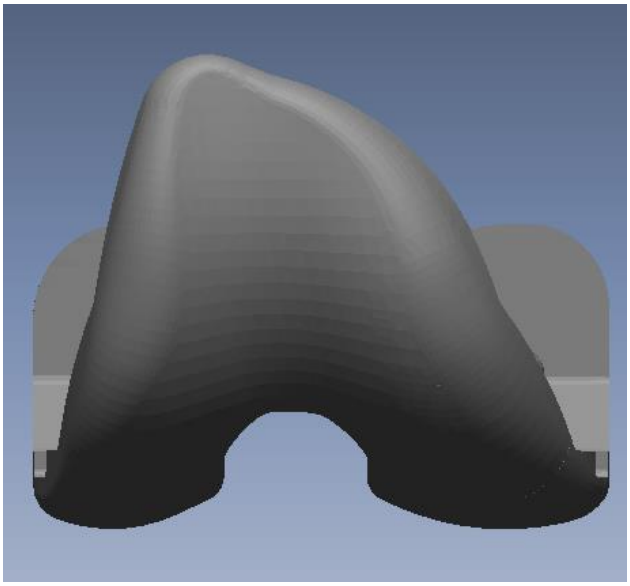

Figure 102: Femur 123 was the baseline reference.

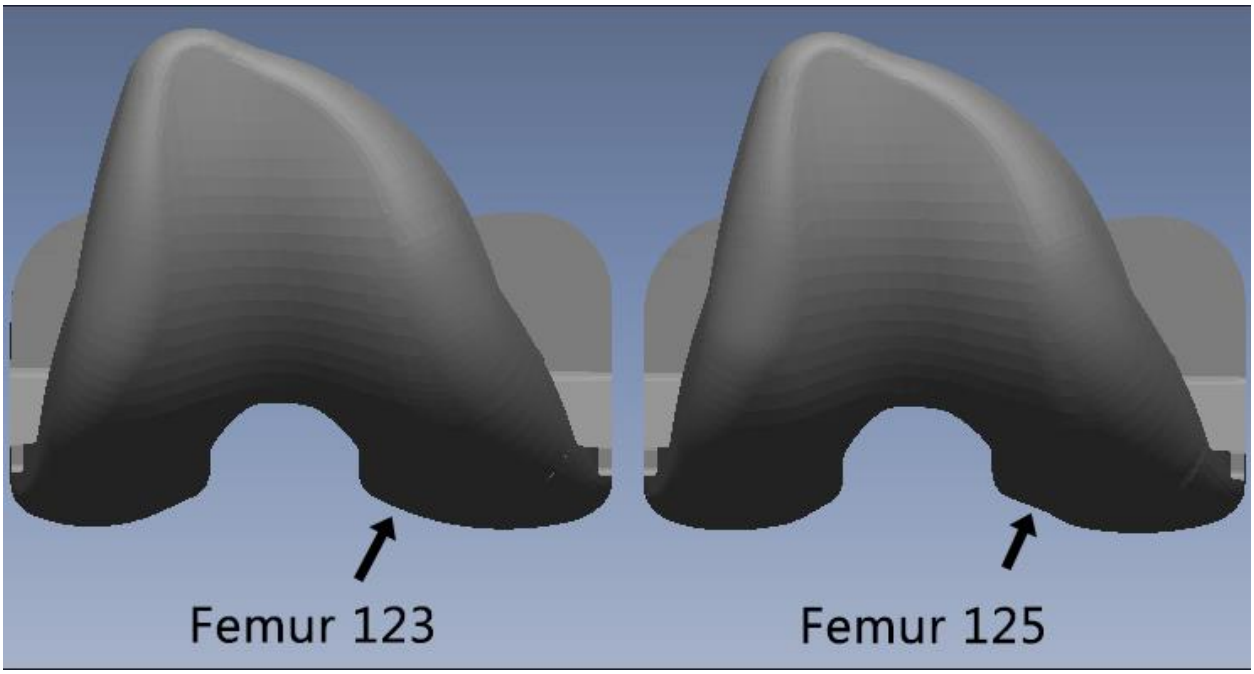

Figure 103: Femur 125 has a trochlear groove that rotates on the femoral component. The arrows show where this difference can be seen.

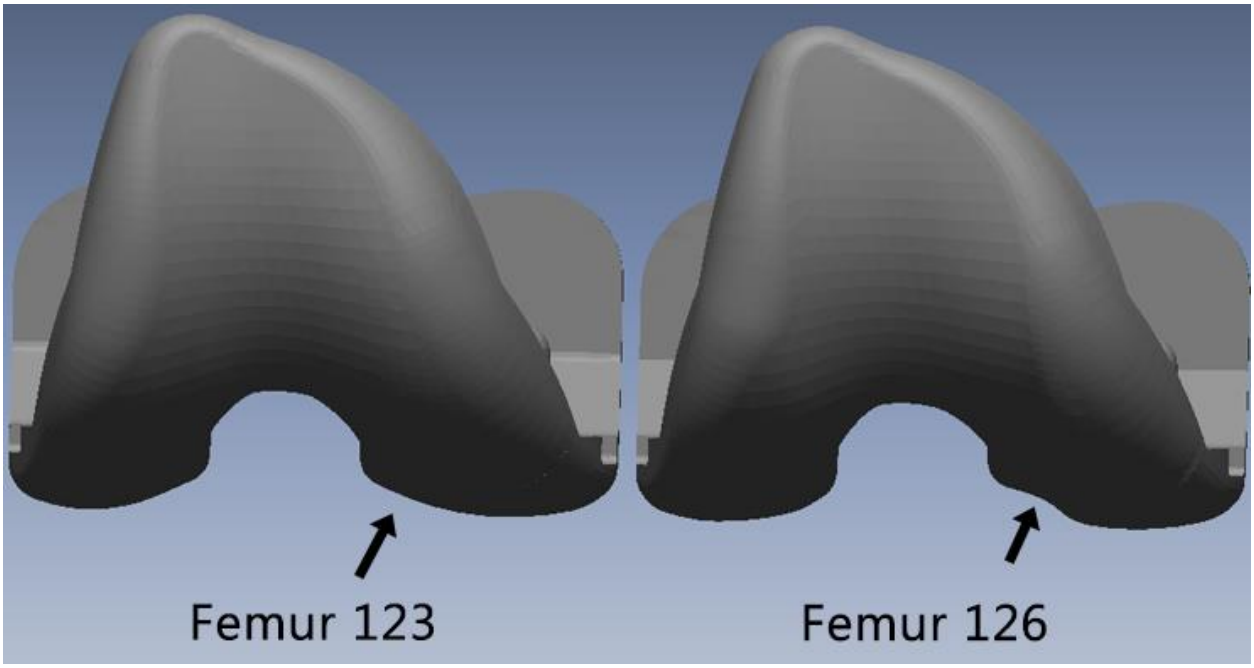

Figure 104: Femur 126 has a trochlear groove that rotates on the femoral component. This rotation is more pronounced than in femur 125. The arrows show where this difference can be seen.

polyethylene designs were asymmetric, and all RP designs were symmetric with a 5 mm lateral offset of the rotation point. Furthermore, each cam and post design was identical among these simulations. Before performing these simulations, several upgrades and changes were introduced to the model.

These were the first simulations to feature full mapping of the trochlear groove (Figure 13) and an accurate cam/post representation (Figure 19 & Figure 20). Furthermore, these simulations shifted the PID controller from flexion to rate of flexion (Figure 24). This model also featured changes to the assumptions of how the patella functioned. Previously, the patella was able to rotate in all three directions relative to the tibia. Now, it is assumed the patellar tendon places a constraint which prevents the patella from spinning or rotating relative to the tibia (rotation about an AP and SI axis, respectively). These assumptions were removed in future version of the forward model, and the patella was given all six degrees of freedom.

Furthermore, the ratio of the vastus lateralis and vastus medialis was previously calculated to minimize patella rotation relative to the femur. Because this rotation is constrained relative to the tibia in the updated model, the controller is now based on minimizing the ML translation of the patella relative to the tibia.

Fixed Bearing Results

As the amount of rotation of the trochlear groove in late flexion increased, the amount of external rotation of the femur with respect to the tibia increased (Figure 105). In general, the rotation was consistently external after 30° of flexion. Prior to this, the rotation was erratic as the models settled in the beginning of the simulation. Femur 123 displayed roughly 2.5° of external rotation while Femurs 125 and 126 displayed 4.1° and 4.5° of external rotation respectively. In the simulations of Femur 125 and 126, the external rotation was completed between 80° and 90° of flexion, and there was relatively little rotation for the remainder of the activity. The modified Femur 127 design had roughly 3.4° of

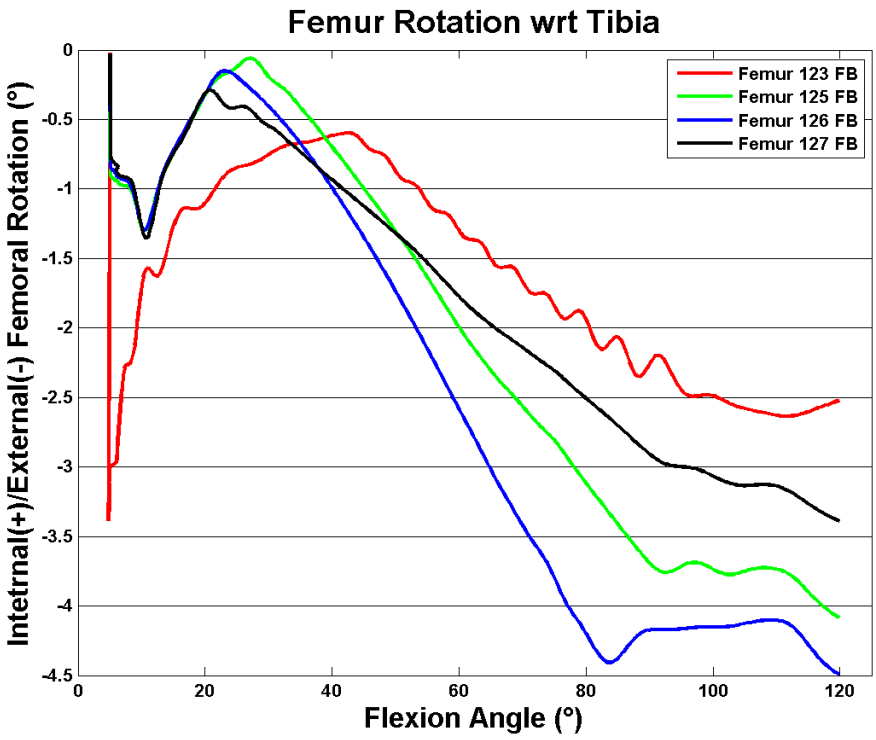

Figure 105: Increasing rotation of the trochlear groove resulted in increasing femoral rotation with respect to the tibia.

external rotation. Therefore, shifting the superior aspect of the trochlear groove medially reduced external rotation.

The medial condyle of all femurs translated from -4.1 mm (4.1 mm posterior) to -6.8 mm during the first 20° of flexion (Figure 106). Then, the medial condyle translated anteriorly until 80° of flexion, at which point the cam engaged, and the medial condyle translated posteriorly. The medial condyle of Femur 123 reached -4.2 mm when the cam contacted the post, before sliding posteriorly to -7.3 mm at the end of the deep knee bend activity. Femur 125 slid anteriorly to -3.7 mm before ending the activity at -6.5 mm. The medial condyle of Femur 126 reached -3.2 mm at 80° of flexion before translating posteriorly to -6.3 mm. In the Femur 127 simulation, the medial condyle reached -4.0 mm before translating anteriorly to -6.9 mm. Implants which had less medial condyle posterior translation had greater axial rotation. Femurs with more axial rotation had less posterior translation of the medial condyle.

The lateral condyle behaved similarly for all simulations (Figure 107). It started at approximately -4.2 mm and slid posteriorly to -7.6 mm at 10° of flexion (-8.3 for the exception of Femur 123). Then, the condyles translated slightly anteriorly until the cam and post contacted at 80° of flexion, at which point, they slid posteriorly. At 80° of flexion, the lateral condyles of Femurs 123, 125, 126, and 127 had translated to -6.0 mm, -6.1 mm, -6.4 mm, and -6.0 mm respectively. At the end of the activity, the ending lateral translations for the condyles were -9.3 mm, -9.8 mm, -10 mm, and -9.5 mm for Femurs 123, 125, 126, and 127, respectively. Femoral designs which produced more axial rotation resulted in more posterior translation of the lateral condyle.

For all designs, increased femoral rotation resulted in decreased tibiofemoral and patellofemoral forces (Figure 108 & Figure 109). The interactive forces were similar in early flexion and diverged as flexion increased. The peak forces occurred at approximately 80° of flexion, at which point all the forces decreased. Femur 123 had peak tibiofemoral forces of 4.5 x BW and patellofemoral forces of 6.4 x BW.

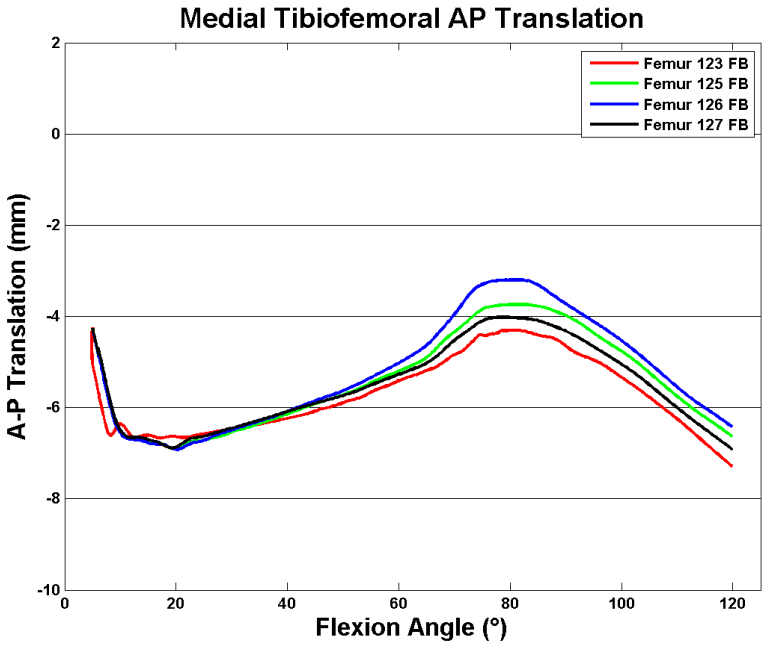

Figure 106: The femurs which had more trochlear rotation had less medial condyle posterior translation.

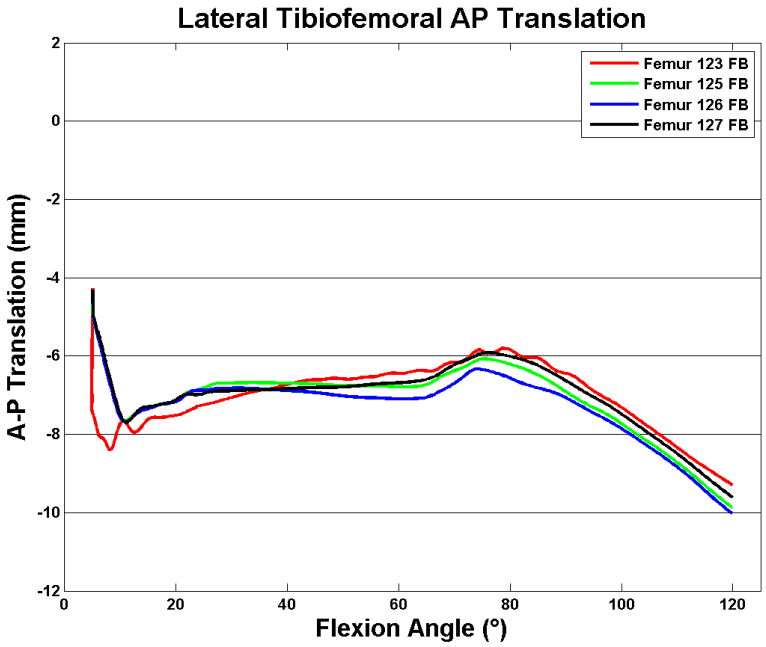

Figure 107: The femurs with more external rotation had more lateral condyle posterior translation.

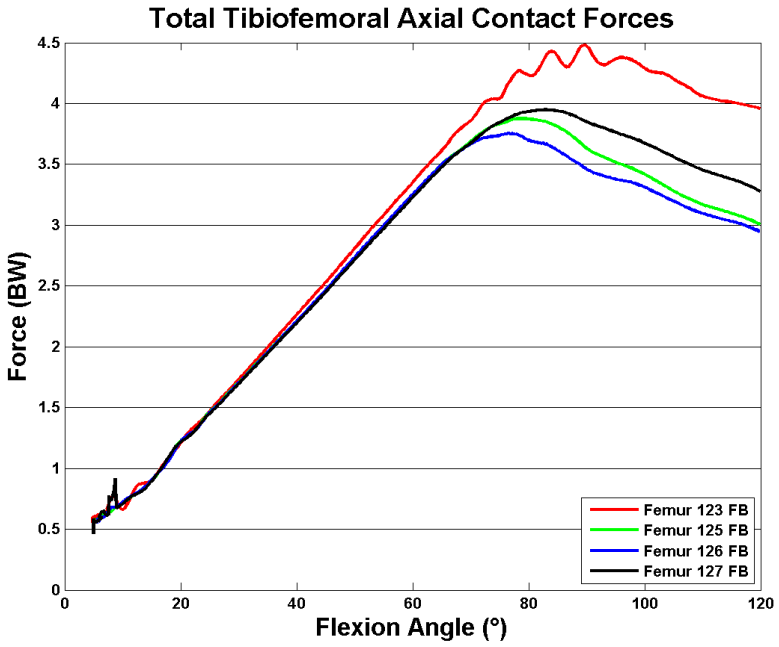

Figure 108: Lower tibiofemoral forces are seen in the implants with more femoral external rotation.

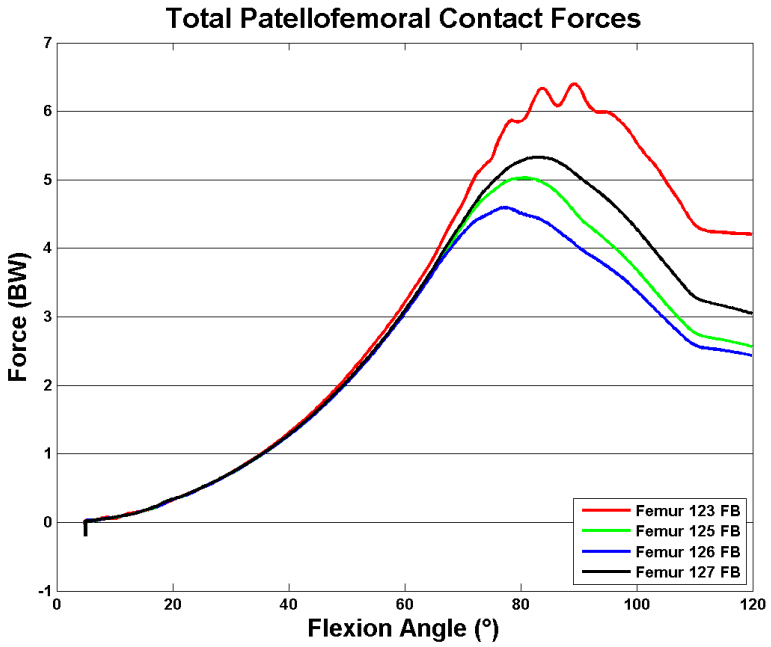

Figure 109: Lower patellofemoral forces are seen in the implants with more femoral external rotation.

These were by far the largest forces of all the FB simulations. In Femur 125, the tibiofemoral and patellofemoral forces were 3.8 x BW and 5.0 x BW respectively. Femur 126 had knee forces of 3.7 x BW and patellofemoral forces 4.7 x BW. Femur 127 had knee forces just shy of 4.0 x BW and patellofemoral forces of 5.3 x BW.

Rotating Platform Results

The femoral component displayed more external rotation with respect to the trochlear groove as the amount of rotation of the trochlear groove increased (Figure 110). Most of the femoral components lead to a finding that external rotation occurred for most of flexion with slight internal rotation at the end of flexion. Femur 123 rotated externally to -3° at 100° of flexion and then rotated internally to 2.7° of external rotation at the end of the activity. Femur 124 rotated 5.3° externally in the first 80° of flexion and then internally to 5° of external rotation. Femur 125 had a maximum external rotation of 4.4° and an ending external rotation of 4.2°. Femur 126 rotated externally to 4.7° and ended at 4.5°. Femur 127 was the only femur to not show a clear internal rotation pattern at the end of flexion. It rotated 3.8° externally in the first 100° of flexion. Then the rate of rotation slowed, and it ended the deep knee bend activity with 4° of external rotation. As with the fixed bearing designs, Femur 127 rotated less than Femur 125. This shows that for both fixed and mobile bearing designs, a medial shift of the superior aspect of the trochlear groove results in less external rotation of the femoral component with respect to the tibia. The polyethylene inserts each rotated externally for approximately the first 80° of flexion until the cam and post engaged (Figure 111). The behavior varied for the remainder of flexion. In the Femur 123 simulation, the polyethylene rotated externally to 3° of external rotation at 90° of flexion and remained there until 105° of flexion. Then it rotated to 3.5° of external rotation during the remainder of flexion. The polyethylene in the Femur 124 simulation rotated externally to 5.3° in the first 80° of flexion. Then it rotated internally to 4.4° of external rotation at 110° and rotated

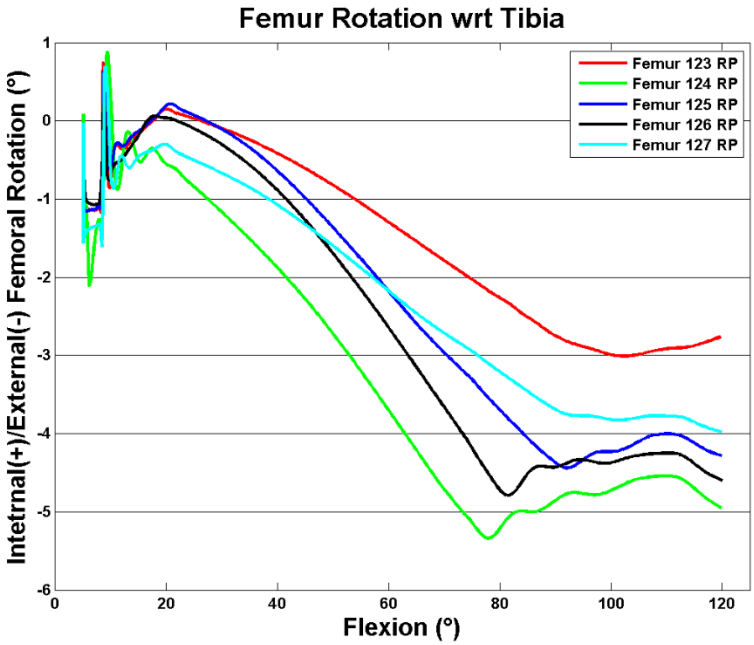

Figure 110: Increasing trochlear groove rotation leads to increasing femoral component axial rotation.

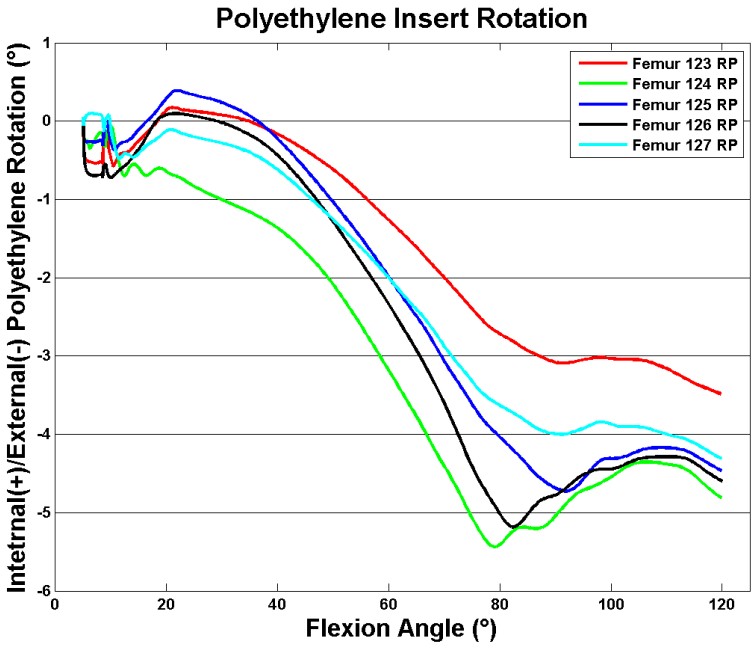

Figure 111: Higher polyethylene rotation occurs in simulations with more external femoral rotation.

externally to 4.8° during the remainder of the activity. The polyethylene in the Femur 125 simulation rotated externally to 4.7° during the first 90° of flexion. It remained relatively neutral for the rest of flexion. In the Femur 126 simulation, the polyethylene rotated to 5.2° externally at 80° of flexion. Then it rotated internally ending at 4.6° of external rotation. In the Femur 127 rotation, the polyethylene rotated externally to 4.0° at 90° of flexion. Then, it stopped rotating until roughly 110° before rotating to an ending external rotation of 4.3°. It should be noted that every femur had a tendency to externally rotate during the last 5° of flexion. It is not clear if this is just part of an oscillation or a resumption of the general trend toward external rotation.

The femur rotation with respect to the polyethylene followed a similar pattern for all implants. It started by rotating externally relative to the polyethylene for approximately 40° of flexion (Figure 112). Then it rotated internally until 80° of flexion, when the cam and post mechanism engaged. It then rotated externally with respect to the femur until 100° of flexion. From 100° of flexion until the end, most implants displayed very little rotation with the exception of Femur 123. In early flexion, Femur 123 rotated externally to 0.25°. Then it rotated to 0.45° of relative internal rotation through mid-flexion. At 100° of flexion, it was neutrally aligned with the tibia. Then, it displayed a rapid internal rotation to 0.70° by the end of flexion. This is likely caused by the femur rotating internally with respect to the tibia at the end of flexion while the polyethylene rotates externally (Figure 110 & Figure 111). Femur 124 experienced the longest initial period of relative external rotation which finished at 50° with 0.6° of external rotation. This simulation then rotated internally to 0.25° of internal rotation at 80° of flexion and proceeded to rotate externally to 0.20° of external rotation by 100° of flexion and remained mostly stationary for the rest of the activity. Femurs 125, 126, and 127 behaved nearly identically for the first 100° of flexion. They rotated to externally 0.45° in the first 45° of flexion and then rotated to 0.4° of internal rotation at 80° of flexion. They then returned to a neutral position at 100° of flexion. From

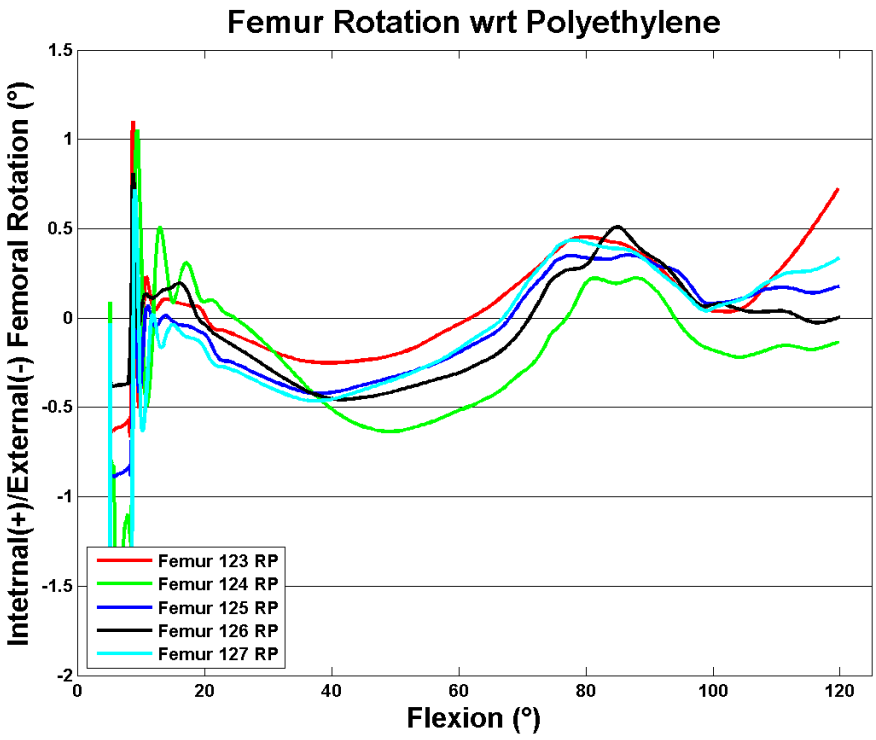

Figure 112: All simulations showed less than 0.5° of relative rotation between the femur and the polyethylene though out mid and late flexion except for Femur 123 and Femur 124. Femur 123 had more than 0.5° of external rotation of the femoral component relative to the polyethylene in late flexion. Femur 124 had more than 0.5° of internal rotation of the femoral component relative to the polyethylene in mid flexion.

there, the three femurs rotated differently. Femurs 125 and 127 ended with 0.2° and 0.4° of internal rotation, respectively. Femur 126 remained in a neutrally rotated position for the rest of the activity.

Once again, increased external rotation of the tibia corresponds to both less medial condyle posterior translation and more lateral condyle posterior translation (Figure 113 & Figure 114). The medial side condyle of the femur translated anteriorly with respect to the femur for the first 80° in all RP simulations. This simulation then rotated posteriorly after cam and post engagement for all trials. The medial condyle started with an initial position of -4.0 mm (4 mm posterior). Femur 123 slid anteriorly to -3 mm then posteriorly to -6.1 mm. Femur 124 slid anteriorly to -1.5 mm before sliding posteriorly to -5.2 mm. In the Femur 125 simulation, the contact point slid anteriorly to -2.2 mm and then posteriorly to -5.4 mm. Femur 126 slid anteriorly to -1.7 m before sliding posteriorly to -5.2 mm. Finally, Femur 127 reached -2.5 mm anteriorly before sliding posteriorly to -5.5 mm.

The lateral condyle started at started at roughly -4.2 mm posterior on the tibia. They showed very little translation before 80° of flexion and then translated posteriorly. The lateral condyle of Femur 123 sat at -4.6 mm at 80° of flexion and translated posteriorly to -8.3 mm at ending flexion. Femur 124 slid posteriorly to -5.5 mm at 80° of flexion and reached -9.2 mm by the end of the activity. The lateral condyle of Femur 125 translated posteriorly to -5.1 mm at 80° of flexion and to -8.9 mm at the end of the deep knee bend activity. In the Femur 126 simulation, the lateral condyle slid posteriorly to -5.4 mm at 80° of flexion and -9.0 at the end of the activity. Femur 127 slid to -4.9 mm at 80° of flexion and finished at -8.8 mm.

Once again, the more external rotation a knee implant produced, the lower its total patellofemoral and tibiofemoral contact forces were (Figure 115 & Figure 116). All knees started with roughly the same amount of force until approximately 70°, where they separated to reach different peaks at 80°. Then the forces decreased fairly uniformly for all knees for the remainder of flexion. Femur 123 generated

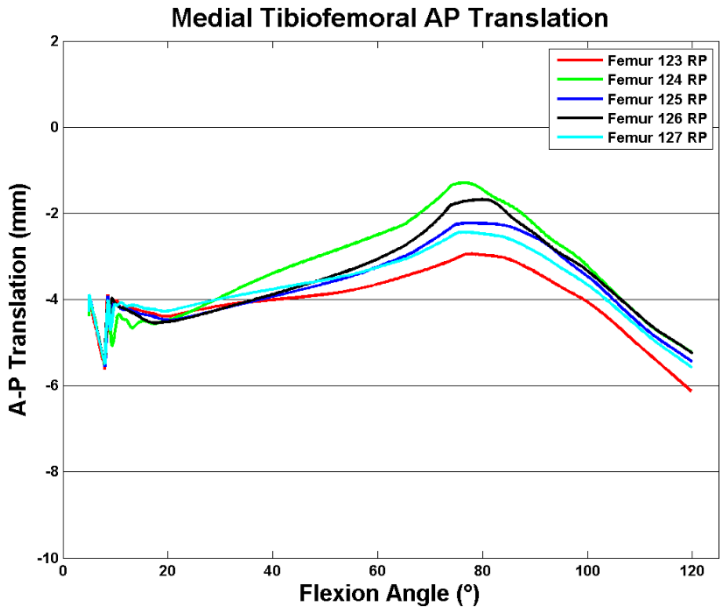

Figure 113: The knee implants with more external rotation of the femur relative to the tibia had less medial condyle posterior translation.

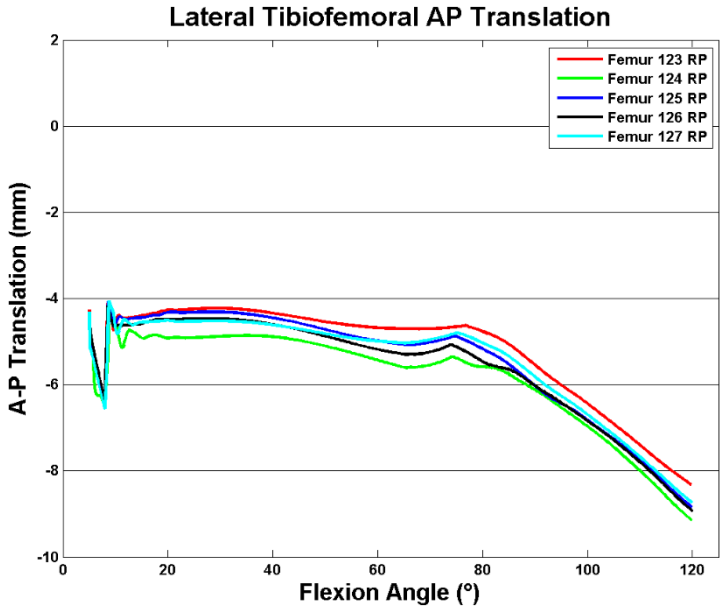

Figure 114: The knee implants with more external rotation of the femur relative to the tibia had more lateral condyle posterior translation.

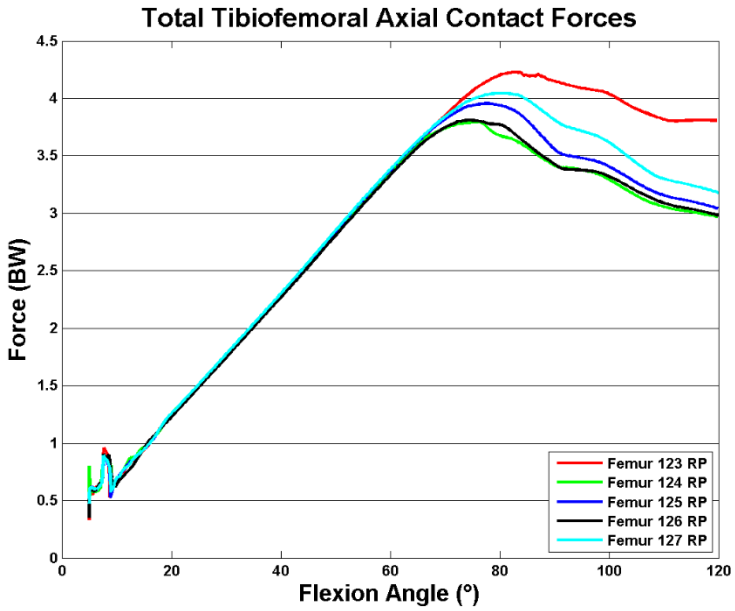

Figure 115: Femoral designs with more axial rotation of the femur relative to the tibia resulted in lower tibiofemoral forces.

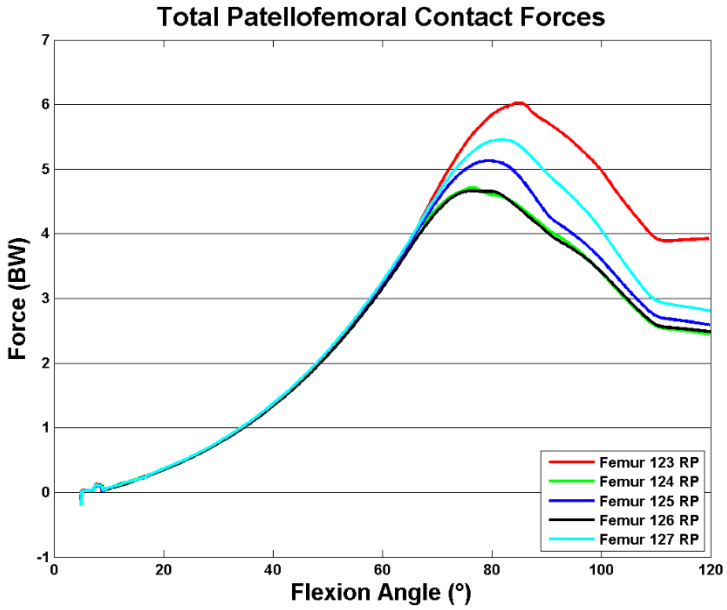

Figure 116: Femoral designs with more axial rotation of the femur relative to the tibia resulted in lower patellofemoral forces.

maximum forces of 4.2 x BW and 6.0 x BW and the tibiofemoral and patellofemoral joints, respectively. In Femur 124 and 126, the two implants with the most external rotation, tibiofemoral forces fell to a peak of 3.8 x BW, and patellofemoral forces fell to a peak of 4.7 x BW. The tibiofemoral forces peaked at slightly under 4.0 x BW in the Femur 125 simulation, while patellofemoral forces peaked at 5.1 x BW. Femur 127 had peak tibiofemoral forces of 4.1 x BW and peak patellofemoral forces of 5.4 x BW.

Femur 123 – 127 Summary

A trochlear groove which rotates internally as it moves inferiorly seems to produce beneficial results. Femur 125 had more external rotation of the femur relative to the tibia than Femur 123, as it had 5° of internal rotation of the trochlear groove at 90° of flexion. Femur 126 produced even more external rotation of the femur relative to the tibia because it had 10° of internal rotation of the trochlear groove at 90° of flexion. These results were consistent for both the FB and RP results.

Furthermore, a medial shift of the superior aspect of the trochlear groove reduced external rotation. Femur 127, which was essentially identical to Femur 125 except for the shift of the trochlear groove, produced less external axial rotation of the femur relative to the tibia. This result was also consistent between FB and RP simulations. Finally, increased external rotation of the femur with respect to the tibia seems to be beneficial. The peak forces for both tibiofemoral and patellofemoral interactions were always lower for implants which produced more axial rotation in these simulations. This may be a result of the lateral condyle posterior translation. In all cases, more external rotation corresponded to more lateral condyle posterior translation.

In the case of the RP simulations, all implants besides Femur 123 and Femur 124 had relative rotation of the femur with respect to the polyethylene of less than 0.5° at all times. Femur 123 ended with the femur 0.7° internally rotated with respect to the polyethylene. Because the femur was rapidly rotating internally with respect to the polyethylene at the end of the deep knee bend simulation, this result may

become even larger in later flexion. Femur 124 briefly reached 0.6° of external rotation of the femur relative to the polyethylene in mid-flexion, but quickly reverted back to less than 0.5° of relative rotation. For these reasons, internal rotation of the trochlear groove design at 90° of flexion seems to be beneficial.

Anatomical vs Mechanical Alignment

Next, the fixed bearing Femur 123 was analyzed a second time using anatomical and mechanical alignment (Incavo 2013). Mechanical alignment produced approximately 2.8° of external femoral rotation while anatomical alignment produced nearly 9° of axial rotation (Figure 117). Additionally, the mechanically aligned simulation had only 9.8 mm of posterior lateral translation while the anatomical alignment had 12.4 mm of rollback (Figure 118). The medial tibiofemoral forces were similar in both simulations at approximately 2.4 x BW (Figure 119). However, the lateral forces were considerably higher in the anatomical simulation with nearly 3.5 x BW as opposed to 1.8 X BW in the mechanical alignment simulation (Figure 120). The resulting peak total tibiofemoral forces were roughly 5.3 x BW for the anatomical simulation and 4.2 x BW for the mechanically alligned simulation (Figure 121). When anatomical and mechanical alignment were compared, anatomical alignment produced more axial rotation and lateral femoral rollback. However, mechanical alignment produced lower tibiofemoral forces.

Rotated Posterior Stabilizing Post - Femur 132 and Poly 327

Next analyzed was a novel polyethylene, Poly 327, which featured a post which was rotated approximately 10° externally so that the lateral portion of the post was more posterior than the medial portion (Figure 122). This design was intended to cause increased axial rotation during a DKB activity by shifting the cam force more laterally on the femoral condyle. It was assumed that a lateralized cam force would create a larger moment driving external rotation on the femur. Additionally, the post was

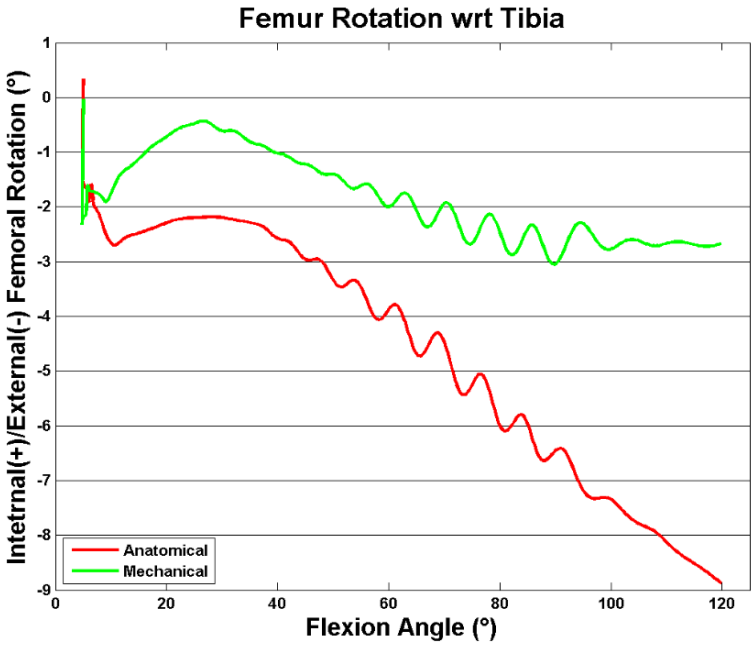

Figure 117: Femur rotation with respect to the tibia is shown for anatomical and mechanical alignment.

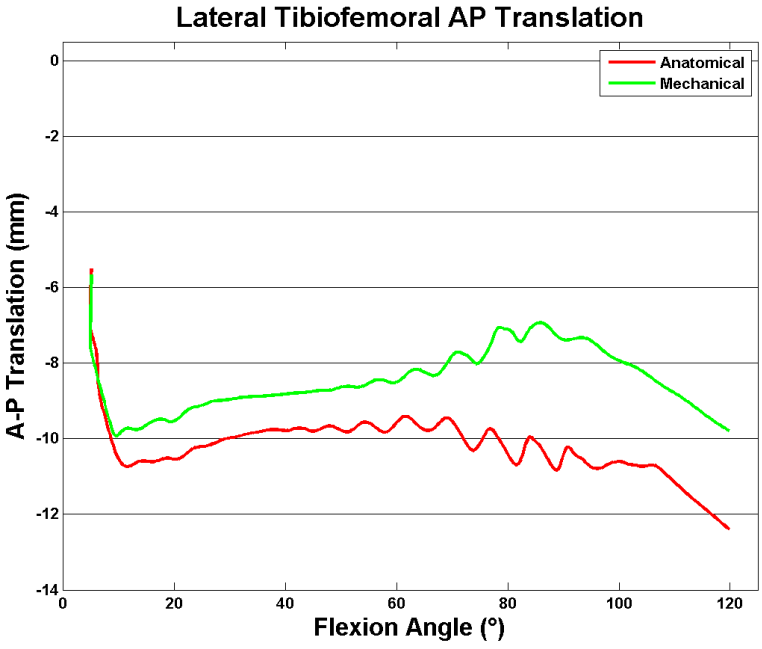

Figure 118: The lateral tibiofemoral translation is shown for anatomical and mechanical alignment.

Figure 119: The medial tibiofemoral forces are shown for anatomical and mechanical alignment.

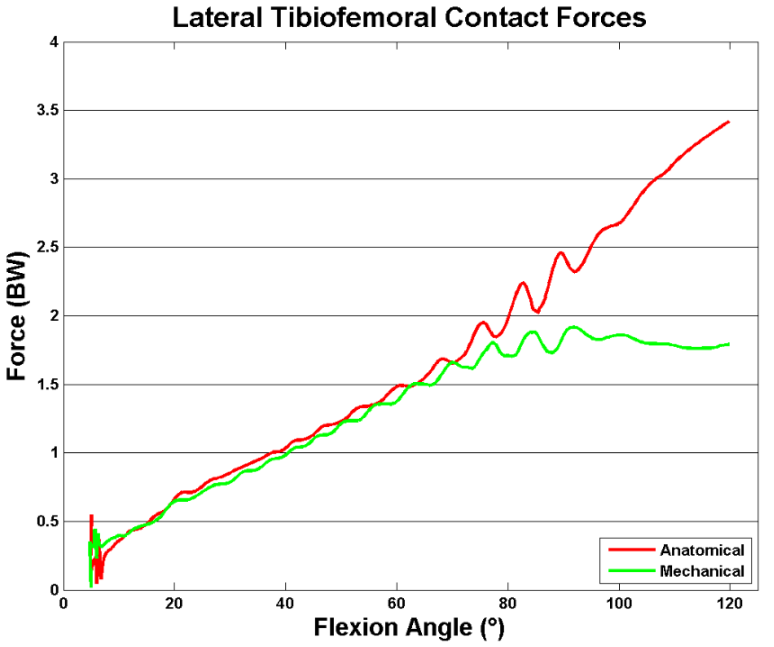

Figure 120: The lateral tibiofemoral contact forces are shown for anatomical and mechanical alignment.

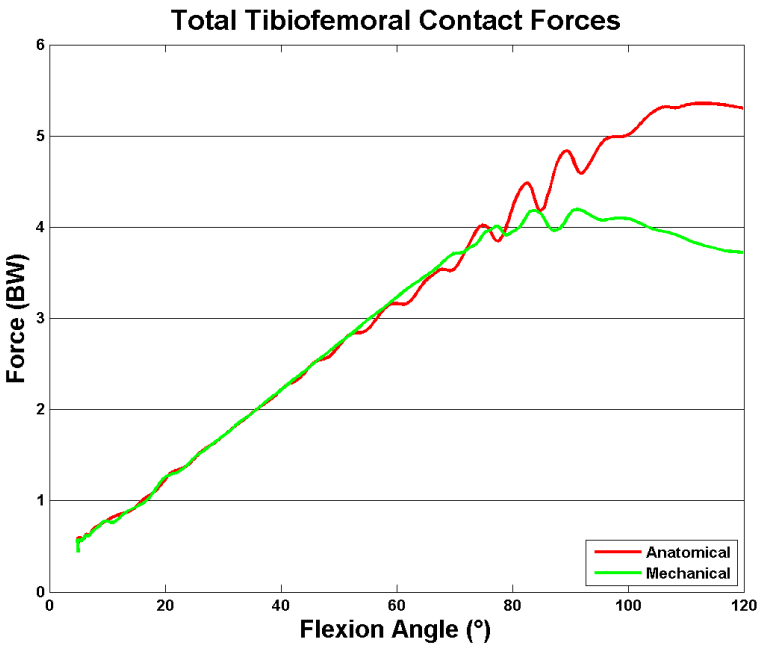

Figure 121: Total tibiofemoral forces are shown for anatomical and mechanical alignment.

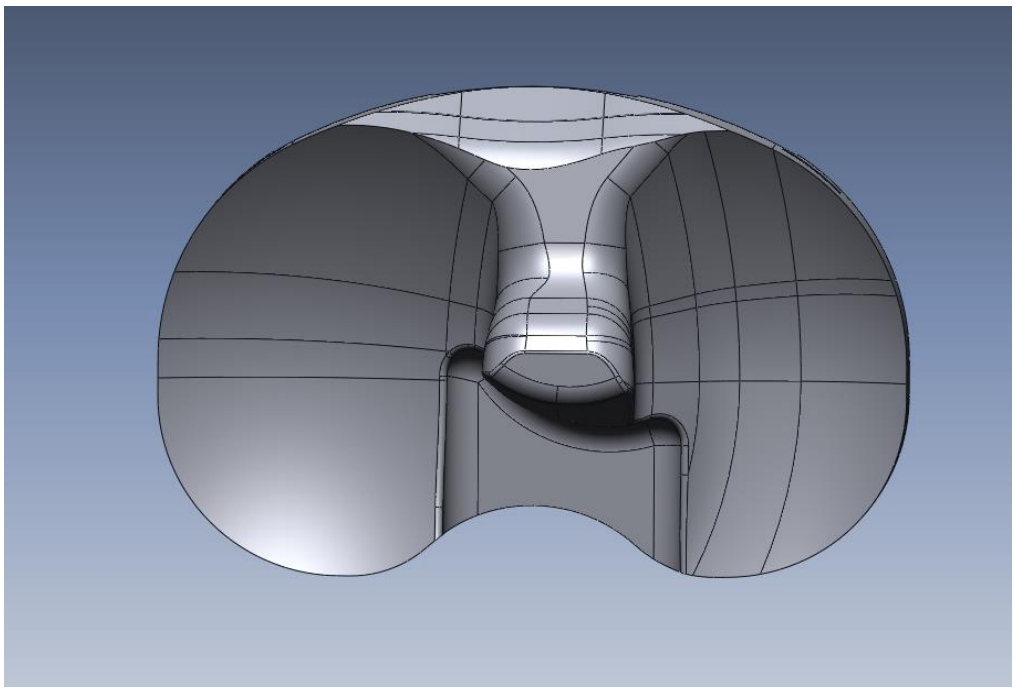

Figure 122: Poly 327 for a right knee is shown with the rotated post.

lateralized for the same reason. The post was then rotated 10° towards neutral, producing a very nearly normal post (Figure 123). Simulations were run with both the original and rotated post to show the effect of these rotations. The femur in these simulations was Femur 132, which was designed to complement Poly 327.

When the simulations were completed, the original poly 327 produced more axial rotation, as expected (Figure 124). Poly 327 achieved 12.8° of axial rotation while the modified version had only 11.8° of axial rotation. Furthermore, Poly 327 achieved more lateral condyle rollback with 14.4 mm versus only 13.2 mm of rollback for the modified version (Figure 125). The total knee forces were nearly identical (Figure 126).

Creation of an Anterior Cam & Post TKA Forward Solution Model

The next step was to analyze the effect of including an anterior cam and post for a TKA design that retained the PCL. Fluoroscopic studies were previously conducted on the Journey TKA, which has an anterior cam/post and posterior cam/post mechanism, but with this TKA design that PCL is sacrificed (Victor 2010). However, designs featuring only an anterior post are analyzed at this time, first to separate the effect of the anterior post from the posterior post. These designs can be referred to as anterior stabilized total knee arthroplasty (ASTKA). To analyze an ASTKA, the initial conditions become very important. The cam and post must sit completely flush, or the results could be highly affected. Instead of attempting to pick these initial conditions by hand, it is more efficient and accurate to allow the computer to generate the initial conditions via a settling program. To this end, a looping DKB simulation was created (Figure 25).

In the looping simulation, the forward solution model ignores the anterior post during the initial descent to greater than 35° of flexion. Then, the forward solution model considers the post during the subsequent extension to standing, where it is predicted the post should engage at approximately 20° of

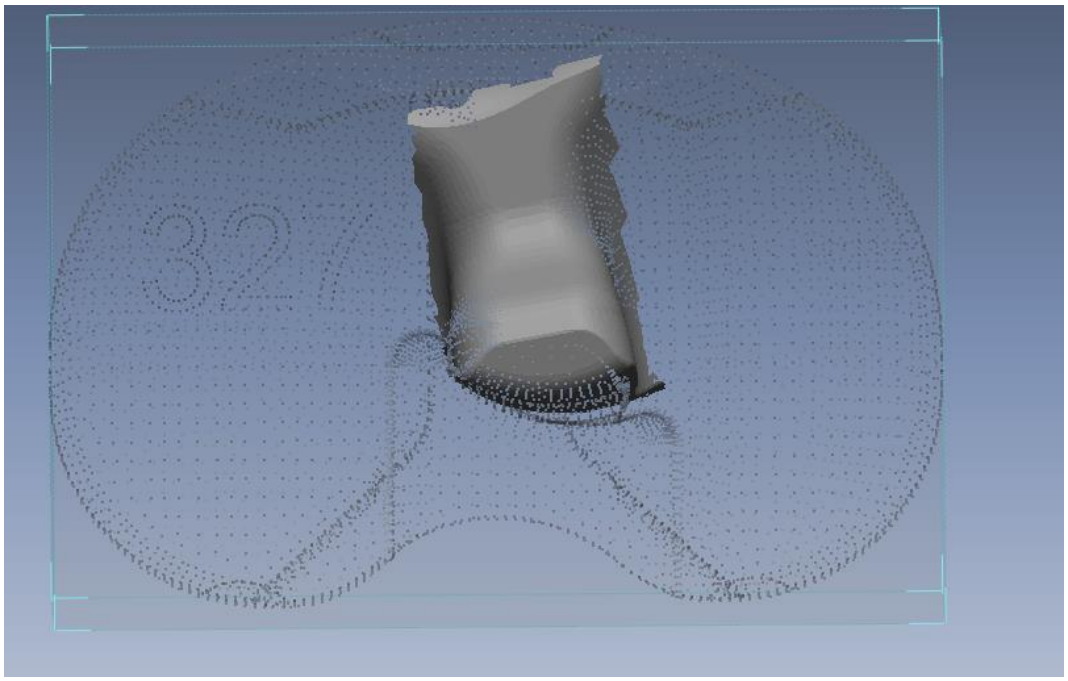

Figure 123: Poly 327 is shown as a point cloud with the rotated post shown as a surface.

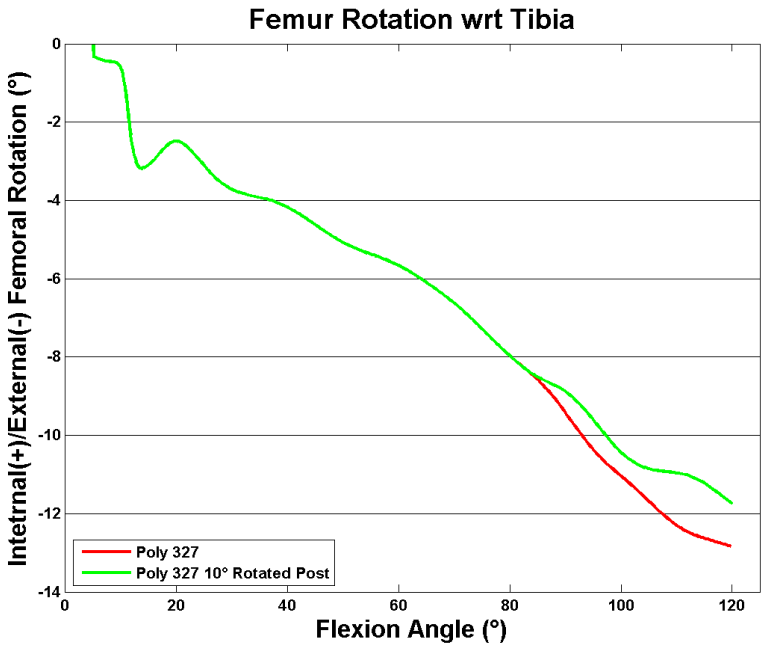

Figure 124: Axial rotation is compared for Poly 327 and the modified Poly 327.

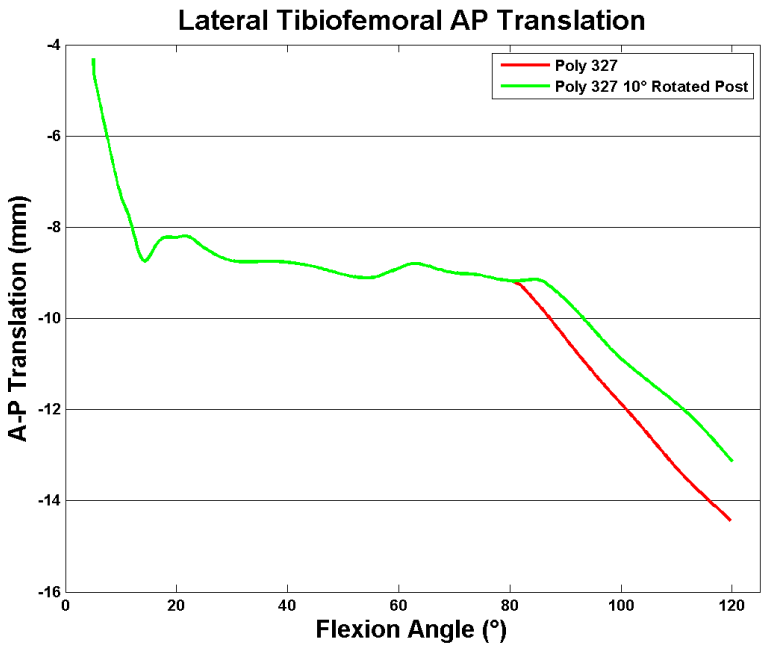

Figure 125: Lateral rollback is compared for Poly 327 and the modified Poly 327.

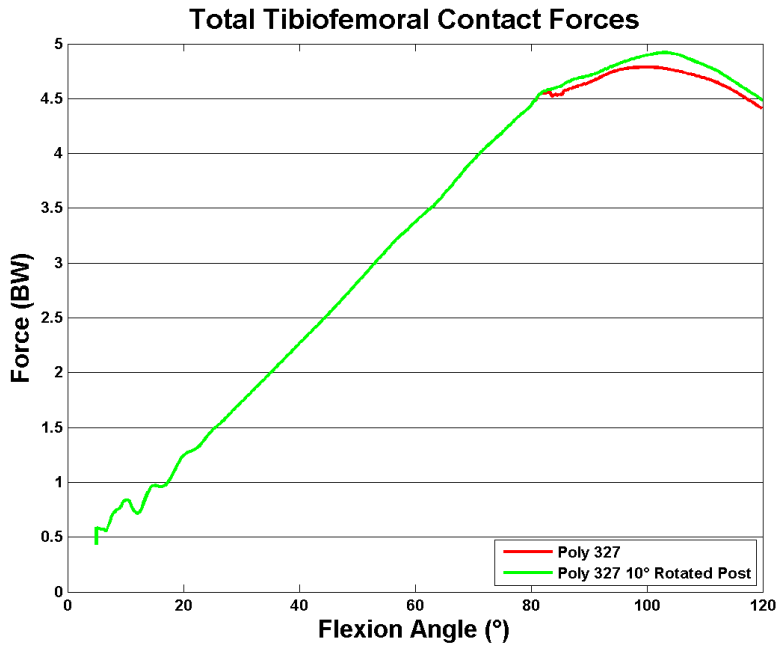

Figure 126: Tibiofemoral forces are compared for Poly 327 and the modified Poly 327.

flexion. Therefore, the last 20° of extension serve as the settling algorithm, and the correct starting position of the ASTKA for the second flexion activity computed.

The anterior post was defined mathematically using a surface polynomial (Figure 22). Also, 12 contact points were selected on the anterior cam, as the full point cloud detection had not yet been implemented for the cam and post (Figure 127). These simulations were time consuming, so the speed of the DKB activity was increased (Figure 128). By decreasing the time elapsed during a simulation from a little over 8 second to closer to 6 seconds, the time of a simulation was reduced by roughly 25%. Note that while the simulation only spans 8 seconds, it can take over an hour to compute what happens during those 8 seconds, so a 25% reduction is significant. Interestingly, this increase in speed made no notable difference in the results (Figure 129 - Figure 133).

With a functional ASTKA model, the first stage of development was selecting the correct location for the anterior cam and post. This was done by taking an existing PCR CAD model based off an on-the-market PCR and adding a cam and post (Figure 134). A suitable location was determined which produced small but noticeable forces in early flexion (Figure 135). As can be seen, cam forces are highest at full extension. The cam engages at 9.5° of flexion during the extension activity, and the cam disengages at 15.5° of flexion during the flexion activity. The peak force is 9.6% BW. This new model was effective at forcing the condyles more anterior in early flexion than in a traditional PCR implant (Figure 136 & Figure 137). The lateral condyle was pulled anteriorly from -3.1 mm to -2.2 mm while the medial condyle was pulled anteriorly from -3.2 mm to - 1.5 mm. Because the medial condyle was pulled more anterior than the lateral condyle, the PCR had less less axial rotation than the ASTKA design (Figure 138). The PCR design had a peak of 0.1 degrees of internal rotation while the design with ASTKA design had 0.5° of external rotation. Because this is the opposite of the intended results, future designs focused on pulling the lateral condyle more anterior than the medial condyle.

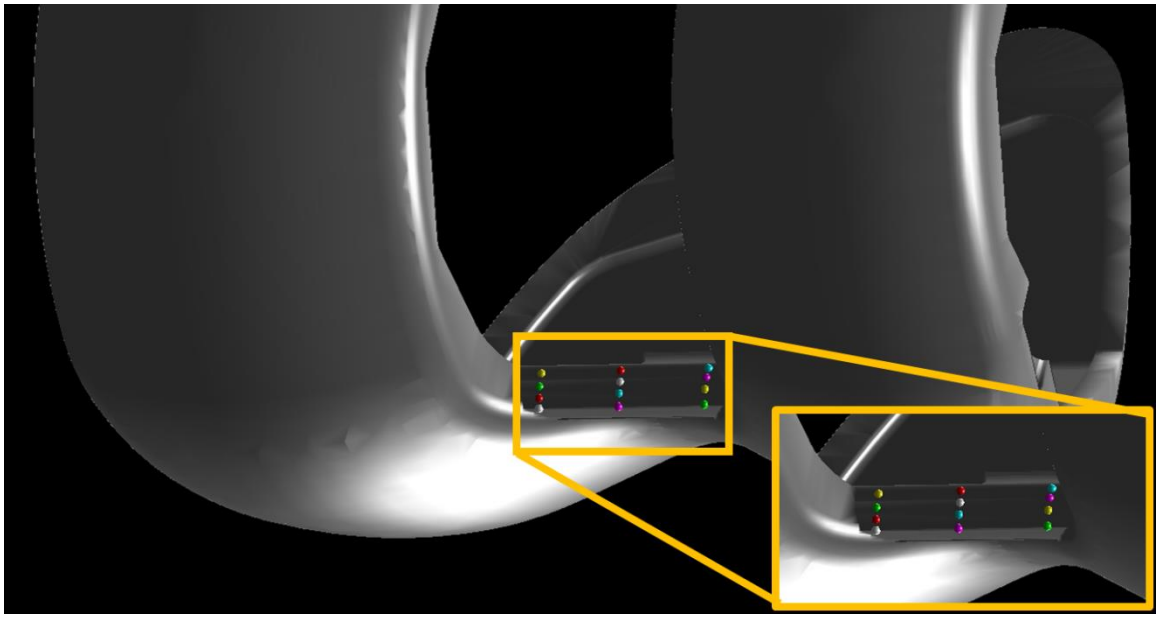

Figure 127: Twelve contact points are defined on the anterior cam.

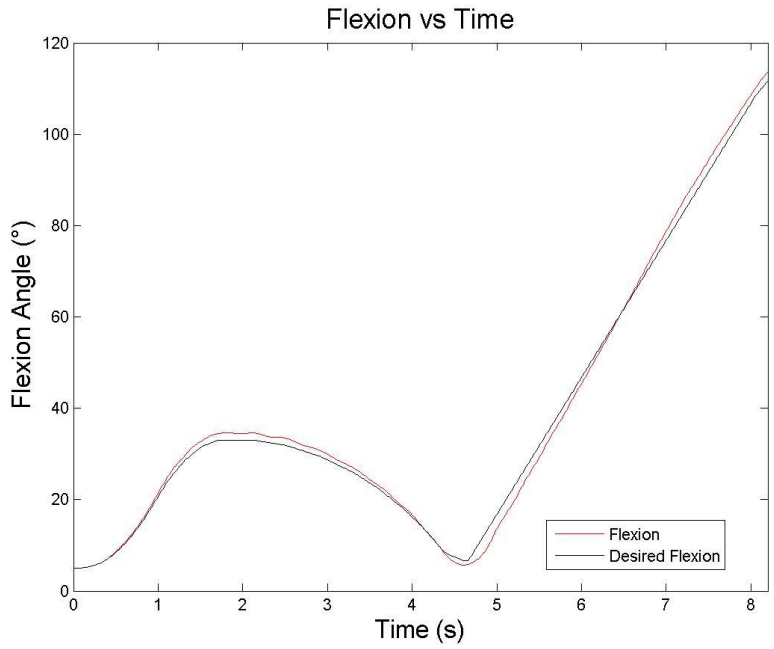

Figure 128: The DKB simulation flexes to approximately 35° and then returns to the upright position before completing the activity.

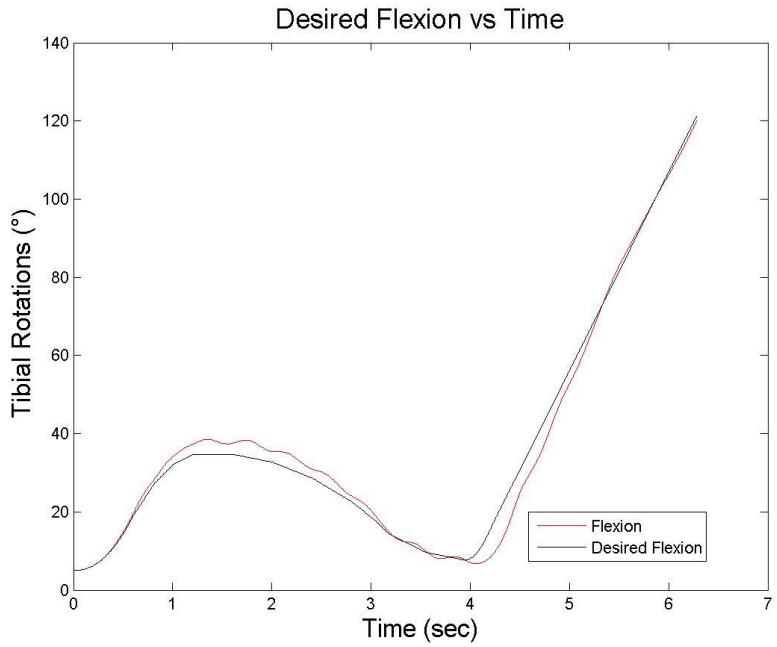

Figure 129: The activity speed was increased to save computational time by only simulating 6 seconds of activity.

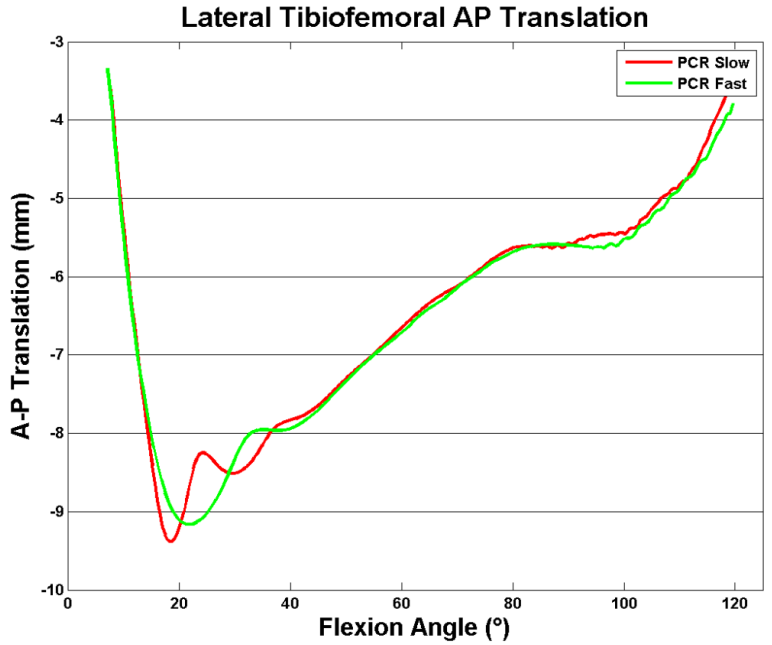

Figure 130: The speed of the activity had no noticeable effect on the lateral condyle translation.

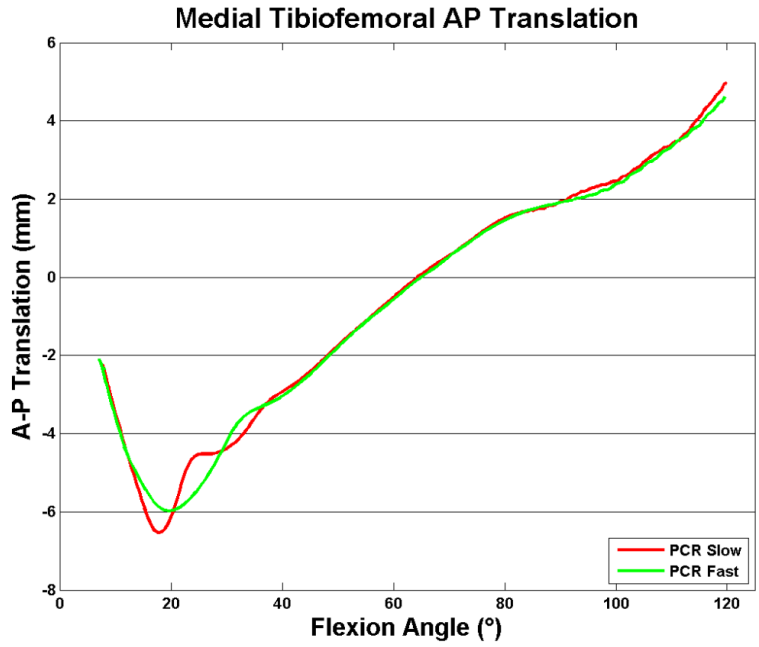

Figure 131: The speed of the activity had no noticeable effect on medial condyle translation.

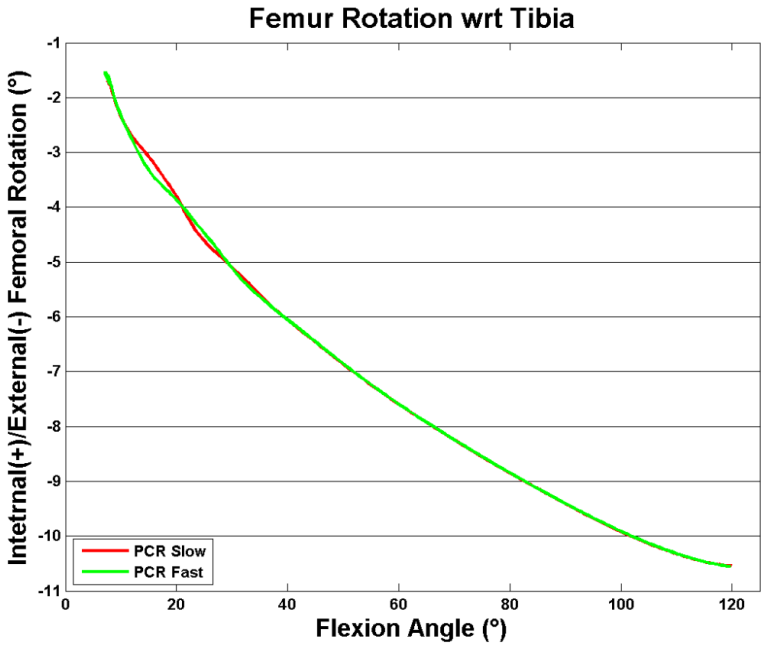

Figure 132: Femur axial rotation was unaffected by activity speed.

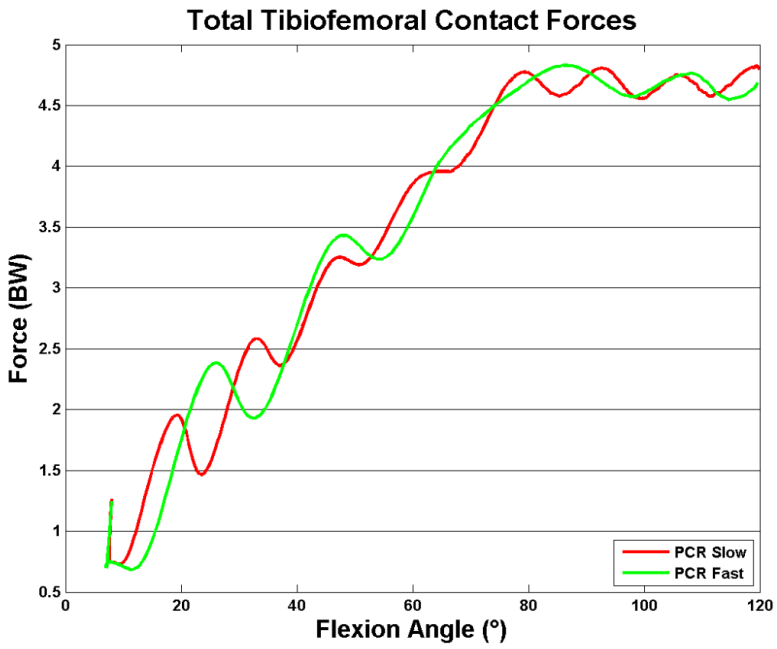

Figure 133: Contact forces did not depend on the activity speed.

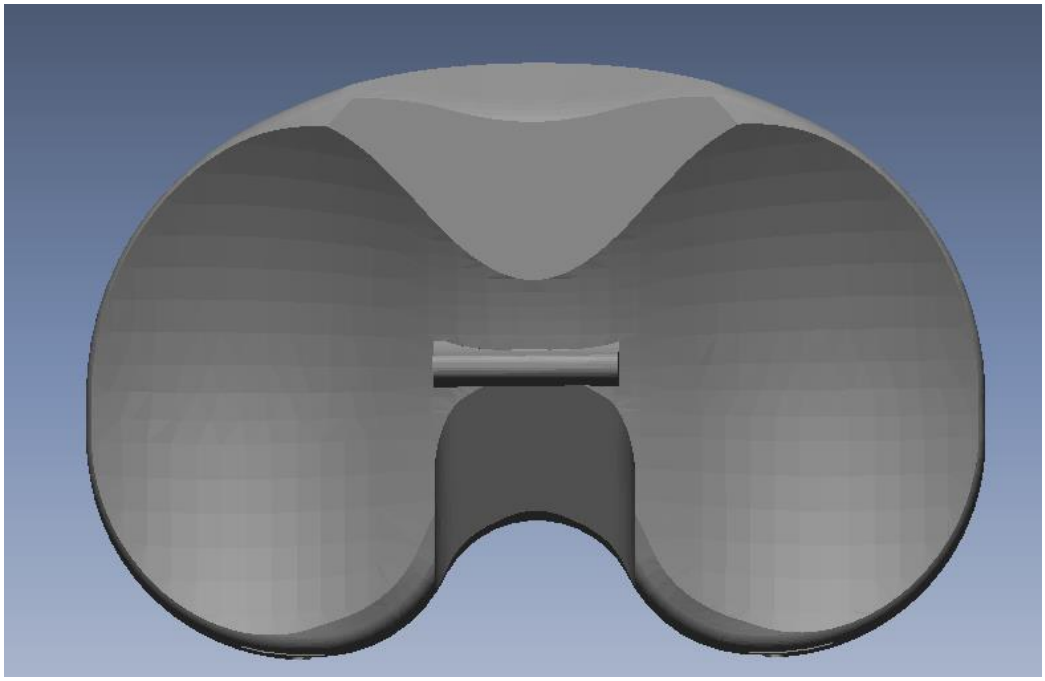

Figure 134: An existing PCR design with a cam/post added. The location was modified to generate small cam forces in extension.

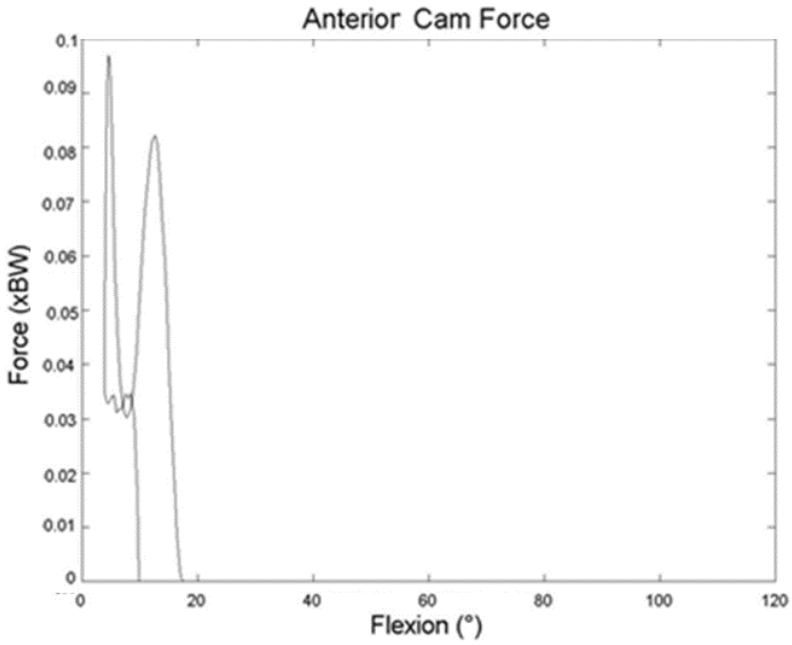

Figure 135: Anterior cam force peaks at approximately 0.1 x BW at full extension.

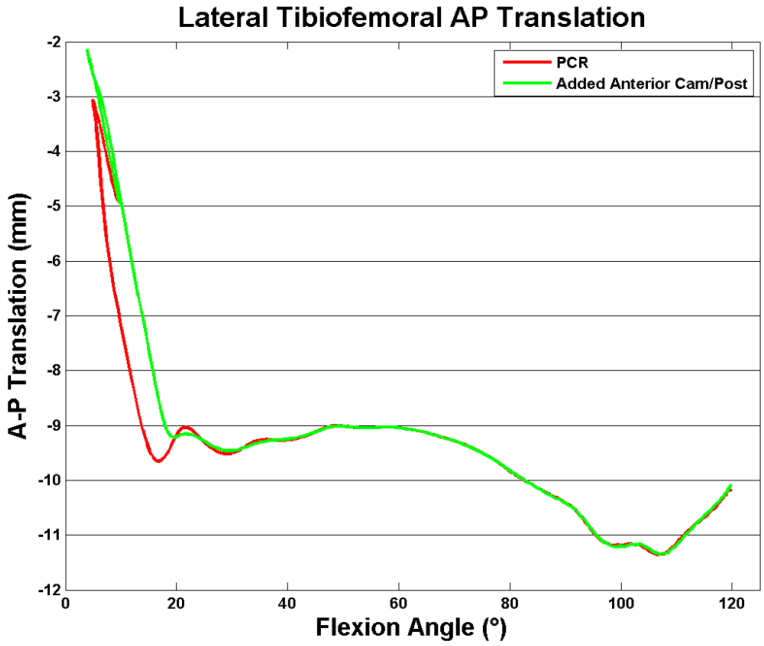

Figure 136: The anterior cam/post pulled the lateral condyle forward in early flexion.

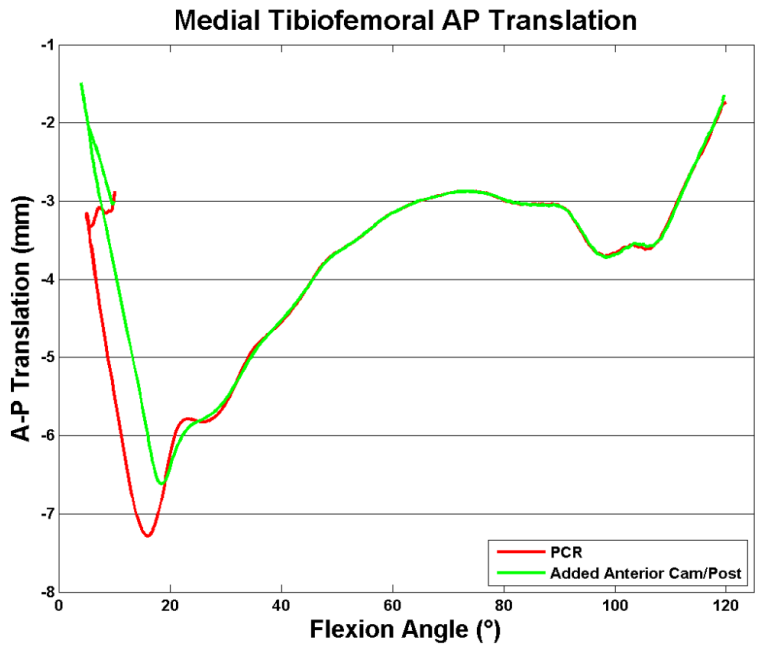

Figure 137: The anterior cam/post pulled the medial condyle forward in early flexion.

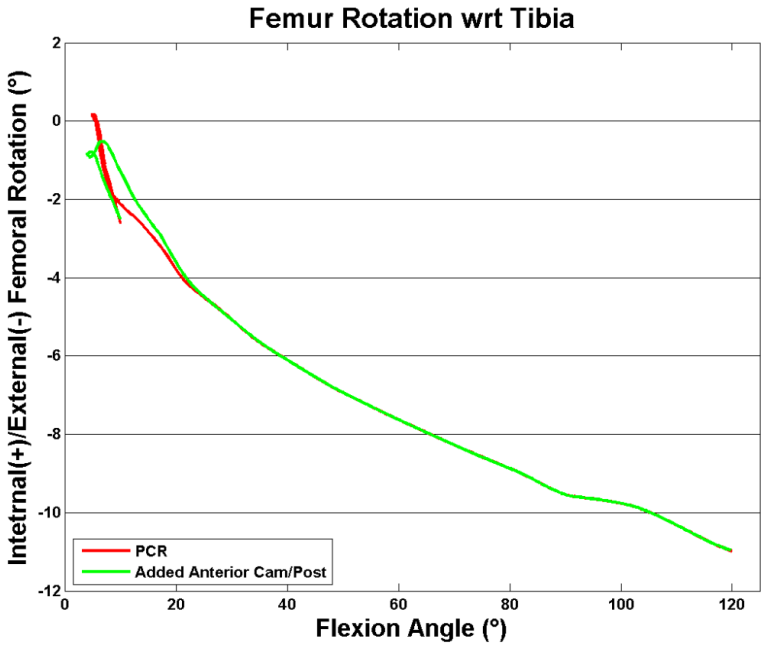

Figure 138: The anterior cam/post had little effect on axial rotation.

ASTKA_R1

After the proof of concept simulations, the polyethylene models were modified in order to generate some initial results. The first modification (ASTKA_R1_V1) included shifting the cam and post as well as lateralizing the cam/post (Figure 139). Using this new baseline polyethylene, two more revisions were created (ASTKA_R1_V2 and ASTKA_R1_V3). They were versions of ASTKA_R1_V1 compressed in the vertical direction. Therefore, ASTKA_R1_V2 had less conformity and a smaller anterior lip than the baseline, and ASTKA_R1_V3 had the least conformity and smallest anterior lip. All three versions featured an identical post. The femur used in these simulations was based on Femur 127. It was lateralized to match with the lateralized polyethylene design, and the cam was shifted to match the post as appropriate.

In full extension, the revised models' lateral condyles were set approximately 3 mm more anterior than the PCR with the anterior post. The revised ASTKA rested near the 0 position while the original PCR design with an anterior post attached sat at approximately 3 mm posterior (Figure 140). During later flexion, the revised models were typically 1.5 mm more anterior than the original. This finding is most likely a result of the anteriorized dwell point. During the initial rollback from 0° to 25°, it can be seen that the models with less conformity rolled further back. Therefore, the PCR model and ASTKA_R1_V1 both reached approximately 9.2 mm posterior. The less conforming ASTKA_R1_V2 reached approximately 9.5 mm posterior, and ASTKA_R1_V3 reached 10 mm posterior. The medial translations followed a very similar trend with all of the revised models sitting at the neutral position in full extension and the original sitting 2.4 mm posterior (Figure 141). However, the original model translated considerably more posteriorly in the first 25° of flexion ending at 6.8 mm posterior. ASTKA_R1_V1, ASTKA_R1_V2, and ASKTA_R1_V3 reached 5.5 mm, 6 mm and 6.4 mm posterior, respectively. Crucially, all the three revised polyethylene models had better axial rotation than the original model. All three

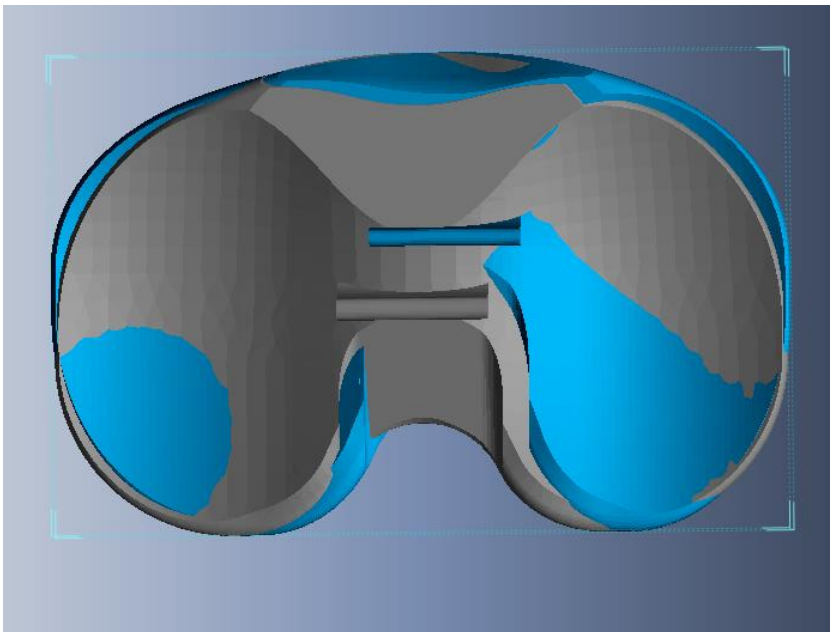

Figure 139: The post was shifted lateral and anterior for ASTKA_R1V1 (blue).

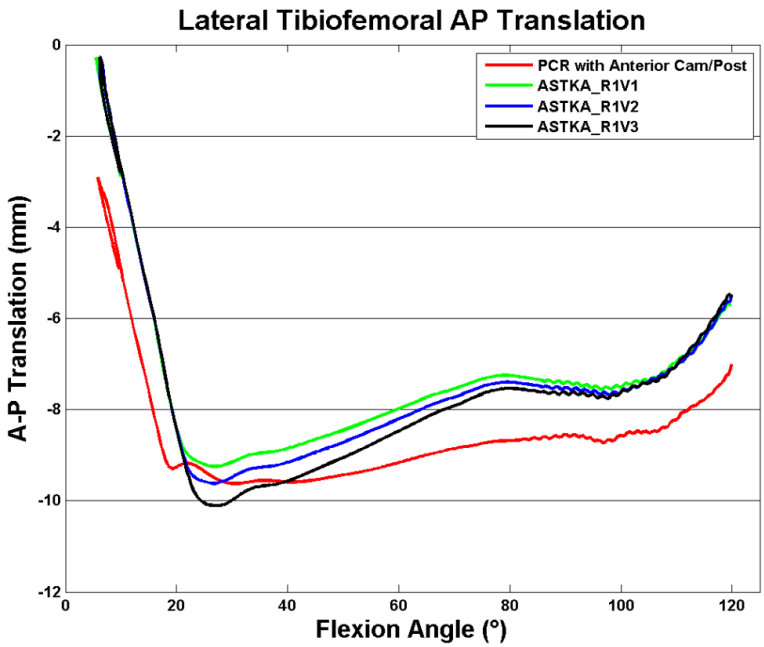

Figure 140: The less constraining ASTKA designs slid further back on the lateral side in early flexion but finished at the same location

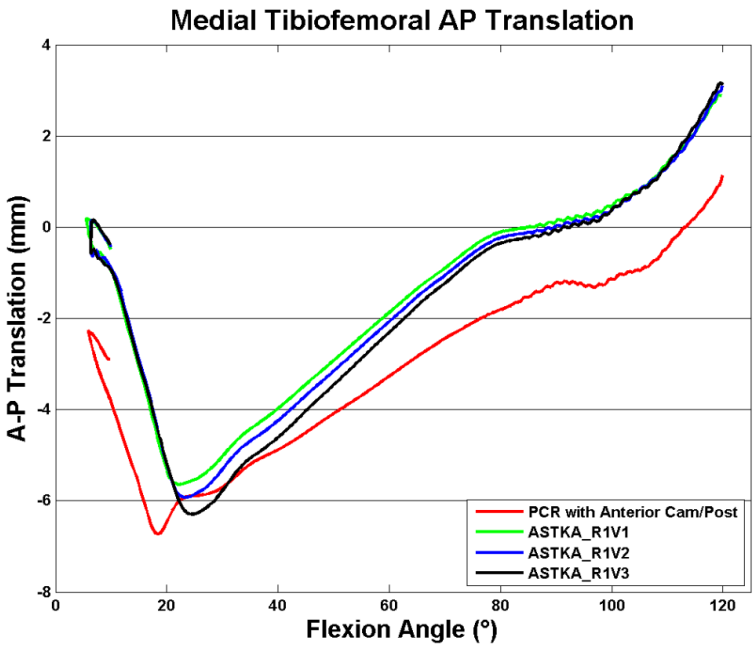

5

Figure 141: The less constraining ASTKA designs slid further back on the medial side in early flexion but finished at the same location.

started the activity at 0.5° of internal rotation and ended at 11.8° of external rotation (Figure 142). The original design went from 0.8° of external rotation to 10.5° of external rotation. Some numbers may differ from previously reported numbers as parameters such as PCL tension are often adjusted (but are identical for all simulations shown on one plot unless otherwise noted).

Next, the effect of implanting this polyethylene with 7° posterior tilt was explored. The posterior tilt simulations had similar results to the original simulations, with the less conforming models showing more posterior slide in early flexion, but ending with very similar overall magnitudes of translations. Laterally, the posterior tilt simulations translated the femur approximately 4 mm more posteriorly in early flexion and ended 3 mm more posteriorly (Figure 143). ASTKA_R1_V1, ASTKA_R1_V2, and ASTKA_R1_V3 translated to 12.6 mm, 13.2 mm, and 14 mm posterior, respectively. All three ended at roughly 8.5 mm posterior. The same pattern occurred on the medial side with the tilted simulations experiencing approximatley 3 mm more posterior translation in early flexion (Figure 144). All three simulations reached between 9 and 9.5 mm of translation in early flexion with the more conforming models having slightly more posterior translation. They all ended at roughly 0.6 mm of posterior translation. For the simulations with no posterior tilt, ASTKA_R1_V1 had roughly 10.2° of external rotation while ASTKA_R1_V2 and ASTKA_R1_V3 had 10.8° of external rotation. For the 7° tilt simulations, ASTKA_R1_V1 had 9.5° of external rotation; ASTKA_R1_V2 and ASTKA_R1_V3 had 10.1° of external rotation (Figure 145). Interestingly, the simulations with the posterior tilt experienced significantly lower PCL forces (0.3 x BW vs 0.45 x BW; Figure 146). This may indicate that a posterior tilt will help preserve the PCL.

ASTKA_R2

Next, ASTKA_R2_V1 (Revision 2, version 1) was nearly identical to ASTKA_V1_R1, but featured a more realistically shaped post which could actually handle loads (Figure 147). From here, ASTKA_R2_V2 and

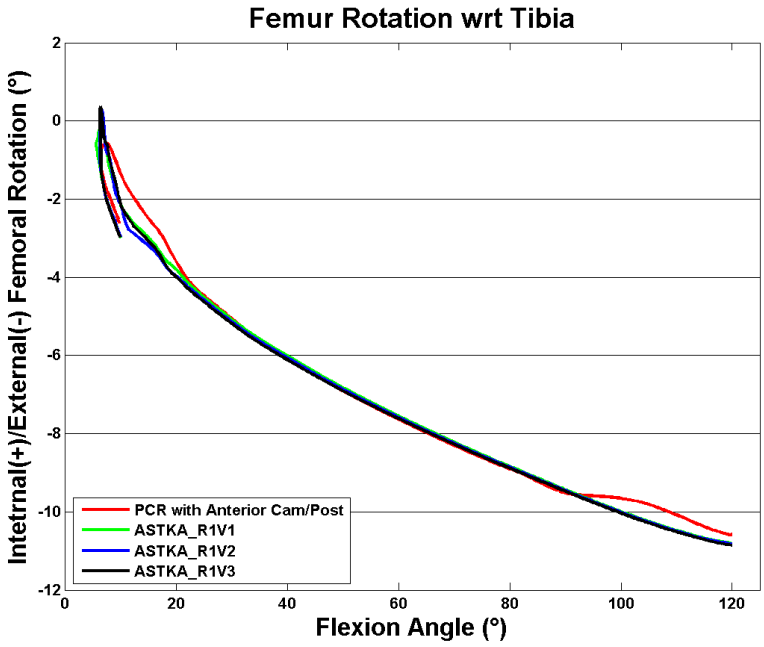

Figure 142: The new ASTKA models showed more internal rotation in early flexion than the original PCR with added cam/post design.

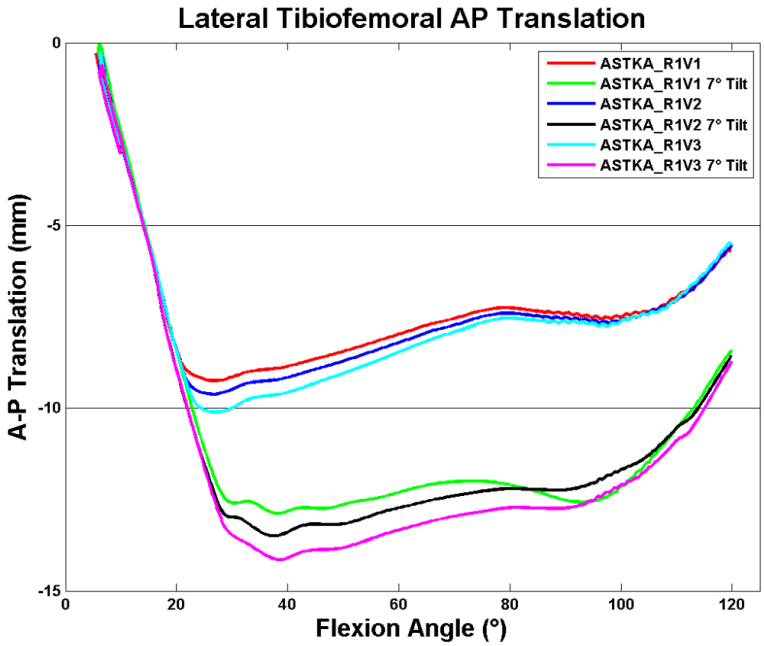

Figure 143: The 7° tilt simulations translated more posteriorly on the lateral side.

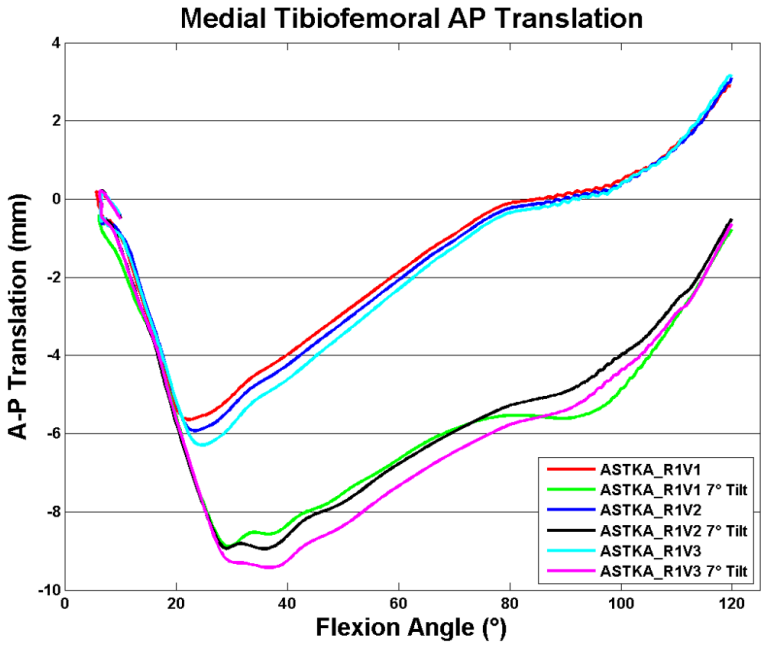

Figure 144: The 7° tilt simulations translated more posteriorly on the medial side.

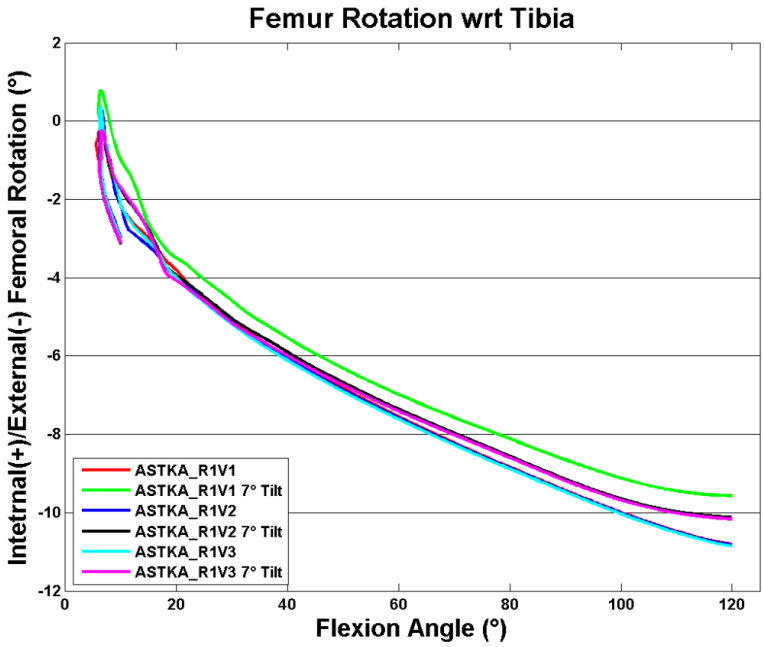

Figure 145: The 7° tilt simulations had slightly different axial rotations.

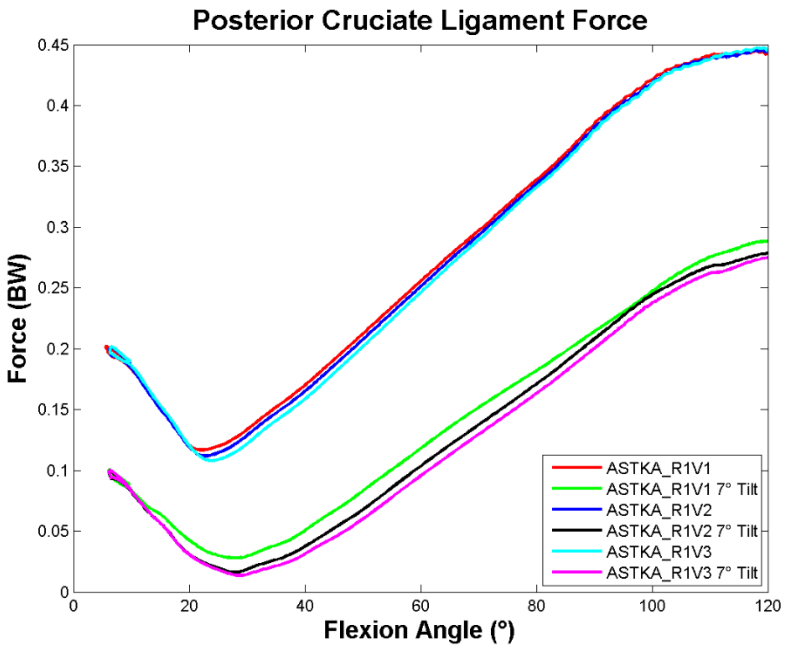

Figure 146: The PCL force was lower in the tilted simulations.

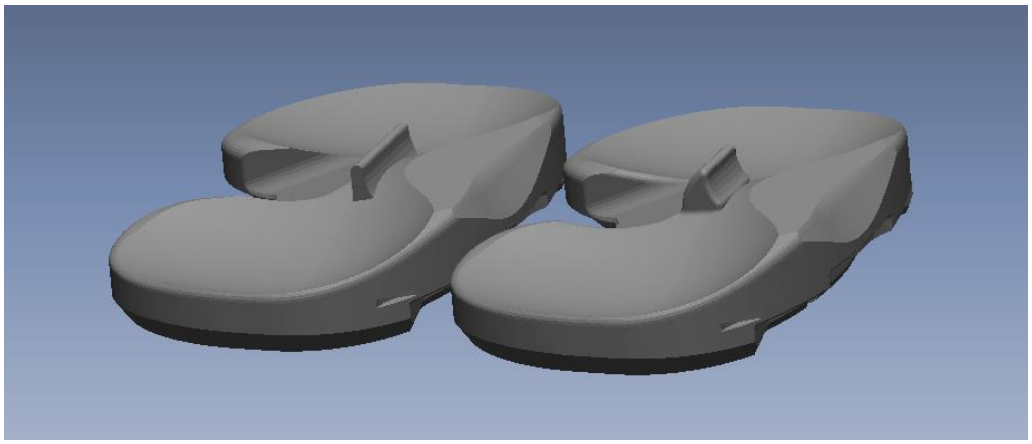

Figure 147: ASTKA_R2_V1 featured a more feasible post shape.

ASTKA_R2_V3 were created by shifting the post 3 mm anteriorly and 3 mm posteriorly, respectively (Figure 148). The rationale of these models is that a more anterior post will force the condyles more anterior as well.

Moving the post anteriorly or posteriorly resulted in medial and lateral starting positions shifting anteriorly and posteriorly, respectively. The ASTKA_R2_V1 had a starting position of 0 mm on both the lateral and medial side (Figure 149 & Figure 150). The design with the anterior post started at 3 mm anterior on the lateral side and 2.5 mm anterior on the medial side. The posterior post design started at -2.4 mm on the lateral side and -2 mm on the medial side. The axial rotations started at essentially 0° for both the neutral and posterior posts and approximately 1° of internal rotation for the anterior post (Figure 151).

Low Rotation simulations

The boundary conditions were modified to produce a second knee implant subject who produced less axial rotation, more typical of what is seen in the average PCR TKA subject. Then, the subject was also implanted with a Modified ASTKA. The defining feature of this ASTKA was a rotated post with the lateral portion of the post more anterior than the medial portion of the post. The hypothesis is that this will hold the knee in internal rotation in extension and allow it to go into external rotation in deeper flexion. The PCL tension was adjusted to be tighter in the ASTKA subject because there is little risk of the knee sitting posterior in extension as the cam/post mechanism holds it forward.

The modified ASTKA was successful in creating a more internally rotated starting position (Figure 152). While the PCR TKA started in a neutral position, the modified ASTKA started at 6.8° of internal rotation. Both implants ended with between 1.5° and 2.0° of external rotation. Overall, the modified ASTKA had 8.5° of external rotation during the activity while the PCR implant had 2.0°. The modified ASTKA started

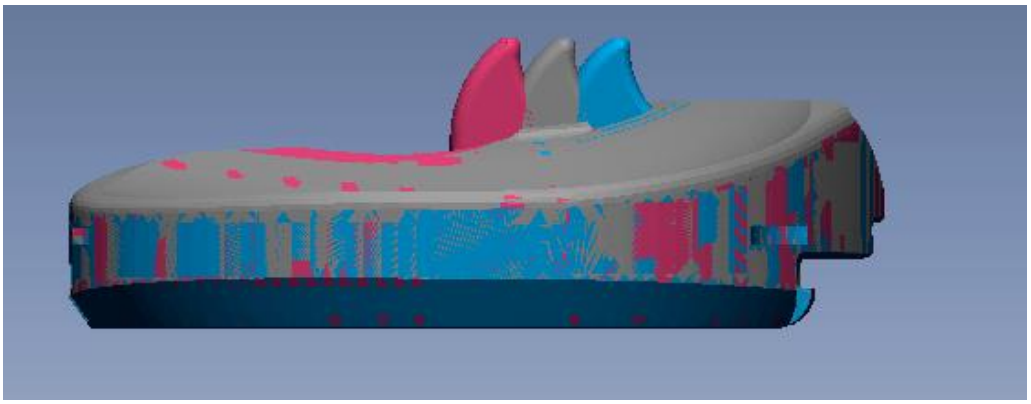

Figure 148: ASTKA_R2_V2&V3 shifted the post anterior and posterior by 3mm.

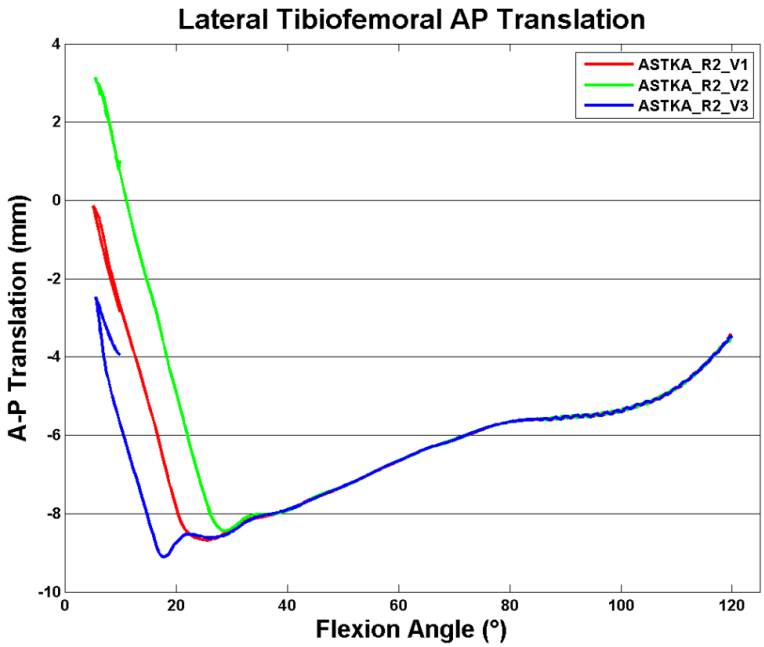

Figure 149: More anterior post positions resulted in more anterior translations of the lateral condyle.

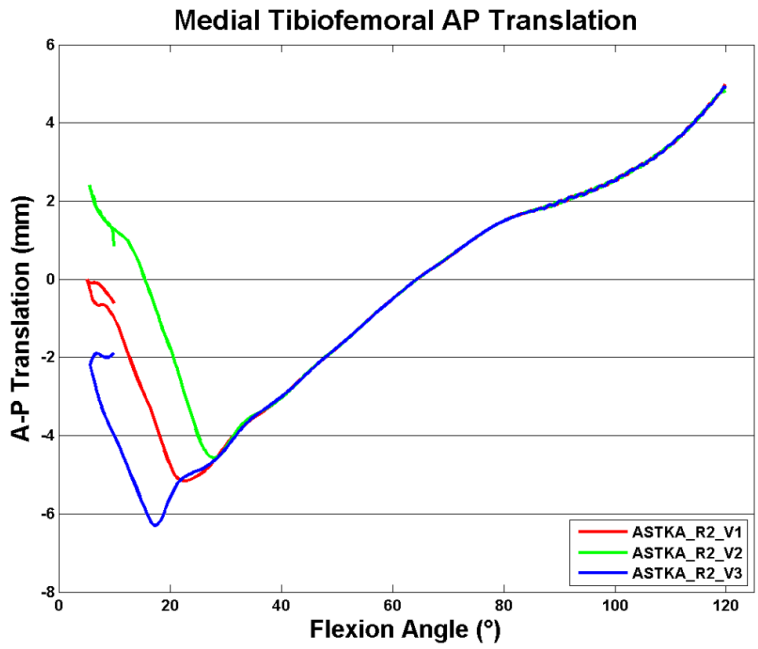

Figure 150: More anterior post positions resulted in more anterior translations of the medial condyle.

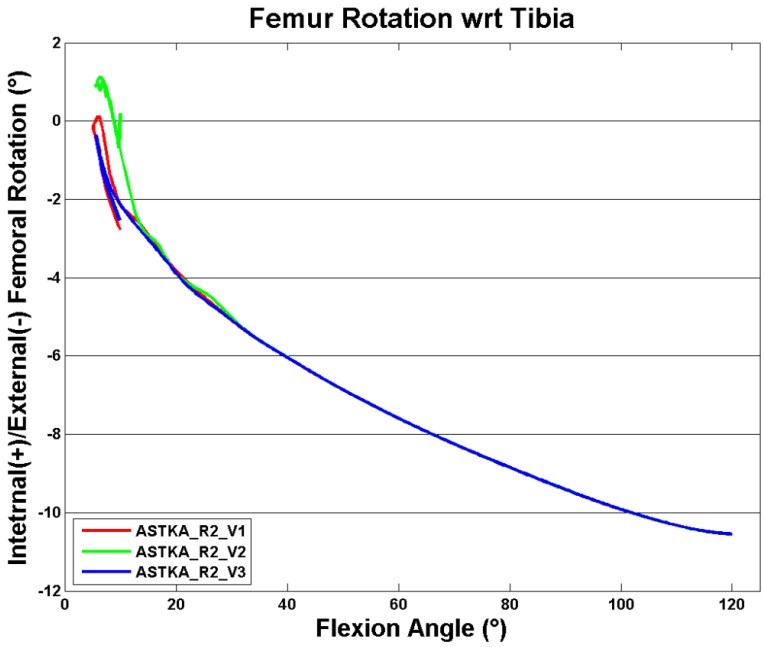

Figure 151: The anterior post design started more internally rotated than the other designs.

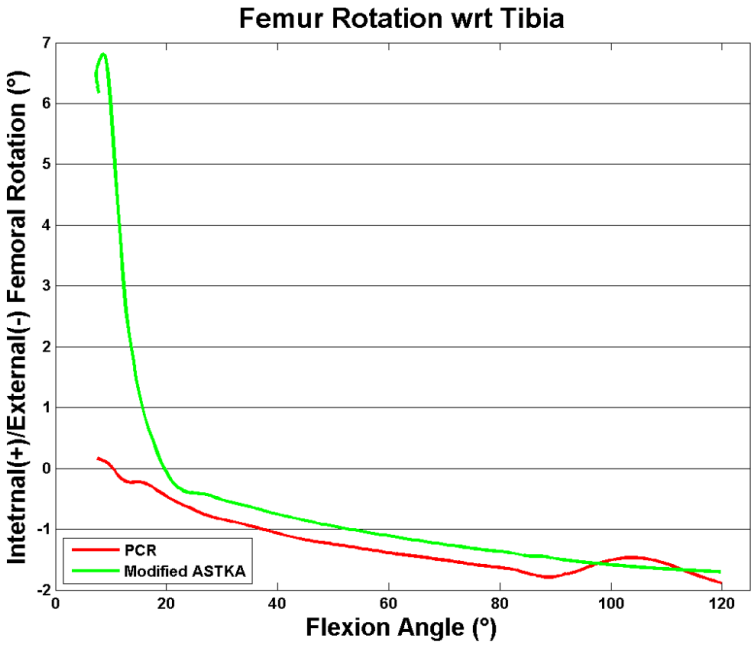

Figure 152: The modified ASTKA started considerably more internally rotated than the PCR model.

more anterior than the PCR. The lateral condyle of the Modified ASTKA started at 5.5 mm while the PCR started -3.5 mm (Figure 153). They both rolled to -8 mm in early flexion. The modified ASTKA ended at -2.5 mm while the PCR ended at -5.2 mm. The effect was less pronounced on the medial side (Figure 154). The modified ASTKA started in a neutral position with the PCR setting at -3.7 mm. They both rolled posteriorly to approximately -7.5 mm. Then, the modified ASTKA ended at -1.2 mm, and the PCR TKA ended at -3.6 mm.

The knee forces had similar profiles for both implants with the maximum force being approximately 5x BW (Figure 155). The Modified ASTKA did display somewhat higher forces for the first 30° of flexion. The LCL had more force in the modified ASTKA, reaching 0.35 x BW in the modified ASTKA and only 0.08 x BW in the PCR TKA (Figure 156). The MCL forces peaked between 0.40 x BW and 0.45x BW for both implants (Figure 157). Finally, the PCL force was considerably higher in the modified ASTKA, owing both to the more anterior location of the implant and the tighter PCL in the simulation (Figure 158). The PCL in the modified ASTKA ranged between 0.25 and 0.9 x BW for the entire activity. This force remained under 0.25 at all times in the PCR with the force at 0 in early flexion. It is likely this force should be non-zero in the native knee in early flexion as the ACL and PCL would be in opposition.

ASTKA_R3

Next, ASTKA_R3_V1 was created by modifying ASTKA_R2_V1. The femur was modified by making the inferior-posterior portion of the femoral condyles larger (Figure 159). The polyethylene from ASTKA_R2_V1 was modified by making the post flat. This change was done so the bottom rounded portion of the post would not act as a pseudo third condyle causing potential lift-off in full extension (Figure 160). Additionally, the anterior portion of the polyethylene was flattened to avoid the femur being wedged between the post and the anterior lip. The cam/post mechanism was lateralized 3 mm for these simulations (Figure 161). This model was run with the baseline anterior cam/post position.

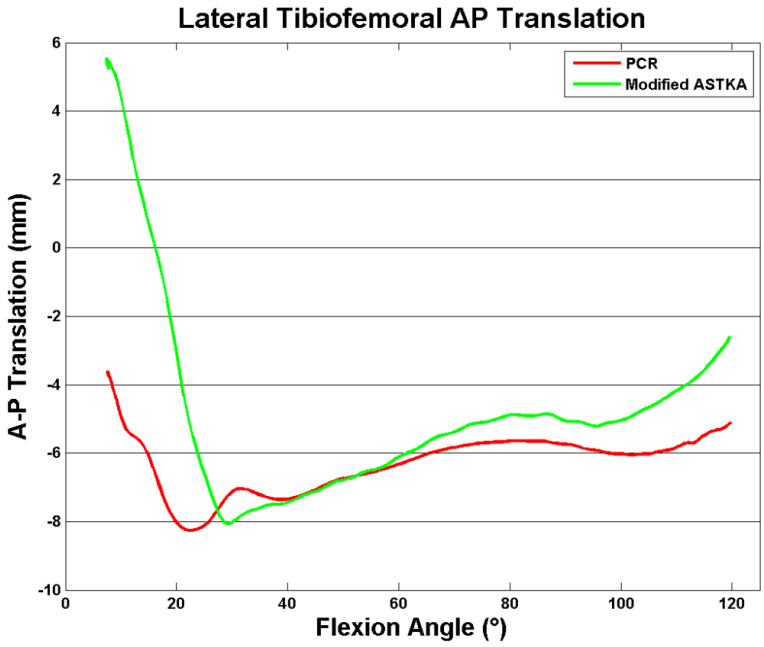

Figure 153: The lateral condyle was considerably more anterior for the modified ASTKA than the PCR design

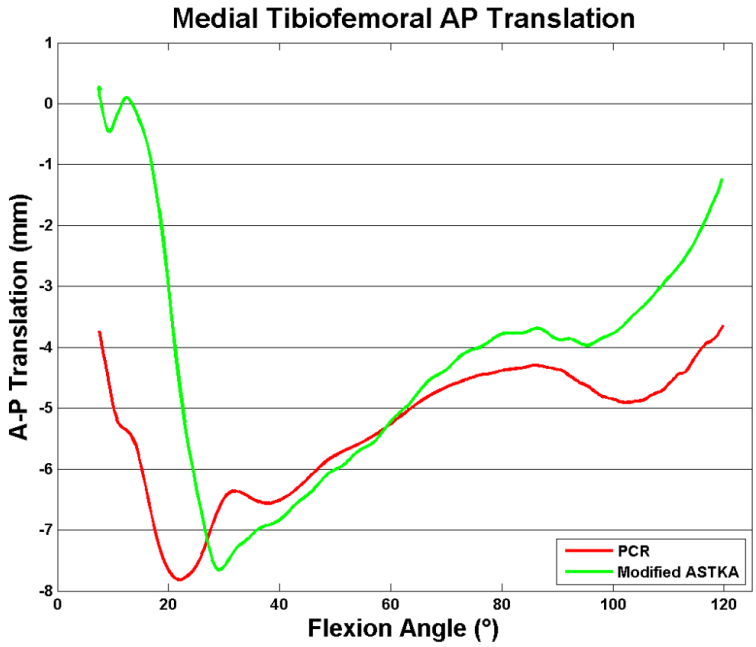

Figure 154: The medial condyle was considerably more anterior for the modified ASTKA than the PCR design.

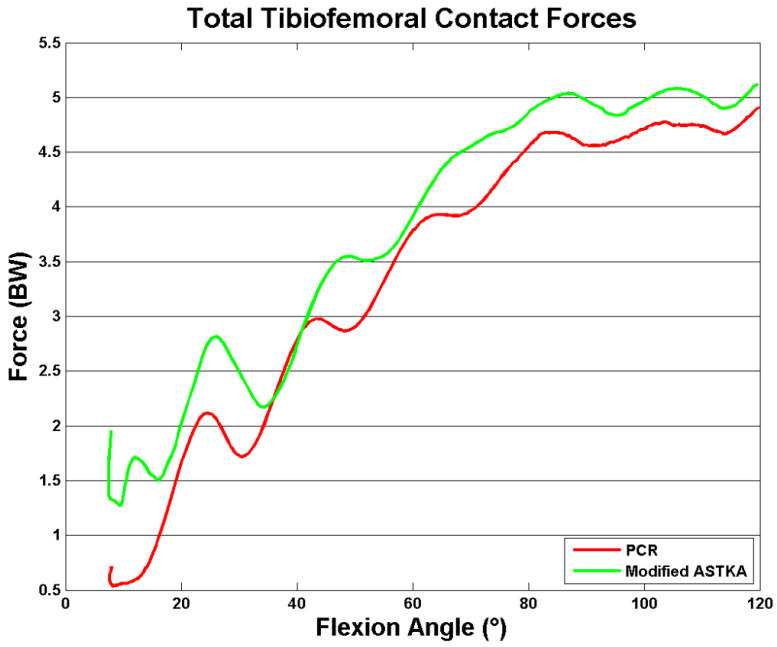

Figure 155: The knee forces were similar for both the modified ASTKA and the PCR TKA.

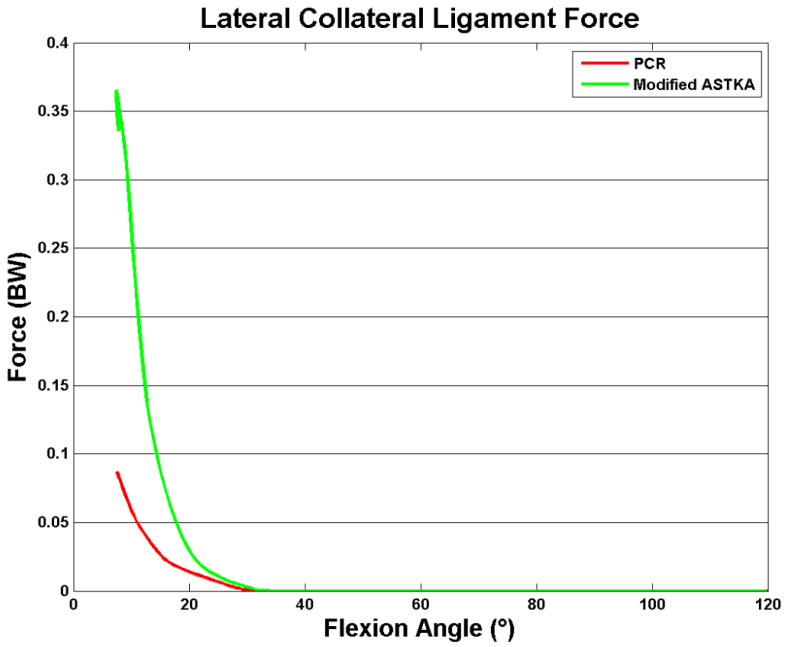

Figure 156: The knee forces were higher for the LCL with the modified ASTKA than with the PCR TKA.

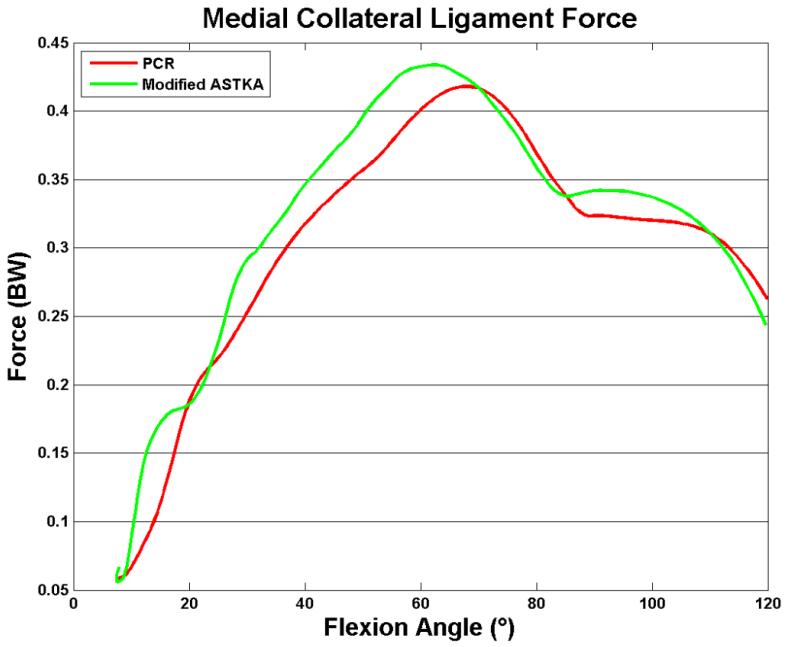

Figure 157: The modified ASTKA and PCR TKA had similar MCL forces.

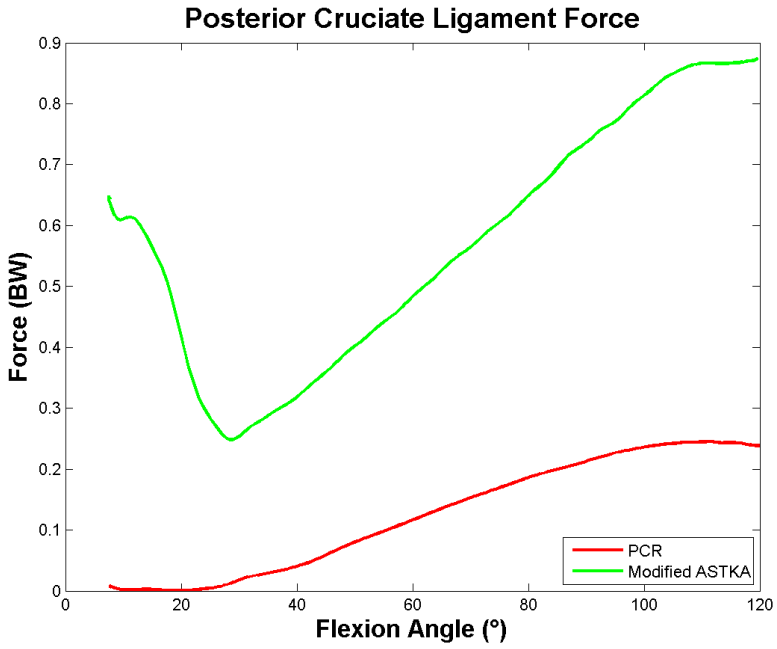

Figure 158: The PCL forces are considerably higher in the modified ASTKA than in the PCR.

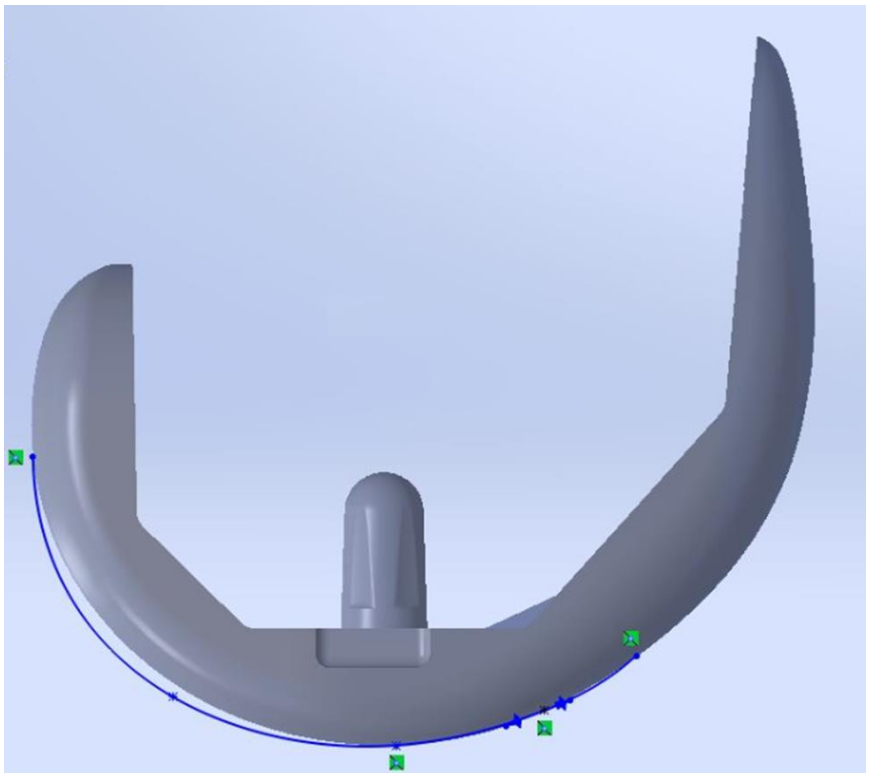

Figure 159: The femur of ASTKA_R2_V1 is shown. The blue line shows the geometry of the femoral component of ASTKA_R3_V1.

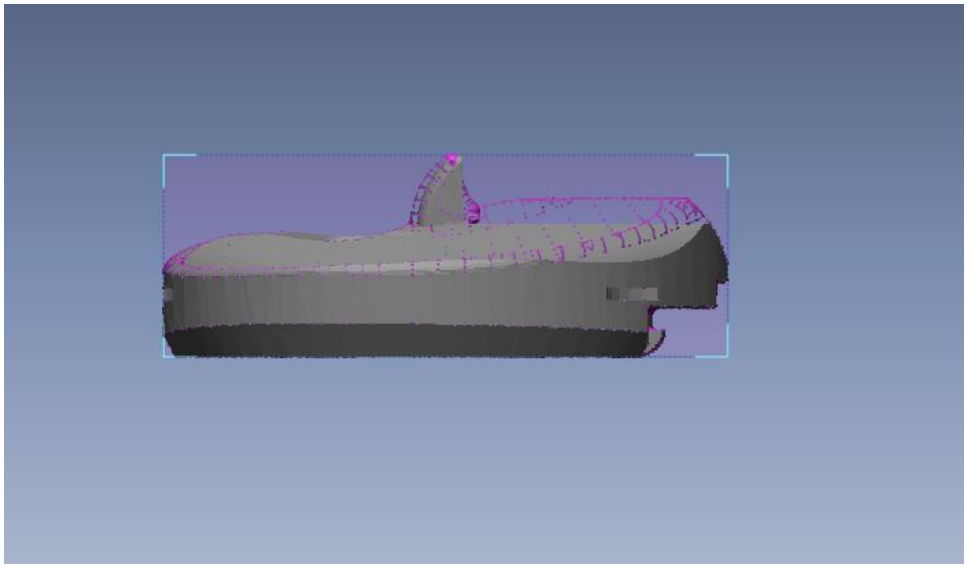

Figure 160: The post of ASTKA_R2_V1 (purple point cloud) was flattened and the anterior lip was reduced in height to produce ASTKA_R3_V1 (Gray Surface).

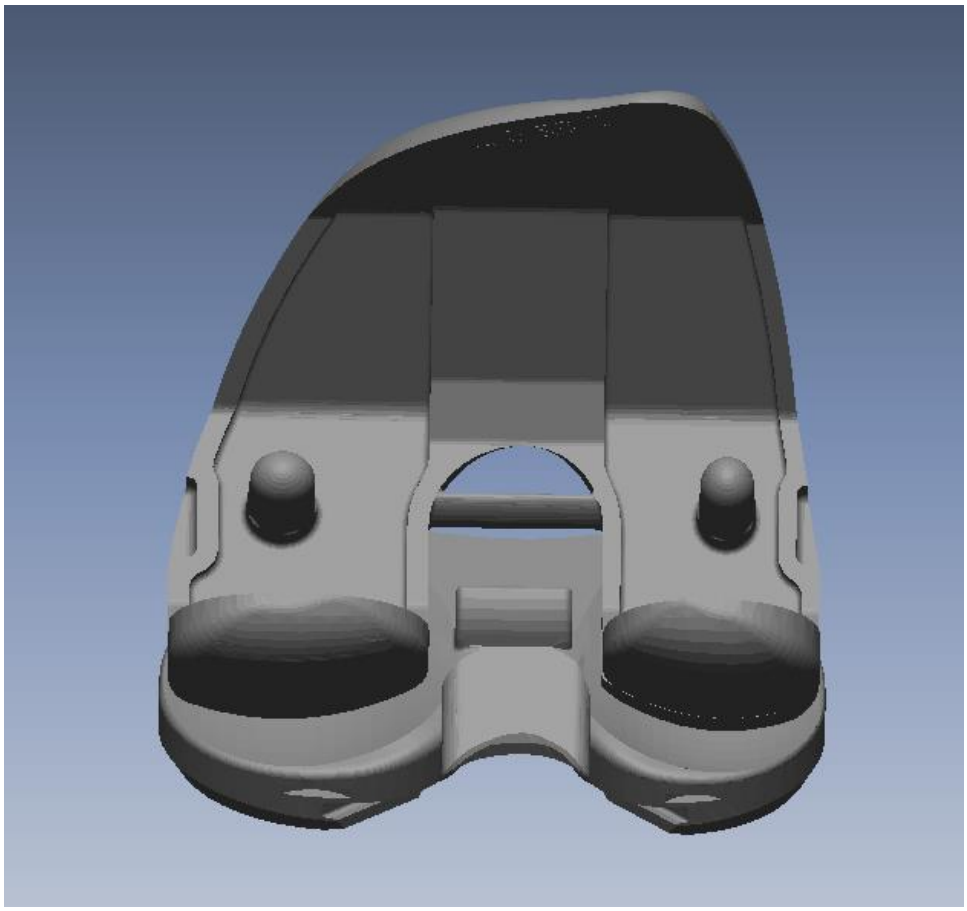

Figure 161: The cam and post mechanism for ASTKA_R3_V1 is lateralized 3 mm.

Then, CAD models were generated for both the cam and post 3 mm anterior and for the cam and post 3 mm posterior. Finally, all 3 femoral condyles were tested with each polyethylene component for a total of 9 simulations. These were the first simulations to feature full contact detection using a point cloud on the femur (Figure 11).

These simulations started at 55° of flexion and went to full extension. As expected, moving the post anteriorly or the cam posteriorly resulted in more anterior translation of the condyles and more internal rotation with extension (screw-home mechanism). Interestingly, whether the cam was moved anteriorly 3 mm or the post was moved posteriorly 3 mm, the results were essentially identical. Therefore, essentially 5 different groups appear in the simulation as follows:

- Group 1: Anterior Cam/Posterior Post: Lowest Cam Forces and Least Anterior Translation.
- Group 2: Middle Cam/Posterior Post and Anterior Cam/Middle Post: Second Lowest Cam Forces and Anterior Translations
- Group 3: Anterior Cam/Anterior Post, Middle Cam/Middle Post, Posterior Cam/Posterior Post: Median Cam Forces and Anterior Translations.
- Group 4: Posterior Cam/Middle Post and Middle Cam/Anterior Post: Second Highest Cam Forces and Anterior Translations
- Group 5: Posterior Cam/Anterior Post: Highest Cam Forces and Anterior Translations

Group 1 experienced no noticeable cam forces, with the only interaction occurring at less than 5° of flexion (Figure 162). Group 2 first had cam/post contact at 9° of flexion and ended with 0.11 x BW. Group 3 engaged at 17° of flexion and reached 0.23 x BW. Group 4 contacted at 24° of flexion and reached 0.47 x BW. Group 5 had cam/post contact at 35°, and forces reached 0.96 x BW.

Moving the post anteriorly or the cam posteriorly caused more internal rotation with extension. Group 1 had -3.3° rotation at full extension (Figure 163). For Group 2, this increased to -3.0° of internal rotation. Groups 3, 4, and 5 had -1.6°, -0.9°, and -0.4° of internal rotation at maximum extension, respectively.

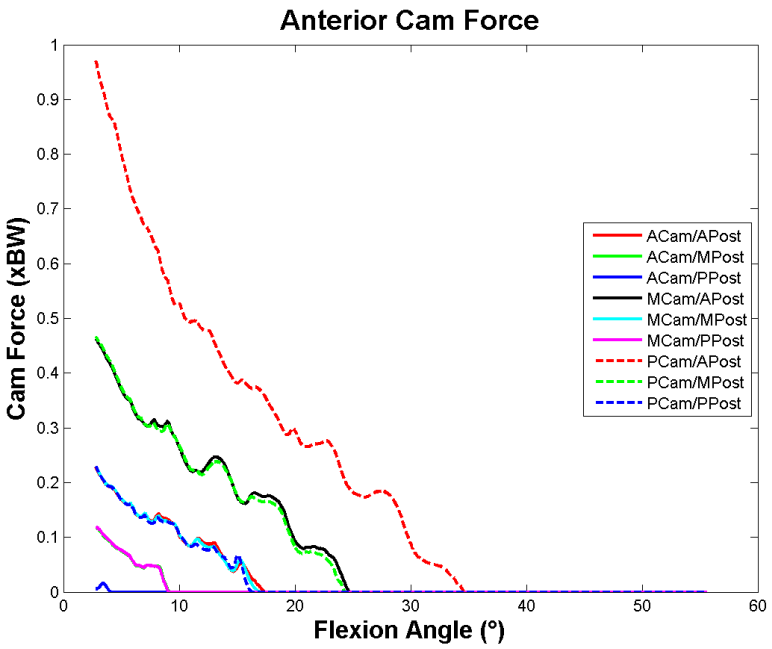

Figure 162: For ASTKA_R1_V3, moving the post anterior or the cam posterior resulted in more anterior cam force.

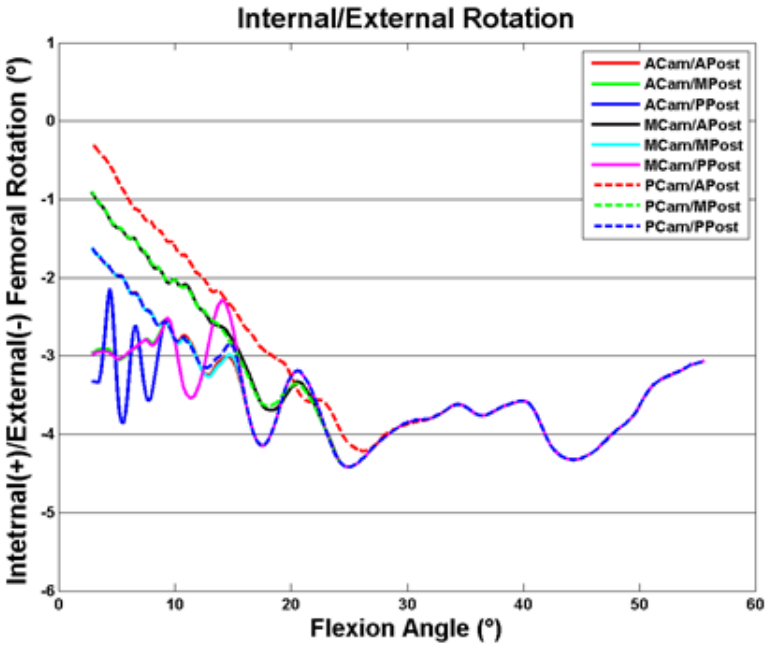

Figure 163: For ASTKA_R1_V3, moving the post anterior or the cam posterior resulted in more internal rotation with extension.

The lateral condyle of all simulations remained between 6.5 mm and 8.0 mm posterior from the beginning of the simulation at 55° until the cam post mechanism engaged (Figure 164). For Group 1, there was no noticeable effect. Group 2 translated from -7 mm at cam post contact to -4.3 mm at full extension. Group 3 translated from -7 mm at cam post contact to -1 mm at full extension. Group 4 reached 2.4 mm at full extension, while Group 5 made it a full 5.5 mm anterior. It is worth nothing that there was just slightly more than 3 mm difference between the ending positions of each group, which is the difference in the cam post position. It appears there is nearly a 1-to- 1 relationship between the amount the post is shifted and the amount the lateral condyle translates.

The medial condyles for all groups stayed between -3 and -5 mm from 50° until cam/post contact (Figure 165). Group 1 ended at -4.7 mm with no noticeable effect from the cam/post mechanism. Group 2 reached -2 mm at maximum extension. Group 3 translated to 0.5 mm anterior at full extension. Group 4 and 5 obtained translations of 3.0 mm and 5.5 mm, respectively, at full extension. It is worth nothing that there is a difference of roughly 2.5 mm between consecutive groups. Since the lateral condyle moves more than 3 mm anteriorly with each successive group while the medial condyles moves closer to 2.5 mm more anterior, each successive group is more internally rotated at full extension (screw-home mechanism). The increasing PCL force may be causing this increased internal rotation.

PCL forces at maximum extension increased from Groups 1 to 5 (Figure 166). The PCL force went to 0 x BW for Group 1. For Groups 2 through 5, 0.02 x BW, 0.06 x BW, 0.13 x BW, and 0.20 x BW. It is likely that these increasing forces cause increasing internal rotation with extension because the PCL originates medially in the intercondylar area. If this is the case, the anterior post is replicating the ACL in function and restoring more normal kinematics patterns. However, the increased anterior translation also results in increased MCL and LCL forces (Figure 167 & Figure 168). The MCL force was 0.11 x BW, 0.11 x BW,

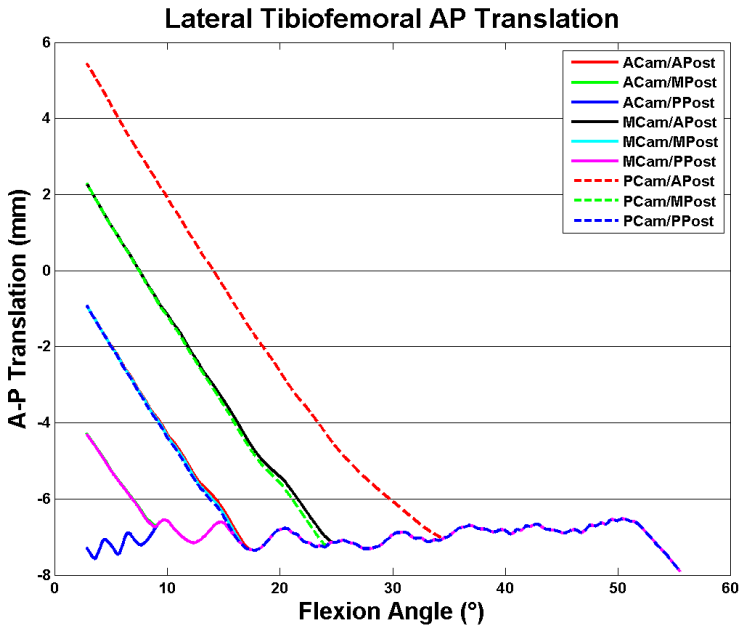

Figure 164: For ASTKA_R1_V3, moving the post anterior or the cam posterior resulted in more lateral condyle translation.

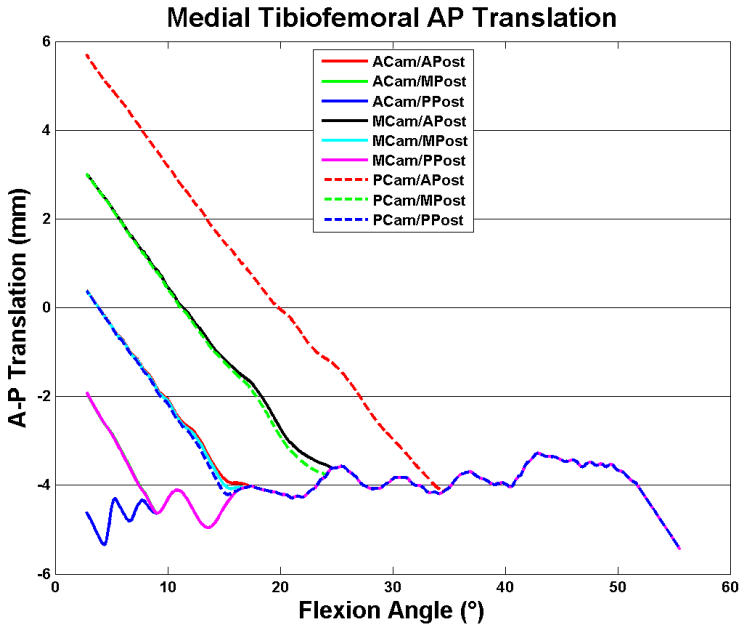

Figure 165: For ASTKA_R1_V3, moving the post anterior or the cam posterior resulted in more medial condyle translation.

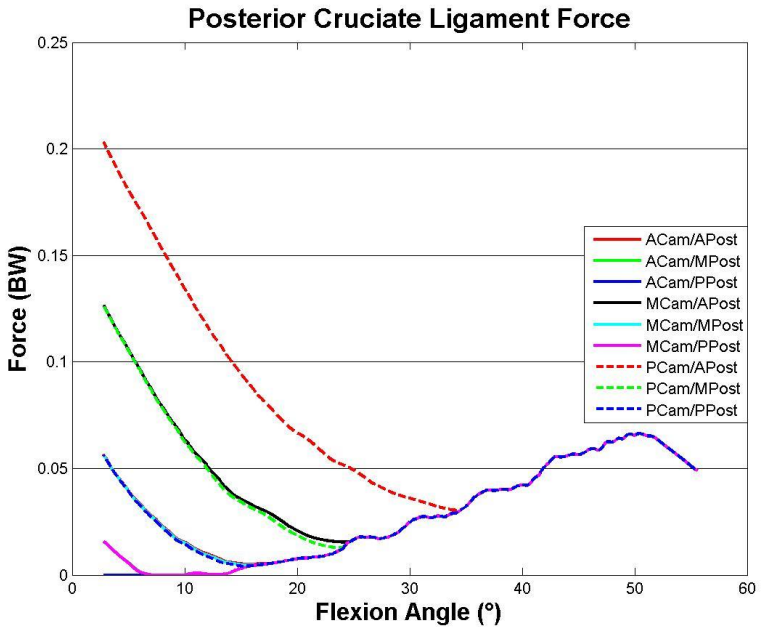

Figure 166: For ASTKA_R1_V3, moving the post anterior or the cam posterior resulted in more PCL force at full extension.

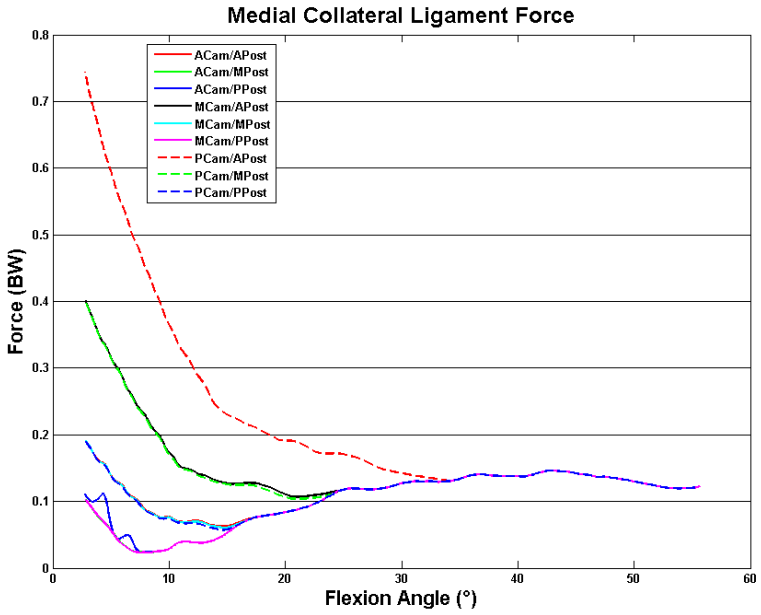

Figure 167: For ASTKA_R1_V3, moving the post anterior or the cam posterior resulted in more MCL force at full extension.

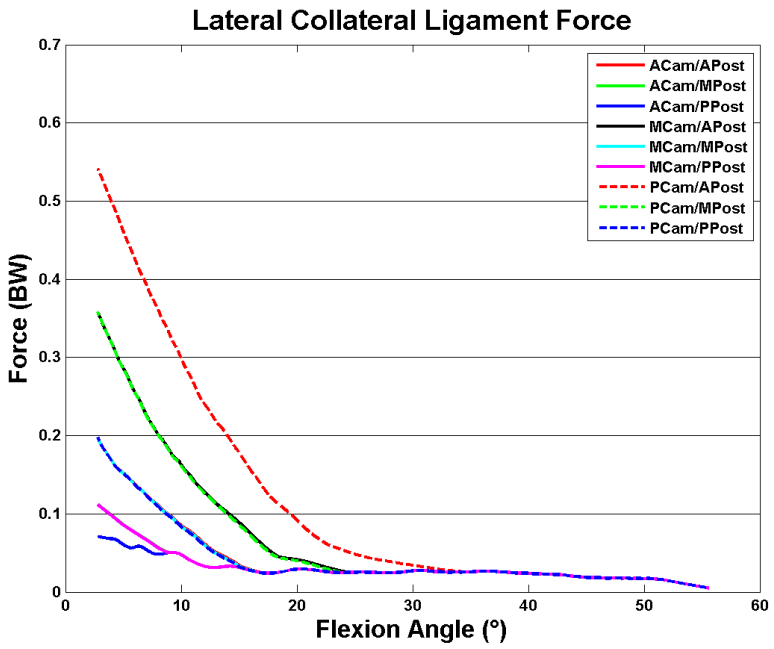

Figure 168: For ASTKA_R1_V3, moving the post anterior or the cam posterior resulted in more LCL force at full extension.

0.19 x BW, 0.40 x BW and 0.75 x BW for Groups 1 through 5, respectively. At full extension, LCL forces reached 0.07 x BW, 0.11 x BW, 0.2 x BW, 0.36 x BW, and 0.54 x BW for Groups 1 through 5, respectively.

Summary

The first simulation featuring a PCR design with an added anterior cam/post demonstrated that an ASTKA was effective in moving the tibiofemoral contact point anteriorly in full extension. Therefore, the ASTKA creates more posterior rollback in flexion which leads to more normal kinematic patterns. Secondly, the femoral condyles were not only more anterior in extension but also more internally rotated. This TKA design lead to the screw-home mechanism being restored. Finally, the model revealed that moving the post anteriorly is equivalent to moving the cam posteriorly for most considerations. This information will aid in designing future ASTKAs to fit the various soft tissue constraints of the human knee and to be easier to implant.

Conformity Variations

To analyze the effect of varying conformity, a new ASTKA was developed with a rounded post (Figure 169). The cam and post were shifted both anteriorly and posteriorly to produce 9 simulations, as with ASTKA_R3_V1. These simulations were then repeated with both the medial and lateral plateau completely flat to see the effect of the anterior post mechanism with no polyethylene geometry constraints (Figure 170). Finally, the simulations were repeated with a flat lateral plateau and increased conformity on the medial plateau in an attempt to generate more medial pivot-like kinematics (Figure 171). These were the first simulations to feature convex hulls (Figure 26).

While 9 simulations were run in total for each polyethylene with different cam and post locations, the reporting focuses on 2 of those variations. First, the central cam with central post is discussed. This represents a moderate amount of cam and post interaction, and the results are only negligibly different

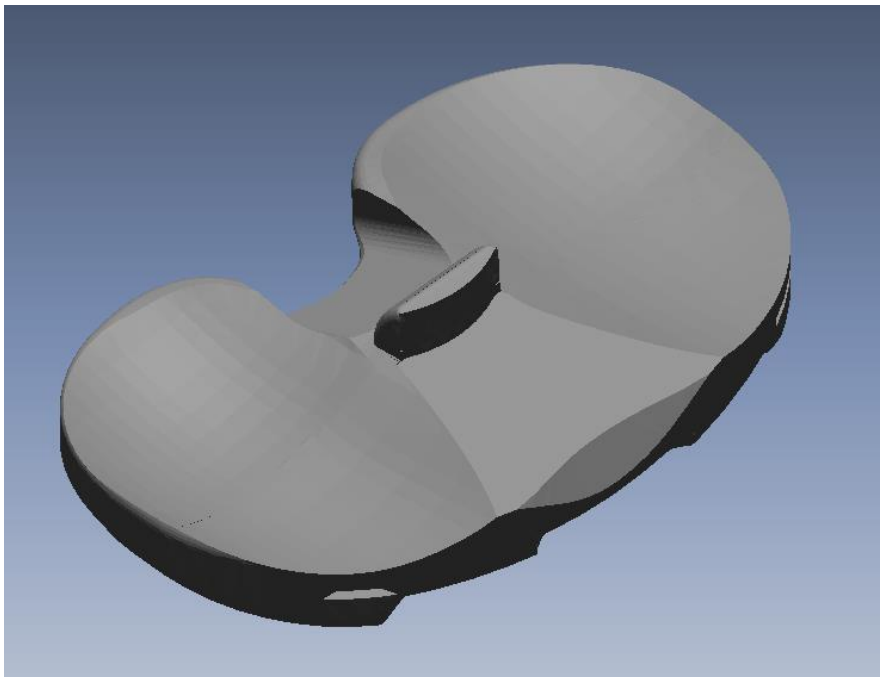

Figure 169: The original design is shown.

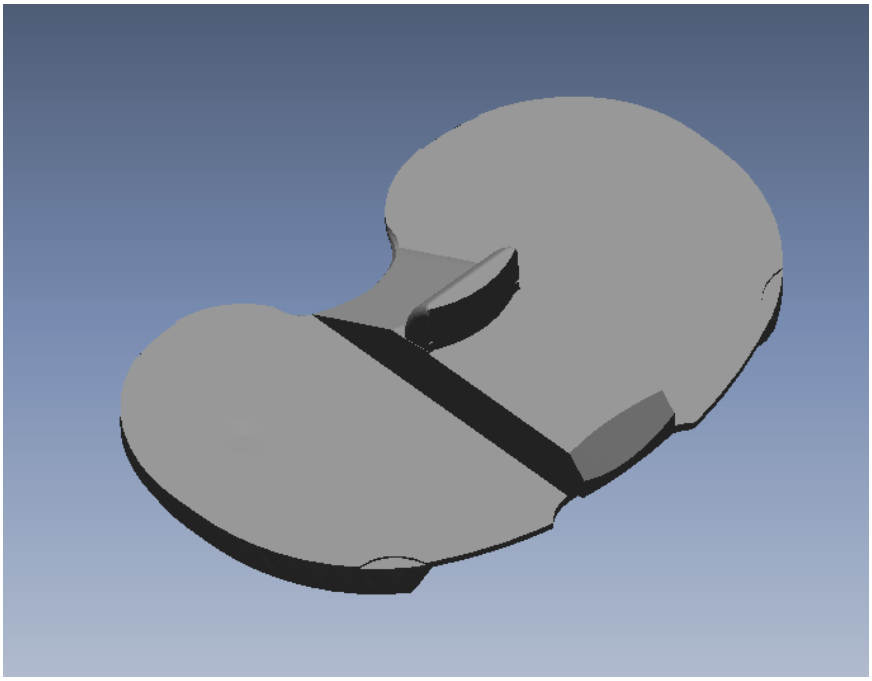

Figure 170: The original design was modified by making both polyethylene plateaus flat.

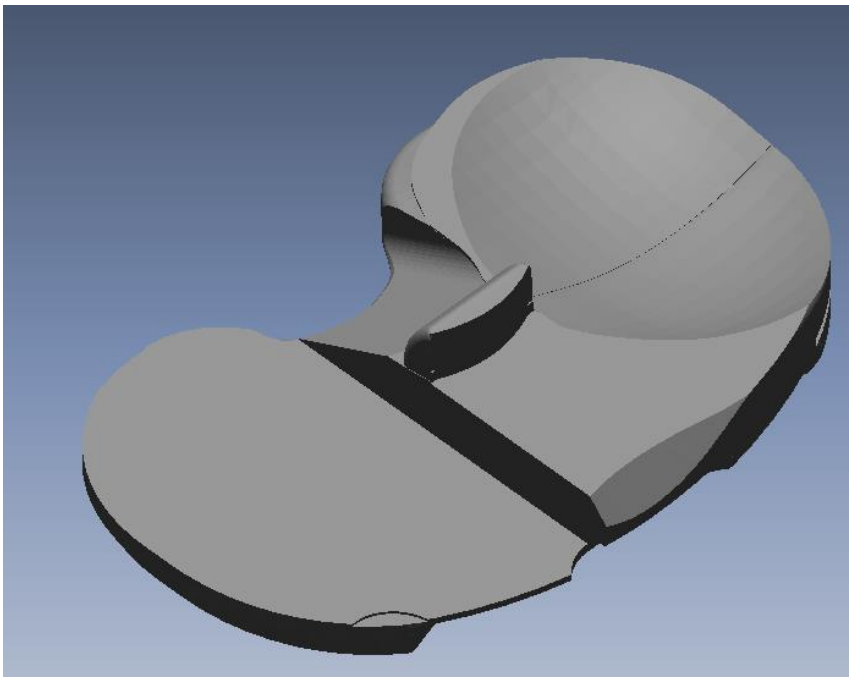

Figure 171: The lateral plateau remains flat while the medial plateau had the conformity increased beyond that of the original.

for both the anterior cam with anterior post and posterior cam with posterior post simulation. Second, the results are reported for the posterior cam with the anterior post. This simulation generates the most cam and post interaction and clearly shows the interplay between geometry and cam/post interactions. These simulations started at 55° of flexion and simulated rising from a deep knee bend to full extension.

Center Positioned Cam Center Positioned Post Simulations

First, the anterior cam force is examined. This shows when the cam/post engaged and aids in interpreting the other results. The original design engaged at 18° and increased in a roughly linear fashion with extension to 0.23 x BW (Figure 172). The simulation in which both polyethylene plateaus are flat engaged at 8° and reached a peak force of 0.08 x BW. The simulation of the medial conforming simulation also engaged at 8°. However, it reached a peak for 0.19 x BW.

The medial plateau of the original design started at 7 mm posterior and quickly slid to approximately 5 mm posterior by 50° of flexion where it remained until 20° of flexion (Figure 173). During the end of the activity where the cam/post mechanism engaged, it slid to 0.5 mm anterior. The simulation with both plateaus flat also started at 7 mm posterior but slid to 3 mm posterior by 45° of flexion, where it remained until roughly 20° of flexion at which point it slid anteriorly to a neutral position. The conforming medial plateau held the medial condyle much more anterior starting at 3.6 mm posterior, moving to 2 mm posterior by 50° of flexion and holding until 30° of flexion. It rolled slowly to a neutral position from there.

The lateral plateau of the original design started at 7.0 mm posterior (Figure 174). Then, it slid forward to 5.5 mm posterior at 50° of flexion. Then, it slid posterior to 7.0 mm again at 18° of flexion. It moved forward to 1.2 mm posterior at full extension. The polyethylene that was flat on both sides also started 7.0 mm posterior before translating forward to 2.9 mm posterior at 45° of flexion. The lateral plateau

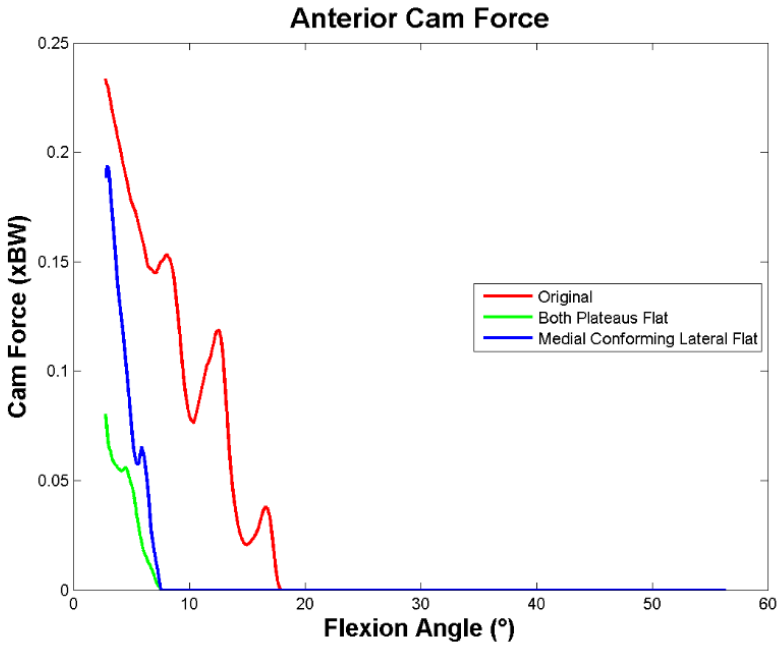

Figure 172: The anterior cam and post interaction forces are shown for the Center Cam Center Post simulations.

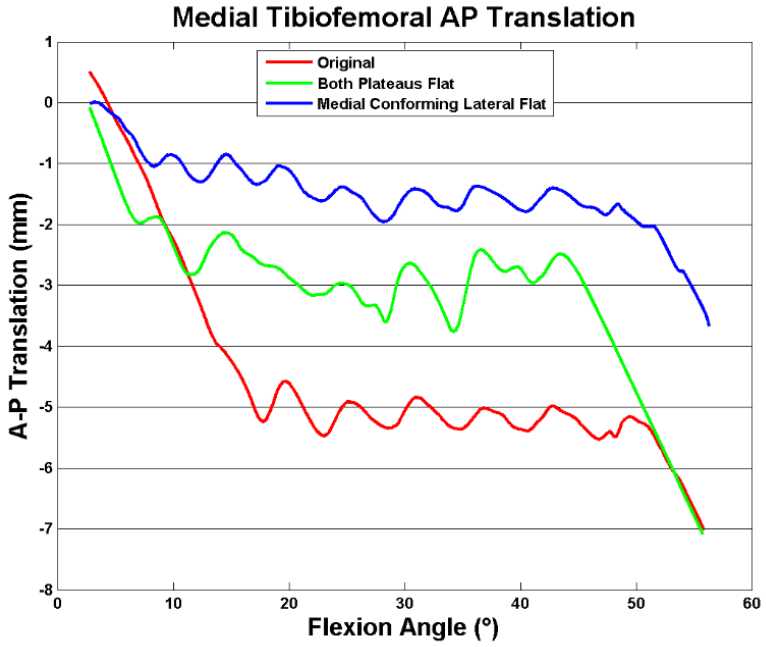

Figure 173: The medial contact point translations are shown for the Center Cam Center Post simulations.

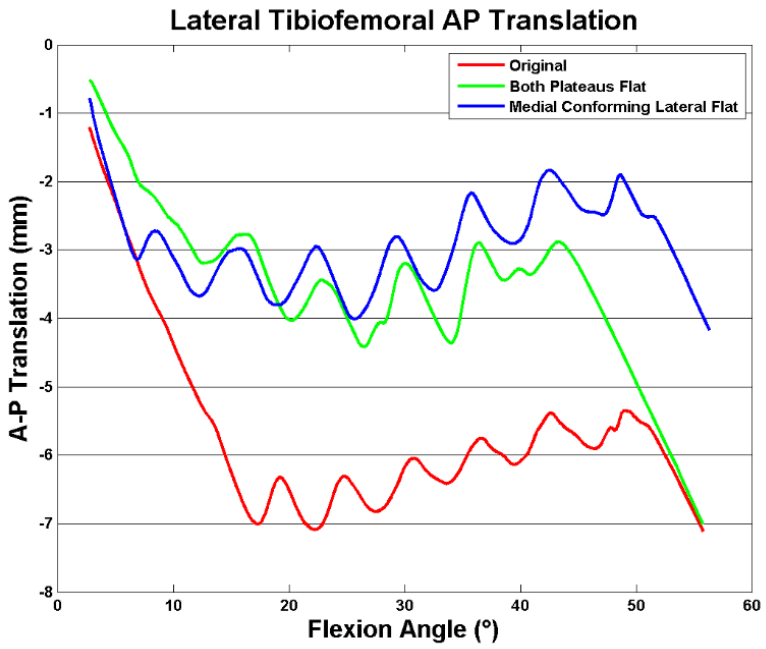

Figure 174: The lateral contact point translations are shown for the Center Cam Center Post simulations.

then slid slightly posterior, oscillating around 4 mm posterior at 25° of flexion before moving anterior to 0.5 mm posterior at full extension. The simulation with the highly conforming medial plateau had a lateral condyle which started at 4.2 mm posterior before translating to 1.9 mm posterior at 50° of flexion. It then oscillated between 3 mm and 4 mm posterior a 25° before translating anteriorly to end the simulation at 0.8 mm posterior.

The original simulation started at roughly -1.2° of internal rotation, rotated to -0.6° at 30° of flexion, and then ended at -0.8° (*Figure 175*). With both the medial and lateral plateaus flat, the simulation started at -1.0°. It rotated internally for most of extension reaching 1.7° of internal rotation at 8° of flexion when the cam engaged. Then, it rotated externally to 0.8° of internal rotation. The simulation with the conforming medial plateau started at -1.8° of internal rotation before rotating to 0.4° at 30° of flexion. It then rotated to -1.5° at 8° of flexion when the cam post engaged. In the final degrees of extension, the post forced the femur to internally rotate to 0.3° of internal rotation. The medially conforming design had very large oscillation in the rotation. This is likely because the medial condyle was held roughly in place by the conforming polyethylene while the lateral condyle was free to oscillate on the flat lateral plateau.

Posterior Positioned Cam Anterior Positioned Post Simulations

The effect of design conformity became much more obvious when the anterior cam/posterior post design was analyzed. First, cam engagement occurred much earlier and resulted in higher forces. The original design engaged at 35° of flexion and had a peak force of 0.9 x BW (Figure 176). In the simulation with both plateaus flat, cam/post engagement occurred at 28° of flexion and had a peak force of 0.4 x BW. The peak force is most likely lower because the post is not pushing the condyles onto the anterior lip of the polyethylene. The medial conforming simulation engaged at 23° of flexion and had a peak

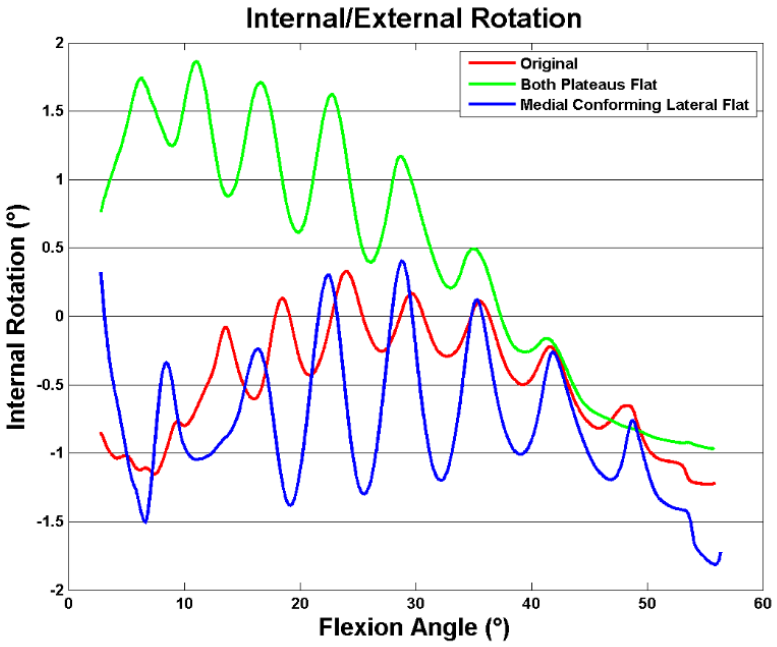

Figure 175: The internal rotation of the femoral components is shown for the Center Cam Center Post simulations.

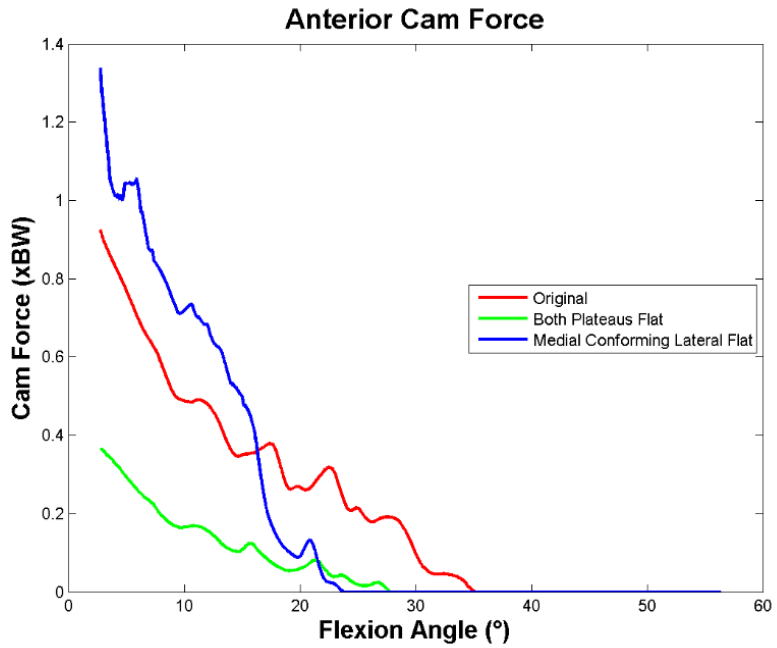

Figure 176: The anterior cam and post interaction forces are shown for the Posterior Cam Anterior Post simulations.

force of 1.35 x BW. The higher peak force is a result of the cam/post mechanism driving the medial contact point onto the highly conforming anterior lip on the medial plateau.

The medial condyle started in the same location as the previous simulations with the central cam and post. The original simulation, both plateaus flat simulation, and medial conforming simulation were at 7 mm, 7 mm, and 3.6 mm posterior, respectively (Figure 177). The original geometry experienced a steady anterior roll from the time the cam engaged at 35° of flexion until full extension, ultimately reaching 5.0 mm anteriorly. The simulation with flat polyethylene plateaus performed as it did previously until the cam engaged at 28° of flexion. Then, it translated anteriorly to 5.5 mm anterior at full flexion. When the cam for the medially conforming simulation reached 23° of flexion, the medial condyle translated from 1.8 mm posterior to 0.5 mm anterior where it remained with minimal movement for the rest of the simulation.

*The lateral condyle had fairly similar translations for all three designs. The original design and the design with both polyethylene plateaus flat each started at 7 mm posterior while the medially conforming design started at 4.2 mm posterior (*Figure 178*). The simulations behaved as they did in the center cam center post until the cam/post mechanism engaged. Then, all simulations rolled forward with the* original design and the flat plateaus design each reaching roughly 5.3 mm anterior. The medially conforming design reached 7.8 mm anterior.

The original, flat plateaus, and medial conforming designs started at -1.2°, -1.0°, and -1.8° of internal rotation, respectively (Figure 179). The original and flat plateaus design rotated internally during extension ending at 1.8° and 0.8°, respectively. The medial conforming design slowly rotated externally until the cam/post mechanism engaged at 23°, at which point the femur rapidly rotated internally to 10°. This was caused by the medial condyle being held posterior by the conforming design while the lateral condyle was driven anteriorly by the post.

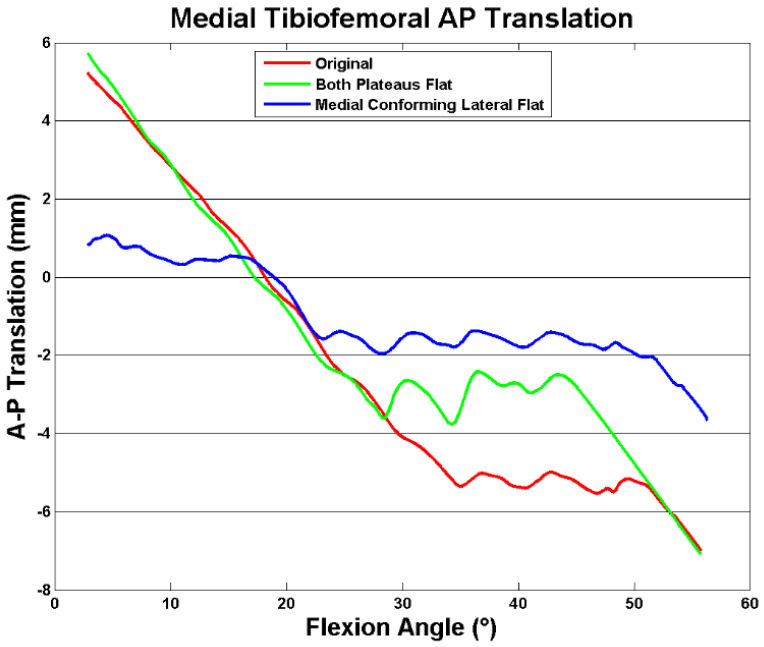

Figure 177: The medial contact point translations are shown for the Posterior Cam Anterior Post simulations.

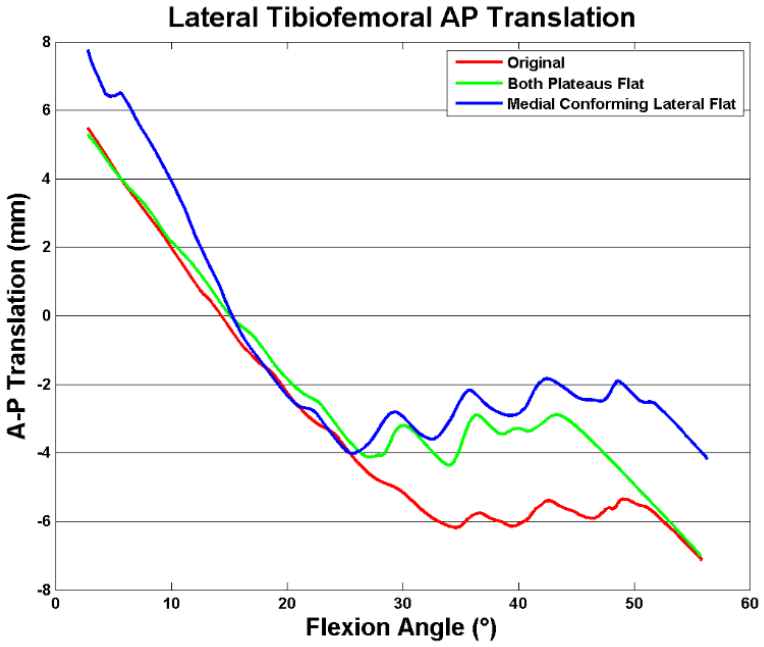

Figure 178: The lateral contact point translations are shown for the Posterior Cam Anterior Post simulations.

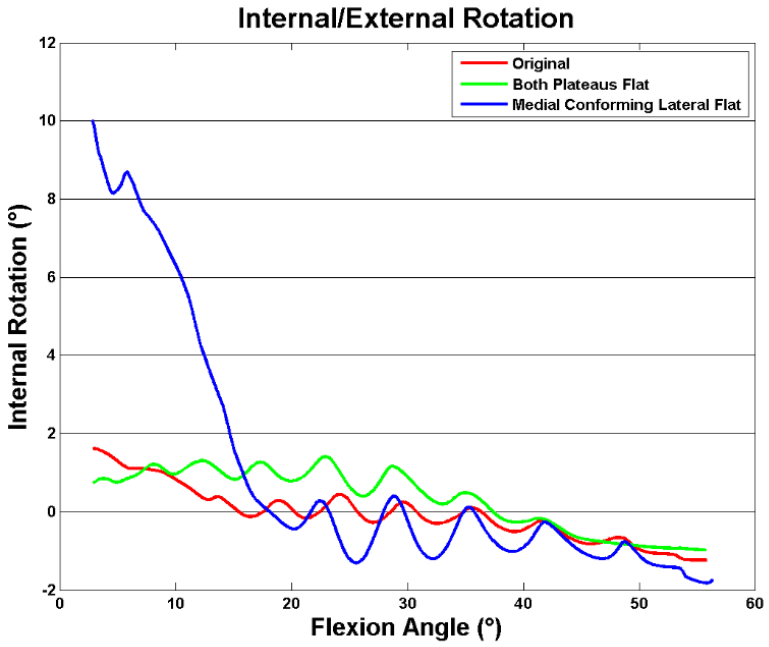

Figure 179: The internal rotation of the femoral components are shown for the Posterior Cam Anterior Post simulations.

PS-TKA Post Comparison

In addition to analyzing the effect of anterior cam placement and shape, the effect of posterior cam shape was analyzed. Simulations were performed for two PS-TKA designs (PS1, PS2). The analysis focused on the location of cam contact on the post a deep knee bend. PS1 was known to have superior slide of the contact on the post from fluoroscopic studies while the PS2 was designed to eliminate this effect.

The cam/post engagement pattern of the PS1 and PS2 were compared during a flexion-only deep knee bend simulation. Both designs engaged at approximately 70° of flexion (Figure 180). From there, the cam force increased roughly linearly with flexion. PS1 had a peak force of 1.5 x BW while the PS2 peaked at 1.3 x BW. The implants had very similar force patterns with the exception of the PS1 having slightly higher forces.

While the total force is similar, the contact maps on the polyethylene are quite different. Previous studies have shown that the contact slides superiorly on the post in late flexion with the PS1. PS2 was designed to have the contact slide down the post with flexion. The simulations produced the expected patterns. The PS1 contacted superiorly on the post then slid posteriorly from 80° of flexion to 100° of flexion (Figure 181). Then, it remained mostly stationary until 110° of flexion. For the final 10°, the contact started to move superiorly again. The contact started superiorly on the PS2 post and slid inferiorly for all of flexion.

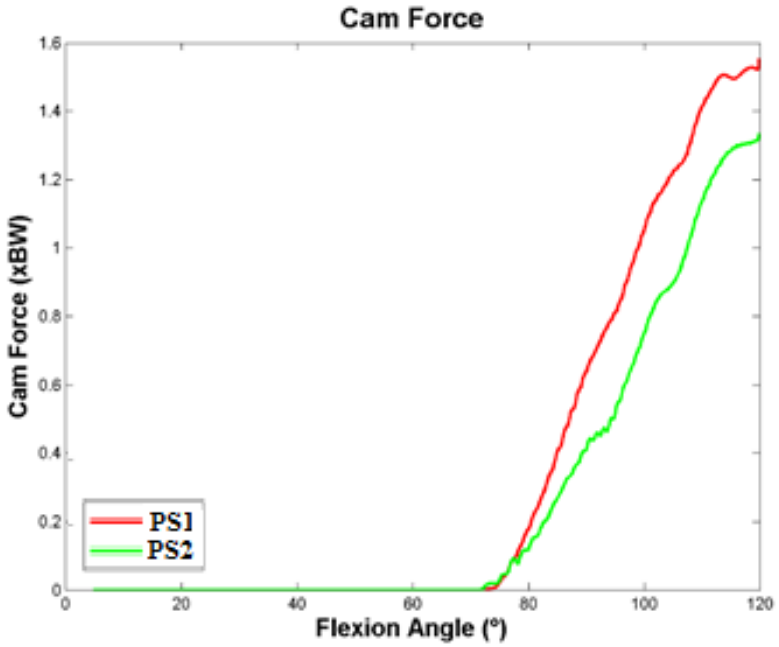

Figure 180: Cam and post contact forces are shown for the PS1 and PS2 during a deep knee bend activity.

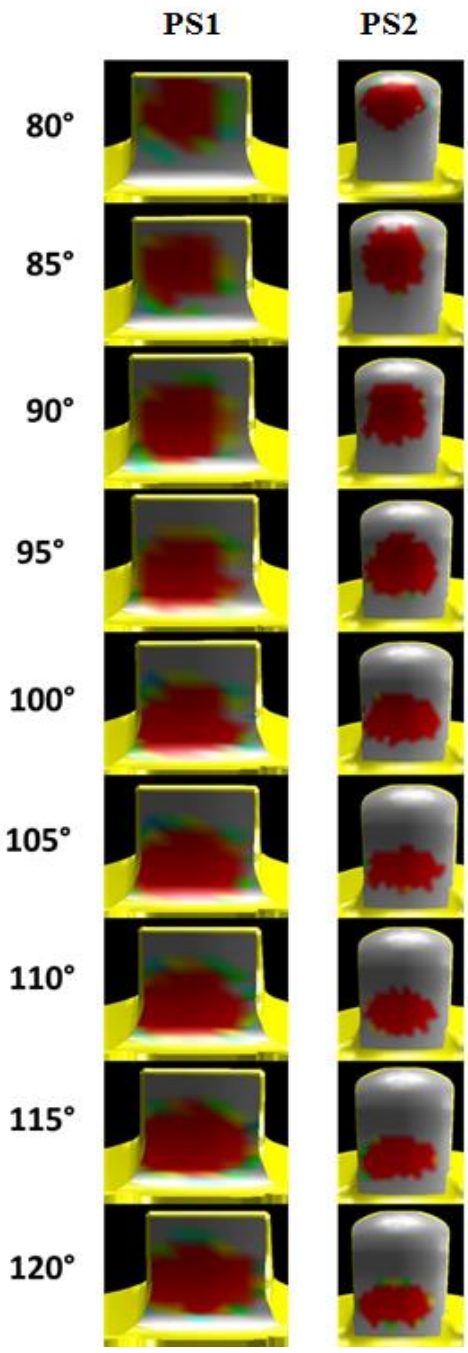

Figure 181: The contact pattern on the post of the PS1 shows inferior translation followed by superior translation. The PS2 contact pattern moves inferiorly on the post for all of the activity.

Chapter 6: Validation

To validate the mathematical model, the tibiofemoral force and medial and lateral contact points were compared to known in-vivo data. The in-vivo data was generated by a subject with a telemetric TKA who was analyzed under fluoroscopy performing a deep knee bend. The forces were determined form the telemetric implant while the medial and lateral contact points were determined from the fluoroscopic analysis using 3D-to-2D registration (D'Lima 2005 & Mahfouz 2003).

To accurately place the implanted components, post-operative CT scans were obtained and segmented to produce 3D models. The tibia was segmented along with the component (Figure 182), which allowed for an approximate placement of the tibial component on the tibia (Figure 183). The backscatter on the femoral component made accurate segmentation of the component impossible, so only the bone was segmented (Figure 184). The backscatter also caused the segmentation of the inferior portion of the femoral bone to be in to be inaccurate. However, the holes for the femoral component pegs were easily identifiable so implant position was based on these (Figure 185 & Figure 186).

Because the CT contained only the distal femur and the proximal tibia, these portions of the bone were first scaled, translated, and rotated to fit bone the default generic models of the full femur and tibia (Figure 187). Then, once the transformations were determined, the generic models were scaled and transformed appropriately to match the CT anatomical bone. As the backscattering certainly caused some inaccuracies in component placement, they were refined to produce a mechanical axis that went through the center of the tibia at the joint line in the model's starting position (Figure 188).

The maximum tibiofemoral force in the model was 4.2 x BW at 105° in the model and 3.8 x BW at 103° according to telemetry (Figure 189). The maximum medial tibiofemoral forces was 1.9 x BW at 103° in the model (Figure 190). In-vivo telemetry found a maximum force of 1.8 x BW at 98°. On the lateral

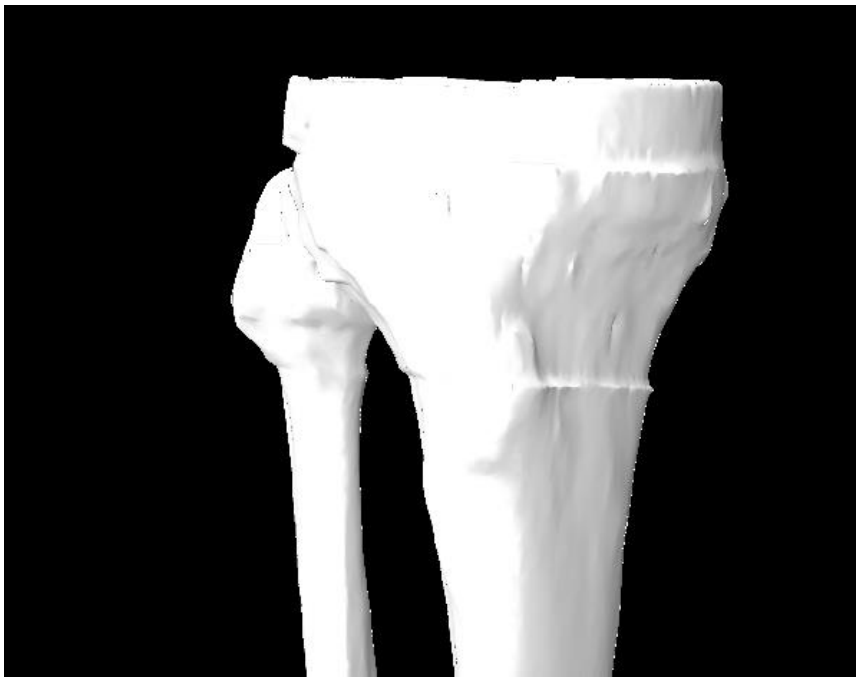

Figure 182: The tibia component was segmented along with the bone.

Figure 183: The tibia component was initially placed based on this segmentation.

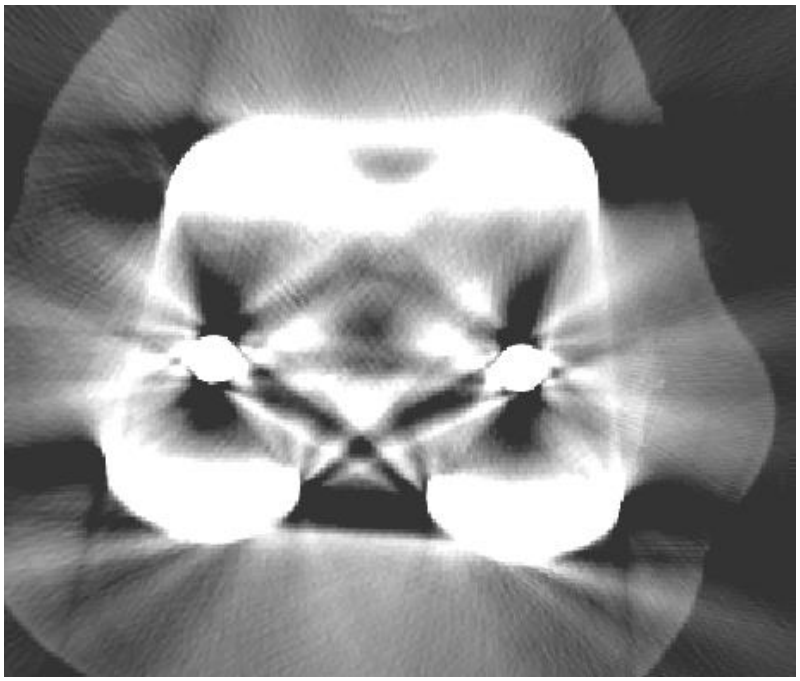

Figure 184: The backscatter prevented the femoral component from being segmented, but the pegs could be identified.

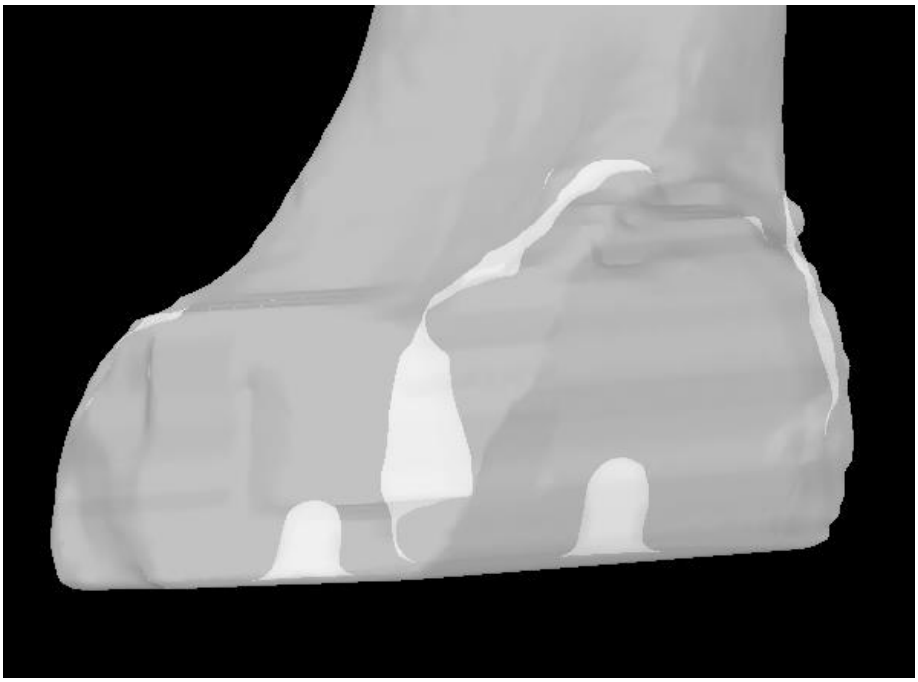

Figure 185: The holes for the pegs are shown in the #D reconstruction.

Figure 186: The femur component is initially fit based on the pegs.

Figure 187: The segmented CT bone was fit to a generic bone model so the proximal hip could be visualized.

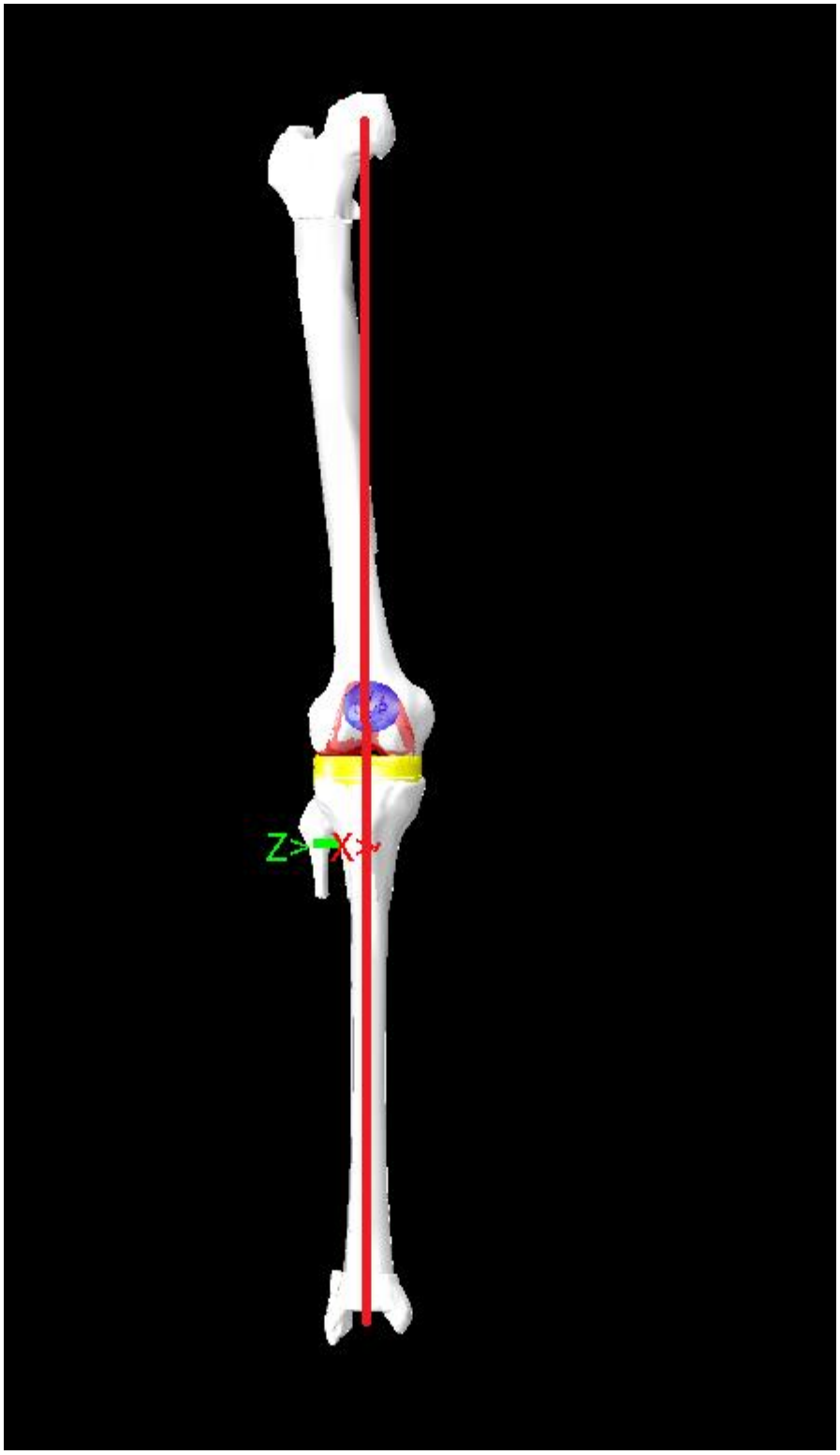

Figure 188: The component alignment on the bone was modified slightly so that the mechanical axis passed through the center of the tibia.

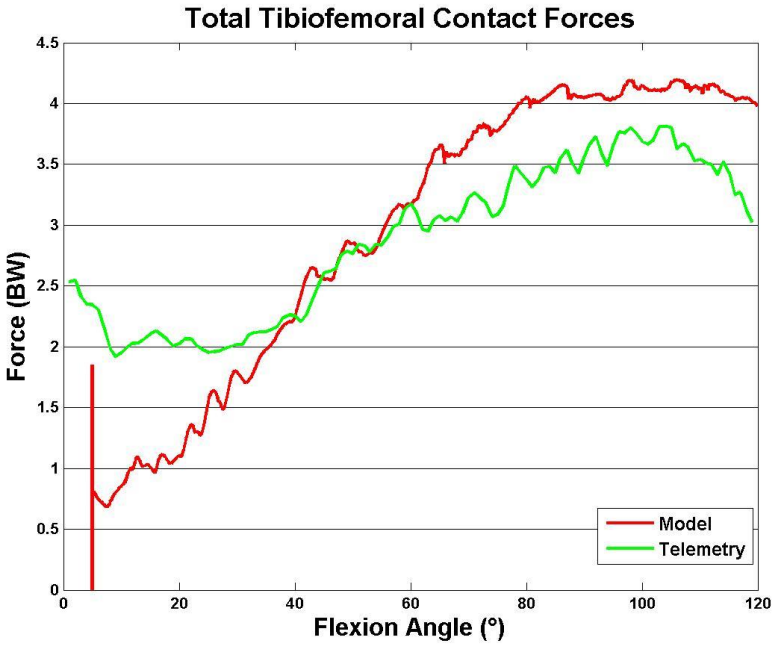

Figure 189: Total tibiofemoral contact forces are compared for the forward solution model and telemetry.

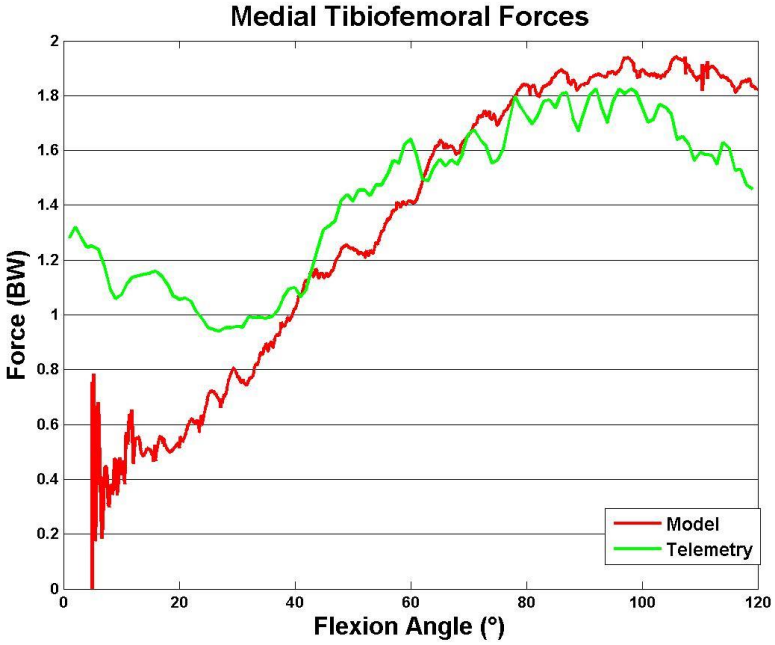

Figure 190: Medial tibiofemoral contact forces are compared for the forward solution model and telemetry.

condyle, the maximum tibiofemoral force was 2.3 x BW at 109° and 2.1 x BW at 107° of flexion for the model and the telemetric data, respectively (Figure 191). The error at for the total force, medial force, and lateral force were 10.5%, 5.5%, and 9.5%, respectively.

The medial condyle of the femur rolled posteriorly to -12.8 mm at 25° of flexion and then translated anteriorly to -4.4 mm at maximum flexion in the model (Figure 192). Fluoroscopy found the medial subject of the femur rolled posteriorly to -8.5 mm at 42° of flexion before translating anteriorly to -4.0 mm at maximum flexion. On the lateral side, the condyle of the femur rolled posteriorly to -13.0 mm at 28° and then translated anteriorly to -6.0 mm at maximum flexion in the model (Figure 193). The in-vivo data shows the lateral condyle translating anteriorly to -10.2 mm posterior before translating anteriorly to -5.8 mm at maximum flexion. The model translations followed the same pattern seen in-vivo and very accurately predicted the ending location of the condyles. There was more error in predicting the early translations, and this may be attributable to the model still settling in early flexion.

With the first validation completed, the simulations were rerun to analyze the effects of changing the mesh density of the femoral point cloud. This was done by creating a much more sparse cloud which had 135 points on the medial point cloud and 136 points on the lateral point cloud (Figure 194). The original had 552 and 537 points on the medial and lateral clouds, respectively (Figure 195). A more dense femur was also analyzed which contained 2494 points medially and 2189 points laterally (Figure 196). The results were compared for lateral translation, medial translation, tibiofemoral forces, patellofemoral forces, and axial rotation (Figure 197 - Figure 203). The translation and force predictions were identical with the exception that increasing density also appeared to increase stability, which is evident from the reduced oscillations.

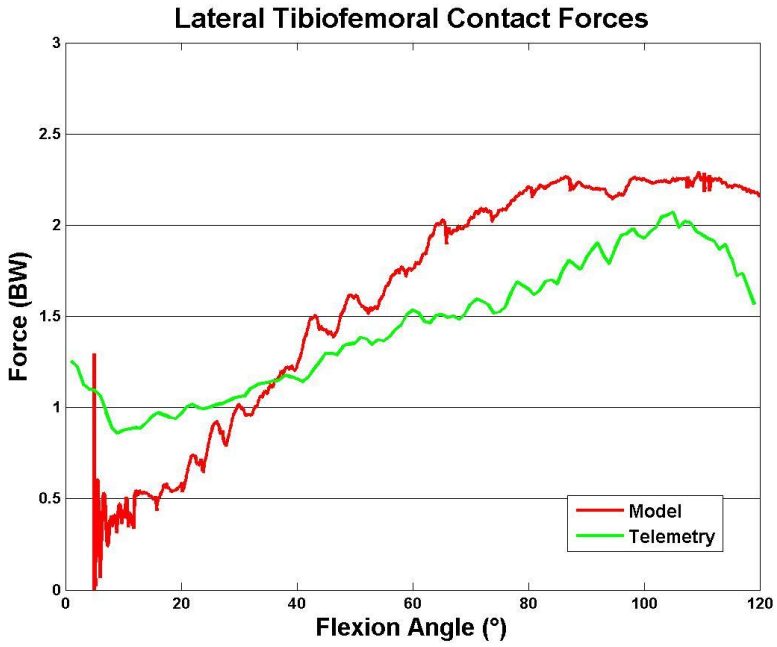

Figure 191: Lateral tibiofemoral contact forces are compared for the forward solution model and telemetry.

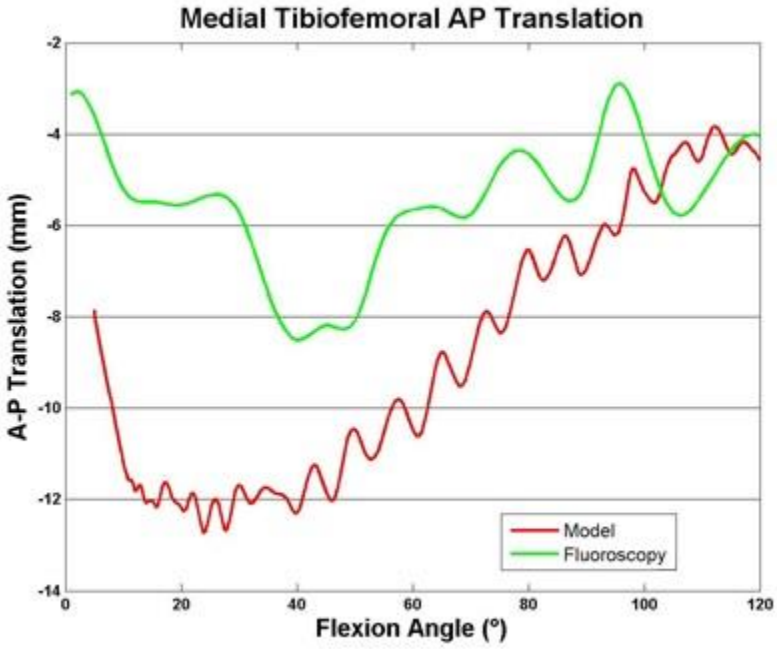

Figure 192: Medial condyle translations are compared for the forward solution model and telemetry.

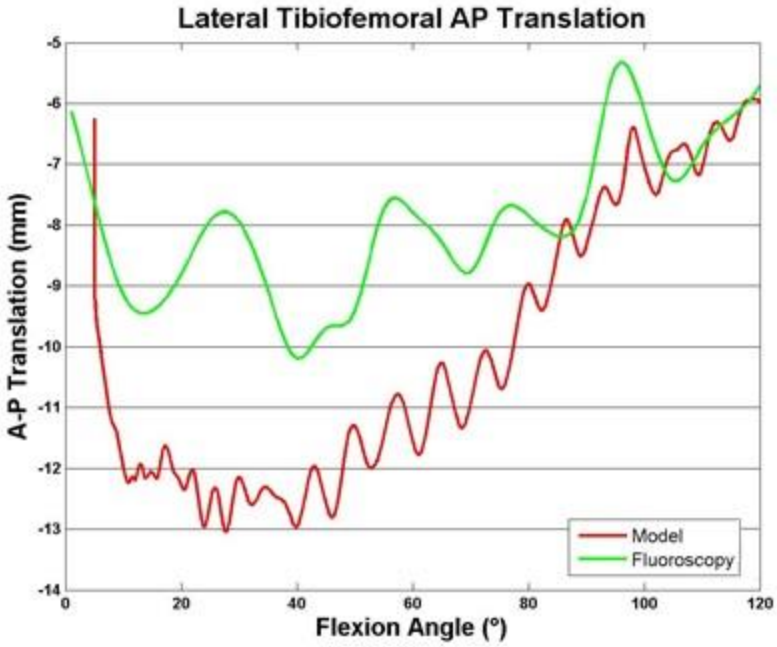

Figure 193: Lateral condyle translations are compared for the forward solution model and telemetry.

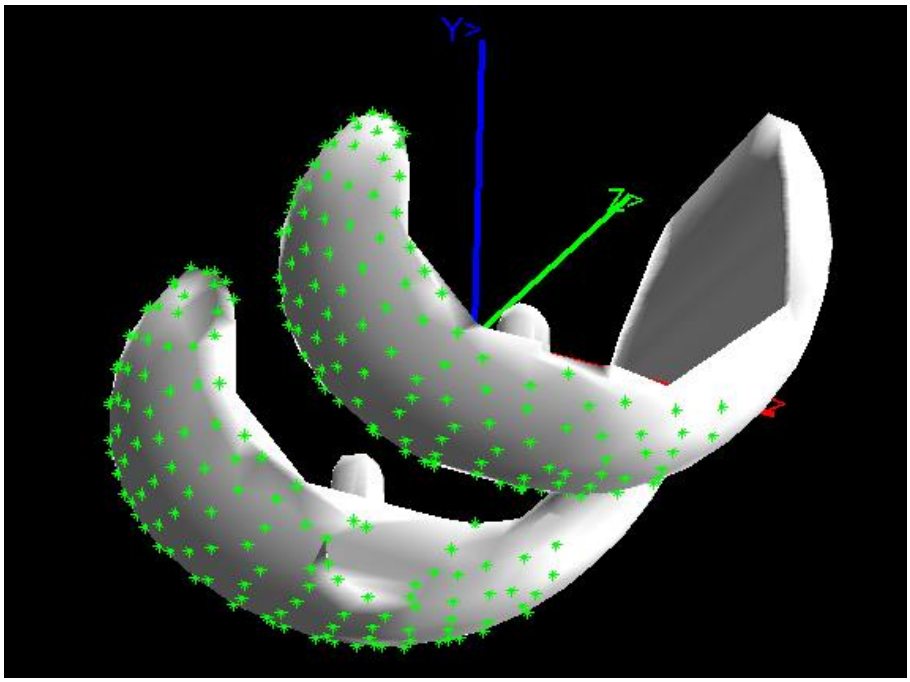

Figure 194: The sparse femoral point cloud is shown.

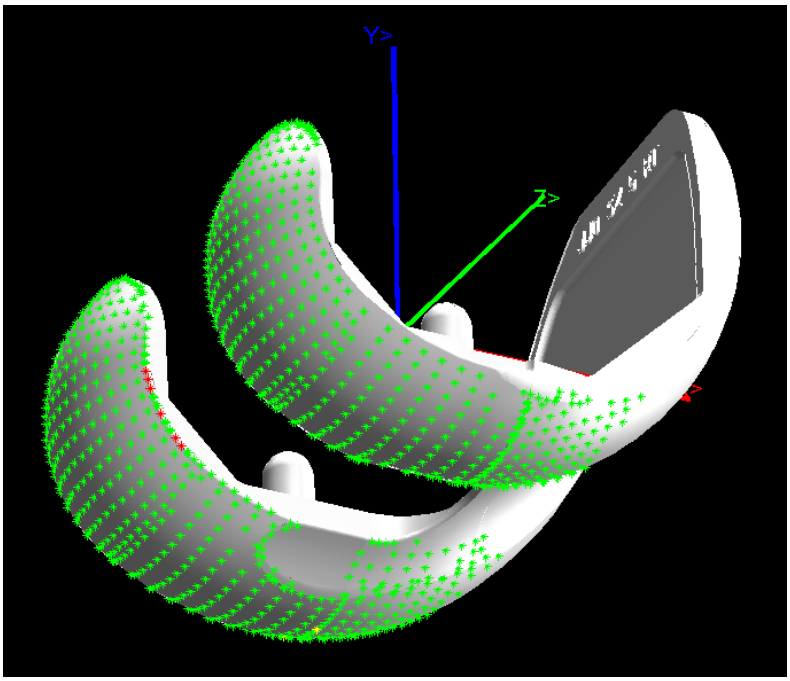

Figure 195: The baseline femoral point cloud is shown.

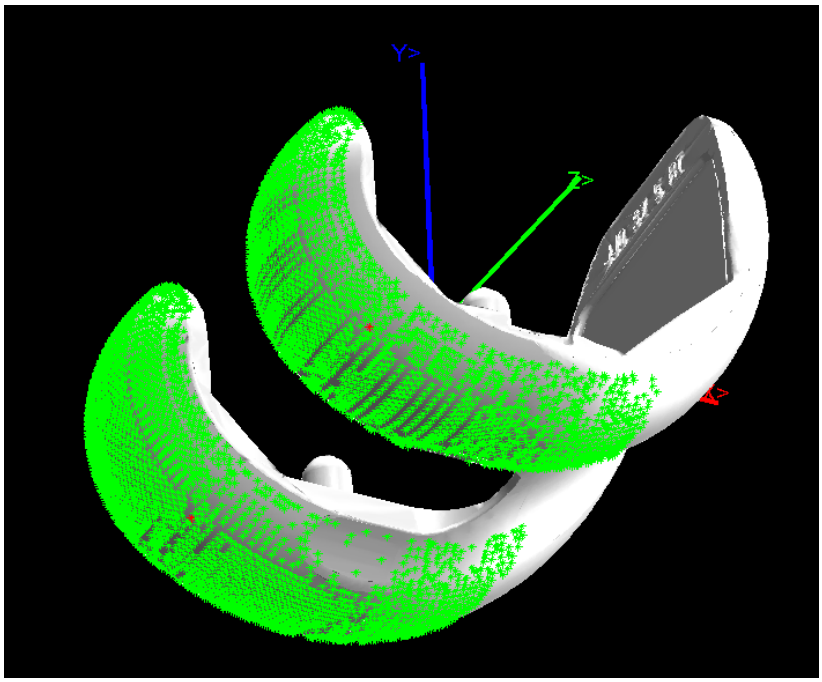

Figure 196: The dense femoral point cloud is shown.

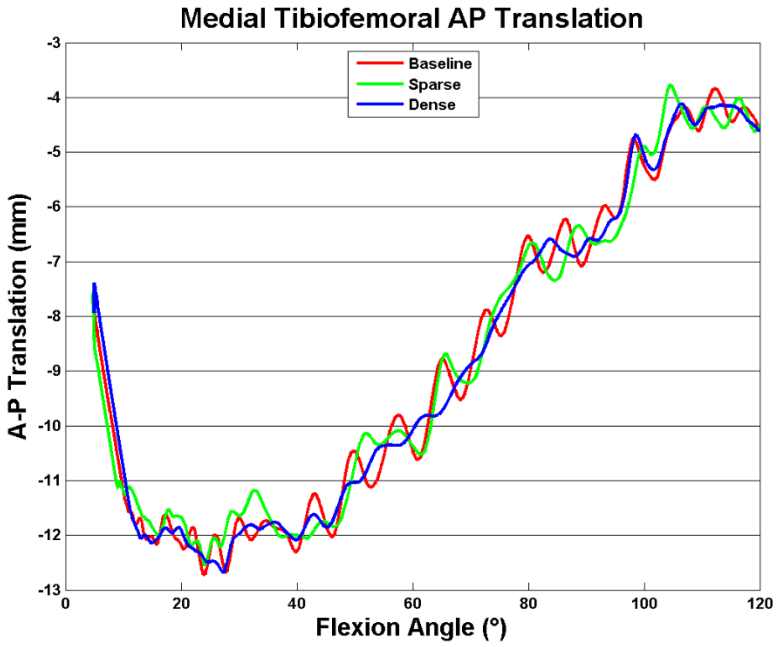

Figure 197: Medial condyle AP translations are shown for the different femoral point cloud density analyses.

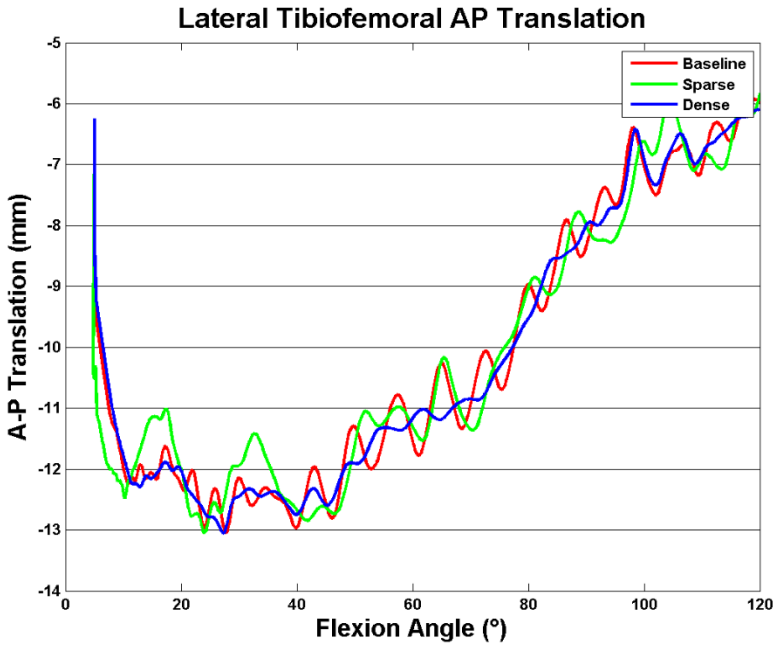

Figure 198: Lateral condyle AP translations are shown for the different femoral point cloud density analyses.

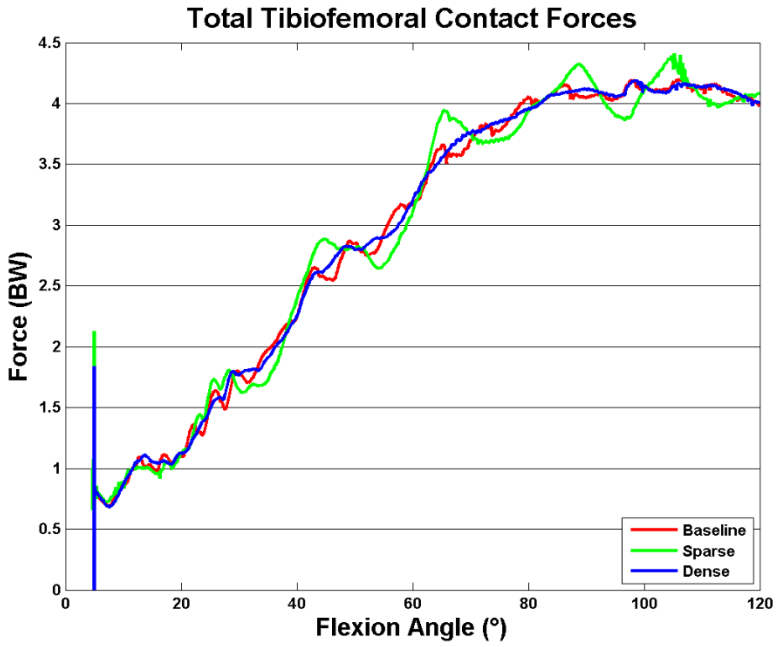

Figure 199: Total tibiofemoral contact forces are shown for the different femoral point cloud density analyses.

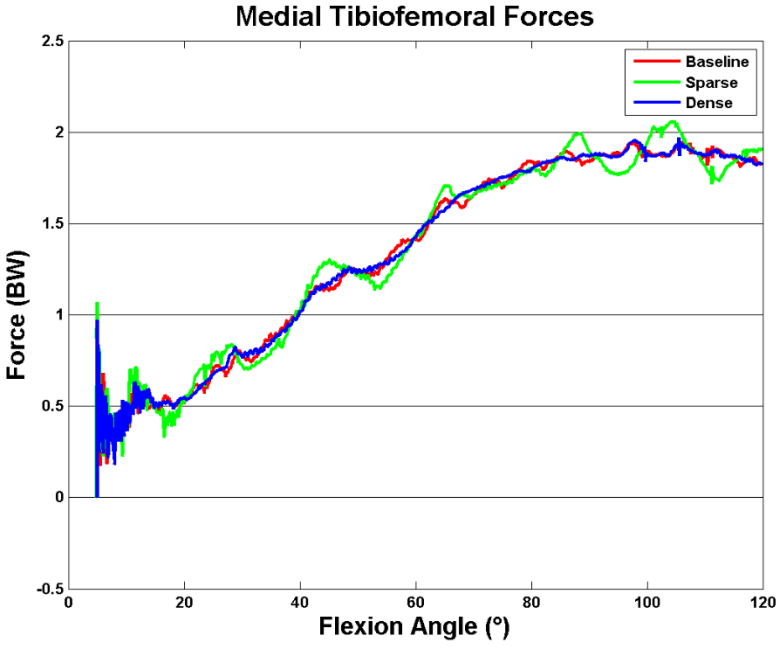

Figure 200: Medial tibiofemoral contact forces are shown for the different femoral point cloud density analyses.

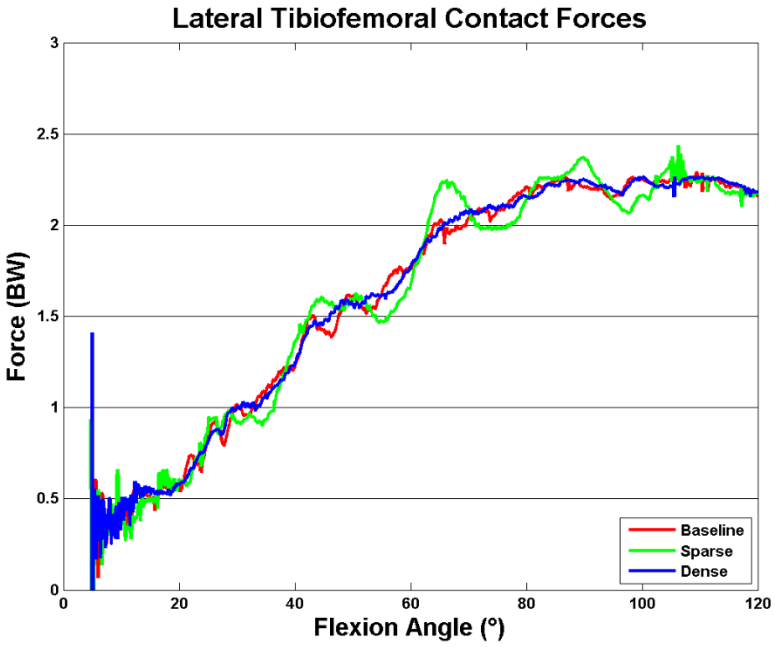

Figure 201: Lateral tibiofemoral contact forces are shown for the different femoral point cloud density analyses.

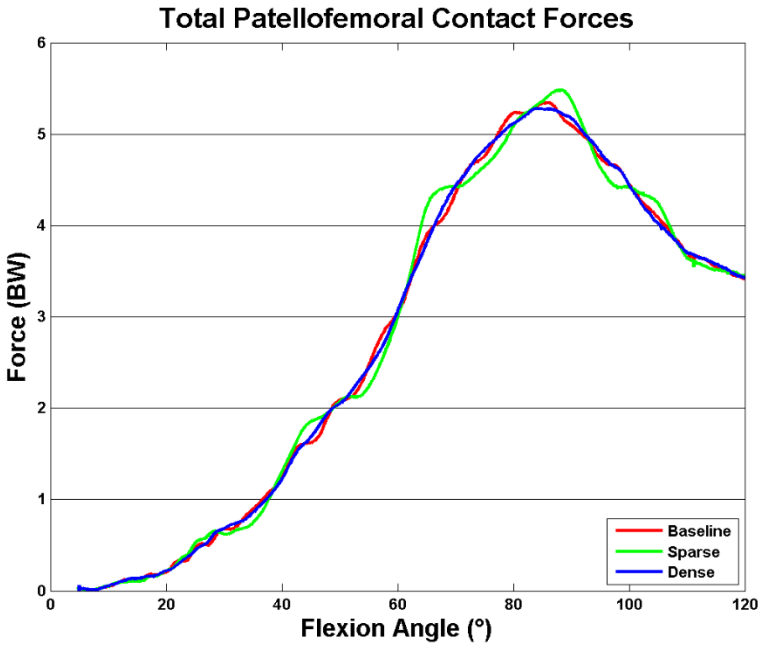

Figure 202: Total patellofemoral contact forces are shown for the different femoral point cloud density analyses.

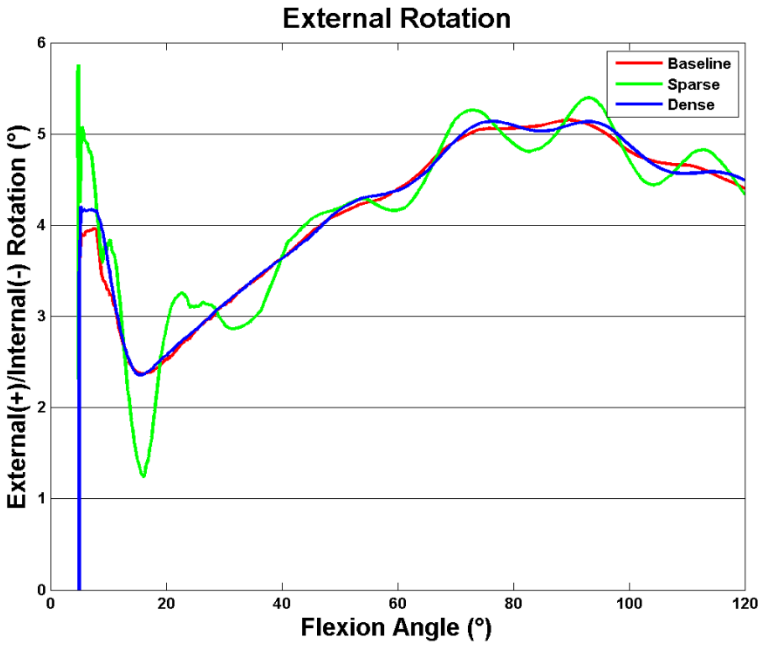

Figure 203: External rotation is shown for the different femoral point cloud density analyses.

Chapter 7: Designing a New Implant

The next step with the GUI was using it as a design tool to create a TKA design which would generate the desired kinematics and kinetics profiles. The target pattern chosen was lateral condyle roll forward and internal rotation in the last 20 degrees of extension for an ASTKA design. Multiple simulations were run in succession in order to develop a successful ASTKA. The first design featured a central cam/post and served as a baseline. The second simulation had a lateralized cam/post. All subsequent simulations featured the same femur with some small variations at the cam while all simulations had a different polyethylene component. For each of these designs, the simulation was run once with the anterior post to simulate an ASTKA. The simulations started at approximately 55° of flexion and were run to full extension. Then, the post was removed and a simulation was run utilizing a PCR TKA for many of the implants. The PCR simulation was not performed for those implants which had cam post contact in the final degrees of extension, as it can be assumed removing the post would have minimal effect on the results.

Set 1

The first set was used as a baseline design. The femur features a lateralized trochlear groove with a central cam and post (Figure 204). The polyethylene featured a similar design on both the medial and lateral plateaus. However, the medial plateau had a more curvature on its medial edge than the lateral plateau did on its lateral edge (Figure 205).

The anterior cam did not engage until approximately 6° of flexion and had a peak force of roughly 0.03 x BW (Figure 206). The PCR simulation was not run because the post engaged so late. Both the medial and lateral condyles showed a rapid anterior slide during the first few degrees of extension (Figure 207 & Figure 208). This stems from the knee settling into the extension activity, so it will be ignored in

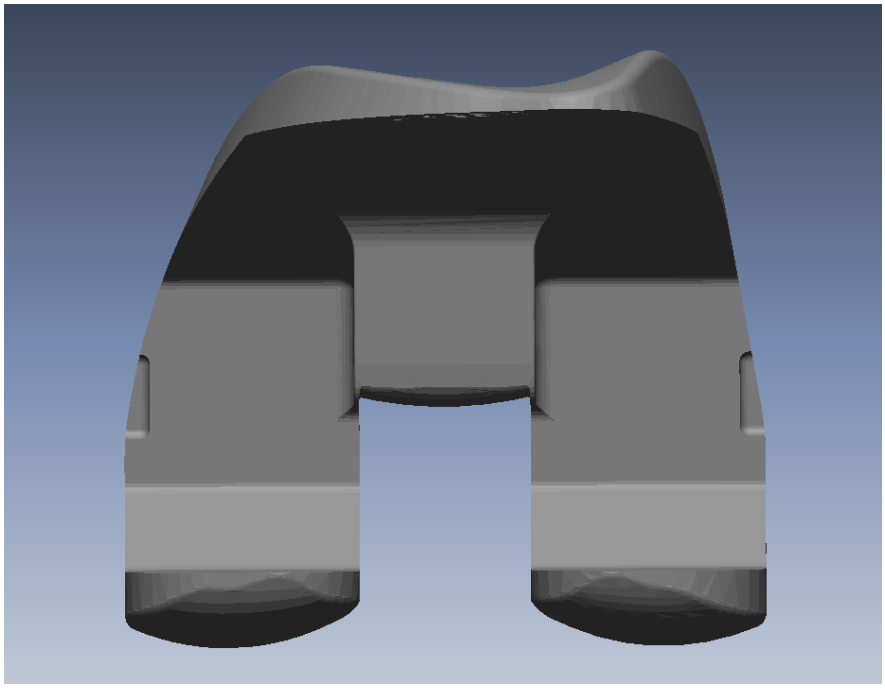

Figure 204: The baseline ASTKA femur design is shown.

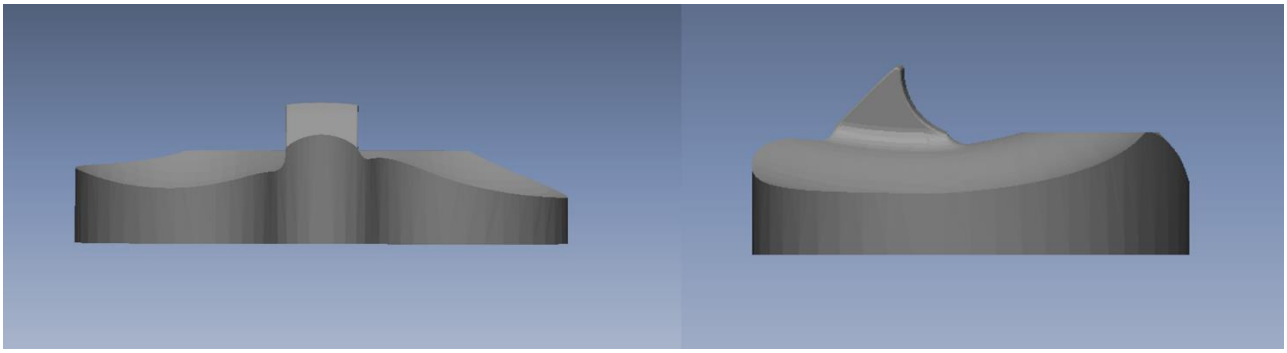

Figure 205: The baseline ASTKA polyethylene design is shown.

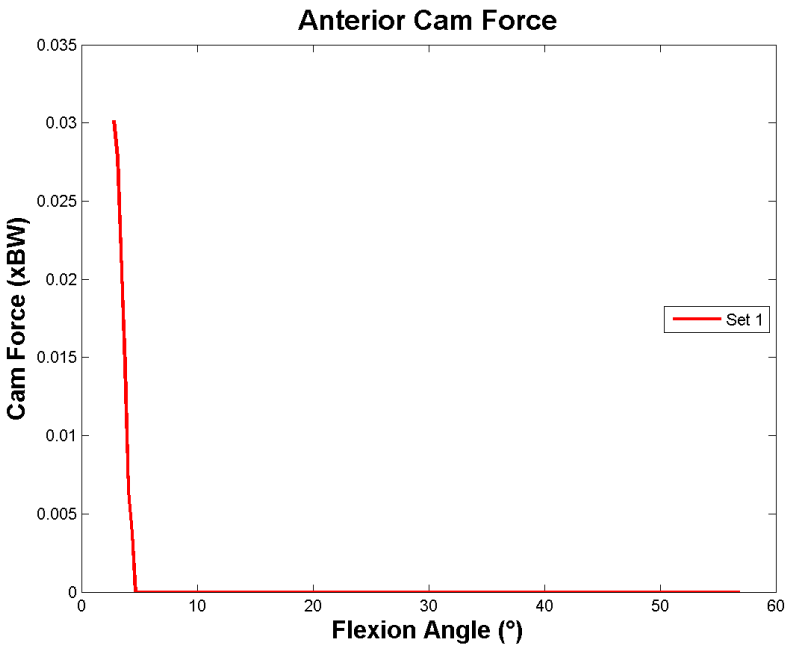

Figure 206: The anterior cam/post force is shown for Set 1.

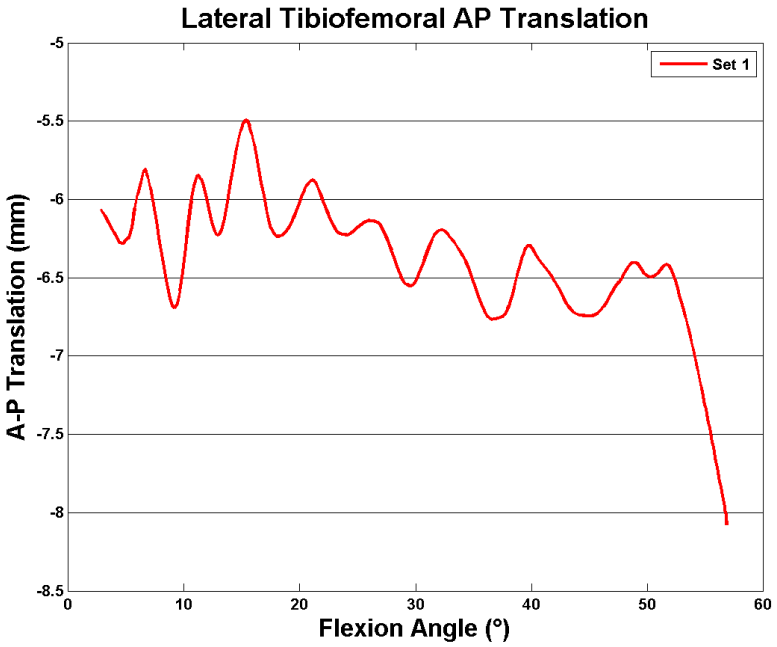

Figure 207: The lateral condyle translations are shown for Set 1.

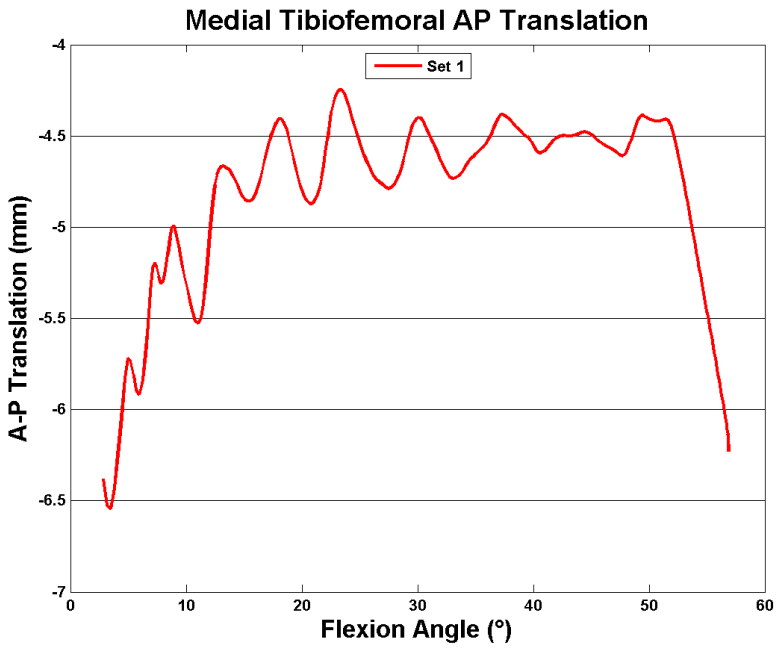

Figure 208: The medial condyle translations are shown for Set 1.

discussing this simulation and future simulations. Both condyles showed many oscillations, with the lateral condyle translating from -6.5 mm to -6.0 mm and the medial condyle translating from -4.5 to -6.5 mm. The femur rotated internally from -2.5° to 0.3° (Figure 209). Internal rotation is normal rotation for an extension activity, but this is much less than would be seen in a healthy knee.

Set 2

Set 2 featured a lateralized cam/post mechanism resulting in a larger medial condyle and smaller lateral condyle (Figure 210). Also, the cam was roughly 3.5 mm more anterior on the Set 2 design than on Set 1. On the polyethylene, the post was also shifted laterally and approximately 3.5 mm more anterior (Figure 211). The increased medial curvature on the medial side was less pronounced than in Set 1 (Figure 212).

The cam/post mechanism of Set 2 engaged at 5° (Figure 213). Therefore, no PCR simulation was performed. The peak anterior cam force was 0.08 x BW. The lateral condyle displayed very similar translations to that of Set 1, moving from approximately -6.5 mm to -6.0 mm if the oscillations are ignored (Figure 214). The medial condyle translated from -4.8 mm to -6.5 mm (Figure 215). Set 2 rotated from -2.0° of axial rotation to roughly 0° if the oscillations are ignored (Figure 216).

Set 3

The femur of Set 3 was identical to Set 2 except for an anterior shift of the cam. It was moved approximately 2 mm anteriorly (Figure 217). The polyethylene of Set 3 was identical to Set 2 except for making the post larger and moving it anteriorly by approximately 5.5 mm (Figure 218 & Figure 219). By moving the post more anterior than the cam, cam/post contact occurs at an earlier angle during extension.

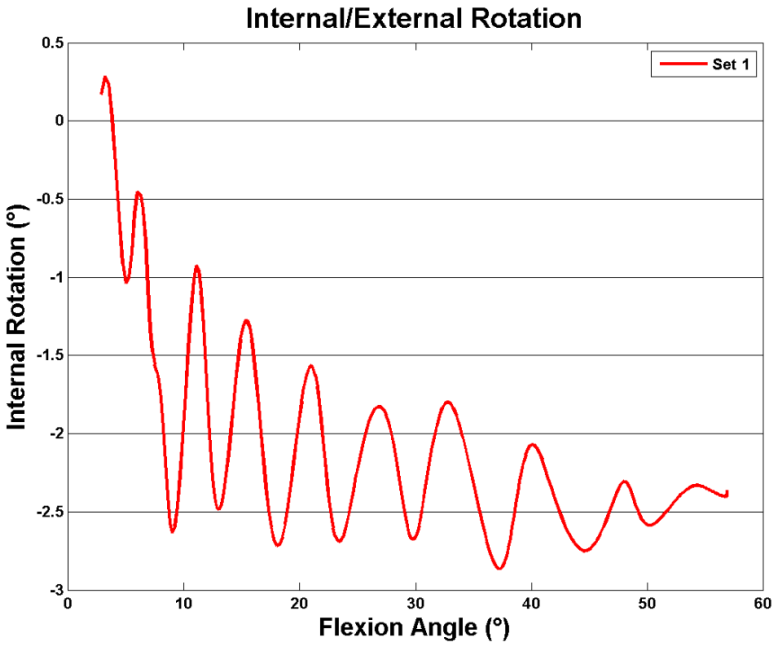

Figure 209: The axial rotations are shown for Set 1.

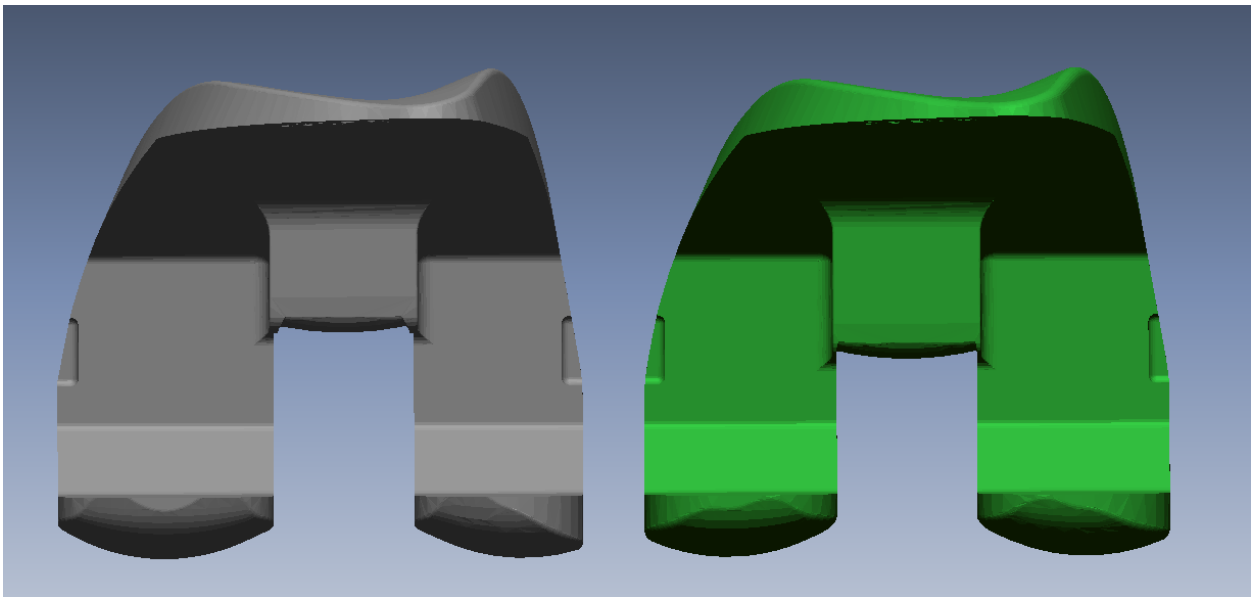

Figure 210: Set 2 (gray) featured a more anterior and lateralized post than Set 1 (green).

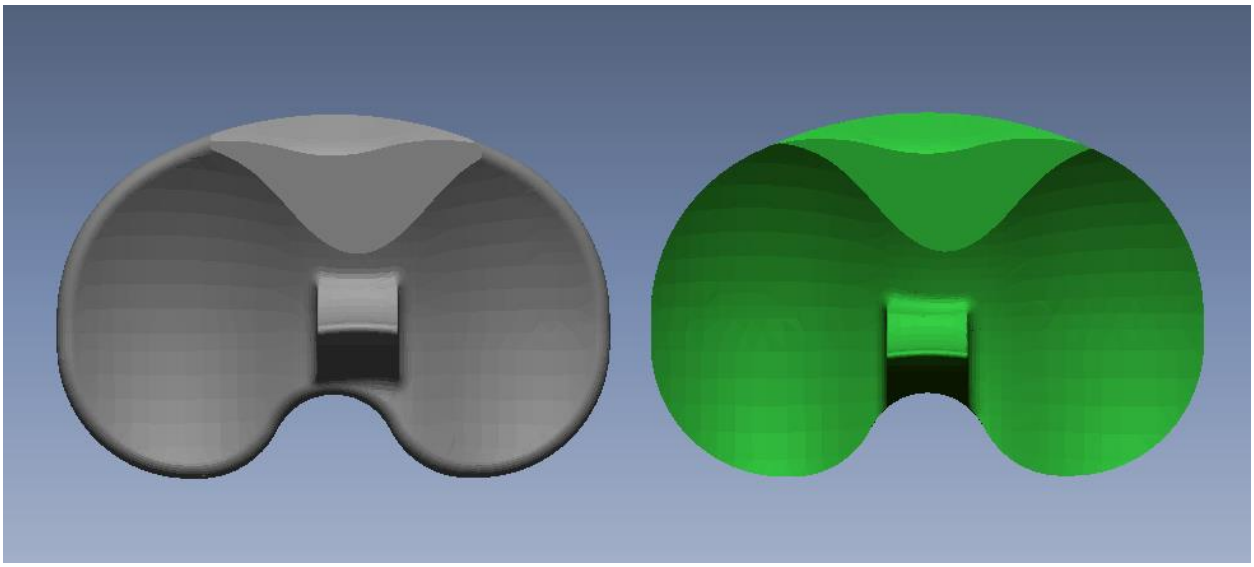

Figure 211: The post was shifted anterior from Set 1 (green) to Set 2 (gray).

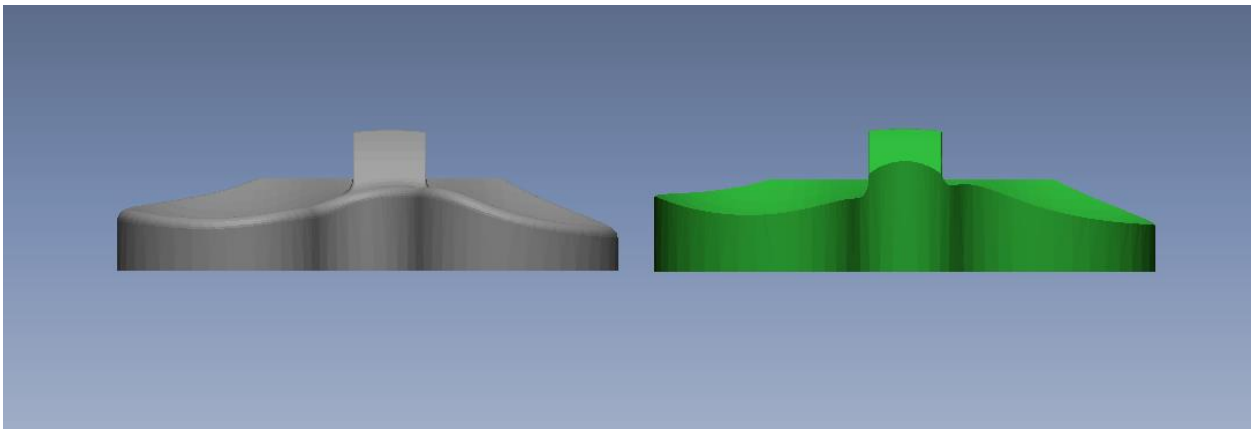

Figure 212: The post was shifted lateral rom Set 1 (green) to Set 2 (gray) and the medial edge was not as high.

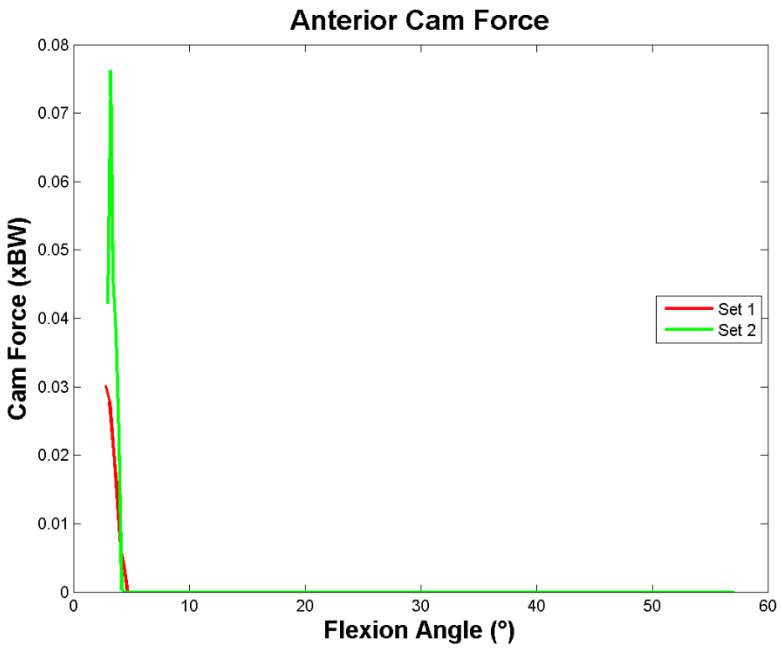

Figure 213: The anterior cam/post force is shown for Set 1 & 2.

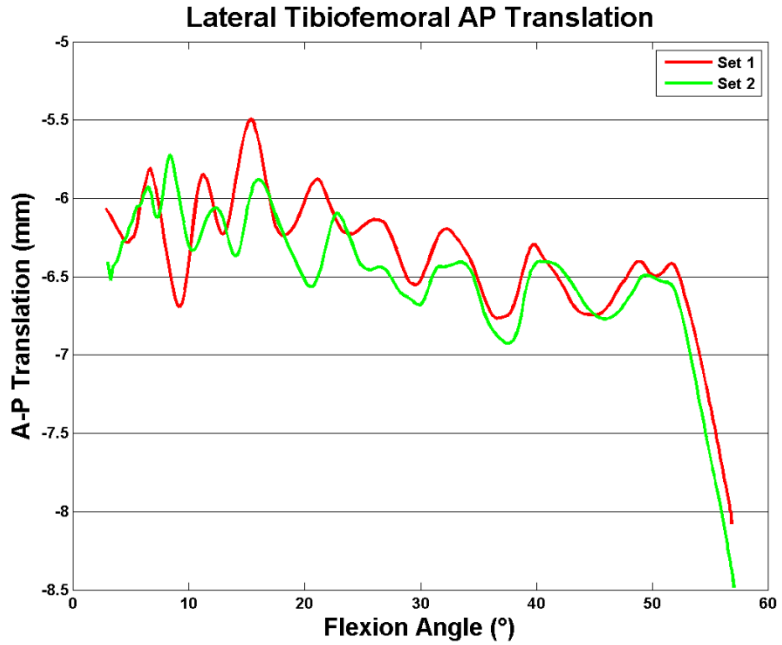

Figure 214: The lateral condyle translations are shown for Set 1 & 2.

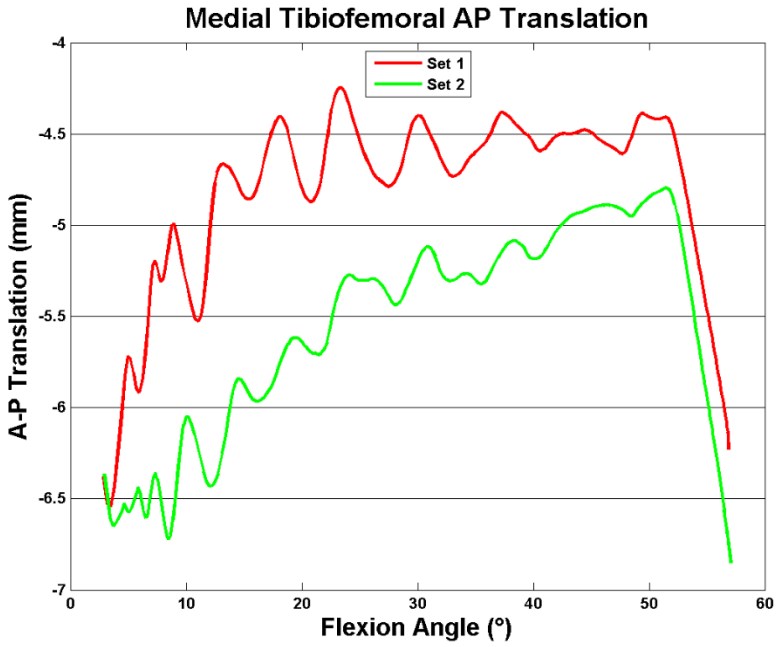

Figure 215: The medial condyle translations are shown for Set 1 & 2.

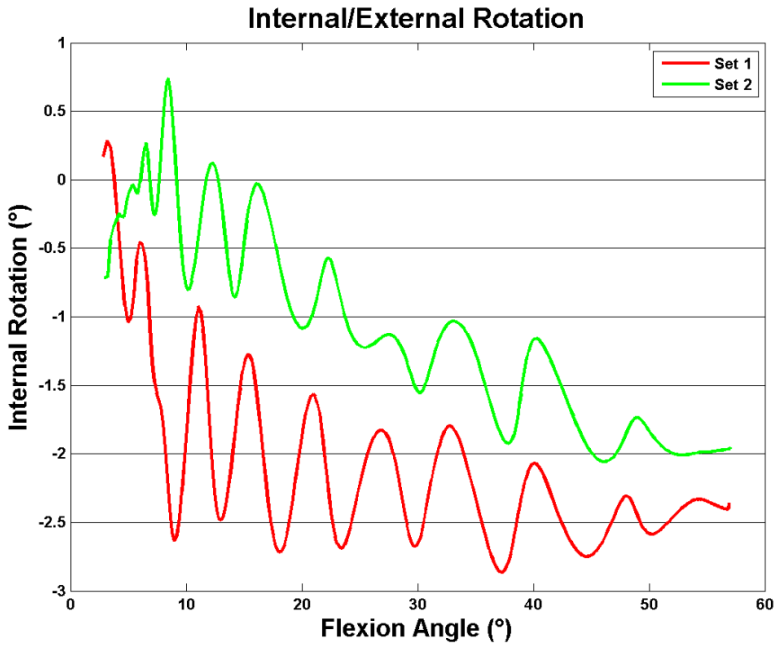

Figure 216: The axial rotations are shown for Set 1 & 2.

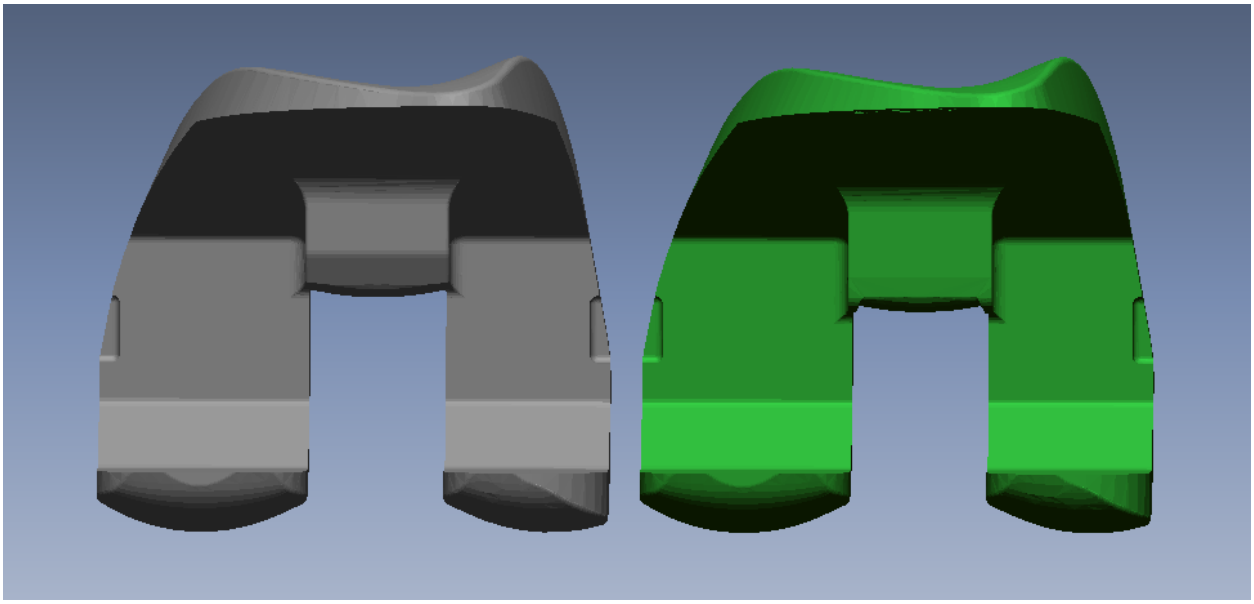

Figure 217: The cam was shifted anterior in Set 3 (gray) relative to Set 2 (Green).

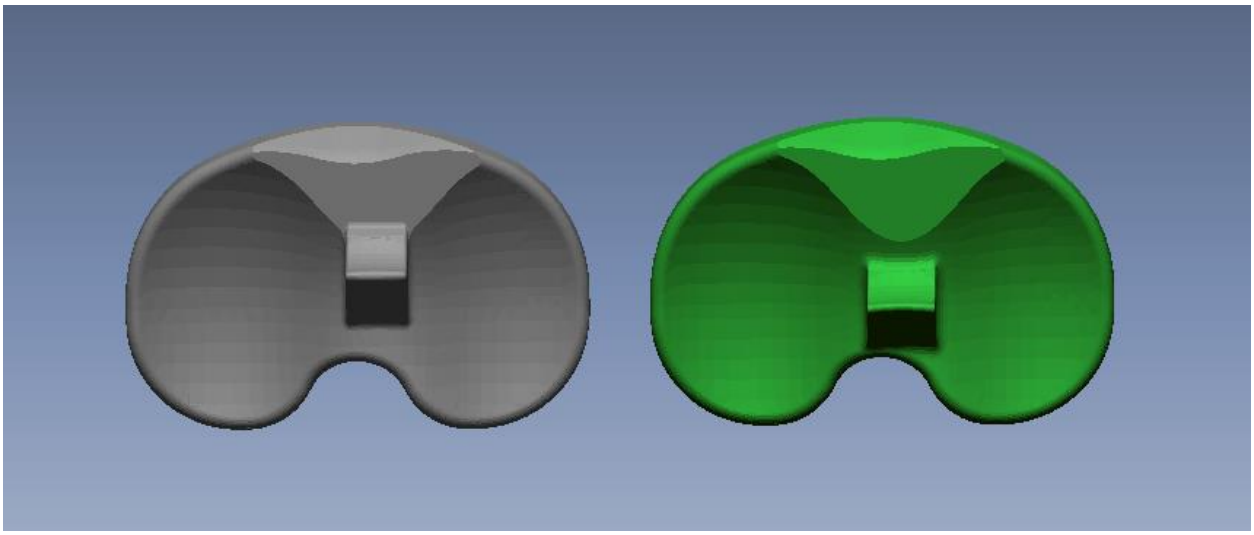

Figure 218: The post was shifted more than 5 mm anterior in Set 3 (gray) relative to Set 2 (green).

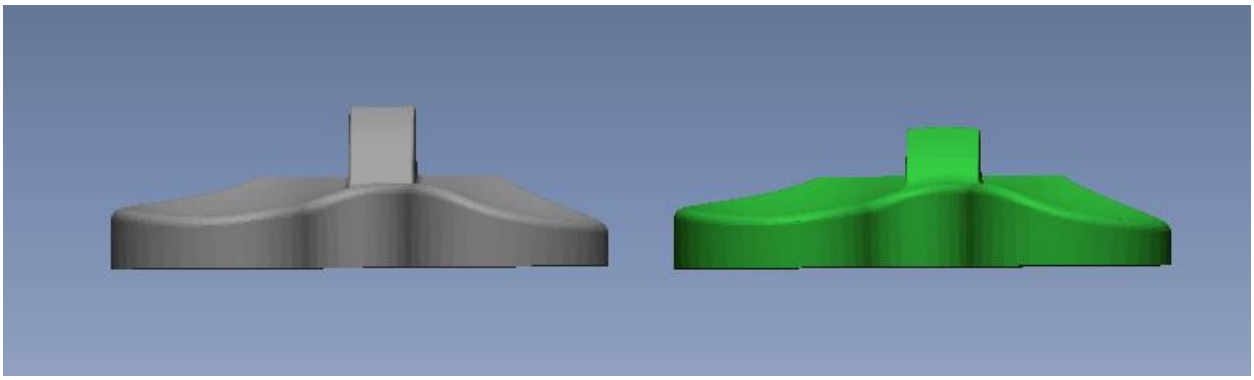

Figure 219: Set 3 (gray) had a much higher post than Set 2 (green).

The PID controller was tuned for Set 3 to minimize the oscillations. The anterior cam/post engaged at 15° in Set 3 and had a peak force of 1.15 x BW (Figure 220). The lateral condyle translated from -6.2 mm to -1.6 mm with most of the translation occurring after the cam/post engaged (Figure 221). The medial condyle translated from -4.6 mm to -1.4 mm (Figure 222). Most of this translation also occurred after the cam/post engaged. The femur internally rotated from -2.0° to -0.8°, the largest amount of rotation that occurred with the cam and post engaged (Figure 223).

It seems likely that the very large force on the post was caused by the post trying to drive the femoral condyles onto the anterior lip of the polyethylene. For this reason, a second simulation was run with the lateral condyle of the polyethylene being completely flat. The simulation proved this hypothesis to be true. It lowered the anterior cam force to less than 0.4 x BW (Figure 224). Furthermore, the lateral condyle ended at 2.5 mm as opposed to -1.6 mm in the original Set 3 simulation (Figure 225). The medial condyle finished more posteriorly at -2.3 mm (Figure 226). The internal rotation at full extension was much larger with the flat lateral condyle (Figure 227). The internal rotation was 5.7° at full extension for the flat lateral condyle simulation versus -0.8° for the original Set 3 simulation.

Set 4

The only difference between the femurs of Set 3 and Set 4 occurs at the inferior portion of the trochlear groove (Figure 228). The condyles and cam are identical. The post on Set 4 is wider than that of Set 3 (Figure 229). It is also angled internally to drive the femur more internally in full extension. Finally, the anterior lip of the lateral plateau is lower, resulting in a less conforming lateral plateau (Figure 230). This should allow the lateral condyle of the femur to slide anteriorly as shown in the Set 3 flat lateral plateau simulation which was the impetus for this design.

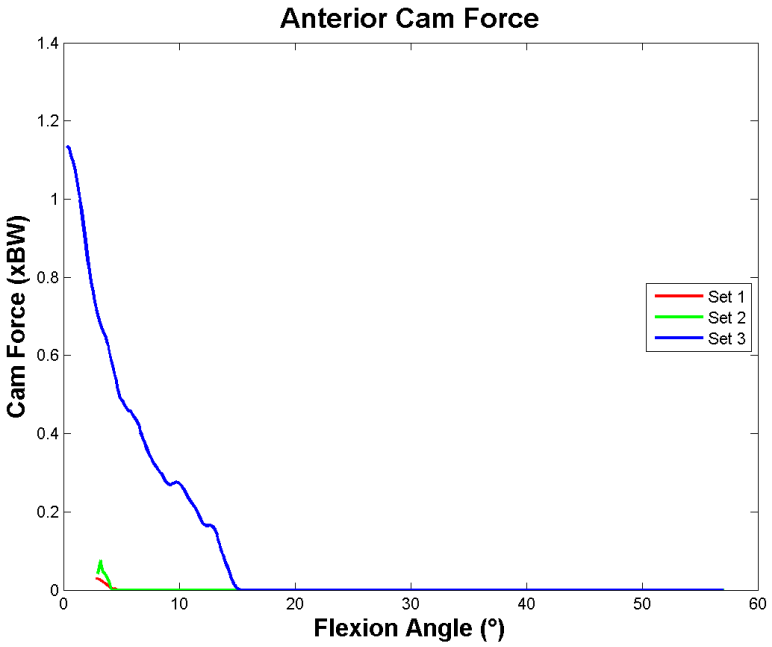

Figure 220: The anterior cam/post force is shown for Set 1, 2, & 3.

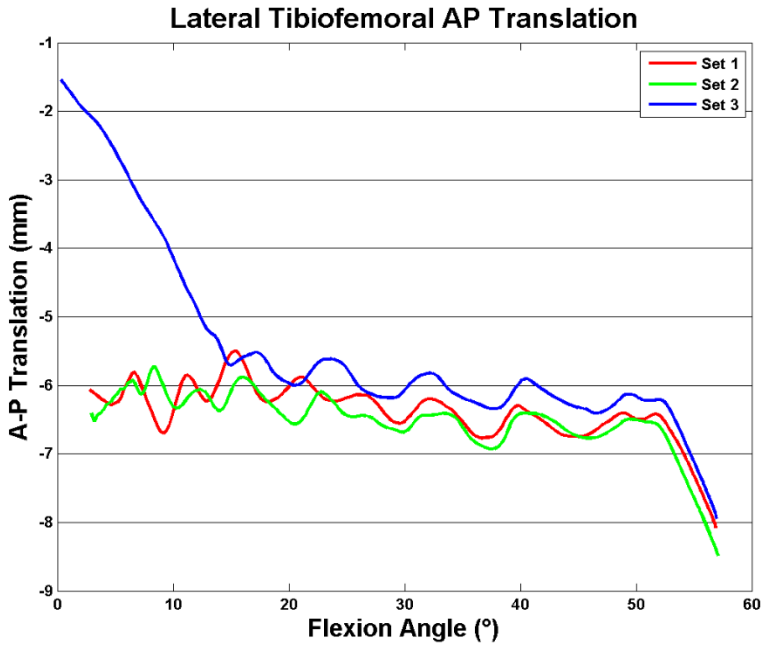

Figure 221: The lateral condyle translations are shown for Set 1, 2, & 3.

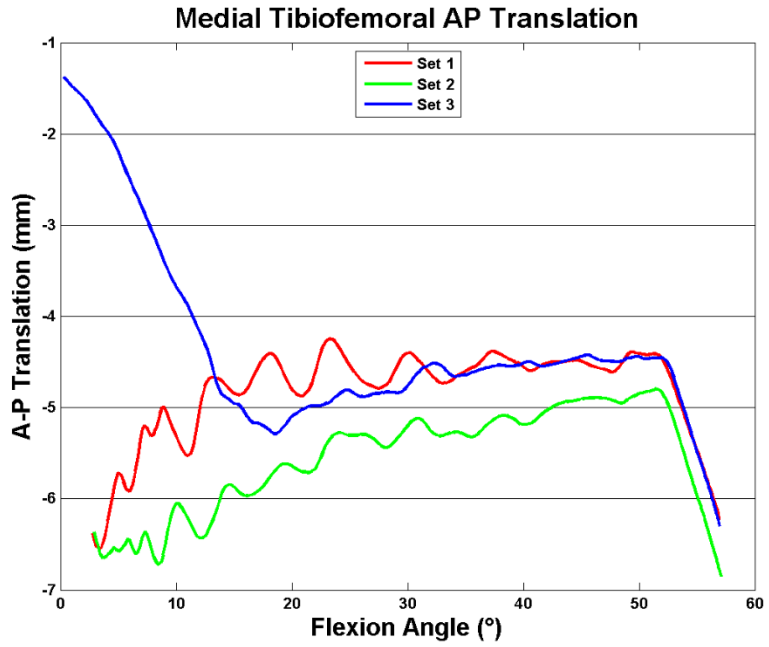

Figure 222: The medial condyle translations are shown for Set 1, 2, & 3.

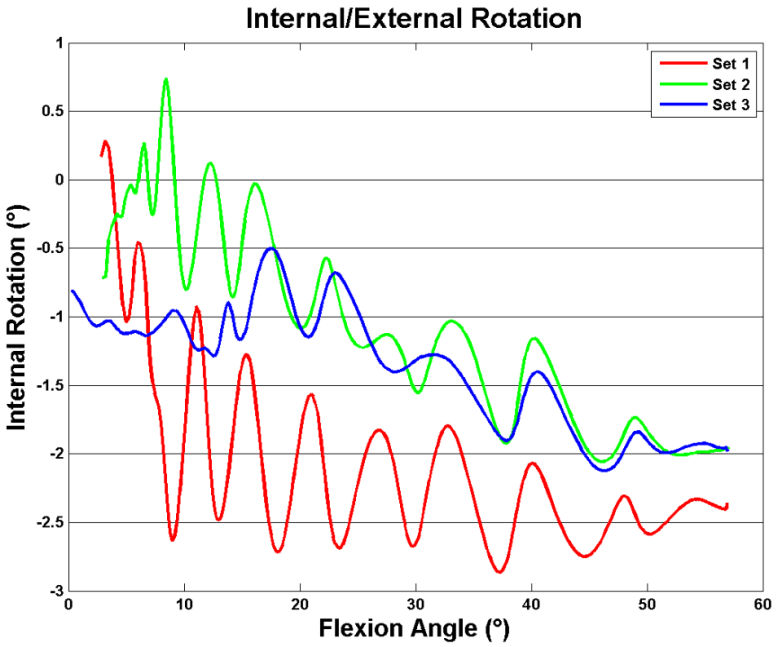

Figure 223: The axial rotations are shown for Set 1, 2, & 3.

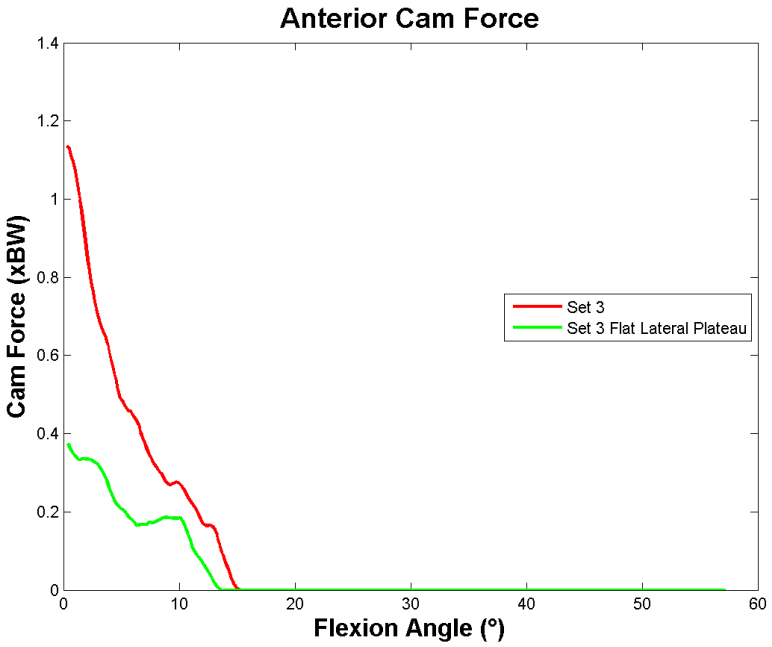

Figure 224: The anterior cam forces for Set 3 with a normal and flat lateral plateau are shown.

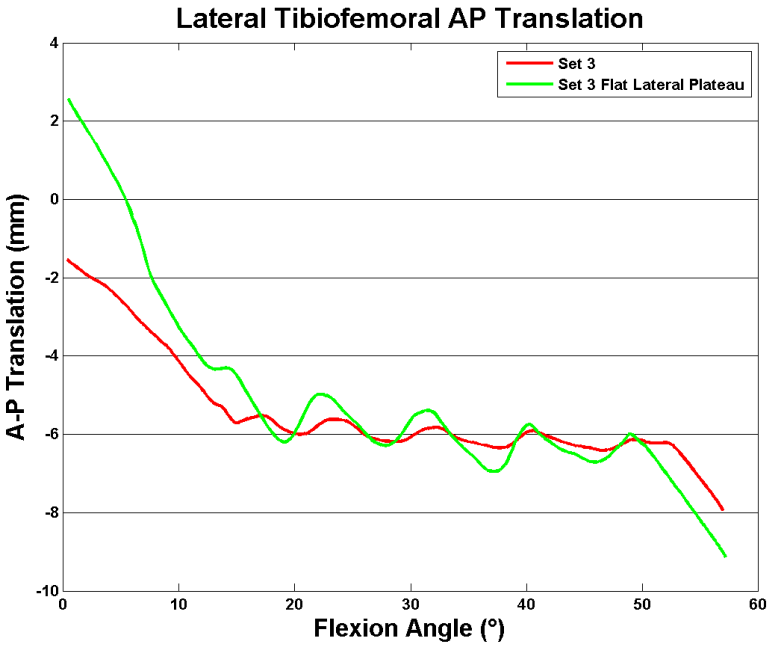

Figure 225: The lateral condyle translations for Set 3 with a normal and flat lateral plateau are shown.

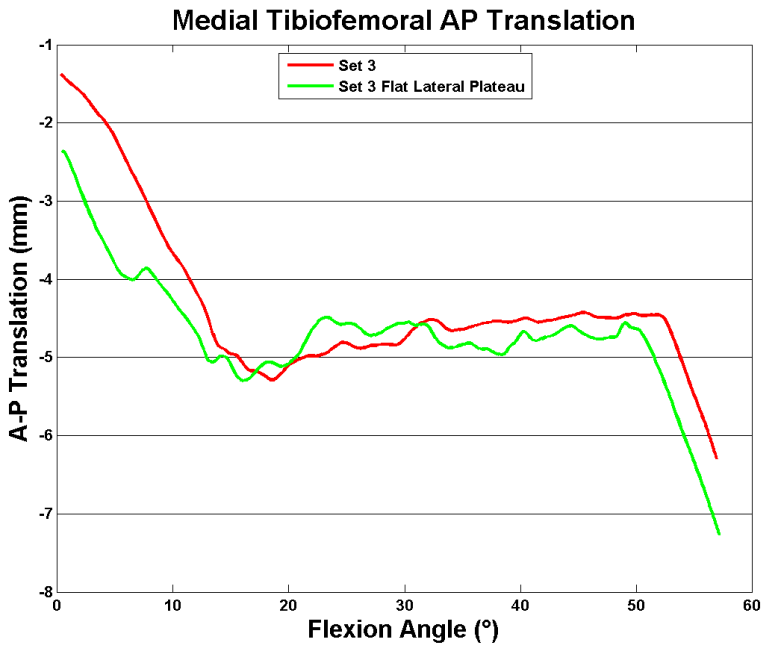

Figure 226: The lateral condyle translations for Set 3 with a normal and flat lateral plateau are shown.

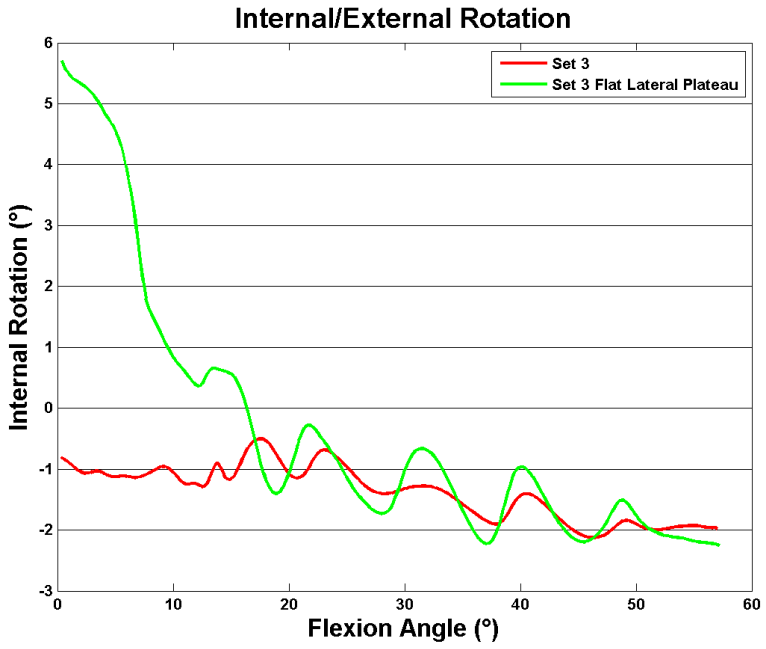

Figure 227: The axial rotations for Set 3 with a normal and flat lateral plateau are shown.

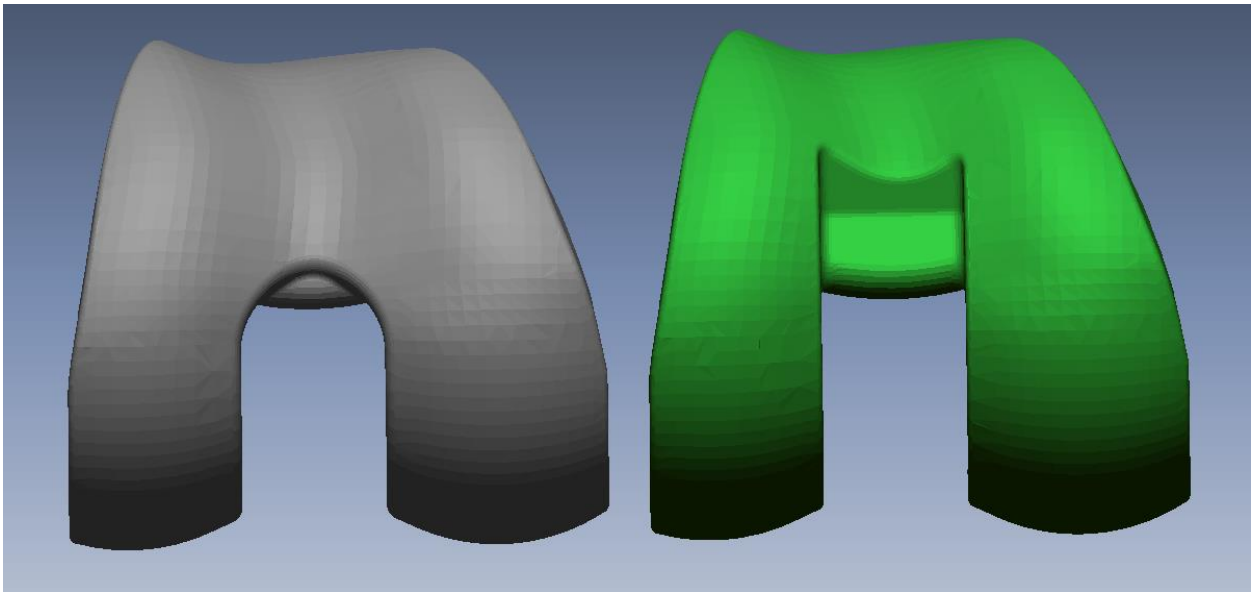

Figure 228: The Set 4 femur (gray) had a trochlear groove that extends more inferior than the Set 3 trochlear groove (green).

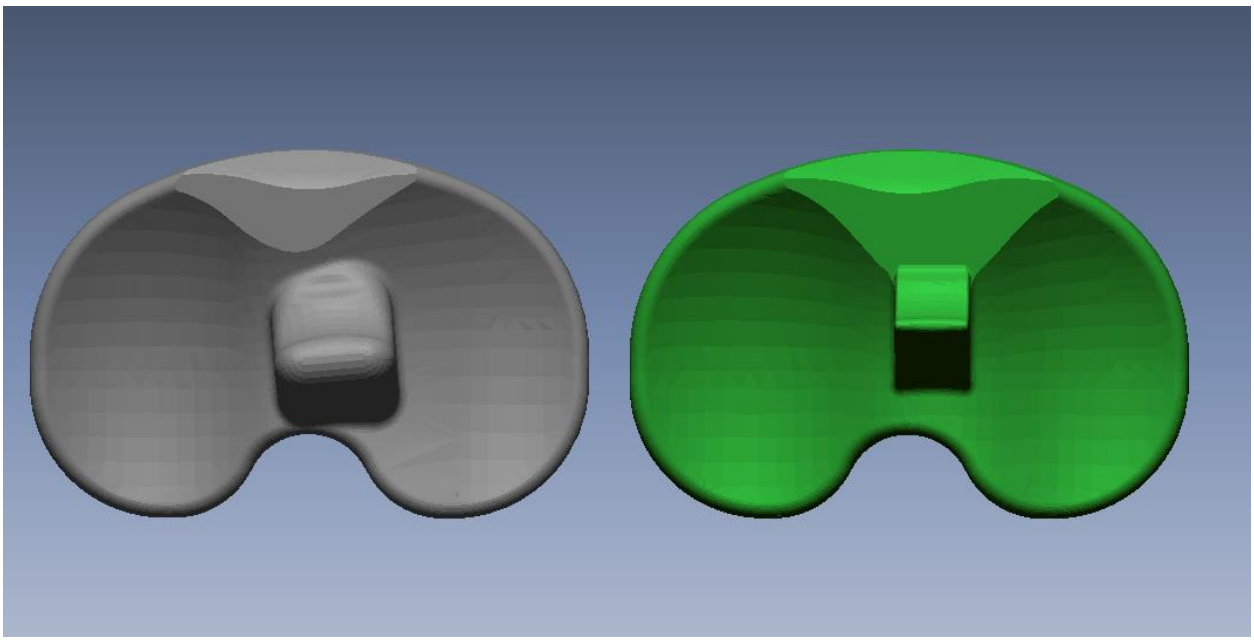

Figure 229: The Set 4 polyethylene (gray) had an angled post that is wider than the Set 3 polyethylene (green).

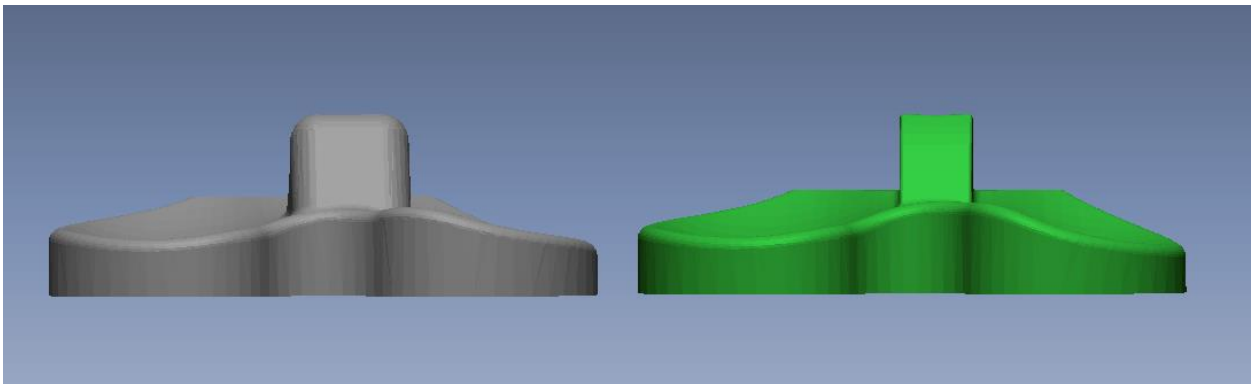

Figure 230: The Set 4 polyethylene (gray) had a lower anterior lip on the lateral condyle than the Set 3 polyethylene (green).

Making the lateral condyle flatter lowered the cam forces, as seen previously in the Set 3 with flat lateral plateau results. The cam force was reduced to 0.1 x BW (Figure 231). The lateral condyle sat more anterior than the other simulations starting at -5.0 mm and translating to -0.4 mm (Figure 232). The medial condyle translated from -4.0 to -6.0 mm (Figure 233). The internal rotation started at -1.2° and ended at 6.8° (Figure 234). Interestingly, the cam force was only active for the last 5° of flexion, indicating that the anterior cam and post was not necessary to obtain these results (Appendix I: PCR Simulations).

Set 5

The Set 4 and Set 5 femurs were identical. The post was similar to the Set 5 post. However, the inferior portion of the post was reduced in the AP direction and rounded more (Figure 235). The polyethylene in Set 5 had the same medial plateau as Set 4. However, the lateral plateau had a lower posterior lip in Set 5, resulting in decreased conformity (Figure 236).

The lower posterior lip allowed the lateral condyle to be more posterior, causing the post to engage at 9° (Figure 237). The peak anterior cam force was 0.2 x BW. The lateral condyle translated from -6.0 mm to -1.7 mm (Figure 238). It sat posterior to Set 4 at all angles due to the reduced posterior lip on the lateral plateau. The medial condyle showed very little overall translation starting at -4.7 mm and ending at -4.8 mm (Figure 239). The knee internally rotated with extension from -2.0° to 3.5° (Figure 240). This is less rotation than Set 4 achieved because the lateral condyle was not pushed as far anterior in extension.

Set 6

Set 5 and Set 6 featured an identical femoral component. The post on Set 6 was slightly wider than on Set 5, resulting in a slightly larger radius of curvature for the curved portion of the post (Figure 241). The polyethylene of Set 6 had a greatly reduced lateral anterior lip designed to allow the lateral condyle to

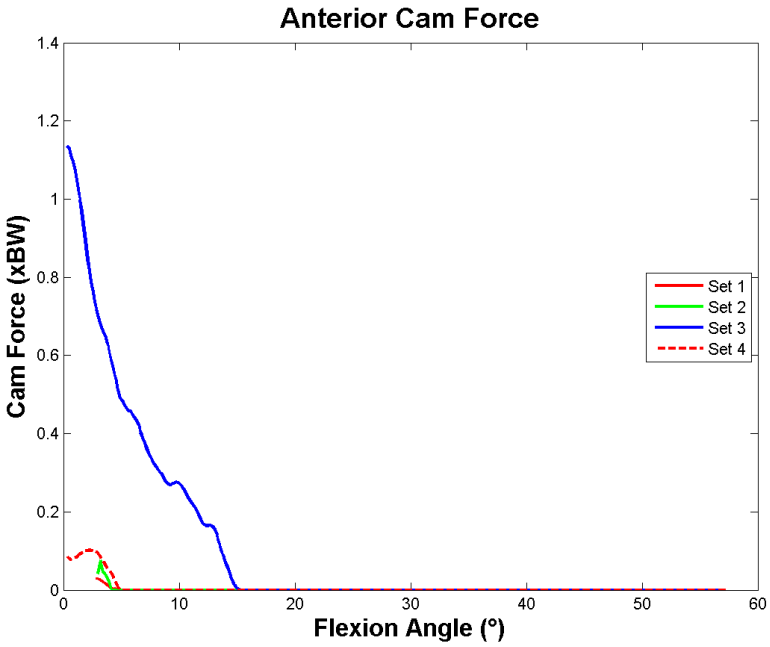

Figure 231: The anterior cam/post force is shown for Set 1 – 4.

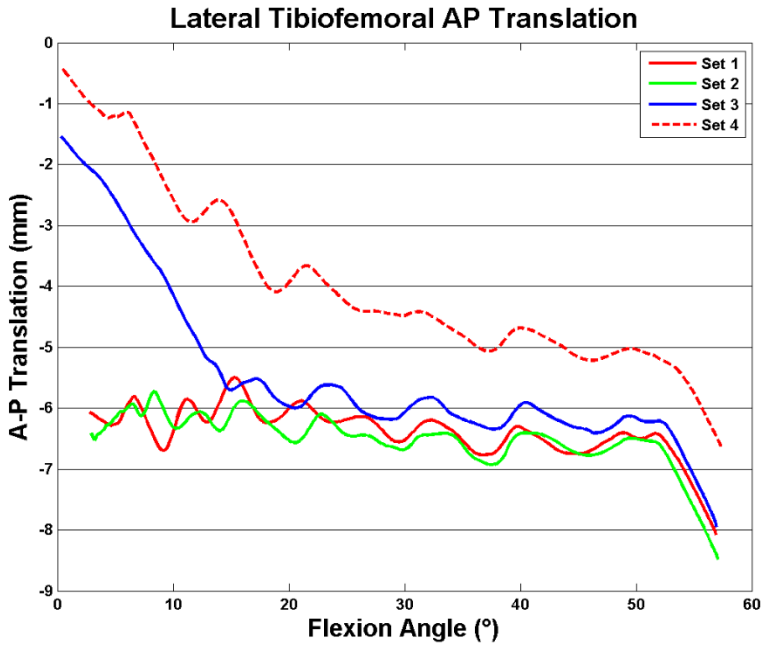

Figure 232: The lateral condyle translations are shown for Set 1 - 4.

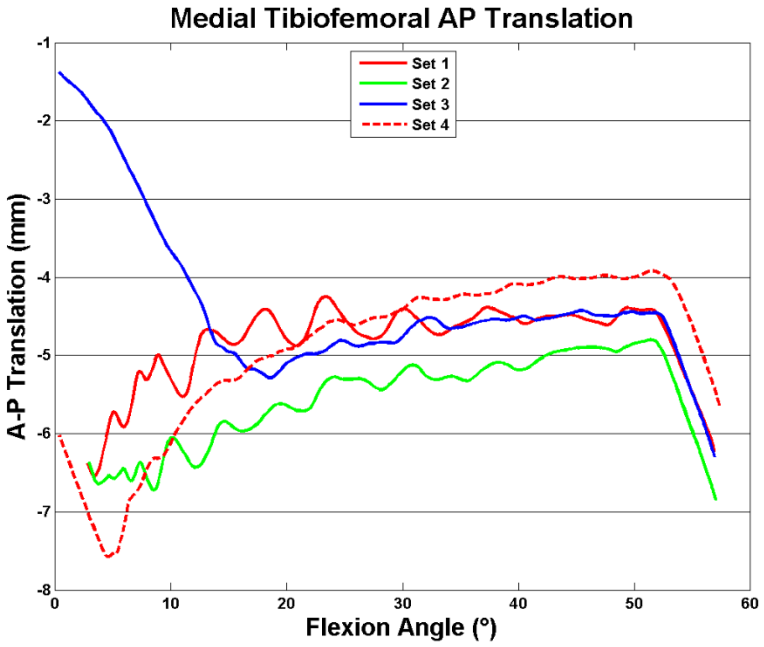

Figure 233: The medial condyle translations are shown for Set 1 - 4.

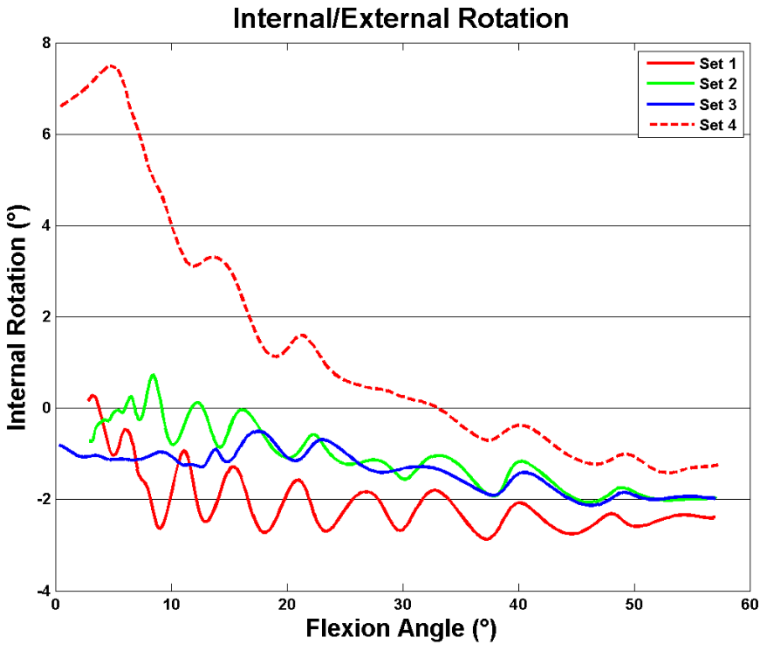

Figure 234: The axial rotations are shown for Set 1 - 4.

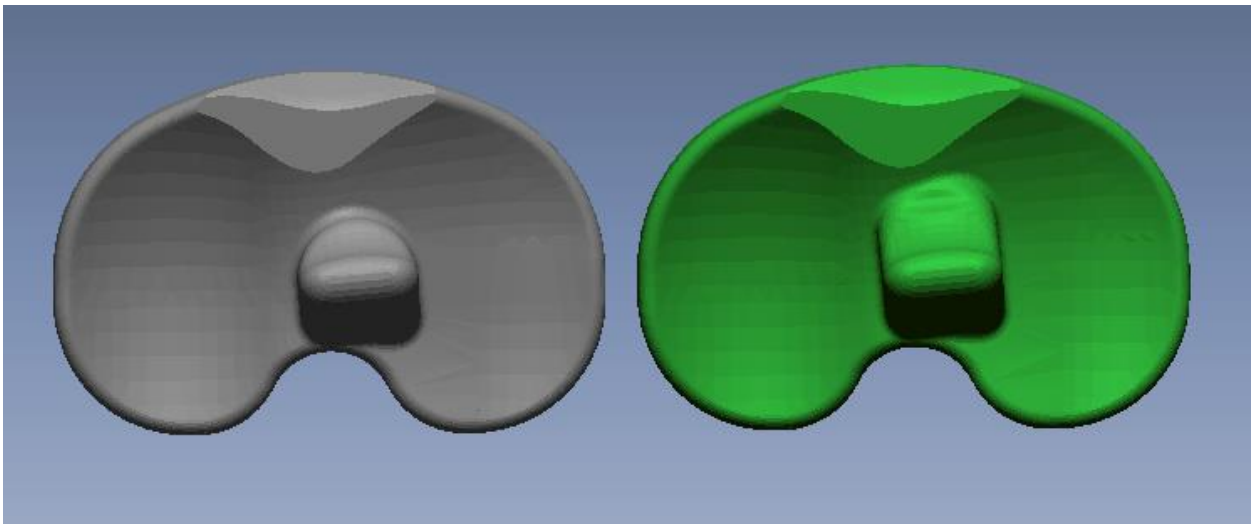

Figure 235: The post on the Set 5 polyethylene (gray) was smaller in the AP direction than that of the Set 4 post (green).

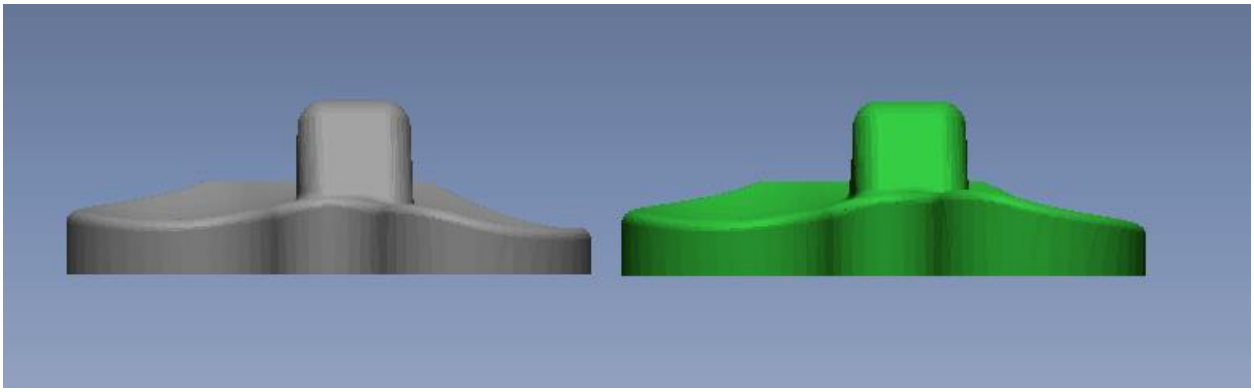

Figure 236: The lateral plateau of the Set 5 polyethylene (gray) had a smaller posterior lip than the Set 4 polyethylene (green).

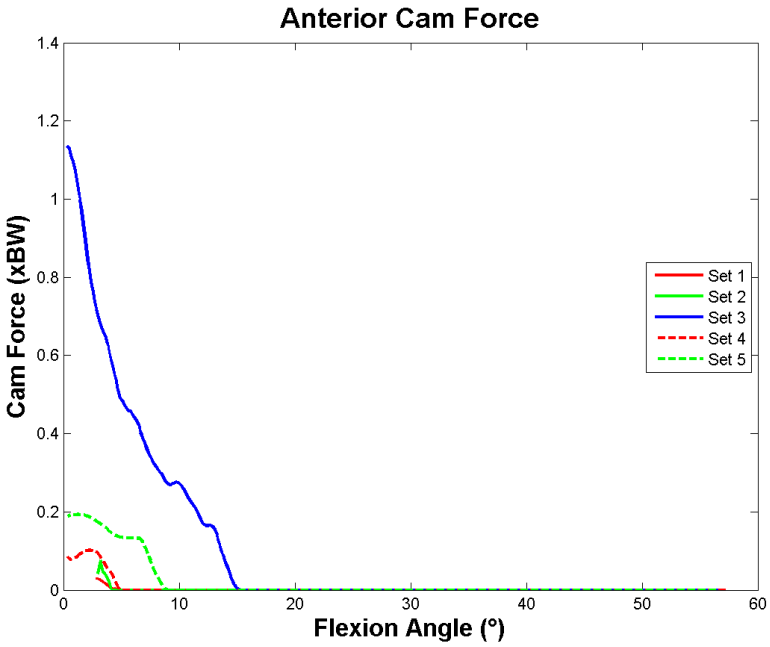

Figure 237: The anterior cam/post force is shown for Set 1 – 5.

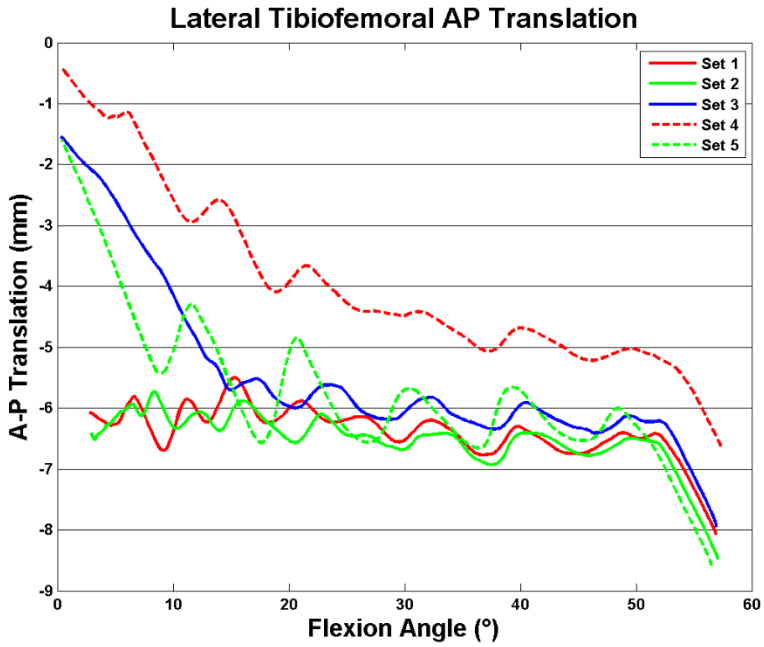

Figure 238: The lateral condyle translations are shown for Set 1 - 5.

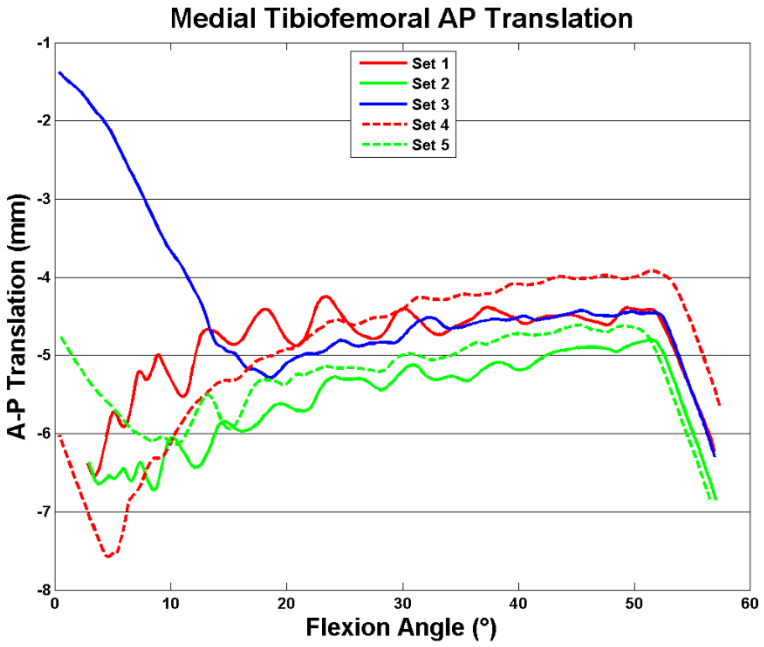

Figure 239: The medial condyle translations are shown for Set 1 - 5.

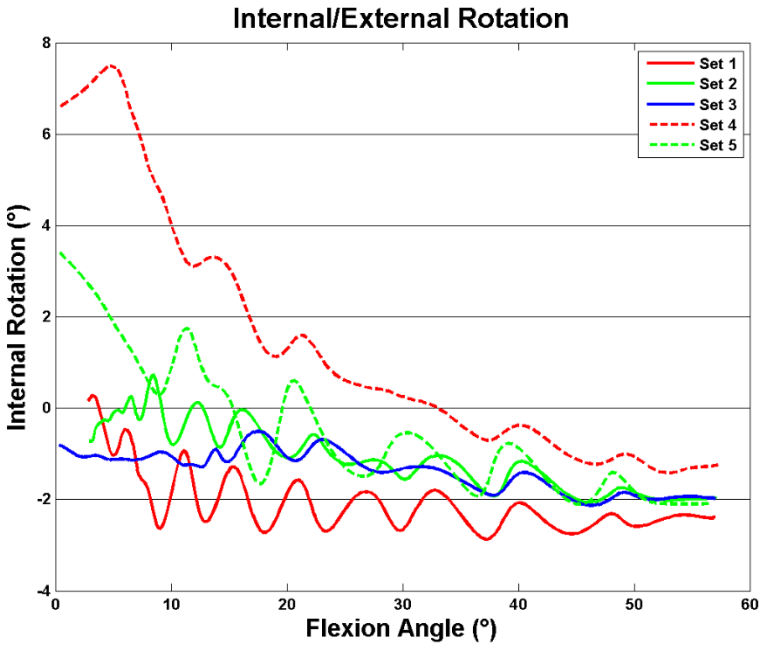

Figure 240: The axial rotations are shown for Set 1 - 5.

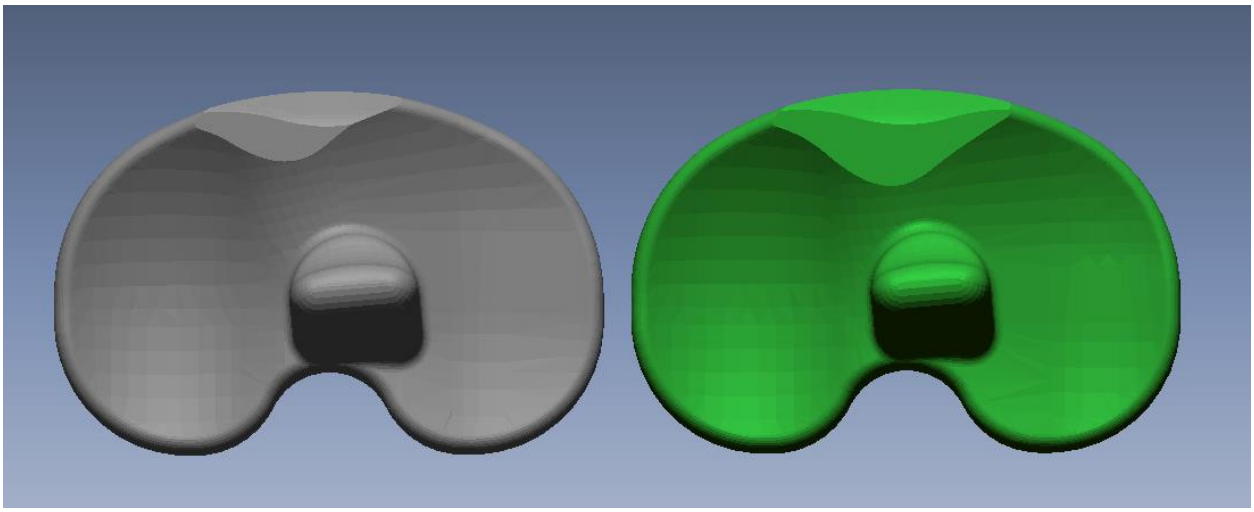

Figure 241: The Set 6 post (gray) was slightly wider than the set 5 post (green).

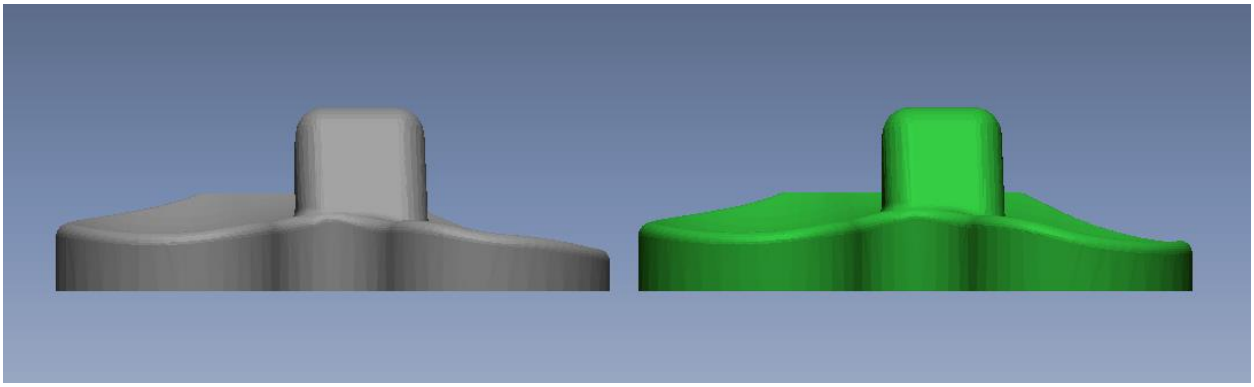

Figure 242: The set 6 lateral plateau (gray) had a smaller anterior lip than Set 5 (green).

roll forward in full extensions when the anterior cam/post mechanism engages (Figure 242). The medial condyles were very similar.

By lowering the anterior lip on the lateral condyle, the lateral condyle sat more anteriorly in extension causing the cam/post mechanism to engage later in extension than Set 5. The cam contacted at roughly 7° of flexion and the peak force was 0.1 x BW (Figure 243). The lateral condyle started at -6.0 mm as Set 5 did but translated more anteriorly ending at -1.0 mm (Figure 244). The medial condyle behaved nearly identically to Set 5 by both starting and ending at -4.8 mm posteriorly (Figure 245). Set 6 had slightly more rotation than Set 5 by starting at -1.8° and ending at 4.4° (Figure 246).

Summary

The simulations confirmed some important theoretical concepts. First, it was shown that sliding the post anterior causes early post engagement with contact angles ranging from 7° to 15°. Secondly, the model showed the dangers of having an anterior post while also having large anterior lips. The cam force was as high as 1.3 x BW when both condyles were forced onto the anterior lip. However, by flattening the anterior lip on the lateral plateau while maintaining the medial lip, these forces worked to the advantage of the subject. The medial condyle was held posteriorly while the lateral condyle was allowed to translate anteriorly, resulting in internal rotation with extension. Finally, decreasing the height of the lateral plateau posterior lip causes the lateral condyle to sit my posteriorly, while decreasing the height of the anterior lips causes the lateral condyle to sit more anteriorly as expected. Overall, model changes which caused the lateral condyle to move anteriorly resulted in more normal axial rotation while changes which caused the lateral condyle to sit more posteriorly had less normal rotation. To compare simulations for Set 3 – Set 6 for ASTKA and PCR designs, see Appendix I: PCR Simulations (Figure 247 - Figure 250).

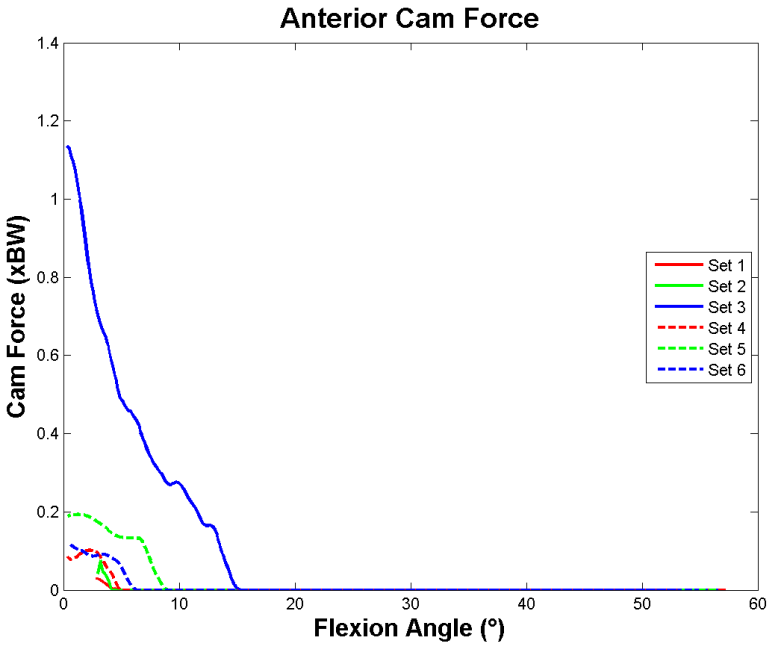

Figure 243: The anterior cam/post force is shown for Set 1 – 6.

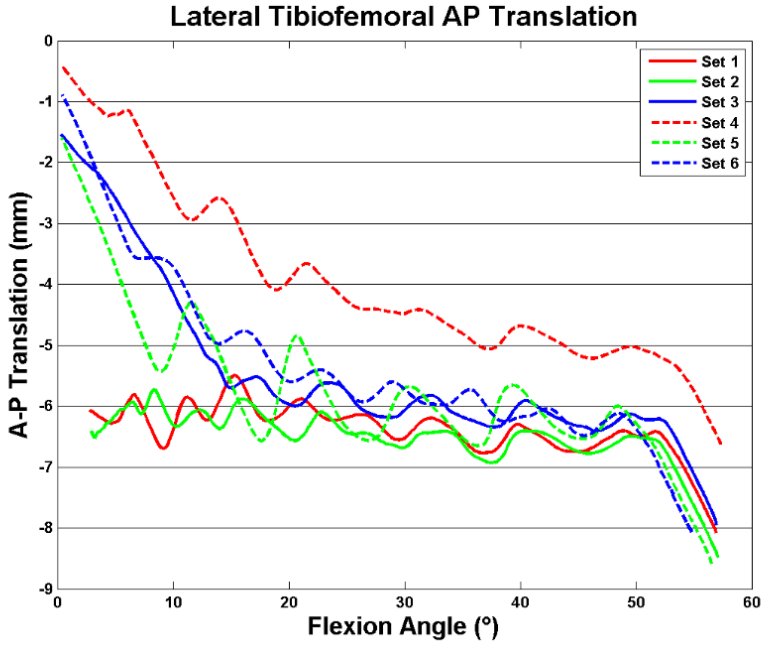

Figure 244: The lateral condyle translations are shown for Set 1 - 6.

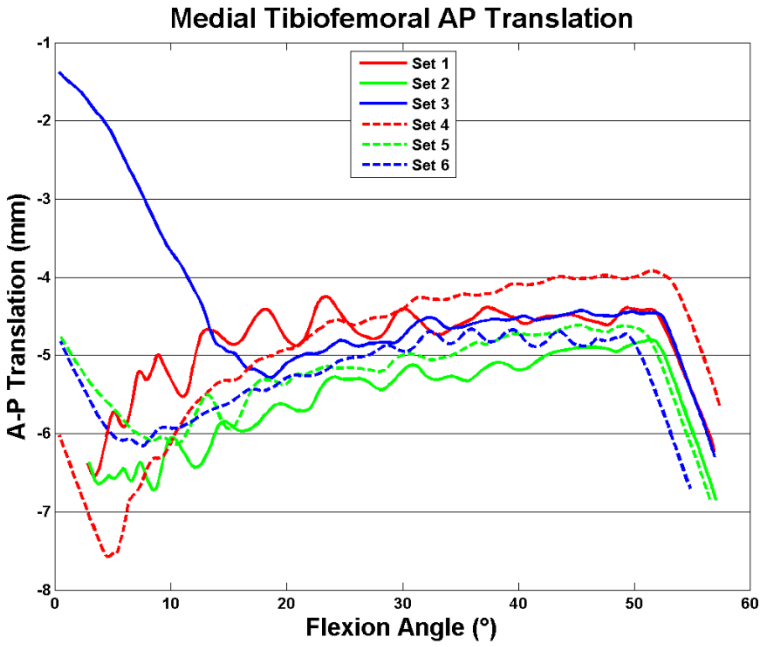

Figure 245: The medial condyle translations are shown for Set 1 - 6.

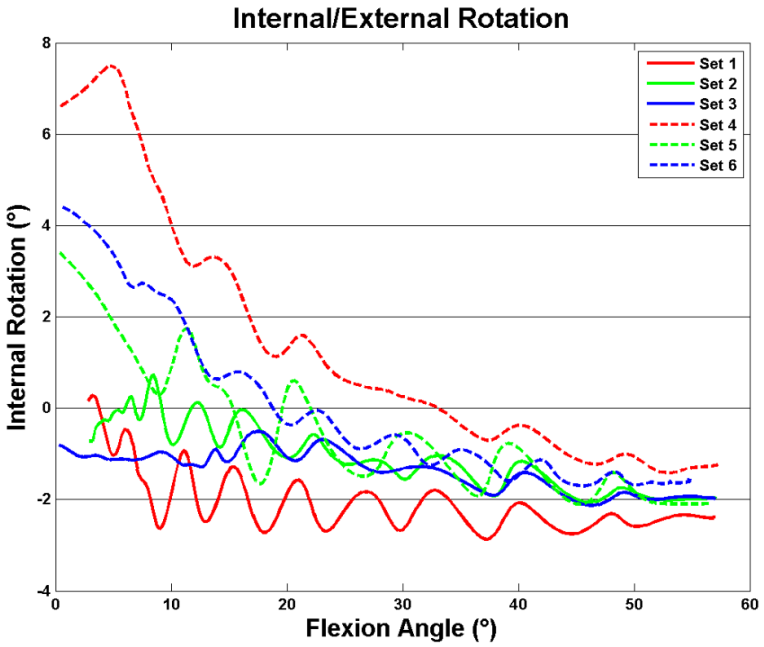

Figure 246: The axial rotations are shown for Set 1 - 6.

Chapter 8: Summary

By refining the model, many important additions have been made. First, the model has been expanded to represent more types of implants. Originally capable of handling FB PCR TKA, the model can now handle PS and MB designs. Furthermore, the code is generic enough that less common designs such as tri-condylar or bi-cruciate stabilizing could be analyzed.

In addition to handling more types of TKA, each TKA is represented more accurately. The full geometry of both the polyethylene and trochlear groove is now captured instead of only curvature in one plane. In addition to the more accurate geometry, some important changes were made to the models assumptions. First, the inaccurate low point contact assumption was replaced by contact detection.

Replacing the low point contact assumption allows for the true contact point to be found, resulting in a more accurate location and direction of the contact force. Furthermore, contact detection allows for the non-holonomic constraints to be removed. This results in a model which can detect lift-off.

The non-holonomic constraints were also removed at the patellofemoral joint. Because the true contact point is now found on the patella component, patellar flexion does not have to be specified. This allows the model to function as a patellofemoral joint simulator in addition to a tibiofemoral joint simulator. While the core objective of providing a forward solution model which can predict knee mechanics and be used as a design tool has not changed from Dr. Mueller's work, the model has been considerably enhanced in this regard. It can now analyze more types of implants as well as more accurately represent the geometries of those implants. With this new model, it is important to look at early results to see the improvements.

In addition to the improvements listed, a new GUI was developed. Now that the model has reached a level of truly functioning as a knee simulator, it is crucial that multiple individuals can use this model to

continue the work set forth here. Therefore, the GUI provides a user-friendly method of setting up new simulations. This includes defining the articulating geometries, allowing users to select implant orientations, and selecting the initial position of the simulation. Furthermore, users can change ligament origins, insertions, stiffness, and reference strains. This GUI also saves and loads simulations to make it easier to modify or double check a given simulation in the future. Finally, the GUI provides a way to plot the results of individual simulations and sensitivity analyses. While the forward model provides a powerful analysis tool, the GUI allows this tool to be accessed and utilized by more people with far less training.

Many simulations were performed using the forward model, and the results presented here show a few very important things about the model. This first is that the model agrees with what intuition would tell us. When shifting the polyethylene rotation centers during the initial Sensitivity Analysis, a lateral shift of the pivot point caused a larger external rotation, as expected. Furthermore, the sensitivity analysis showed several expected results. Most notably, both condyles rolled considerably posteriorly after the cam and post engaged. Furthermore, the asymmetric polyethylene designs had large internal rotations because the posterior lip of the lateral plateau was too low. These simple checks show the model can be trusted when it makes predictions where our intuition is not as strong.

The second important takeaway from these results is the sensitivity of the model. Altering the location of the pivot point in the TKA-I and TKA-II designs resulted in a polyethylene rotational difference of 10°. In the sensitivity analysis, femoral design caused the femoral rotation to change by more than a degree. Because the model is sensitive, it can be trusted to differentiate between theoretical designs.

After the sensitivity analysis, the transition to a four-point contact model revealed the importance of an area contact instead of point contact. Both the length and width of the contact box strongly affected polyethylene rotation. Furthermore, the ratio of the force between the points highly impacted the

results, showing that the force cannot be uniform across the contact area. These simulations showed less sensitivity after cam/post engagement. However, these simulations did not have the updated cam/post definition and assumed the post was a vertical plane. Having a curved post would allow for more rotation of the polyethylene relative to the femur and could increase the sensitivity. For these reasons, a 49 point contact grid was developed which still used non-holonomic constraints.

Further improvements were made by shifting to contact detection using point clouds on the femoral component condyles and cam and the patella. This allows for more accurate contact maps which do not have to include the low point on the femur (as the non-holonomic constraints did). Furthermore, the contact point on the patella is no longer specified. This means the correct moment arms for the quadriceps muscles and patella ligament on the patella are utilized. Therefore, patella flexion does not have to be specified, and the patella has six degrees of freedom making the forward solution model useful as a patellofemoral joint simulator.

The simulations of Femur 123-127 showed that rotating the trochlear groove could produce femoral rotations in deep flexion. For Femur 123, Femur 125 and Femur 126, the least external rotation was seen in Femur 123 which did not have any rotation of the trochlear groove. Femur 125 had more rotation as the trochlear groove was rotated 5°. The most external rotation was seen in Femur 126 which had 10° of rotation in the trochlear groove. These results held true for both the fixed bearing and mobile bearing designs. It was caused by less medial femoral rollback and increased lateral femoral rollback. It also resulted in lower tibiofemoral and peak femoral forces. While these results are promising, it is important to remember that it was assumed the patella could not axially rotate due to the constraints of the patellar tendon. In-vivo the patellar tendon likely has some motion allowing for axial rotation of the patella.

The results of anatomical verses mechanical alignment were inconclusive. While the simulations showed more normal axial rotation and with anatomical alignment, the lateral and total tibiofemoral forces were much higher with anatomical alignment. These results also cannot be extended to all TKA types based on the results of a single TKA. While these simulations were important for demonstrating the model's sensitivity to implant alignment, they do not suggest one alignment is preferable.

The rotated results of Poly 327 with the rotated post show that post shape can affect implant performance. By externally rotation the post, the lateral tibiofemoral contact point was pushed more posterior resulting in more external rotation. However, the rotated post also had earlier engagement so the results are a combination of post shape and post placement. Analysis of the ASTKA confirms the importance of post placement.

The analysis of ASTKA_R1, ASTKA_R2, and ASTKA_R3 provided valuable insight into how polyethylene design and cam/post design affect each other. First, it was demonstrated that shifting the cam anterior or the post posterior have the same results on implant performance. Next, the conformity variations on the polyethylene plateaus provided a great deal of information that aided in developing the new design. These simulations showed that if both the medial and lateral plateau were conforming, they would both shift forward similar amount when the cam/post engaged and there would be little effect on axial rotation. If the both plateaus were flat, similar results are seen. If the lateral plateau is made flat while the medial plateau is made more conforming, the lateral condyle can slide anterior while the medial condyle cannot. This resulted in restoration of the screw home mechanism.

With all changes to the model finalized, the model was validated against telemetry. The validation found the model had errors of 5% to 10% for predicting maximum tibiofemoral contact forces. The medial and lateral condyle translations were similar to those found in fluoroscopy. In both the model and telemetry, the condyles slid posteriorly in early flexion and anteriorly in late flexion. The condyles

experienced more posterior translation in the model than in-vivo, but the model very accurately predicted the medial and lateral condyle location at maximum flexion.

Once the model was validated, an effort to create a new ASTKA was undertaken. The objective was to design an implant which had lateral condyle roll forward in the last 20° of an extension activity to restore the screw home mechanism. Over the course of six simulations, the post was shifted laterally and the shape of the plateaus was varied many times. Eventually, a realistic post design was developed along with a relatively flat lateral plateau which resulted in a functional design with the desired kinematics. Through these simulations, the model truly proved its value as a theoretical knee simulator.

In summary, a forward solution model has been developed which functions as a theoretical knee simulator, and a GUI has been developed to setup simulations. Many simulations were performed which provided insight into how implanted design affected performance. They also provided insight into how the model could be improved. The improvements were implemented, and eventually the model was used to help develop a TKA which produced a desired kinematic profile in the simulator.

Chapter 9: Contributions

In the development of a novel total knee arthroplasty (TKA), there are currently no accurate methods to predict the performance of the new implant. Typically, the success of a knee implant is determined by tracking the success rate of an implant over many years. However, it would be ideal to predict the success of an implant before it went to market. Previously, wear simulators and cadaveric simulators offer the best options, but these do not recreate truly in-vivo conditions. Furthermore, they require the physical manufacture of the TKA, which limits the number of implants which can be tested.

To remedy these problems, Dr. John Mueller developed a forward solution model of the human knee. The original Mueller model simulates a patient virtually on a computer, allowing multiple knee implants to be quickly simulated. The model provided a useful tool which was validated against both fluoroscopy and telemetric implants and shown to provide successful results at predicting both kinematics and kinetics. However, as with all models, there is room for refinement. The end of Dr. Mueller's dissertation suggests several criteria for improving the model including the following as quoted from the dissertation.

1. Expand and refine the articulating 3-D geometry representation of the tibial tray and trochlear groove. This could include using splines and the ability to use NURBS.
2. Expand the GUI to make more user friendly and allow instant simulation with a new TKA design.
3. Add additional constraints so that posterior stabilized (PS) knees can be modeled and also add mobility to the insert so that rotating platform and mobile bearing TKA can be analyzed.
4. Allow for condylar lift off in the model.

Each of these was addressed along with the following contributions:

1. Expand polyethylene geometry representation to include both coronal and sagittal curvature.
2. Expand trochlear groove geometry representation to include both coronal and sagittal curvature.
3. Expand trochlear groove geometry representation to include the most inferior portions of the trochlear groove. The GUI has been refined more user friendly implementation of new designs.
4. Expand cam/post geometry representation to accurately describe post geometry.
5. Incorporate mobile bearing TKA using rotation friction.

6. Replace non-holonomic constraints at the tibiofemoral joint with contact detection, making lift-off theoretically possible.
7. Use contact detection at the tibiofemoral joint allowing the true contact point to be determined.
8. Use contact detection at the patellofemoral joint to make the model a better patellofemoral joint simulator.
9. Remove the constraint on patellar flexion so the patella will have all six degrees of freedom.
10. Develop the model in a way flexible enough to allow for novel designs to be incorporated with only minimal modifications. These could include non-centered rotation points for a mobile bearing design*, anterior stabilizing posts in bi-stabilizing designs, and tri-condylar designs.*

List of References

Dennis DA, Komistek RD, Mahfouz MR, et al. A multicenter analysis of axial femorotibial rotation after total knee arthroplasty. CORR 428 180:189, 2004.

Komistek RD, Steihl JB, Dennis DA, et al. Mathematical model of the lower extremity joint reaction forces using Kane's method of dynamics. J Biomech, 31(2): 185-9, 1998.

Mueller, John. “Development of a Rigid Body Forward Solution Physiological Model of the Lower Leg to Predict Non Implanted and Implanted Knee Kinematics and Kinetics” Diss. University of Tennessee. 2011

Komistek RD, Dennis DA, Mahfouz M. In vivo fluoroscopic analysis of the normal human knee. CORR 410 69:81, 2003.

Dennis DA, Komistek RD, Mahfouz MR: In vivo fluoroscopic analysis of fixed-bearing total knee replacements. Clin Orthop 410 114:130, 2003.

Cates HE, Komistek RD, Mahfouz MR, et al. In vivo comparison of knee kinematics for subjects having either a posterior stabilized or cruciate retaining high-flexion total knee arthroplasty. J Arthroplasty 23(7) 1057:1067, 2008

D’Lima DD, Townsed CP, Arms SW, et al. An implantable telemetry device to measure intra-articular tibial forces. J Biomech 38(2) 299:304, 2005.

D’Lima DD, Steklove N, Fregly, BJ, et al. In Vivo Contact Stresses during Activities of Daily Living after Knee Arthroplasty. J Orthop Res 26 1549:1555, 2008.

Anderson FC, Pandy MG. Dynamic optimization of human walking. J Biomech Eng. 123: 381-390, 2001.

Komistek R.D, Stiehl JB, Dennis DA. Mathematical model of the lower extremity joint reaction forces using Kane’s method of dynamics. J Biomech 31 185-189, 1998.

Komistek RD, Kane TR, M Mahfouz, Ochoa JA, Dennis DA. Knee Mechanics: A review of Past and Present Techniques to Determine In Vivo Loads. J Biomech 38(2) 215:228, 2005.

Delp SC, Anderson FC, Arnold AS, et al. OpenSim: Open-Source Software to Create and Analyze Dynamic Simulations of Movement. IEEE Trans Biomed Eng 54 1940:1950, 2007.

Thelen DG, Anderson FC. Using Computed Muscle Control To Generate Forward Dynamic Simulations of Human Walking from Experimental Data. J Biomech 39 1107:1115, 2006.

Arnold EM, Ward SR, Liber RD, Delp SL. A Model of the Lower Limb for Analysis of Human Movement. Ann Biomed Eng 38 269:279, 2010.

Innocenti B, Pianigiani S, Labey L, et al. Contact Forces in Several TKA Designs during Squatting: A Numerical Sensitivity Analysis. J Biomech. 44 1573:1581, 2011.

Damsgaard M, Rasmussen J, Christensen ST, et al. Analysis of Muscoloskeletal Systems in the AnyBody Modeling System. Simulation Modeling Practice And Theory. 14 1100:1111 2006.

Marra MA, Vanheule V, Fluit R, et al. A Subject-Specific Musculoskeletal Modeling Framework to Predict In Vivo Mechanics of Total Knee Arthroplasty. J Biomech Eng. 137 2015.

Sharma, Adrija. "Development of a Computational Model to Predict the In Vivo Contact Mechanics of Modern Total Knee" Diss. Univeristy of Tennessee. 2008.

Incavo SJ, Schmid S, Sreenivas K, et al. Total knee arthroplasty using anatomic alignment can produce mid-flexion laxity. Clin Biomech 28 429:435, 2013.

Victor J, Mueller JK, Komistek RD, et al. In vivo kinematics after a cruciate-substituting TKA. CORR 468(3) 807:814, 2010.

D'Lima DD, Townsend CP, Arms SW, et al. An implantable telemetry device to measure intra-articular tibial forces. J Biomed. 38(2) 299:304, 2005.

Mahfouz MR, Hoff WA, Komistek RD, Dennis DA. A robust method for registration of three-dimensional knee implant models to two-dimensional fluoroscopy images. IEEE Trans Med Imaging. 22(12) 1561:1574, 2003.

Appendices

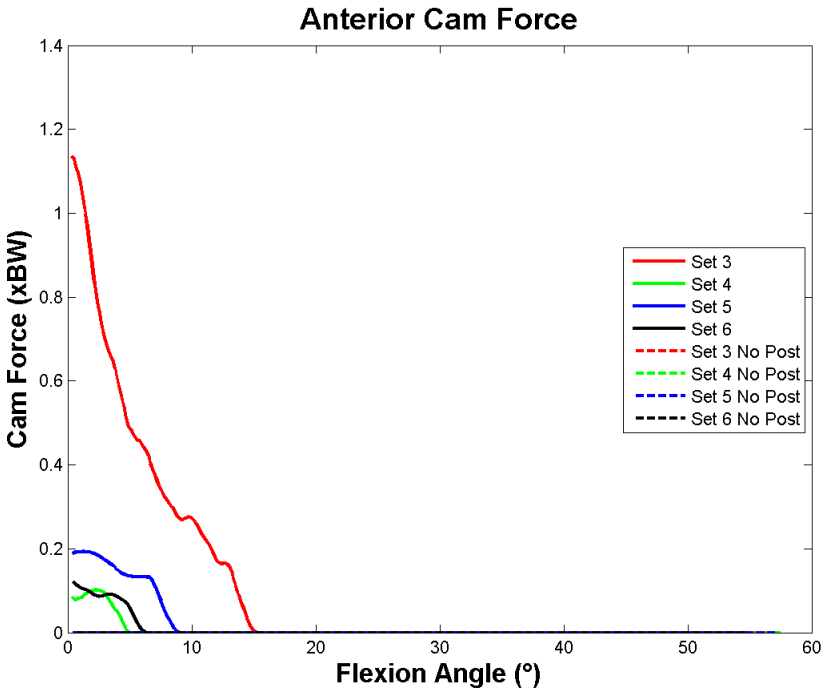

Figure 247: The ASTKA forces are shown. They are 0 for the no post simulations by definition.

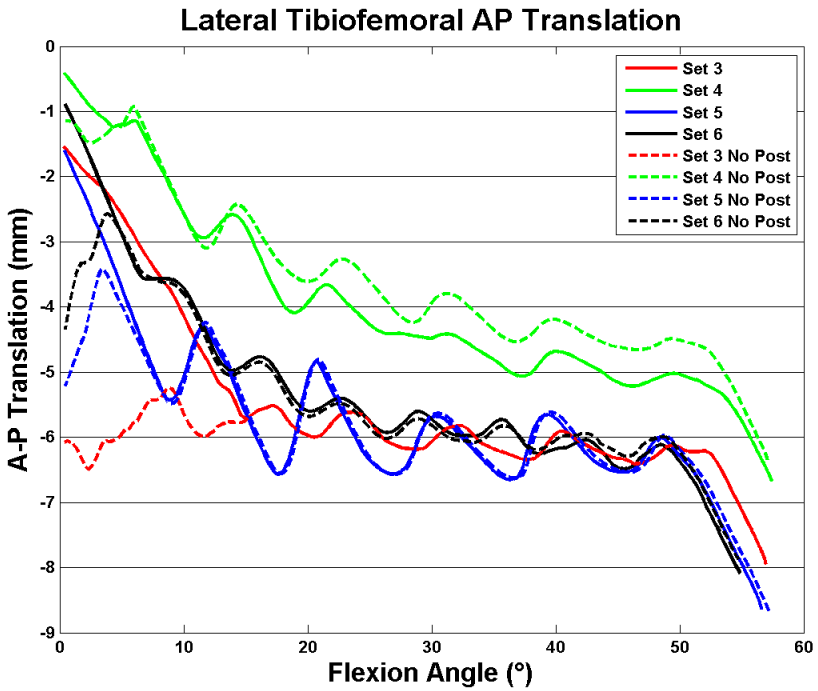

Figure 248: The lateral translations move more anterior in the ASTKA simulations than the PCR simulations.

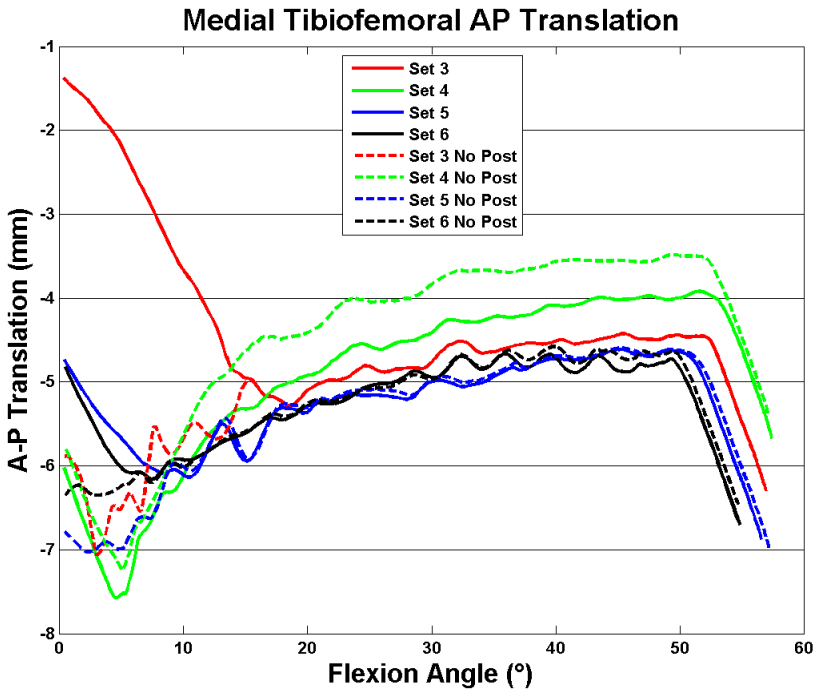

Figure 249: The difference in medial translation between ASTKA and PCR simulations was fairly small regardless of the post except for in Set 3.

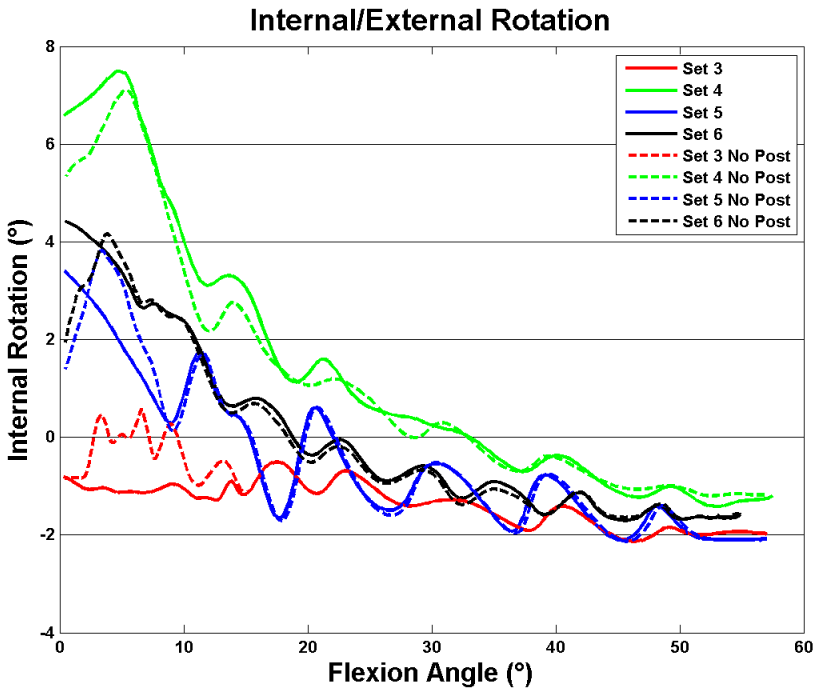

Figure 250: Internal rotation angles are shown for ASTKA and PCR simulations. N.B. Even though Set 3 had the largest cam forces, it saw no change in rotation due to the medial and lateral plateaus being fairly symmetric.

Vita

Brad Meccia was born on July 31st, 1986 in Fort Leonard Wood, Missouri. He inherited a love of mathematics, science, and athletics from his father. Academically motivated, Brad enrolled in advanced placement classes in high school. After placing among the top ten students in the Fermat Math Exam, Brad received a full scholarship to the University of Tennessee.

As an undergraduate, Brad continued his interest in both the academics and athletics by majoring in biomedical engineering and competing for the University of Tennessee Rugby Club. As a senior, he enrolled in a graduate level mathematical modeling class which led to a position at the Center for Musculoskeletal Research.

During his time at the Center for Musculoskeletal Research, Brad performed fluoroscopic analysis of both the shoulder and the knee. He also spent considerable time developing knowledge in the field of mathematical modeling. This knowledge was used to perform the work documented here. It also provided him the opportunity to write a chapter for “Surgery of the Knee” by Insall & Scott, a leading resource in the field.

As a firm believer that life requires a balance between the mind and body, Brad took up partner dancing when injuries forced him to retire from rugby. His passion for dance combined with a life-long basis in athletics resulted in him becoming an internationally recognized instructor. Upon graduation, Brad intends to spend the next year traveling the world and then continuing his career in orthopaedics.